UNIVERSITÀ
DEGLI STUDI
FIRENZE

# DOTTORATO DI RICERCA IN SCIENZE CHIMICHE

CICLO XXXI

COORDINATORE Prof. Piero Baglioni

# LOWER ENVIRONMENTAL IMPACT FORMULATIONS FOR EUROPEAN SHALE GAS PLANTS

# FORMULAZIONI A BASSO IMPATTO AMBIENTALE PER FORMAZIONI EUROPEE DI GAS DA ARGILLE

Settore Scientifico Disciplinare CHIM/02

**Dottorando**
Dott. Tatini Duccio

**Tutore**
Prof. Lo Nostro Pierandrea

**Coordinatore**
Prof. Piero Baglioni

Anni 2015/2018

# Abstract

Nowadays, shale gas is the fastest growing natural unconventional gas resource worldwide, as a result of the combination between major technological developments and geopolitical events. Despite the great potential in terms of exploitable reservoirs, several environmental issues have been associated to shale gas extraction and hydraulic fracturing, like induced seismicity, greenhouse gas emissions, and water contamination. In this perspective, the formulation of environmentally-safe fracturing fluids plays a crucial role in the minimization of the environmental footprint of shale gas exploitation. In this work we proposed two completely green and eco-compatible fracturing fluid formulations specific for the shale gas formations in Europe. These formulations must possess well-defined properties in terms of composition and operative performances, including the absence of controlled or toxic substances, an appropriate viscosity for proppant transport, the effectiveness in high pressure, temperature and salinity conditions and the presence of specific additives to limit the extraction of Naturally Occuring Radioactive Materials (NORM). The first formulation we developed is a linear gel based on four different green polysaccharides, namely guar gum, sodium hyaluronate, sodium alginate and hydroxpropylcellulose. The second is a viscoelastic surfactant-based (VES) fluid, composed by an eco-compatible surfactant, sodium oleate, and a inorganic salt, KCl. Rheological measurements, Optical Microscopy, Differential Scanning Calorimetry (DSC) and Small Angle X-Ray Scattering experiments were performed in order to assess the main physico-chemical properties of the formulations and their fluid behaviour. All the formulations show a very high viscosity (optimal to avoid proppant sedimentation), a high shear resistance and a good thermal stability. Moreover, we tested their effectiveness at high temperature, high pressure and salinity content, demonstrating that the variation in these geochemical parameters can be effectively used to modulate the fluid rheological behaviour.

The polysaccharide-based and the VES formulations were then implemented by the inclusion of two specific additives, Carbon Black and Azorubine, which induces a fluid responsiveness to specific external stimuli, namely an applied electrical voltage and UV light. Rheological, DSC and SAXS experiments demonstrated that in both cases the fluid viscosity can be modulated using an applied input. The addition of Carbon black brings about also an enhanced thermal resistance and the possibility to recover and re-use the fluid.

In the last part of the work we developed two completely safe and environmental friendly approaches to limit the amount of NORM in the flowback water and for the treatment of wastewaters after the extraction of the shale gas. The first method is a physical treatment consisting in the exposure of the fracfluid to a weak static magnetic field before being pumped in the pipelines (Magnetic Water Treatment, MWT). The second method is based on the use of green innovative scale inhibitors, polyglutammate and polyaspartate, to replace the non-ecocompatible polyacrilates in fracfluid formulations. Optical microscopy, Fluorescence Spectroscopy and X-Ray Diffraction experiments showed that the combined effect of an external magnetic field and high temperature reduces the amount of insoluble alkali earth metals scales ($CaCO_3$, $BaCO_3$, $SrCO_3$and $CaSO_4$) and limits NORM extraction, since the formation of fewer scales of larger dimensions makes more difficult the flowback of NORM ions. Qualitative precipitation and solubility experiments demonstrated the effectiveness of the green antiscalant agents in reducing the precipitate and controlling the crystals size of $CaSO_4$ and $SrSO_4$. The high temperature does not affect the anti-scaling performances, which are even enhanced when added to a polysaccharide-based formulation. For this reason, the use of very small amounts of these green additives could be a simple way to limit the formation al of mineral scales, also in the presence of radioactive materials, such as radium salts.

# Table of Contents

# List of Figures

# List of Tables

# List of Abbreviations

| | |
|---|---|
| **CB** | Carbon black |
| **CMC** | Critical Micelle Concentration |
| **DSC** | Differential Scanning Calorimetry |
| **EMG** | Exponentially modified Gaussian function |
| **GG** | Guar Gum |
| **HB** | Hydrogen bond |
| **HEC** | Hydroxyethyl cellulose |
| **HPC** | Hydroxypropyl cellulose |
| **MF** | Magnetic Field |
| $\mathbf{M_w}$ | Molecular Weight |
| **MWT** | Magnetic Water Treatment |
| **NaOL** | Sodium Oleate |
| **NORM** | Naturally Occurring Radioactive Material |
| **PAC** | Polyacrylate sodium salt |

| | |
|---|---|
| **PAS** | Polyaspartate sodium salt |
| **PG** | Polyglutamate sodium salt |
| **SAXS** | Small Angle X-Ray Scattering |
| **SA** | Sodium Alginate |
| **SH** | Sodium Hyaluronate |
| **VES** | Viscoelastic Surfactant |
| **XRD** | X-ray Diffraction |

# Chapter 1 Introduction

## 1.1 Shale Gas

Over the last century the importance of securing abundant, economic, and environmentally conscious energy sources for the continuous improvement of our standards of living and for sustaining our economy has been a crucial issue addressed by governments, academia, private corporations and stakeholders.[1] Europe currently imports 50% of the natural gas it uses, and every year it must seek new gas contracts, often in competition with Asia. Because conventional oil reserves are diminishing and renewable energy sources are not yet able to provide sufficient and affordable energy in the large scale and consistently, shale formations have the potential of providing large sources of gas for decades to come.[2]

Shale gas is natural gas that is found trapped within shale formations.[3] Shale is a sedimentary rock formation which contains clay, quartz and other minerals. The natural gas contained in shale reservoirs has the same primary chemical composition as the natural gas contained in conventional reservoirs – normally up to 95% methane. The main difference is in the geological and physical properties of the reservoirs in which the natural gas is stored rather than the composition of the gas itself. Shale reservoirs are often classified as ‘unconventional’ (like coal-bed methane, gas from tight sandstones, and methane hydrates) because they contain oil and natural gas that were generated in the shale itself, and because they do not naturally have sufficient permeability to allow the oil and gas to flow at commercial rates.[4] In order to overcome this limitation, a specific process was developed to increase the effective permeability through the creation of high conductivity channels in the form of fractures within the formation. This process is called Hydraulic Facturing (or “Fracking”).

Shales are present worldwide in the sedimentary sequence. Large sedimentary basins, where sediments accumulated over millions of years, are favourable places to find large extent shale deposits of sufficient thickness. Certainly not all shales contain reasonable quantities of natural gas. Geologic modelling can lead exploration geologists to promising locations, and the subsequent investigation of drilled rock samples will eventually give information on the gas content of the shales.

Since large-scale shale gas production is ongoing only in North America, information on the location of gas shales worldwide is rather incomplete. The 2013 U.S. EIA report[5] summarized information on 95 shale basins in 41 countries, which are shown in Figure 1.1.

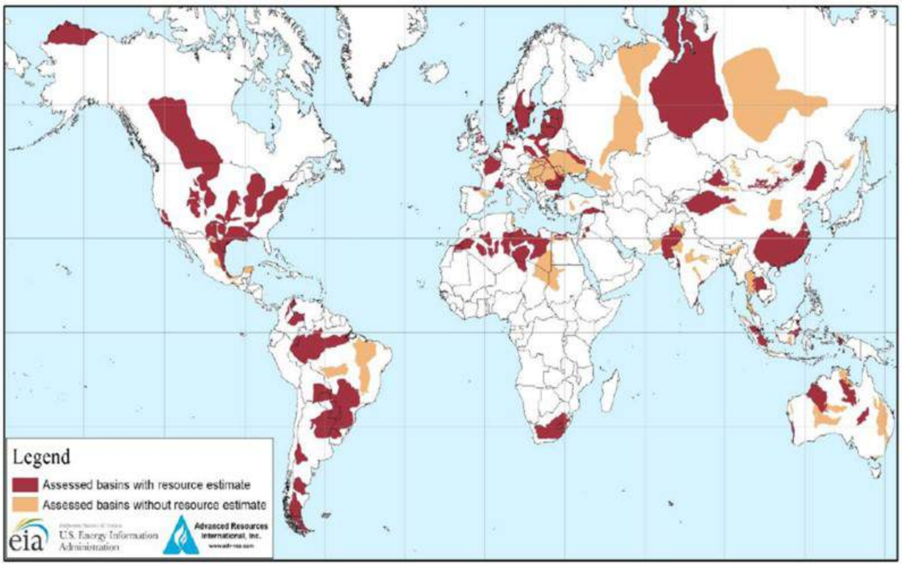

Figure 1.1 – Map of major shale gas basins in 41 countries. From ref.[5]

In Europe shale gas represents an unconventional resource abundant and not yet exploited. The European Commission, EC, suggests that ‘shale gas could meet about 10% of the EU gas demand by 2035’.[6] The US Energy Information Administration, EIA, in 2013 estimated reserves in Europe of ~470 trillion cubic feet, tcf, (26 in the UK, 137 in France, 32 in Denmark, 17 in Germany, 8 in Spain, 148 in Poland, 51 in Romania, etc.), which is less than those estimated for the USA (567 trillion cubic feet), but more than those estimated for the former Soviet Union, Australia and Brazil.[5] Most shale formations in Europe are inland, but some are also off shore, especially in the North and Baltic Seas and in the East Irish Sea.

However, unlocking natural gas and oil trapped in shale plays not only remains challenging, but also has a poorly understood environmental impact. The fractured wells are not always productive, the productivity of a gas well decays rapidly with time, and natural gas yields are at most 15-20% when liberated using hydraulic fracturing.[7] Further, and more importantly, alarming reports (albeit sometimes controversial) suggested the possible causality between the fracturing of shale formations and contamination of drinking water,[8] micro-seismicity,[9,10] and release of gases with high global-warming potential.[11,12] The EC warns that public concern will persist as long as legal uncertainty remains: there is a lack of transparency and the possible negative impacts and risks are not addressed, managed, and mitigated. Moreover the environmental impacts, including greenhouse gas emissions and water and air quality, do not respect national borders.[6]

In this perspective, in Europe one of the primary objective is to assess the environmental footprint of shale gas exploitation in terms of water usage and contamination, induced seismicity and fugitive emissions, using a comprehensive approach which takes into account all the processes involved in the extraction of natural gas from a shale play. In particular the formulation of hydraulic fracturing fluids plays a major role in limiting the production of wastewater and the extraction of undesired substances from a formation, minimizing the environmental impact and maximizing gas production.

## 1.2 Hydraulic Fracturing

A distinctive feature of shale reservoirs is the very low permeability, which prevents the shale gas to readily flow into a well. Thus, an additional stimulation is required to increase the permeability and facilitate the gas flow thorough the rocks, optimizing the gas production. This process is the Hydraulic Fracturing, which consists in the high-pressure injection of a 'fracking fluid' (primarily water, containing sand, the ‘proppant’, suspended with the aid of thickening agents, and other chemicals) into a wellbore to create cracks in the deep-rock formations.[13] Figure 1.2shows a schematic representation of hydraulic fracturing process.

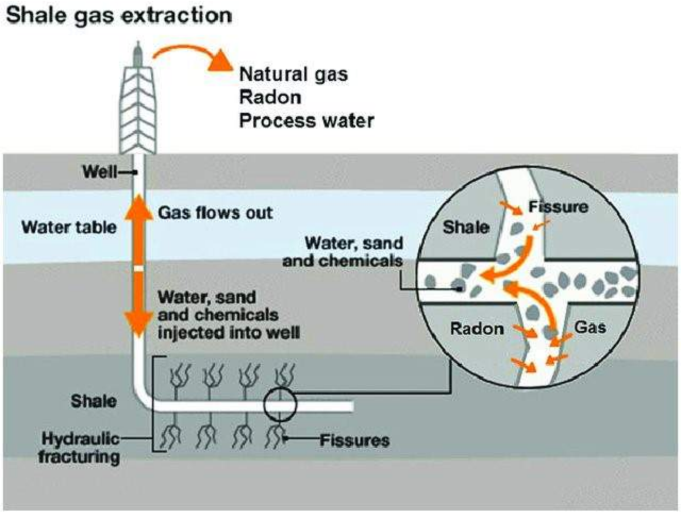

Figure 1.2 – Schematic representation of the hydraulic fracturing process. From ref.[14]

Once a well has been drilled and cased, explosive charges perforate holes along selected intervals of the well within the shale formation from which shale gas is produced. Pumps are used to inject fracturing fluids under high pressure into the well. The injection pressure generates stresses in the shale that exceed its strength, opening up existing fractures or creating new ones. The fractures extend a few hundred metres into the rock and the newly created fractures are propped open by the sand. Additional fluids are pumped into the well to maintain the pressure in the well so that fracture development can continue and proppant can be carried deeper into the formation.[15] A well may be too long to maintain sufficient pressure to stimulate fractures across its entire length. Plugs may be inserted to divide the well into smaller sections called 'stages'. Stages are fractured sequentially, beginning with the stage furthest away and moving towards the start of the well. After fracturing, the plugs are drilled through and the well is depressurised. This creates a pressure gradient so that gas flows out of the shale into the well. Fracturing fluid that flows back to the surface ('flowback water') contains saline water with dissolved minerals from the shale formation ('formation water'). Fracturing fluid and formation water returns to the surface over the lifetime of the well as it continues to produce shale gas ('produced water').[16] Although definitions vary, flowback water and produced water collectively constitute 'wastewaters'. [17]

## 1.3 Fracturing fluids

Since the first reported fracturing operations for productivity enhancement in oil and gas reservoirs[18–21] several classes of fracturing fluids have been developed, but in all cases the formulations are composed by a base fluid (usually water, which represents the 90-95 % w/w of the formulation), the proppant (about 5-7 %) and different chemical additives (0.5 – 2 %) that impart specific properties to the fluid.[22] Figure 1.3 shows a generalized example of fracturing fluid composition for shale fracturing.

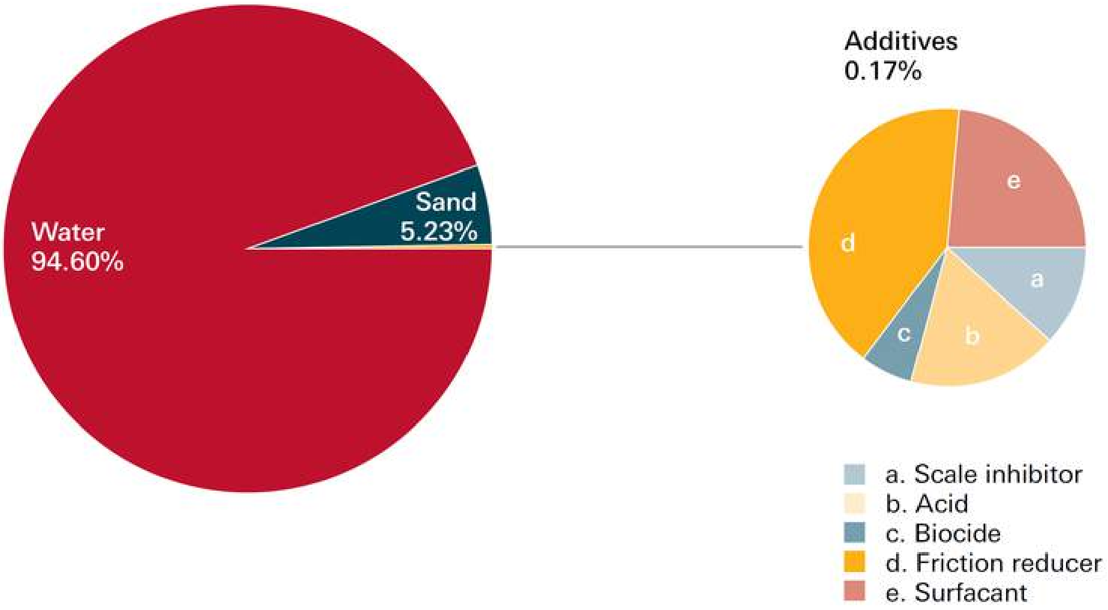

Figure 1.3 – Generic composition of hydraulic fracturing fluids.

Water-based fluids are used in approximately 80% of all wells.[23] The base fluid can be fresh water, seawater, brine, or a saturated brine, and the fluid selection depends on the well conditions or on the specific interval of the well which is drilled.[24] Among water-based fluids, the formulations can be divided in:

- "Slickwaters" (water with small amounts of added chemicals)
- Linear gels

- Crosslinked gels
- Viscoelastic surfactant (VES) gel fluids.

Oil-Based Fluids are used on water-sensitive formations that may experience significant damage from contact with water based fluids.[22] Gelled oil systems were the first class of fluids which have been used in hydraulic fracturing and have the major advantage of being compatible with almost any type of rock formation.[25] Despite this, the environmental impact of the oil-based fluids is massive, so their application is limited to very specific well conditions.[13]

Some gases, such as $CO_2$ and $N_2$, have also been tested for use as fracturing fluids (foam based systems), showing the unique advantage of eliminating water usage with minimal chemical application. However, the limited capacity to transport proppants is a major drawback. In addition, the potential leakage of gases such as $CO_2$ may cause environmental issues.[26]

The proppant is a solid material, typically sand, treated sand or man-made ceramic materials, designed to keep an the fracture open, during or following a fracturing treatment. The proppant must be strong enough to resist the fracture closure stress; if not, it will be crushed and the fracture will close causing a drastic decrease of fracture permeability.[22]

The most critical factors for the control of the proppant settling rate from the frac-fluid and placement, or accumulation, in the fracture are the fluid viscosity and the density of the proppant. Moreover, fracture conductivity depends to a large extent on the type, uniformity and size of the proppants, amount of embedding into the matrix, crushing of the proppant, and placement in the fracture. The proppant must be refined for uniformity in size because fine particles will block flow channels and seriously decrease the permeability of the fracture.[27]

Additives for fracturing fluids fulfill three main functions: enhance fracture creation, improve the capability to carry the proppant and minimize formation damage.[28] The companies generally do not disclose the specific chemicals used to prepare the fracturing fluids for competitive reasons, but the principal compositions of the frac-fluids is accessible.

Additives which are commonly used to extend the fracture creation and enhance proppant transport include:

- **Viscosifiers - Thickeners.** Organic polymers like guar, xanthate and cellulose gums (which are also used in food products) can modify the viscosity of the water solution to obtain a gel-like fluid at ambient conditions.[29,30]
- **Crosslinking agents.** Organic Borate complexes are, by far, the most common cross linker in use today. Borate-crosslinked fracturing fluids can be applied across a wide range of treating conditions and are resistant to shear degradation. Anyway, Borate-crosslinked systems are limited to temperatures below 120 °C and pH's above 8; for this reason other metals including Titanium and Zirconium are used as crosslinkers for guar and cellulose derivatives to broaden the range of application.[22,31]
- **Temperature Stabilizers.** They are usually added to improve the fluid thermal stability in higher-temperature environments, and include low molecular weight copolymers, organometallic ligands and nanoparticles.
- **pH-control agents.** Buffers are used in conjunction with polymers to reach the optimal pH for polymer hydration. When the optimal pH is reached, the maximal viscosity yield from the polymer is obtained. The most common example of fracturing fluid buffers is a weak-acid/weak-base blend, whose ratios can be adjusted so that the desired pH is reached. Some of these buffers dissolve slowly allowing the crosslinking reaction to be delayed.[22]
- **Fluid loss-control materials.** Several types of polyacrylamide polymeric compounds are able to reduce pressure and loss of fluids due to friction and turbulence when pumped through pipes. Friction reduction can promote enormous pumping rates up to ≈ 16000 L/min.[32]

Formation damage is reduced with such additives as gel breakers, corrosion control and scale inhibitors, biocides, surfactants, and clay stabilizers.

- **Gel breakers.** Breakers are added to the fracturing fluid to reduce the molecular weight of the various polymers used. This reduces the viscosity and facilitates the blowback of residual polymer which allows for cleanup of the proppant pack. Ideally these materials would be totally inactive during the treatment and then instantly "spring to action" when pumping stops, rapidly breaking the fluid back to a low viscosity preparing the fracture and formation for flow. This is very difficult to achieve as the breaker activity is very dependent on fluid temperature which varies with time. The three general types of breakers are: Oxidizers (like ammonium persulfate, sodium persulfate, and calcium and magnesium peroxides), Acid (Hydrochloric acid or acetic acid) and Enzymes (hemicellulase, cellulase, amylase and pectinase).[22]

- **Scale inhibitors.** Water used during the hydraulic fracture stimulation can mineral scales when coming in contact with naturally occurring water in the producing formation. Additionally, changes in temperature and pressure during initial production can cause mineral solids to precipitate from the fluid. To prevent this, a scale inhibitor is injected throughout the hydraulic fracturing fluid. Owing to their compatibility with other fracturing additives, the most commonly used chemistries are carboxylic acid and acrylic acid polymers. Scale inhibitors are usually used at relatively low dosages throughout the frac fluid (75 to 120 ppm) and make up 0.0075% - 0.012% of the total fluid volume.[32]

- **Corrosion Control.** To prevent the degradation of the casing due to the acidic treatment, an acid corrosion inhibitor is utilized throughout the entire acid volume. Acid inhibitors tend to be complex products as they are tasked with a protecting the steel casing without reducing the acid's ability to dissolve iron oxides that is usually present on the surface of the pipe. Acid inhibitors tend to contain amines, amides and/or amido-amines and often contain formic acid as an intensifier for higher temperature applications. Usage rates can vary from 2,000 to 5,000 ppm in the acid only which equates to 0.0004% - 0.0043% of the total fluid volume.[22,32]

- **Biocides.** Many bacteria can degrade the gels used for building fluid viscosity and have the potential to aggressively attack the metal equipment used both downhole and on the surface for producing natural gas and liquids from the well. Biocides are added to the source water to sanitize the fluid and greatly reduce the concentration of bacteria. There are several chemistries utilized as biocides in hydraulic fracturing. Historically, glutaraldehyde and blends of glutaraldehyde have been used.[33] Another product that is highly biodegradable is DBNPA (2,2-dibromo,3-nitriloproprionamide). There are some operators who use sodium hypochlorite (the active ingredient in household bleach) for sanitation of source waters.[34] Methanol and naphthalene are added to control aerobic bacterial that can form metabolic products (such as slimes) and destroy additives used in the frac-fluid in storage and mixing tanks.[27] Biocides are commonly applied throughout the whole hydraulic fracturing fluid at a rate of 75 to 500 ppm and represent 0.075% - 0.05% of the total fluid volume.[32]

- **Surfactants.** Surfactants have been historically used in hydraulic fracturing to reduce interfacial tension between the fluid and the shale and between different phases of fluid. The term "surfactant" covers a multitude of products and those used in hydraulic fracturing can be as simple as a laurel sulfate, butanol and ethlylene monobutyl esters to complex fluoro- and nano-surfactants. Surfactants are typically used at 500 to 1,000 ppm throughout the fluid which would account for 0.05% - 0.1% of the total fluid volume.[35–37]

- **Clay control agents**. KCl or an organic clay stabilizer is added to the base fluid to prevent the water from interacting with the reservoir mineralogy. KCl is typically added at a concentration of 2% but can be used at concentrations as high as 8% depending on laboratory testing results. Most testing on the commercially available organic clay stabilizers, which are typically some form of Quaternary Amine compound, has found them to be ineffective at the normal concentrations recommended. KCl is unique in its ability to stabilize clays and is much more effective than other inorganic salts such as NaCl, $CaCl_2$ etc.[22,28,38]

This exceptionally large variety of chemical additives is necessary in order to impart a predictable set of properties to the fracturing fluid formulation. The ideal fracturing fluid should possess definite physical properties which are crucial during the fracturing and the production stage. First of all the fluid must provide an appropriate viscosity for proppant transport: if viscosity is too low, proppant sedimentation occurs with a consequent pipeline obstruction. Second , it must have a high shear resistance, which prevents viscosity loss upon high shearing during the pumping operations. Third, the fluid should be compatible with the formation composition, as in the case of clay-rich formations: in the presence of water clays swell causing a remarkable loss in the well productivity. Fourth, the fluid should be able to lose viscosity (break) and clean up efficiently from the fracture, allowing an efficient recovery and an effective gas extraction.[39]

Nevertheless, the high variability in the geochemical conditions between different shale formations combined with the strict requirements for the fluid properties make the formulation of hydraulic fracturing fluids a very challenging task, which demands a considerable effort in terms of basin analysis and fluid components selection.

## 1.4 Environmental Risks associated to Hydraulic Fracturing

As anticipated in Paragraph 1.1, several environmental issues have been attributed to the hydraulic fracturing process. A high demand for freshwater, the production of large amounts of waste water, induced seismicity, greenhouse gas emissions, and groundwater contamination have all been linked to hydraulic fracturing technology in the past. Moreover, dense well-spacing, noise from operations and increased truck traffic are further concerns for the environment and the public.

Some environmental impacts have already been effectively reduced using new technological developments, like the reduction of greenhouse gas emissions during shale gas production[11,40] and the reduction of freshwater demands by increased recycling and re-use of wastewater.[41,42] Other issues still need more attention from research and development, e.g. the prevention of induced seismicity.[43]

### Water contamination

Groundwater contamination can occur through spillage of fracturing fluids via the surface or by leakage from the wellbore. Leakage of fluids through the targeted shale formation and adiacent freshwater aquifers is possible in principle, but very improbable.[44]

Besides fracturing fluid leakage, the second major source of contamination is the stray gas, i.e the migration of natural gas into groundwater, surface water and soil.[8,45]

Another major issue is represented by wastewater, which is produced in shale gas operations mainly during the flowback phase. In addition to proppant and chemicals which are initially present in the fracturing fluid, the wastewater contain elements that originate from contact with the shale rocks. Among these Naturally Occurring Radioactive Materials (NORM) represent a critical problem. NORM consist of waste materials or by-products enriched with radioactive elements found in the shale formation environment, such as barium, radium and radon.[46] In shale gas extraction NORM are created in the production process, when produced fluids from reservoirs carry sulfates and carbonates up to the surface. Barium, calcium and strontium sulfates and carbonates are larger compounds, and the smaller atoms, such as radium-226 and radium-228, can fit into the empty spaces of the compound and be carried through the produced fluids.[46] As the fluids approach the surface, changes in the temperature and pressure cause the barium, calcium, strontium and radium sulfates to precipitate out of solution and form scale on the inside, or on occasion, the outside of the tubulars and/or casing. This latter case may represent a serious health hazard for the operators and the population around the shale gas extraction site.[47,48]

For this reason the wastewater, needs proper treatment for recycling or disposal. Specific strategies must be developed for the limitation and elimination of NORM. This can be achieved with available technologies, which are currently being developed further to be more efficient and less costly.[49] However, discharge of contaminated waters into rivers, delivery to unsuitable publicly owned treatment works, and spills due to improper surface handling of wastewater have all occurred and need to be investigated, remediated and, importantly, learned from.[43]

### Induced seismicity

Hydraulic fracturing causes millions of very small and localized seismic events when the fractures are produced in the shale formations.[9,10,50] In almost all cases the maximum magnitude of the induced seismicity is below the maximum magnitude of a naturally occurring earthquake in a particular region. Shale gas operators benefit strongly from this seismic response by pinpointing the spatial and temporal distribution of produced fractures in the underground.[51,52] On the other hand, the stress applied to the rocks by hydraulic fracturing can combine with the pre-existing stress field underground and might induce seismic events that can be larger than the deliberately produced microseismicity. Seismic events apparently connected to shale gas hydraulic fracturing have been documented,[50] and although of small magnitude, have prompted much attention and thorough investigation. Operational best practices which aim to reduce the risk of induced seismicity have been developed in geothermal energy production, where similar hydraulic fracturing techniques are applied.[53] These best practices can be applied in much the same way to shale gas production. However, since precise knowledge of the prevailing underground stress field and mechanical properties of the rocks is always limited, induced seismicity risk-reduction is a complex and challenging task.[43]

### Greenhouse gas emissions

Methane, the main component of natural gas, may act as a potent greenhouse gas that contributes to global warming. Large quantities of methane may be released into the atmosphere during the flowback-phase of a shale gas well: when the fracturing fluid is returning to the surface, it brings along natural gas that can be released from the freshly-fractured shale. It was common practice in shale gas developments to release the gas produced during flowback into the atmosphere or to flare it. Flaring (burning) the gas results in the conversion of methane to carbon dioxide, which is also a greenhouse gas.[54] Available technologies, so-called Reduced Emission Completions (REC), can capture the emerging gas at the wellhead. RECs are increasingly applied by shale gas operators for various reasons, one of them being the revenue from selling the captured natural gas.[43,55]

**Water demands**

Variable, but large amounts of water are used for hydraulic fracturing, coming from natural sources such as rivers or groundwater. Increasing volumes of flowback water are being recycled by operators. This practice has two positive effects. The first is reducing the amount of freshwater demand, and the second is reducing the amount of wastewater that must be disposed of. In practice, the amount of recycling varies by play and depends on the availability of fresh water, the cost of disposing of wastewater, and the quality and quantity of wastewater.[41,42,56] The shale gas industry´s water demands usually make up only a small share of total water usage in a given region. However, this demand must be properly managed in a collaborative effort by industry and regional water planning agencies. In general, the availability of water for shale gas operations should only pose a problem in the world´s arid regions.[43]

Alongside the ecological risks a far-reaching view of shale gas development must include economic factors.[57] The economic risk with shale gas wells is that they require horizontal drilling and hydraulic fracturing, which significantly increases capital costs. Major factors in calculating economic risk and uncertainty include 1) poorly constrained, eventual long-term gas production of shale gas plays, and 2) long-standing and possibly long-term low world market natural gas prices. The economic success of shale gas developments, which has been reported recently, may continue in the future, but is no self-seller.[43]

## 1.5 Aim of this work

The general purpose of this work is the formulation of green hydraulic fracturing fluids specific for the shale formations found in Europe. Since every shale formation is unique, fracturing fluids that are effective in North American shale basins might not be efficient in European ones. For this reason the study of formulations with physico-chemical properties that match the pressure-temperature conditions and the composition of shale gas formations is fundamental for the potential exploitation of European shale basins.

At the same time, the environmental concerns about shale gas extraction cast doubts on the toxicity of the chemicals which are present in fracturing fluids. Thus, in order to minimize the environmental impact of hydraulic fracturing and reduce the amount of pollutants in the flowback and produced water, all the substances which are potentially dangerous are excluded and  replaced by greener alternatives. On this basis, the four primary objectives of this study are:

1) the formulation of hydraulic fracturing fluids that contain no hazardous or controlled substances;

2) the development of fracturing fluid formulations that are effective at high salt concentrations, high temperature and pressure;

3) the control of the formulation viscosity during the different stages of the shale gas extraction operations, in order to maximize the efficiency of the fluid and the gas production;

4) the design of specific additives that limit the extraction of Naturally Occurring Radioactive Materials (NORM) from shale formations.

## 1.6 Our Approach

In order to address all the aforementioned issues we propose a multistage approach which covers all the aspect related to the design of green fracturing fluids, from the formulation and physico-chemical assessment of their properties to the performance testing in multiple conditions, trying to reproduce the real operative ones.

### 1.6.1 Green Hydraulic Fracturing Fluids

In the first part of this work we developed two different fracturing fluid formulations which are completely safe and environmentally-friendly. The first is a linear gel polysaccharide-based formulation: it represents one of the oldest example of fracfluid formulations developed by the industries, but, despite this, they are still widely used in a large number of extraction sites.[25] The second is a ViscoElastic Surfactant-based (VES) formulation, that contains a green surfactant as the main ingredient. The presence of a surfactant (which act also as viscosizing agent) imparts very interesting properties to the formulation, such as a remarkable viscoelasticity and the possibility to control viscosity through the variation of the environmental conditions. Since the use of VES have been described in the patent literature for friction reduction and as well treatment fluids since the early 80s, their use as fracturing fluids is relatively a new phenomenon.[58]

For the linear gel formulation, we investigated four different polysaccharides as the main component: Guar Gum (GG), Sodium Hyaluronate (SH), Sodium Alginate (SA) and Hydroxypropylcellulose (HPC). Their chemical structures are reported in Figure 1.4.

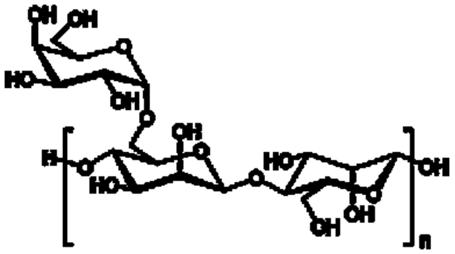

Guar Gum

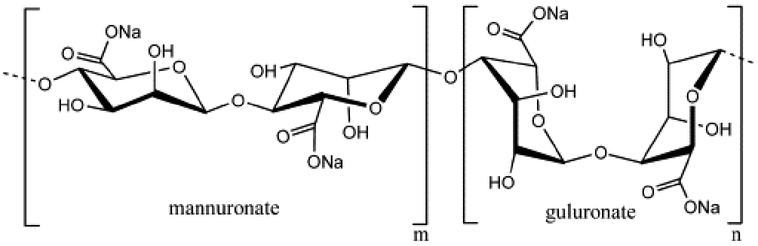

Sodium Alginate

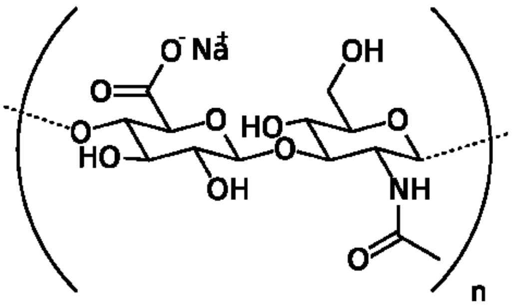

Sodium Hyaluronate

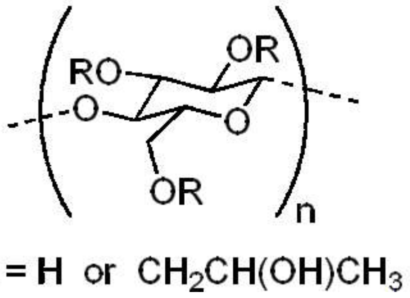

Hydroxypropylcellulose

Figure 1.4 – Chemical structures of GG, SA, SH and HPC.

The criteria for the selection of these polysaccharides were their complete biocompatibility and their remarkable viscosizing properties, which allow the formulation of environmentally safe formulations containing very small amounts of polymer with optimal fluid performances.[59–63]

Guar is a longchain high-molecular-weight polymer, composed of mannose and galactose sugars, and has been widely used to viscosify water for fracturing applications.[58] Guar concentrations of 0.12–0.96% w/w are reportedly used for fracturing operations.[25,31] The polymannose backbone of guar is insoluble in water but the galactose branches confer solubility in water. Up to 6–10% by weight insoluble residue is expected from guar. This initial insoluble residue causes damage to the proppant pack. In addition to the residue made during the preparation, the breakers also generate additional residues.[25] For this reason guar derivatives, like Hydroxypropyyl guar are used for their less insoluble content and better resistance to harsh conditions.[64] Nevertheless we selected guar as a standard reference for the other polysaccharide formulations, exploring at the same time innovative strategies for the viscosity modulation without the addition of oxidizers or enzymatic breakers.

The chemical structure of sodium hyaluronate is represented as a linear polyelectrolyte based on β1-4-d-glucuronic acid and β1-3-*N*-acetyl-d-glucosamine alternated in the repeat unit. The main uses of HA are ophthalmic surgery, arthritic treatment, and, more recently, cosmetics.[65,66] Despite this, its unique rheological properties[62] make SH a potential candidate for other innovative applications, like fracturing fluid applications. For this reason we decided to evaluate the use of SH as viscosizing agent in fracfluid formulations.

Alginate is a linear copolymer of α-L-mannuronic acid (M) and β-D-guluronic acid (G). The composition of the natural polymer varies depending on its origin in different seaweed and some bacteria, and has been shown to strongly influence its physical properties. Alginate has strong affinity for divalent ions. In concentrated solutions of high molecular weight alginate, divalent ions cross-link alginate polymers into a hydrogel network, which forms the matrix for encapsulation of cells. Although ionic cross-linking has mainly been attributed to long G-blocks5, alternating M and G sequences (MG-blocks) have also shown to participate in Ca-alginate gel formation.[67] These properties give SA a variety of uses in many fields, for example food industry, cosmetics, biomedical science and engineering.[61,68,69] As in the case of SH, its biocompatibility and gelation properties prompt us to study its potential application as viscosizing agent in fracfluid formulations.

Hydroxypropyl cellulose (HPC) is one of the most important chemical derivatives of cellulose because of its high solubility in water.[70] HPC is an ether of cellulose in which some of the hydroxyl groups in the repeating glucose units have been hydroxypropylated forming $-OCH_2CH(OH)CH_3$ groups using propylene oxide. HPC, as other water soluble cellulose derivatives, is biocompatible and can be used as thickener, binding agent, emulsifiers, film formers, suspension aid, lubricant and stabilizer, especially as additives in food, pharmaceutical, and cosmetic industries.[71] Due to the presence of hydrophobic and hydrophilic groups, HPC shows a peculiar phase behaviour, with a lower critical solution temperature (LCST) at 45 °C. At temperatures below the LCST, HPC is readily soluble in water; above the LCST, HPC is not soluble.[63] This feature, combined with the fact that other cellulose derivatives like HydroxyEthyl Cellulose are currently used in fracfluid formulations[58], made HPC a very interesting candidate for our polysaccharide-based fluids.

All the polysaccharide were added in a concentration of 0.5 – 1 % w/w to pure water (see Paragraph 2.2.1 for further details) and their rheological and thermal properties were investigated by flow curve experiments and Differential Scanning Calorimetry (DSC) measurements. As stated in Paragraph 1.5 the main focus of this work is the study of the fluid viscosity, which must be controlled during all the different stages of fracturing operations. The same physico-chemical properties were also assessed in specific conditions that mimic the real operative conditions in the extraction wells. In particular we evaluated the effect of simple inorganic salts and a mixture of them (called "shale water", see Paragraph 2.2.3) on the flow and thermal behaviour of the four polysaccharide formulations. Then we tested our fluids at high temperature (up to 120 °C) and pressure (from 1 to 390 Pa) in order to evaluate their rheological response in these extreme conditions. Finally, we detected the salt toleration threshold for the stability of the different polysaccharide formulations.

The second investigated formulation is a ViscoElastic Surfactant-based (VES) fluid. In this class of fracfluid specific surfactants are used as the main component in combination with inorganic salts (or charged molecules). These surfactants can form long elongated micellar structures in solution that contribute to the viscoelastic behaviour and increase fluid viscosity.[72] As the concentration of surfactant increases in water, micelles start to form. By further addition of surfactant, the concentration exceeds the critical micelle concentration (CMC) and the molecules start interacting with each other. These interactions are based on ionic forces and can be amplified by adding electrolytes (salts) or other ionic surfactants. Depending on the ionic charges, the size, the shapes of the surfactants and these counter-ions, ordered structures start to form, which increases viscosity and elasticity.[73–75] The reverse mechanism is valid for breaking these systems. The structures can be disrupted by adding other surfactants, ionic additives and hydrocarbons or can be diluted by additional water.[76] These fluids are operationally simple: only one or two additives are added without any need to hydrate polymers. They do not require any biocides because they do not contain any biopolymers. They do not require additional flowback surfactants because they have inherently low surface and interfacial tension. No additional clay control additives are needed.[58] On the other hand, the high cost and undesirable viscosity reduction at high temperature have been reported as the main shortcomings of these systems.[25]

For our VES formulation we selected sodium oleate (NaOL), a non-toxic, biocompatible anionic surfactant combined with potassium chloride (KCl), which is one of the most effective clay control agent in fracturing fluid formulations (see Paragraph 1.3). The chemical structure of NaOL is shown in Figure 1.5.

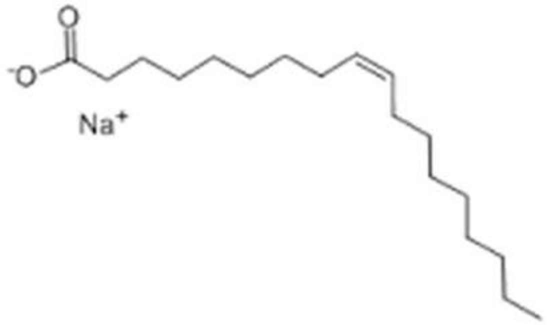

Figure 1.5 – Chemical structure of Sodium Oleate

Sodium oleate is a $C_{18}$-tailed anionic surfactant that self-assemble into wormlike micelles upon addition of simple salts[73] or other surfactants.[77] Several studies have focused on the influence of different additives on the micellar structure and viscoelastic behaviour of NaOL solutions.[72,78–80]

NaOL offers several advantages in many applications, since anionic systems tend to be biodegradable and less toxic compared to cationic ones and are therefore considered to be more environmentally friendly.[81] In particular, anionic surfactants are widely used in enhanced oil recovery because the oil sand in the reservoir possesses negative charges and consequently adsorbs cationic surfactants.[73]

We performed rheological experiments (flow curves) and DSC measurements on the NaOL/KCl VES formulations by varying the concentration of the surfactant and the counter-ion in order to understand the interplay between the two components and its effect on the viscosity and the thermal properties of the overall system. Then, as in the case of the polysaccharide-based formulations, we tested the VES fluids in high P, T and salinity conditions in order to assess their stability and resistance.

## 1.6.2 *Stimuli*-responsive Formulations

After evaluating how the variation in the specific physico-chemical properties of a shale formation (i.e. temperature, pressure and salinity) can be effectively used to modulate the viscosity and the rheological behaviour of the formulations, we explored two innovative approaches to formulate responsive (or "smart") fluids whose rheological and thermal properties can undergo controlled and reversible changes in response to an external stimulus. The use of stimuli-responsive systems is widely reported for a large number of applications,[74,82,83] particularly when it is impossible or very difficult to switch on/off their properties and a remotely controlled trigger is necessary, as in the case of shale gas extraction.

In the second part of our work we studied the effect of the inclusion of two different additives both on the polysaccharide and VES formulations, in order to impart a responsiveness to specific external stimuli, namely an applied electrical voltage and UV light. The aim is the formulation of green smart fluids that undergoes rapid changes in viscosity in response to these applied inputs.

The first investigated additive is Carbon Black (CB): CB is an anthropogenic carbonaceous materials that is essentially a pure form of soot, which is produced from incomplete combustion of hydrocarbons.[84] Different manufacturing processes produce different types of carbon black, including furnace black, thermal black and connect black. CB is used extensively as a filler in the rubber industry to prepare composites with improved strength, stiffness and wear resistance properties.[85] CB also finds a remarkable use in the polymer industry, especially in the production of polypropylene, polyvinyl chloride, polyester and polyethylene.[86–88] The presence of carbonaceous particles confers an enhanced electric conductivity and an increased resistance to thermal degradation, abrasion and tear to the polymer matrix.[89] Moreover, the addition of CB brings about other advantages, i.e. the reduction of polymeric materials (with no significant modification of their mechanical properties) and the reinforcement of the polymer viscoelastic behaviour.[90] For these reasons we studied the inclusion of carbon black in our fracfluid formulations (the polysaccharide dispersions and VES based formulations) for the control and improvement of their thermal properties, rheological behaviour, conductivity and electrical responsiveness.

The second investigated stimuli-responsive additive is Azorubine (disodium 4-hydroxy-3-((4-sulphonatonaphthyl)azo) naphthalenesulfonate), also known as Carmoisine, Food red 3 or E 122. Azorubine is a synthetic azo dye approved for food decorations and coatings and as drink additive.[91] Its chemical structure is shown in Figure 1.6. The presence of the azo moiety enables the *trans-cis* isomerization upon irradiation with light at an appropriate wavelength, usually in the UV region.[92–94]

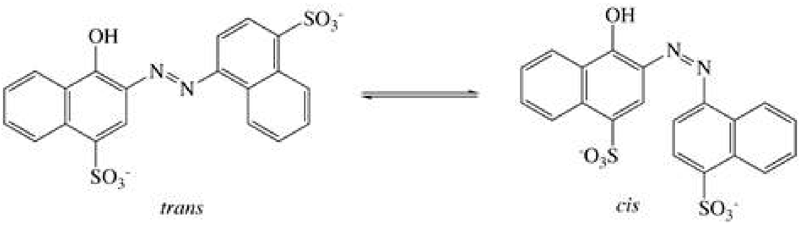

Figure 1.6 – Trans-cis isomerization of azorubine.

The process may revert spontaneously upon heating since the trans isomer is thermodynamically more stable, or can be induced through irradiation with a visible light.[95] Previous studies reported on the introduction of different chromophores in VES systems in order to obtain light-responsive fluids with tunable rheological properties. These photo-active molecules include synthetically modified azobenzenes,[96–98] *p*-coumaric acid[99,100] and cinnamic acid derivatives.[101,102] We select azorubine by virtue of its unique advantages in terms of availability, simple manipulation, low cost and complete safety. The dye is added in very small amounts to the aqueous viscoelastic formulation based on NaOL and KCl.

The goal is the combination of completely biocompatible and non-toxic materials to obtain a versatile formulation with a viscosity and rheological behaviour that can be remarkably modified through the irradiation with UV light. This “smart” system could represent a real breakthrough in the formulation of hydraulic fracturing fluids: to scale up this concept from the laboratory to a real shale gas extraction plant, the light stimulus could be propagated into the well in a safe and relatively inexpensive way through optical fibres.

### 1.6.3 Strategies for NORM Reduction

In the last part of this work we propose two innovative green strategies for the limitation of the extracted NORM. The first investigated approach is the magnetic water treatment (MWT), which is one of the most commonly used techniques for water and wastewater purification:[103] it is a physical treatment that avoids the use of expensive and harmful chemicals, such as polyphosphates or corrosive substances. It was discovered in the first decades of the 20th century observing that the placement of an external magnet on steel pipelines causes a reduction of scale deposition.[104] Starting from this observation, commercial magnetic water treatment devices were produced and are still used. Several theories were developed to explain this curious phenomenon: the most accepted states that magnetic field affects the structure of water molecules surrounding ions in solution, thus changing their hydration and so the precipitation mechanism.[105]

We started studying the effect of a weak static magnetic field (MF) on the precipitation of insoluble calcium carbonate in water to assess if MWT can be a feasible way to reduce the likelihood of pipeline obstruction normally occurring when water used during the hydraulic fracturing comes in contact with naturally occurring water in the producing formation. Some experiments on magnetically treated and untreated solutions of calcium sulfate were also performed since $CaSO_4$ is another component of mineral scales; in addition, experiments on different calcium salts allow to clarify if the chemical nature of the anion exposed to the MF affects the efficacy of the magnetic treatment.

Finally, the study was extended to the effect of magnetic field on the precipitation of Sr(II) and Ba(II) carbonates since they possess very low solubility in water so are responsible for scales formation: however, no literature works report on the use of MF for the reduction of their precipitation. In addition, barium and strontium salts possess chemical properties similar to those of radium, which is the main component of NORM. Considering that radioactive materials cannot be handle in our lab, Ba(II) and Sr(II) compounds were chosen to mimic the behaviour of radium. The idea was to assess if MWT is effective in the control of other alkali earth metals salts in order to understand if it can be efficiently used as a “green strategy” to reduce the drawback of NORM extraction and/or to treat flowback waters containing NORM ions.

All the experiments were carried out at 25 and 60 °C in order to explore the role played by temperature: indeed, in real operating conditions during shale gas extraction, the temperature reached in the pipelines is above 100 °C.[106]

The second investigated approach is based on the use of scale inhibitors as additives for the limitation of scales formation. Water used during the hydraulic fracture stimulation can mineral scales when coming in contact with naturally occurring water in the producing formation. Additionally, changes in temperature and pressure can cause mineral solids to precipitate from the fluid. To prevent this, a scale inhibitor is usually injected throughout the hydraulic fracturing fluid at relatively low dosages throughout the frac fluid (75 to 120 ppm) and make up 0.0075% - 0.012% of the total fluid volume.[32] Owing to their compatibility with other fracturing additives and their resistance to chemical and biological breakdown, the most commonly used chemicals are carboxylic acid and acrylic acid polymers.

In our work, we investigated polyacrilate (PAC), polyglutammate (PG) and polyaspartate (PAS) sodium salts. PACs are already used as scale inhibitors but they are not green additives so in this study they were tested as reference to compare the performances obtained with green innovative chemicals, such as PG and PAS. Figure 1.7 shows the chemical structures of the investigated NORM-reducing additives, while Table 1.1 lists their molecular weights.

Table 1.1 – Molecular weights of the used antiscaling agents.

| | ***Molecular weight (kDa)*** |
|---|---|
| ***PAS*** | 2-11 |
| ***PG-low*** $M_w$ | 3-15 |
| ***PG-high*** $M_w$ | 15-50 |
| ***PAC-low*** $M_w$ | 1.2 |
| ***PAC-medium*** $M_w$ | 8 |
| ***PAC-high*** $M_w$ | 15 |

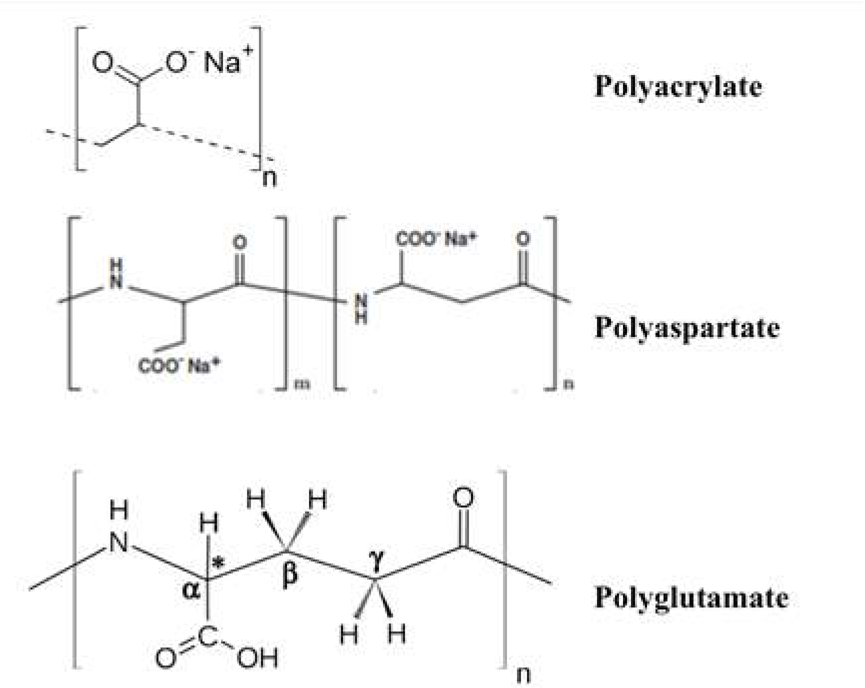

Figure 1.7 - Chemical structures of the investigated scale inhibitors.

All the additives were used at a concentration of 10 mg/L (i.e., 0.001 wt% of the total formulation), in line with the data found in the literature.[23,107]

First of all, we qualitatively evaluated their efficacy against calcium sulphate formation in pure water; tests were performed both at 25 and 60 °C to assess the performances of the scale inhibitors also at high temperatures, such as in real operative conditions. Then, the behaviour of these additives was studied in the final polysaccharide dispersions developed during the work: sodium hyaluronate-based formulation containing 0.5 wt% of polysaccharide and 0.001 wt% of antiscalant agent was chosen as model system.

Finally, the effect of antiscalants on the precipitation of other insoluble salts, such as strontium sulphate, was investigated as well in order to gain information on their effectiveness against the precipitation of other sparingly soluble salts of alkali earth metals. Again, the idea was to understand if the use of very small amounts of green antiscalants could be a feasible method to limit the formation of mineral scales, also in the presence of radioactive materials, such as radium salts.

# Chapter 2 Materials & Methods

## 2.1 Chemicals

Guar gum and hydroxypropyl cellulose (average molecular mass 2000 and 1600-1800 kDa, respectively) were supplied by Lamberti S.p.A. (Milan, Italy); high molecular weight (1800–2000 kDa) sodium hyaluronate was purchased from Stanford Chemicals Company (Fairbanks, CA). NaF, NaI, NaSCN, $NaClO_4 \cdot H_2O$, $NaH_2PO_4$ were purchased from Fluka(Milan, Italy). KCl, KBr, $CaCl_2$, NaCl, NaBr, $Na_2SO_4$, $Na_3PO_4 \cdot 3H_2O$, $Na_2HPO_4 \cdot 7H_2O$, trehalose, sodium alginate (average molecular mass 240 kDa; mannuronate/guluronate ratio 0.44) and saponin were supplied by Sigma-Aldrich (Milan, Italy). Urea, $SrCl_2 \cdot 6H_2O$ and sodium oleate were purchased from Riedel de Haen (Germany). $BaCl_2 \cdot 2H_2O$, $Na_2CO_3 \cdot 10H_2O$ and $Na_2SO_4$ were purchased from Merck (Germany). Azorubine (E122, food grade quality) was supplied by F.lli Rebecchi S.r.l., Piacenza, Italy. Carbon Black VULCAN® XC-72R was provided by Cabot Corporation (Boston, USA). All the chemicals were reagent grade (≥99%) and used as received. All solutions and dispersions were prepared with bidistilled Milli-Q water (resistivity > 18 MΩ·cm at 25°C).

## 2.2 Green Fracturing Fluids

### 2.2.1 Polysaccharide-based formulation preparation

Guar gum, sodium alginate, sodium hyaluronate and hydroxypropyl cellulose water mixtures were prepared by slowly adding a weighted amount of polysaccharide powder to water under constant stirring at room temperature. In these conditions complete dissolution occurs in about one hour for all the investigated biopolymers. The samples containing the different salts or co-solutes were prepared following the same procedure, replacing water with 0.5 M aqueous solutions of the salts or neutral co-solutes.

In general gelling agents for fracturing formulations are used up to 1% w/w.[108,109] The addition of a crosslinker lowers the concentration to 0.1–0.5%.[31] We started investigating a polysaccharide concentration of 1% in order to avoid the addition of a crosslinker and focus exclusively on the effect induced by the variation of operational parameters (i.e. pressure, temperature and salt content). Once the principal physico-chemical properties, as well as the thermal resistance and the tolerance to high salinity conditions were assessed we lowered the polysaccharide concentration to 0.5 %, in order to reduce the overall formulation cost and impact, while maintaining optimal operative performances.

### 2.2.2 VES Formulation Preparation

Sodium oleate viscoelastic formulations were prepared by the addition of a weighted amount of surfactant to KCl aqueous solutions at different concentrations (0, 0.1, 0.5, 1, 2, 3, 3.5, 4 % w/w) under constant stirring at room temperature. The final concentration of NaOL was 13 % in all the samples. The azorubine-loaded light responsive samples were prepared following a similar procedure: we added different amounts of potassium chloride to a 0.18 % w/w azorubine aqueous solution to obtain KCl concentrations of 0.1, 0.5, 1, 2, 3, 3.5, 4 % w/w, then we added the surfactant.

### 2.2.3 “Shale Water”

The polysaccharide and the VES formulations were tested in a mixed salt solution that mimics the salinity conditions in real shale formations. We prepared this solution (indicated as “shale water”) starting from the literature data related to the flowback water salinity content of some European and US shale basins.[110–112] This solution is prepared by mixing weighted amounts of salts in water in order to obtain the following concentrations:

- NaCl 1 M
- $CaCl_2$ 0.2 M

- KBr 0.014 M
- $SrCl_2$ 0.01M
- $BaCl_2$ 0.002 M

### 2.2.4 Carbon Black-loaded formulations

Carbon black was added to the polysaccharide or to the VES samples following two different procedures:

1. To effectively include CB in the polysaccharide matrices, a 2% w/w saponin solution was first prepared. Saponins belong to a class of natural surfactants which are effectively used to stabilize carbonaceous particles in water dispersions.[113,114] This solution was added to a weighted amount of CB in order to obtain a final CB concentration of either 1% or 3% w/w and magnetically stirred for a few minutes. The mixture was sonicated for 1 hour at 40 kHz and the polysaccharide was added under magnetic stirring.
2. In the case of the VES systems, no additive was necessary for the dispersion of CB, as sodium oleate itself is able to disperse the carbonaceous particulate. Hence, the VES solution was simply added to a weighted amount of CB (10% w/w), then the mixture was sonicated for 30 minutes.

## 2.3 Limitation of NORM

### 2.3.1 Effect of Magnetic Field - Sample preparation

$CaCO_3$, $BaCO_3$, $SrCO_3$ crystals were precipitated from the corresponding salt solutions by mixing equal volumes (2 mL) of 8 mM $Na_2CO_3$ with 8 mM $CaCl_2$, $BaCl_2$ or $SrCl_2$ either at 25 or 60 °C. The temperature was controlled using a water bath (± 0.1 °C). In the case of calcium sulphate, the crystals were precipitated by mixing 2 mL of 0.5 M $Na_2SO_4$ and 0.5 M $CaCl_2$ at 25 °C.

## 2.3.2 Magnetic Treatment

The effect of magnetic field on salt precipitation was investigated by exposing 2 mL of each ion solution to a 0.4 T static magnetic field for 15 minutes at room temperature before the mixing. After the magnetic treatment, the magnetized solutions were removed from the magnet and mixed at 25 and 60 °C. The intensity of the magnetic field (measured with a Hall effect sensor) and the exposure time were chosen on the basis of previous literature data, especially after Higashitani, who showed a magnetic effect on $CaCO_3$ for magnetic field greater than 0.3 T and exposure times longer than 10 minutes.[115]

The terrestrial MF, with an average intensity between 2 and $7 \cdot 10^{-5}$ T, is too weak for practical applications in anti-scaling treatments. Hence, in industrial applications the starting solutions ought to be exposed to a more intense MF before being pumped in the pipelines. However this circumstance does not represent a limit for real applications since previous works already demonstrated a so-called “water memory effect”: magnetized water retains its properties from few hours[116] to 60 hours[117] up to 3-4 days.[118]

## 2.3.3 Green Anti-Scaling additives

$CaSO_4$ and $SrSO_4$ were precipitated from the corresponding salt solutions by mixing equal volumes (2 mL) of 0.5 M $Na_2SO_4$ and 0.5 M $CaCl_2$ . Polyacrilate (PAC), polyglutammate (PG) and polyaspartate (PAS) sodium salts were previously added to the precursor solutions in order to have a final antiscalant concentration of 10 mg/L (0.001 wt% of the total formulation). For the evaluation of the anti-scaling efficiency in the polysaccharide formulation, the procedure was the same, except for the addition of sodium hyaluronate to the precursor solution to have a final polysaccharide concentration of 0.5 % after mixing.

# 2.4 Experimental techniques

## 2.4.1 Fracturing fluid formulation characterization

### 2.4.1.1 Rheological experiments

Rheological measurements were carried out on a Paar Physica UDS 200 rheometer using a plate-plate geometry (diameter 40 mm; gap 300 μm). Under these conditions the total amount of the sample in the cell was about 0.5 mL. The measurements were performed at 25, 30, 40, 50 and 60 ± 0.1 °C (Peltier temperature control system). After being loaded, the samples were equilibrated for 15 min at the set temperature.

Figure 2.1 – Paar Physica UDS 200 rheometer

The flow curves were acquired working in the controlled shear-stress mode in a torque range between $10^{-3}$ and 2000 mN·m for the polysaccharide-based formulations and between 0.1 and 5000 mN·m for the VES formulations.

Frequency sweep measurements were carried out within the linear viscoelastic range at a strain value of 1%, which was previously determined by means of an amplitude sweep test. The storage and loss moduli (G’ and G’’, respectively) were measured over the frequency range of 0.001 to 100 Hz.

For the polysaccharide formulations we applied the Bird–Carreau–Yasuda (BCY) rheological model to fit the flow curves. This model, sometimes referred to as Carreau–Yasuda or Carreau model,[119] was empirically developed to describe the mechanical behaviour of systems that exhibit both a Newtonian and a shear thinning region.[120] In particular it is used to study the rheology of polymeric water-based dispersions and solutions, e.g. those from polyacrylamide,[121] polypropylene,[122] and polysaccharides such as sodium hyaluronate,[123] guar gum,[73] xanthan gum and carboxymethylcellulose.[121,124,125] In the BCY model the following equation describes the dependence of the viscosity value $\eta$:

$$\eta = \eta_\infty + (\eta_0 - \eta_\infty) \cdot [1 + (\lambda\dot{\gamma})^a]^{(n-1)/a} \tag{2.1}$$

where $\eta$, $\eta_0$, $\eta_\infty$, $\dot{\gamma}$, $\lambda$, $n$, and $a$ are the viscosity, the zero shear rate viscosity, the viscosity at infinite shear, the applied shear rate, the yield of shear rate above which the system shows a shear thinning behaviour, the power law index, and the Yasuda parameter indicating the width of the transition region between $\eta_0$ and $\eta_\infty$ respectively.[120,126,127]

For the VES formulations the experimental curves were fitted according to the Cross model[128] to obtain the zero-shear viscosity, $\eta_0$, and an estimation of the shear relaxation exponent, $m$:

$$\eta = \eta_\infty + \frac{\eta_\infty - \eta_0}{1 + (C\dot{\gamma})^m} \tag{2.2}$$

here $\eta$ is the viscosity, $\eta_\infty$ the infinite-shear viscosity, $\dot{\gamma}$ the shear rate and $C$ the consistency. Similarly to the BCY model, this model describes both Newtonian and shear thinning behaviour, and it is commonly used to fit the viscosity data of viscoelastic surfactant solutions.[129,130]

### 2.4.1.2 High Pressure Rheology

High pressure rheological measurements were carried out in collaboration with the Chemical Engineering Department of University of Huelva (Spain), under the supervision of Prof. Francisco José Martinez-Boza. Viscous flow measurements were performed with a controlled-stress rheometer (MARS II, Thermo Scientific, Germany) using a coaxial cylinder geometry (38 mm diameter, 80 mm length) coupled with a pressure cell D400/200 (Thermo Scientific, Germany). The pressure cell D400/200 is a vessel of 39 mm inner diameter. Inside the cell, the geometry is put into contact with a sapphire surface, at the bottom of the vessel, by a steel needle. This geometry is equipped, at the top, with a secondary magnetic cylinder (36 mm diameter, 8 mm length), magnetically coupled to a tool outside the cell, which is connected to the motor-transducer of the rheometer. The pressure cell is connected to a hydraulic pressurization system composed by a high pressure hand pump (Enerpac, USA), three high pressure valves, and a chamber. Before pressurizing, a vacuum pump, which is connected to a high pressure line through a high pressure valve, is switched on to avoid bubbles in the circuit. Subsequently, the sample is introduced into the high pressure line with a syringe attached to another valve. Between the hand pump and the high pressure circuit, a chamber, consisting of a cylinder fitted to a piston, separates the pressurizing fluid and the sample. This cylinder-piston arrangement provides the requested pressure to the sample, by the displacement of the piston along the cylinder. A pressure transducer GMH 3110 (Gresingeg Electronic, Germany), able to measure differential pressures ranging from 0 to 400 bar (0.1 bar resolution), is used. The temperature in the high pressure cell is regulated with a circulating silicone bath (DC30 Thermo Scientific, Germany), with an uncertainty of ±0.1 °C.

#### 2.4.1.3 Differential Scanning Calorimentry (DSC)

Differential Scanning Calorimetry (DSC) was performed by means of a DSC-Q2000 by TA Instruments (Philadelphia, PA). The samples were first cooled from 20 °C to − 60 °C at 10 °C/min, then heated up to 50 °C at 5°C/min. Measurements were conducted in $N_2$ atmosphere, with a flow rate of 50 mL/min. For the samples which show overlapping endothermic peaks, the deconvolution of the thermogram was performed by means of the Igor Pro 6.36 software, using a summation of exponentially modified Gaussian (EMG) functions.[60,131] The single EMG function is defined as:

$$f(T) = \sqrt{\frac{\pi}{2}}\frac{hw}{|s|}\exp\left[\frac{w^2}{2s^2}\left(\frac{T_0 - T}{s}\right)\right]\operatorname{erf}\left[\frac{T_0 - T}{2\left(w + \frac{w}{|s|}\right)}\right] \tag{2.3}$$

where *h* is the height, *T₀* the center, *w* the width of the peak and *s* is the distortion factor (shape). For the deconvoluted peaks, the peak temperatures correspond to $T_0$, while the enthalpy changes are calculated using the total area under the peak.

### 2.4.1.4 Small Angle X-Ray Scattering Experiments (SAXS)

SAXS measurements were carried out using a HECUS S3-Micro (Kratky camera) equipped with two position-sensitive detectors (PSD-50M) containing 1024 channels of 54-μm width. Cu Kα radiation of wavelength 1.542 Å was provided by a GeniX X-ray generator (Xenocs, Grenoble) working with a microfocus sealed-tube operating in the power range 12÷50 W. The sample to detector distance was 281 mm. The volume between the sample and the detector was kept under vacuum during the measurements to minimize scattering from the air. The Kratky camera was calibrated using silver behenate, which is known to have a well-defined lamellar structure (d = 58.38 Å).[132] Scattering curves were monitored in a q-range from 0.01 to 0.55 Å−1. Liquid samples were recorded in a borosilicate glass capillary tube. In all measurements the temperature was kept constant at 25 °C controlled by a Peltier element, with an accuracy of ± 0.1 °C. All the scattering curves were corrected for the empty capillary contribution considering the relative transmission factors. Desmearing of the SAXS curves was not necessary because of the sophisticated point microfocusing system. The scattering length density values were calculated for each component on the basis of its chemical composition.

### 2.4.1.5 UV Irradiation

The UV irradiation experiments were carried out on the azorubine-loaded VES formulations by placing about 10 mL of sample in a quartz container and irradiated using a Camag UV lamp (wavelength 254 nm, 8 W, Muttenz, Switzerland) for 8 hours. All the experiments were conducted at 25 °C, and the distance between the sample and light source was fixed at 5 cm.

### 2.4.1.6 Electrical Stimulation

The electrical responsiveness of VES and polysaccharide-based systems was assessed by applying a 30 V voltage for 1 hour through a Hewlett Packard Harrison 6112 A DC power supply. Two platinum wires of 1.0 mm diameter (Sigma-Aldrich) were dipped into the dispersions and used as electrodes, as depicted in Figure 2.2.

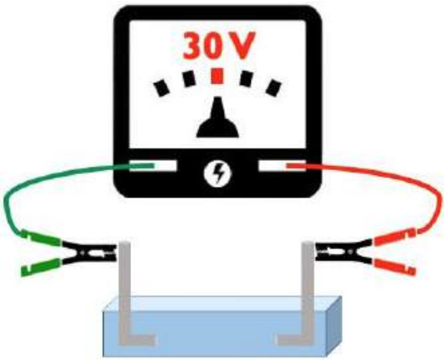

Figure 2.2 – Schematic representation of the electrical treatment setup.

## 2.4.2 Limitation of NORM

### 2.4.2.1 Optical microscopy

A Nikon Eclipse Ti-S Inverted Microscope was used to obtain optical images of crystals precipitating at 25 and 60 °C from either regular or magnetized solutions. All measurements were performed using an objective with a 20X magnification. At least three different regions of each sample were analyzed in order to obtain a statistically meaningful result.

### 2.4.2.2 Fluorescence spectroscopy

Fluorescence measurements were performed at 25 °C using an LS50B Perkin Elmer spectrofluorimeter equipped with a Haake thermostat. Samples were adjusted into 1 cm optical path length quartz cuvettes. Emission spectra were recorded in the 240−700 nm range using different excitation wavelengths, which are listed in Table 2.1.

Table 2.1 – Excitation wavelengths used for fluorescence measurements on all the studied salts.

| **Sample** | **Excitation wavelength (nm)** |
|---|---|
| $CaCO_3$ | 220, 238, 254, 272 |
| $BaCO_3$ | 220, 238, 255, 296 |
| $SrCO_3$ | 220, 238, 255, 265, 300 |
| $CaSO_4$ | 220, 238, 290 |

Fluorescence spectra were recorded on crystals in solution after 1 week from the mixing of the starting precursors in order to obtain reproducible signals related to the different species in solution.

### 2.4.2.3 X-ray Diffraction (XRD)

XRD measurements on dry $CaCO_3$ crystals were carried out at room temperature in air by using a Bruker New D8 Da Vinci diffractometer (Cu Kα radiation, 40 kV × 40 mA), equipped with a Bruker LYNXEYE-XE detector, scanning range $2\theta = 20-60°$, 0.03° increments of $2\theta$, and a counting time of 0.3 s/step.

# Chapter 3 Results and Discussion

## 3.1 Physico-chemical characterization of base formulations

In this section we provide an extensive characterization of the mechanical and thermal properties of the polysaccharide and the VES base formulations. The fluid behaviour is studied by means of rheological experiments (flow curves, oscillatory measurements), DSC and contact angle measurements. The results are included in Paper I, “Specific ion effects in polysaccharide dispersions”, Copyright 2017 Elsevier, which is attached in 0.

### 3.1.1 Polysaccharide-based formulations

Figure 3.1 shows the flow curves obtained for GG, SH, SA 1% w/w dispersions.

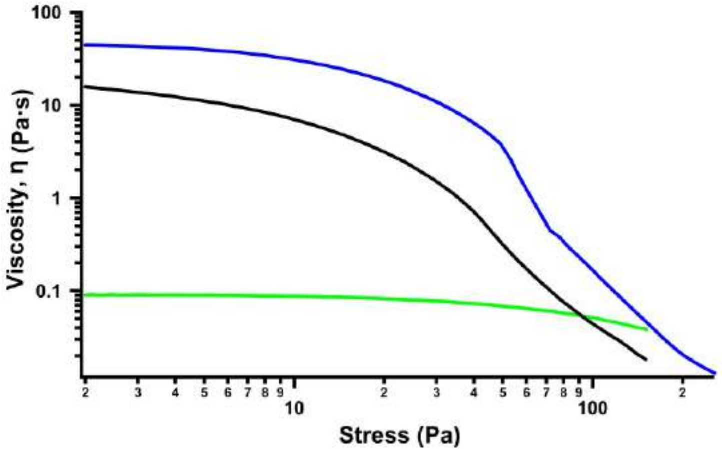

Figure 3.1– Flow curves for 1% w/w SA (green), GG (black) and SH mixtures (blue).

All the samples exhibit a Newtonian plateau at low shear stress, followed by a shear-thinning region as the shear stress increases. The viscosity drop at high shear stress is more pronounced for GG and SH while for SA the shear-thinning is almost negligible. This behaviour is widely reported in literature for solutions of conformationally disordered ('random coil') polysaccharides, at concentrations above the onset of coil overlap and entanglement.[133,134]

The experimental curves were fitted according to the Bird–Carreau–Yasuda (BCY) model to obtain the zero-shear viscosity, η0, and an estimation of the other relevant flow parameters (see Paragraph 2.4.1.1). The results are listed in Table 3.1.

Table 3.1 – The zero shear rate viscosity ($\eta_0$, in Pa·s), power law index (n), the reciprocal of the critical shear rate at which the viscosity begins to drop down ($\lambda$, in s), the width of the transition region between $\eta_0$ and $\eta_\infty$ (a), and the χ2 extracted from the fitting of the flow curves for 1% aqueous mixtures of GG, SH and SA.

| Polysaccharide | $\eta_0$ (±2.5%) | *n* (±5%) | $\lambda$ (±5%) | *a* (±3%) | $\chi^2$ |
|---|---|---|---|---|---|
| GG 1 % | 24.41 | 0.20 | 1.36 | 0.58 | 6.96 |
| SH 1 % | 44.66 | 0.20 | 2.22 | 1.21 | 51.71 |
| SA 1 % | 0.091 | 0.54 | 0.0014 | 1.20 | 1.32 |

SH dispersion shows the higher viscosity over the measured range of shear rates, followed by GG. SA has a very low viscosity, since its ability to form hydrogel is strictly related to the presence of polyvalent cations in solution.[61,135] SH and GG are also significantly more shear-thinning (lower values of *n*), as evidenced by the experimental flow curves (Figure 3.1).

The thermal properties of the polysaccharide dispersions are investigated by means of DSC, and the results are included in 0 - “Specific ion effects in polysaccharide dispersions”.

All the samples exhibit an endothermic peak, related to the melting of free water, which is always centered slightly above 0 °C, presumably because of a kinetic effect. GG shows the highest melting temperature (7.88 °C), associated to the lowest melting enthalpy (307.3 J/g), while SH possesses the lowest peak temperature and the largest melting enthalpy (2.18 °C and 353.0 J/g respectively). SA shows intermediate values (5.36 °C and 336.4 J/g). The peak related to the melting of freezable bound water is not observed in the thermograms for pure GG, SA and SH dispersions. Presumably the freezable bound and the free water melting peaks overlap together in the broad endothermic signal which is centered around 0°C in the heating scans. The addition of a salt or a co-solute can modify the interactions between water and the polysaccharide chains, and changes the distribution of water between the two states: freezable bound and free water. This results in the separation of the two overlapping peaks, which is strictly dependent on the salt/cosolute nature. The effect of different salts/cosolutes on the mechanical and thermal properties of the polysaccharide formulations is extensively discussed in Paragraph 3.2.

### 3.1.2 VES-based formulations

NaOL can self-assemble in aqueous solution into wormlike micelles upon the addition of salts, which reduce the electrostatic interactions between the charged headgroups and promote the growth of long, flexible cylindrical aggregates. As discussed in Paragraph 1.6.1, these wormlike micelles become entangled into a transient network under certain conditions, giving rise to a remarkable viscoelastic behaviour of the fluid. We investigate the effect of both surfactant and salt concentration on the mechanical and thermal properties of the VES fluids to determine the optimal NaOL/KCl ratio for the formulation refining, through the addition of several multifunctional additives (See Paragraph 1.6.1). Figure 3.2 shows the flow curves obtained for the NaOL samples at different concentration (1.5 %, 3 %, 5 %, 7 %, 10 % and 13% w/w) in the presence of KCl 4 % w/w. The addition of potassium chloride to hydraulic fracturing fluids in concentration between 2 and 15 % w/w is recommended in order to minimize the swelling of the reactive clays.[136] Generally, the older shale formations like the Carboniferous Bowland Shale in England and its correlatives in Ireland,[137] require KCl levels in the 3 to 5 % w/w range;[138] for this reason we fixed the salt concentration at 4 % w/w in this set of experiments.

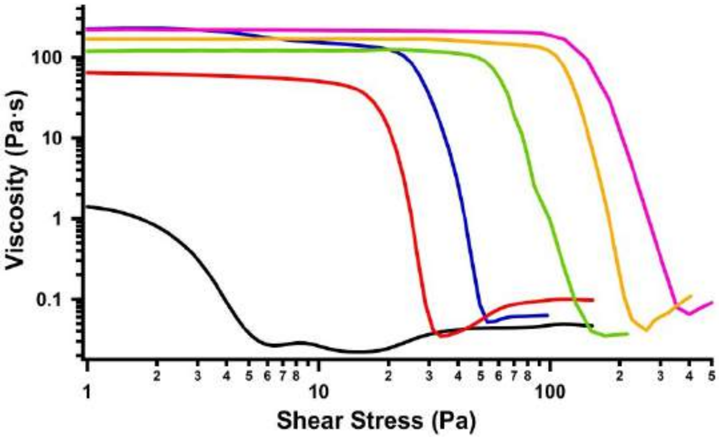

Figure 3.2– Flow curves for NaOL mixtures in the presence of 4 % w/w KCl at different concentrations: 1.5 % (black), 3 % (red), 5 % (blue), 7 % (green), 10 % (yellow) and 13 % w/w (pink).

All the samples show a shear-thinning profile, with an extended Newtonian plateau followed by a steep decrease in viscosity in the high shear stress region. This rheological behaviour is ascribed to the presence of wormlike micelles,[73,81,139] that bring about a rapid drop in the viscosity due to their shear-induced alignment.[106]

In the case of NaOL 1.5 % w/w the effect is less pronounced because at a low surfactant content only short rod-like micelles may form and interact, increasing the viscosity by a small amount. Upon surfactant addition the length of rodlike micelles increases further, allowing the formation of a close entangled network and resulting in a rapid increase in the viscosity.

Moreover, as the surfactant concentration increases the critical stress at which the viscosity breaks down shifts to higher values, indicating a progressive strengthening of the micellar network.

The flow curves are fitted according the Cross model (See Paragraph 2.4.1.1 for the detailed procedure) to extrapolate the zero-shear viscosity, $\eta_0$, and an estimation of the shear relaxation exponent, $m$. The values are listed in Table 3.2.

Table 3.2 - Zero-shear rate viscosity $\eta_0$ (Pa·s), infinite rate viscosity $\eta_\infty$ , Cross time constant $C$ (s), shear relaxation exponent $m$ and $R^2$ obtained by fitting the experimental viscosity data with the Cross model.

| Surfactant Concentration | $\eta_0$ (±2.5%) | $\eta_\infty$ (±2.5%) | $C$(±3%) | $m$ (±3%) | $R^2$ |
|---|---|---|---|---|---|

| | | | | | |
|---|---|---|---|---|---|
| 1.5 % | 1.80 | 0.011 | 0.485 | 1.03 | 0.998 |
| 3 % | 66.18 | 0.014 | 2.05 | 1.08 | 0.999 |
| 5 % | 158.32 | 0.025 | 3.33 | 1.01 | 0.998 |
| 7 % | 141.20 | $7\cdot10^{-3}$ | 3.25 | 0.99 | 0.998 |
| 10 % | 191.6 | 0.011 | 1.91 | 1.00 | 0.999 |
| 13 % | 228.0 | 0.025 | 0.813 | 1.05 | 0.998 |

When the surfactant concentration exceeds the value of 3 % w/w the fluid viscosity increases by 1-2 orders of magnitude. Moreover, for all the samples the shear relaxation exponent $m$ is very close to 1, which is the theoretical value for plastic materials, suggesting a strong shear-induced modification (*i.e.* alignment) of the micelles.[129] All these findings are consistent with the literature data[73,129,140,141] and confirm the formation of a entangled wormlike micellar network for the NaOL/KCl system.

The thermal behaviour of the NaOL formulations at different surfactant concentration was investigated by means of DSC. The thermograms are reported in Figure 3.3.

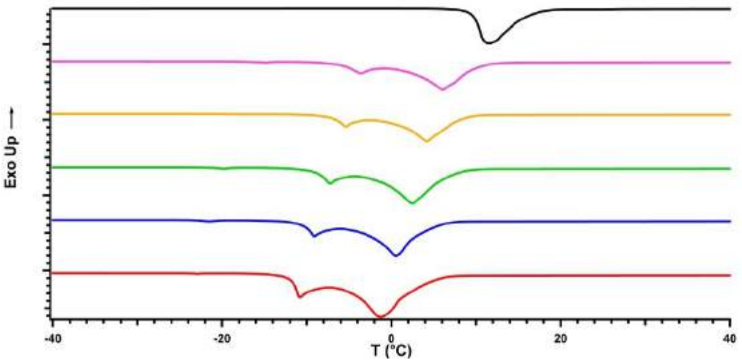

Figure 3.3 – DSC heating curves for NaOL mixtures in the presence of 4 % w/w KCl at different surfactant concentrations: 0 % (black), 3 % (red), 5 % (blue), 7 % (green), 10 % (yellow) and 13 % w/w (pink).

All the samples show a broad endothermic peak centered around 0 °C, which is related to the melting of the free water. The concentration of free water ($W_f$ expressed in % w/w) is calculated according to the following equation:[142]

$$W_f = \Delta H_{mf} \cdot 100/\Delta H_{mfw} \tag{3.1}$$

Here $\Delta H_{mf}$ is the experimental enthalpy change, and $\Delta H_{mfw}$ is the heat of fusion of pure water (333.79 J/g in the experimental conditions used in this study).[143]

When KCl is added to the formulations a second endothermic peak appears in the thermograms around −11 °C. This transition is related to the melting of "interfacial" water, *i.e.* the water confined within the region separating the oleate micelles. Due to their wormlike structure the micelles behave like polymer chains and create an entangled network with solvent-rich domains entrapped between the chains. The water molecules confined in these pores interact with the surfactant polar head groups and the counterions at the micellar surface, and exhibit distinctive thermodynamics and dynamic properties, different from those of bulk water.[144] Similar thermal transitions are detected in several surfactant-based systems, such as micellar solutions[145], microemulsions[142] and liquid crystalline phases.[146] The amount of the interfacial water ($W_i$ expressed in % w/w) is calculated as:

$$W_i = \Delta H_{mi} \cdot 100/\Delta H_{miw} \tag{3.2}$$

where $\Delta H_{mi}$ is the experimental enthalpy change for the melting of interfacial water obtained from the DSC curves and $\Delta H_{miw}$ is the heat of fusion of interfacial water. This enthalpy change depends on the specific polymorphic form of ice produced by the interfacial water.[147] Some authors neglect the polymorphism of ice and use the enthalpy value of water without introducing an appreciable error.[148] We followed Senatra *et al.* and used the corrected enthalpy value of 312.28 J/g.[149]

In the presence of the salt a third endothermic peak with a very small enthalpy change located at about -22 °C appears in the thermograms. The occurrence of this peak reveals the presence of another type of water, the fraction of interfacial water molecules that are closely associated to the carboxylic moieties of NaOL. The presence of a nearby charged surface alters the thermodynamic properties of these water molecules, leading to remarkably reduced melting temperature and enthalpy of fusion.[142,150] This kind of water is usually referred to as freezable bound water.[60,147,149–152] The melting peak temperatures, the corresponding enthalpy changes and amount (%) of the free and interfacial water ($T_{mf}$, $\Delta H_{mf}$, $W_f$ $T_{mi}$, $\Delta H_{mi}$and $W_i$ respectively) are listed in Table 3.3.

Table 3.3 - Melting temperature, the relative enthalpy change and amount (%) of free water ($\Delta H_{mf}$, $T_{mf}$ and $W_f$) and interfacial water ($\Delta H_{mi}$, $T_{mi}$and $W_i$) for all the examined samples.

| **Formulation** | **$\Delta$H$_{mf}$ (J/g)** | **T$_{mf}$ (°C)** | **W$_f$ (%)** | **$\Delta$H$_{mi}$ (J/g)** | **T$_{mi}$ (°C)** | **W$_i$ (%)** |
|---|---|---|---|---|---|---|
| Sodium Oleate 13 % | 319.9 | 2.50 | 95.8 | - | - | - |
| Sodium Oleate 13 % + KCl 4 % | 150.5 | -1.87 | 45.1 | 27.92 | -11.77 | 8,9 |
| Sodium Oleate 10 % + KCl 4 % | 161.7 | -1.74 | 48.4 | 33.11 | -11.50 | 10,6 |
| Sodium Oleate 7 % + KCl 4 % | 166.0 | -1.47 | 49.7 | 27.77 | -11.37 | 8,9 |
| Sodium Oleate 5 % + KCl 4 % | 166.8 | -1.37 | 50.0 | 31.49 | -11.19 | 10,1 |
| Sodium Oleate 3 % + KCl 4 % | 154.9 | -1.02 | 46.4 | 34.81 | -10.91 | 11,1 |

In a second set of experiments, we investigated the effect of salt concentration on the rheological and thermal properties of NaOL/KCl dispersions. The surfactant concentration is fixed at 13% w/w, since sodium oleate can spontaneously form cylindrical aggregates in solution when its concentration exceeds the critical value of 12% w/w, passing from a diluted to a concentrated micellar regime.[129] The salt concentration ranges from 0.1 to 4 % w/w. The results are reported in Paper III, “Light-modulated rheological properties in green innovative formulations” (manuscript in preparation), which is attached in 0.

In the flow curve experiments all the samples exhibit a Newtonian plateau at low shear stress, followed by a shear-thinning region as the shear stress increases. The viscosity drop at high shear stress is more pronounced in the presence of KCl, while for the pure NaOL dispersion the shear-thinning is almost negligible. In the literature this rheological behaviour is generally ascribed to the presence of wormlike micelles,[73,81,139] that bring about a rapid drop in the viscosity due to their shear-induced alignment.[106] The experimental curves were fitted according to the Cross model (see Paragraph 2.4.1.1) to obtain the zero-shear viscosity, $\eta_0$, and an estimation of the infinite rate viscosity $\eta_\infty$ , the Cross time constant *C* (s), and the shear relaxation exponent, *m*. The extracted fitting parameters are listed in Table 3.4.

Table 3.4 - Zero-shear rate viscosity $\eta_0$, infinite rate viscosity $\eta_\infty$ , Cross time constant *C* (s), shear relaxation exponent *m* and $R^2$ obtained by fitting the experimental viscosity data with the Cross model.

| | KCl (% w/w) | $\eta_0$ (Pa·s) | $\eta_\infty$(Pa·s) | C (s) | m | $R^2$ |
|---|---|---|---|---|---|---|
| NaOL 13% | 0 | 0.074 | 0.031 | $5.62\cdot10^{-4}$ | 1.91 | 0.998 |
| | 0.1 | 3.91 | 0.24 | 2.09 | 0.73 | 9.998 |
| | 0.5 | 27.86 | 0.008 | 0.211 | 0.98 | 0.999 |
| | 1 | 443.4 | 0.014 | 1.33 | 1.18 | 0.999 |
| | 2 | 1051 | 0.037 | 2.54 | 1.08 | 0.999 |
| | 3 | 486.8 | 0.053 | 1.133 | 1.08 | 0.999 |
| | 3.5 | 351.4 | 0.052 | 0.765 | 1.13 | 0.999 |
| | 4 | 228.0 | 0.025 | 0.813 | 1.05 | 0.998 |

The trend of the viscosity values suggests a structuring effect of KCl on the NaOL micellar network. For all samples the *m* exponent is very close to 1, suggesting a significant shear-induced modification or alignment of the particles.[129] In several wormlike micellar of ionic surfactants the slope of the power-law region is about 0.9.[140,141] The comparison between the literature data and our results confirms that the shear thinning behaviour of the NaOL-based formulations arises from the anisometric nature of the long, flexible cylindrical aggregates and their orientation in high shear-rate regimes.

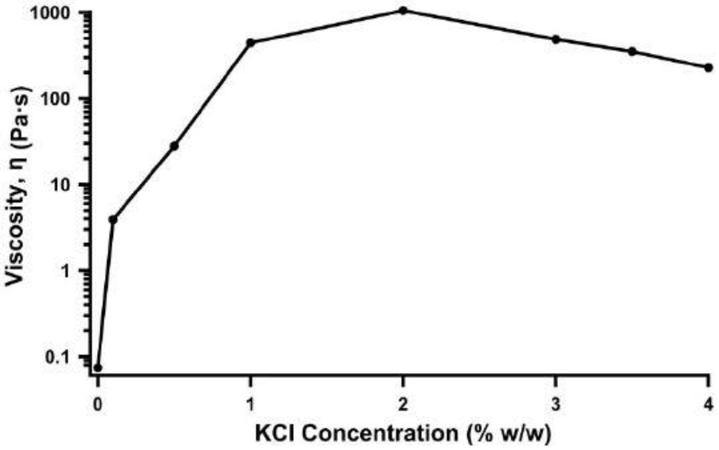

Figure 3.4 – Zero-shear viscosity ($\eta_0$) for the formulations containing NaOL 13 % w/w as a function of the salt concentration.

Figure 3.4 shows the values of $\eta_0$ as a function of KCl concentration. The viscosity steeply increases in the dilute regime, then it reaches a maximum and progressively decreases at higher concentrations of salt. This behaviour is widely reported for cationic[139,153–158], anionic[72,96,159] and non-ionic surfactant[153,160–162] systems that form wormlike micelles, and it is usually referred to as the *salt curve*.[163,164] In the dilute regime the steep increase in the viscosity reflects the one-dimensional growth of the NaOL micelles, resulting in the formation of wormlike structures that overlap and form entangled networks. The presence of a maximum followed by a decrease in the fluid viscosity is usually ascribed to the formation of micellar branched structures.[154,165,166] From a thermodynamic standpoint the increase in the salt concentration results in an increment in the end-cap energy of the linear micelles, which is compensated by the formation of branch points with an opposite curvature.[106] Two further mechanisms contribute to the formation of intermicellar junctions: (i) during the process a partial dehydration of the polar headgroups occurs and some hydrating water molecules are pushed back into the bulk aqueous phase, leading to an increment in entropy, and (ii) as the concentration of branches increases, the semispherical endcaps can fuse together to form a continuous cylindrical bridge that connects different rods.[167] Branched micelles show a lower viscosity compared to linear entangled micelles because they have an additional route for stress relaxation, which involves the sliding of branch points along the micellar body.[106,136]

The viscoelastic properties of wormlike systems are investigated by means of oscillatory shear measurements as a function of KCl concentration. Figure 3.5 andFigure 3.6 show the storage (*G'*) and loss (*G''*) moduli obtained by frequency sweep experiments for the dispersions of sodium oleate in the presence of KCl at different concentrations.

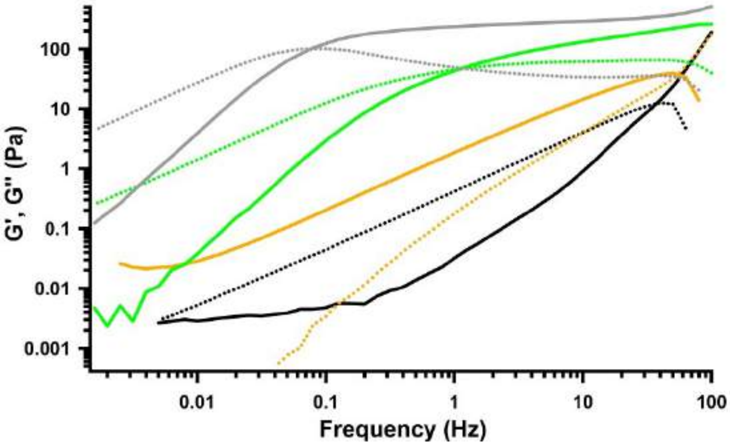

Figure 3.5 –Storage (solid line) and loss (dashed line) moduli for the formulations containing NaOL 13% in the presence of KCl at 0 % (black), 0.1 % (orange), 0.5 % (green) and 1 % (grey).

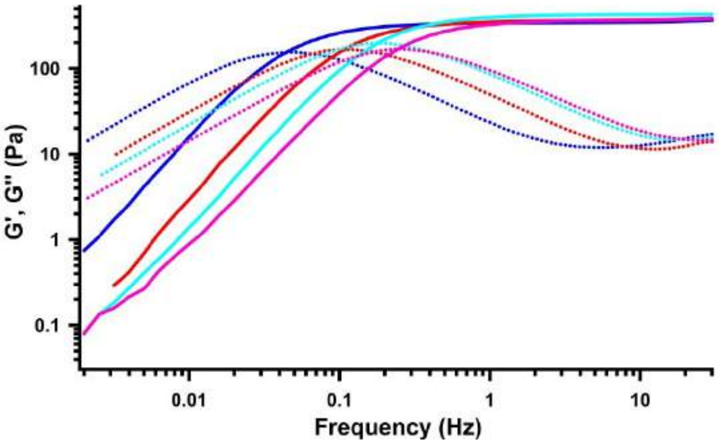

Figure 3.6 –Storage (solid line) and loss (dashed line) moduli for the formulations containing NaOL 13% in the presence of KCl at 2 % (blue), 3 % (red), 3.5 % (light blue) and 4 % (pink).

For the sample containing only sodium oleate, as well as in the presence of very small amounts of KCl (0.1%) the loss modulus *G''* is predominant almost over the entire range of investigated frequencies, indicating a typical viscous-fluid behaviour. When KCl concentration exceeds the value of 0.5 % all the samples exhibit the characteristic rheological behaviour of viscoelastic fluids, with two distinct regimes. At low frequencies, when $\omega < \omega_c$ ($\omega_c$ is the crossover frequency between the two moduli) the loss modulus *G''* exceeds the storage modulus *G'*, indicating a predominantly viscous behaviour. At higher frequencies, when $\omega > \omega_c$, *G'* dominates, and the system is mainly elastic. In simple physical terms, this crossover separates the plateau regime of the collective network dynamics from the single-filament regime.[168] The crossover frequency shows a progressive decrease as the salt concentration increases, indicating at first approximation a slower relaxation dynamics of the system due to a more entangled network.

The viscoelastic behaviour of entangled wormlike micelles is usually described by the Maxwell model for viscoelastic fluid with a single relaxation time $\tau_R$. If the strain amplitude is small enough the fluid structure is not disturbed by the deformation and the resulting stress is controlled by the rate of spontaneous rearrangements. The storage modulus and the viscous modulus are given by the following equations:[165,169]

$$G' = G_0 \frac{\omega^2 \tau_R^2}{\omega^2 \tau_R^2 + 1} \tag{3.3}$$

$$G'' = G_0 \frac{\omega \tau_R}{\omega^2 \tau_R^2 + 1} \tag{3.4}$$

here $\omega$ is the oscillation frequency, $G_0$the elastic modulus extrapolated to infinite frequency (also referred to as the plateau modulus) and $\tau_R$ the characteristic relaxation time of the system.

Combining Equations (3.3) and (3.4) a new expression is obtained:

$$G''^2 + (G' - G_0/2)^2 = (G_0/2)^2 \tag{3.5}$$

Thus, the plot of $G'$ against $G''$ (the so-called Cole–Cole plot) represents another useful tool to demonstrate the Maxwell behaviour.

In entangled wormlike micelles the overall stress-relaxation dynamics is the result of the competition between two effects. The first is reptation, which is commonly observed in entangled solutions of flexible polymers.[154,156] It consists in a snake-like diffusion of the micelle along its own contour, determined by topological constraints and with a characteristic time $\tau_{rep}$. The second mechanism arises from the breaking and recombination of the micelles, since the surfactant molecules can be exchanged reversibly between different worms, and it is characterized by a relaxation time $\tau_B$.[154] In the so-called "fast breaking limit" (*i.e.* $\tau_B \ll \tau_R$) several scission/recombination events occur within the reptation time scale, and the Maxwell model accurately predicts the trend of $G'$ and $G''$. As $\tau_B/\tau_R$ increases, the rheological behaviour deviates from the theoretical model at high frequencies, showing an upturn in the viscous modulus. This discrepancy is related to the transition from "slower" reptation to additional faster relaxation processes, such as Rouse (stretching of chains shorter than the entanglement length) or 'breathing' modes (tube-length fluctuations).[106] Figure 3.7Figure 3.8 report two examples of the fitting obtained by applying the Maxwell model to the frequency sweep data and the relative Cole-Cole plots.

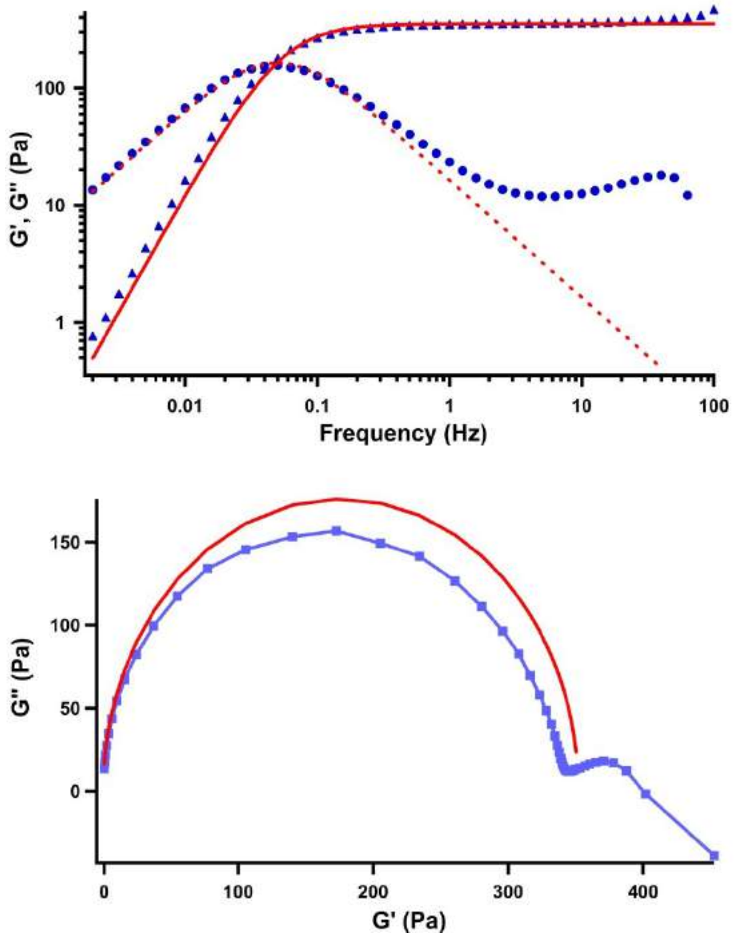

Figure 3.7 – Top: the storage (triangles) and loss (circles) moduli for NaOL 13 % in the presence of KCl at 2 % with the respective fitting (red lines) according to the Maxwell model. Bottom: the relative Cole-Cole plot.

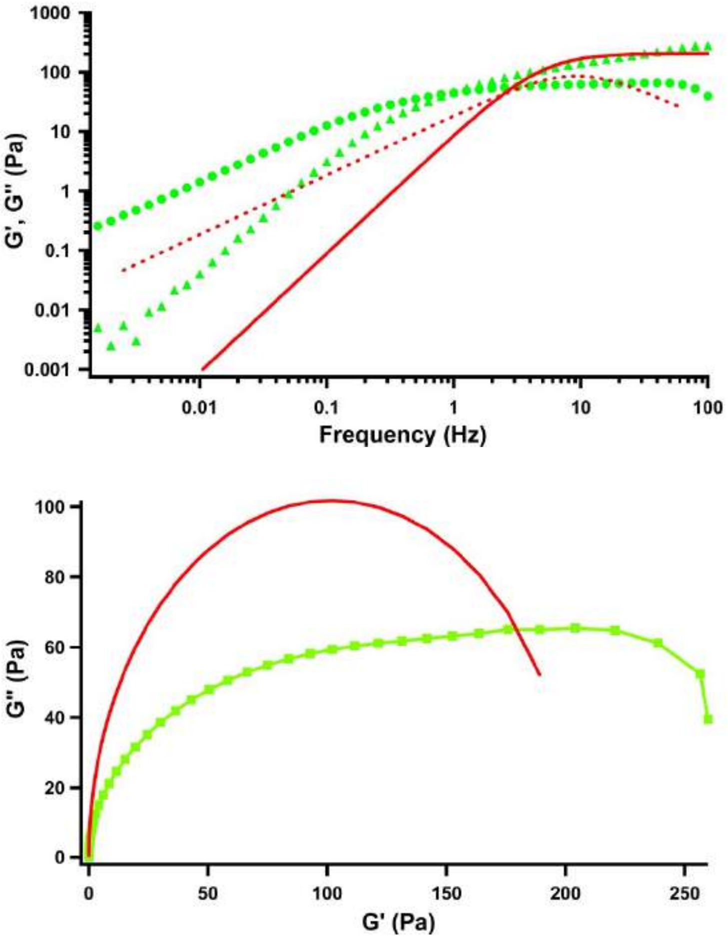

Figure 3.8 – Top: the storage (triangles) and loss (circles) moduli for NaOL 13 % in the presence of KCl at 0.5 % with the respective fitting (red lines) according to the Maxwell model. Bottom: the relative Cole-Cole plot.

The relaxation dynamic of the NaOL/KCl systems cannot be described by a single-element in the Maxwell model since major discrepancies are observed between the experimental data and the predicted values for most samples. To overcome this problem, we use both $G'$ and $G''$ to calculate the time-weighted relaxation spectrum $H(\tau)$.[170,171] Figure 3.9 reports the time-weighted relaxation spectrum for four formulations containing NaOL 13 % at different KCl concentration.

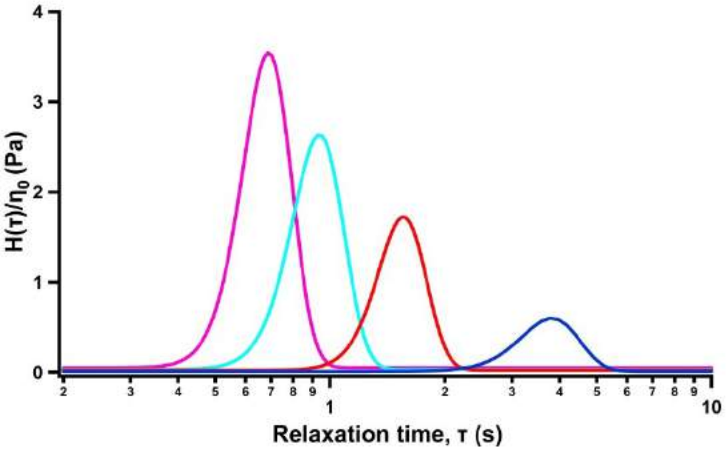

Figure 3.9 - Normalized relaxation spectra obtained for the samples containing NaOL 13 % in the presence of KCl 2 (blue), 3 (red), 3.5 (light blue) and 4 % (pink).

All the relaxation spectra shows a broad primary peak from which we estimate the relaxation times. For most samples multiple secondary peaks are observed, indicating the presence of different relaxation mechanisms (reptation, breaking and recombination, Rouse, etc.). The relaxation times extracted from the spectra are reported as a function of KCl concentration in Figure 3.10.

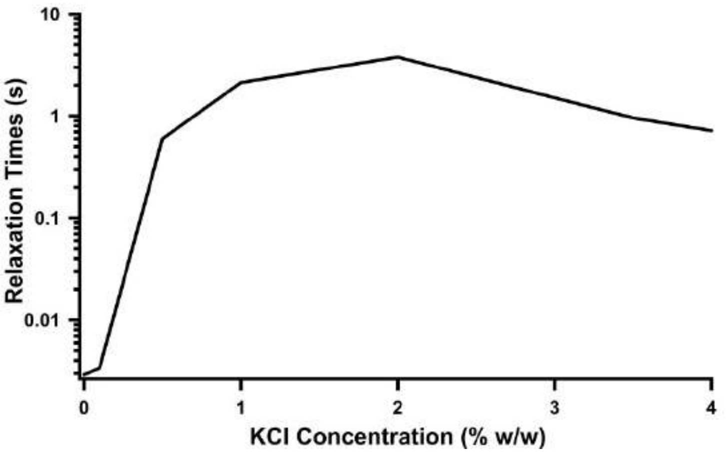

Figure 3.10 – Relaxation time ($\tau$) for the formulations containing NaOL 13 % as a function of KCl concentration.

The relaxation times follow the same trend of the viscosity as the salt concentration increases (compare Figure 3.10 and Figure 3.4). This behaviour confirms the strengthening effect of

KCl on the entangled micellar network, giving rise to similar modifications in the viscosity and in the dynamic rheological properties of the formulations.

The thermal behaviour of the NaOL 13 % formulations at different KCl concentration was investigated by means of DSC. The melting peak temperatures, the corresponding enthalpy changes and amount (%) of the free and interfacial water ($T_{mf}$, $\Delta H_{mf}$, $W_f$ $T_{mi}$, $\Delta H_{mi}$and $W_i$ respectively) are listed in Table 3.5. For the thermograms, see Paper III in 0. As the salt concentration increases, $W_f$ rapidly decreases, passing from 96% to 46%. When KCl concentration exceeds 0.5% a second endothermic peak due to the melting of interfacial water appears in the thermograms between –15 and –11 °C. A depression of the melting peak temperatures $T_{mi}$is observed with increasing KCl content, while $\Delta H_{mi}$ shows an opposite trend, increasing from about 1 J/g in the case of KCl 0.5% to about 27 J/g for KCl 3.5%. The addition of the salt progressively screens the electrostatic repulsion between the micelles and leads to the formation of a more entangled network. Thus, the number of water molecules confined within the intermicellar domains increases, as indicated by the values of $W_i$, that passes from 0.4% to 8%. In the case of KCl 4%, the DSC curve shows a third endothermic peak with a small enthalpy change located at about -22 °C. This signal is related to the melting of freezable bound water, i.e. the fraction of interfacial water molecules that are closely associated to the surfactant headgroups.

From these results we can infer that the presence of a salt affects the interactions between the surfactant and the water molecules, altering the hydration state of the wormlike micellar structures. This effect induces a modification in the network entanglement, which reflects in remarkable viscosity variation as a function of salt concentration.

Table 3.5 - Melting temperature, the relative enthalpy change and amount (%) of free water ($\Delta H_{mf}$, $T_{mf}$ and $W_f$), interfacial water ($\Delta H_{mi}$, $T_{mi}$and $W_i$) and freezable bound water ($\Delta H_{mb}$, $T_{mb}$and $W_b$) for all the examined samples

| | **KCl (%)** | **ΔH$_{mf}$ (J/g)** | **T$_{mf}$ (°C)** | **W$_f$ (%)** | **ΔH$_{mi}$ (J/g)** | **T$_{mi}$ (°C)** | **W$_I$ (%)** | **ΔH$_{mb}$ (J/g)** | **T$_{mb}$ (°C)** | **W$_b$ (%)** |
|---|---|---|---|---|---|---|---|---|---|---|
| **NaOL 13 %** | 0 | 319.9 | 2.50 | 95.8 | - | - | - | - | - | |
| | 0.1 % | 300.2 | 1.97 | 89.9 | - | - | - | - | - | |
| | 0.5 % | 286.5 | 1.30 | 85.8 | 1.221 | -14.67 | 0.4 | - | - | |
| | 1 % | 232.5 | 1.69 | 70.0 | 8.367 | -12.88 | 2.7 | - | - | |
| | 2 % | 217.7 | 0.39 | 65.2 | 18.22 | -11.58 | 5.8 | - | - | |
| | 3 % | 169.6 | 0.12 | 50.8 | 21.66 | -11.02 | 6.9 | - | - | |
| | 3.5 % | 163.3 | -0.94 | 48.9 | 27.47 | -11.22 | 8.8 | - | - | |
| | 4 % | 152.8 | -1.06 | 45.8 | 25.16 | -11.45 | 8.1 | 3.507 | -22.69 | 1.12 |

## 3.2 Effect of Salts and Cosolutes

Once the main physico-chemical properties of the two base formulations (namely the polysaccharide and the VES fluid) were assessed, we evaluated the effect of high salinity conditions on the formulation rheological and thermal behaviour. The goal is to understand how and to which extent the nature and/or the salt concentration affect the viscosity of the fluids, in order to have an accurate and steady control of the viscosity during all the stages of fracturing operations. Since each shale formation is unique, the composition of flowback and produced water may change significantly: this specificity can be used to formulate fracturing fluids in which the viscosity is sensitive to specific salts or a combination of them. This strategy allows the modulation of the fluid properties *in situ* during the different phases of the basin exploitation, without the addition of extra chemicals like gel breakers that usually have a massive environmental impact.

For the polysaccharide-based formulations, we followed a three-stage approach in order to check the effectiveness of our formulations in high salinity conditions.

At first we tested our formulations in the presence of thirteen different salts or neutral co-solutes, which were individually added to the formulation at the concentration of 0.5 mol/L. The salts and co-solutes examined are sodium fluoride (NaF), sodium chloride (NaCl), sodium bromide (NaBr), sodium iodide (NaI), sodium sulfate ($Na_2SO_4$), sodium thiocyanate (NaSCN), sodium perchlorate ($NaClO_4$), trisodium phosphate ($Na_3PO_4$), disodium monohydrogen-phosphate ($Na_2HPO_4$), sodium dihydrogen-phosphate ($NaH_2PO_4$), urea ($CH_4N_2O$) and trehalose ($C_{12}H_{22}O_{11}$). Rheological and DSC experiments provided crucial insights into the specific ion effect on the formulation behaviour, elucidating in particular the role of the anion. More specifically, we observed which additives efficiently modify the properties of our formulations and which other are substantially ineffective. The results are included in Paper I, “Specific ion effects in polysaccharide dispersions”, Copyright 2017 Elsevier, which is attached in 0.

Secondly, we tested our formulations in a mixed salt solution that mimics the salinity conditions in real shale formations. We prepared this solution (indicated as “shale water”) starting from the literature data related to the flowback water salinity content of some European and US shale basins.[110–112] Shale water is composed by NaCl 1 M, $CaCl_2$ 0.2 M, KBr 0.014 M, $SrCl_2$ 0.01M and $BaCl_2$ 0.002 M, as reported in Section 2.2.3. The assumption is that the salt composition and concentration of the flowback water should be not too dissimilar from the salinity conditions present downhole during the extraction stage of the fracturing operations. Thus, testing our formulations in shale water allow us to predict how these fluids behave in salinity conditions near to the operating ones.

Finally, we performed additional tests to qualitatively detect the salt toleration thresholds of the different polysaccharide formulations. For this purpose we overstressed the salt concentration up to 5 mol/L, which is an exceptionally higher value in comparison with the average total salinity of European flowback water. Since sodium chloride is the most abundant salt present in the flowback water, we carried out our experiments by simply varying the concentration of NaCl from 0.1 to 5 M.

For the VES formulation we performed preliminary tests by changing the nature of the salt to qualitatively evaluate the effect of different anions on the texture of the viscoelastic fluids. In these experiments potassium chloride was replaced by the other potassium halides, *i.e.* KF, KBr and KI. Moreover we studied the stability of the NaOL formulations in high salinity conditions using the shale water, in order to assess their salt resistance and effectiveness in the fracturing operating conditions.

### 3.2.1 Effect of Simple Salts on polysaccharide formulations

Flow curves experiments for GG, SH and SA 1 % dispersions in the presence of the different salts and cosolutes (NaF, NaCl, NaBr, NaI, $Na_2SO_4$, NaSCN, $NaClO_4$, $Na_3PO_4$, $Na_2HPO_4$, $NaH_2PO_4$, $CH_4N_2O$, $C_{12}H_{22}O_{11}$) were acquired and the results were fitted according the BCY model. The extrapolated values of $\eta_0$, λ, $a$ and $n$ are reported in Table 3.6.

Table 3.6 - The zero shear rate viscosity ($\eta_0$, in Pa·s), power law index (n), the reciprocal of the critical shear rate at which the viscosity begins to drop down (λ, in s), the width of the transition region between $\eta_0$ and $\eta_\infty$ (a), and the χ2 extracted from the fitting of the flow curves for 1% aqueous mixtures of guar gum and sodium hyaluronate, in the presence of different salts or neutral co-solutes. The concentration of all co-solutes is always 0.5 M, unless otherwise specified.

| additive | $\eta_0$ ±2.5% | $n$ ±4% | $\lambda$ ±5% | $a$ ±3% | $\chi^2$ | $\eta_0$ ±1.5% | $n$ ±15% | $\lambda$ ±9% | $a$ ±4% | $\chi^2$ |
|---|---|---|---|---|---|---|---|---|---|---|
| | Guar Gum 1% | | | | | Sodium Hyaluronate 1% | | | | |
| none | 24.41 | 0.20 | 1.36 | 0.58 | 6.96 | 44.66 | 0.20 | 2.22 | 1.21 | 51.71 |
| NaF | 33.30 | 0.19 | 1.64 | 0.65 | 13.29 | 28.05 | 0.19 | 0.87 | 0.57 | 7.12 |
| NaCl | 25.23 | 0.22 | 1.19 | 0.58 | 7.28 | 44.84 | 0.21 | 2.14 | 1.00 | 72.92 |
| NaBr | 23.68 | 0.22 | 1.24 | 0.57 | 3.64 | 40.95 | 0.26 | 2.07 | 0.93 | 98.98 |
| NaI | 19.70 | 0.24 | 1.11 | 0.51 | 6.88 | 46.23 | 0.15 | 1.22 | 0.55 | 6.25 |
| $Na_2SO_4$ | 43.53 | 0.21 | 3.14 | 0.67 | 32.67 | 21.01 | 0.22 | 0.76 | 0.59 | 3.75 |
| NaSCN | 28.27 | 0.16 | 1.12 | 0.42 | 7.05 | 40.96 | 0.27 | 2.11 | 0.68 | 39.50 |
| $NaClO_4$ | 23.87 | 0.22 | 1.47 | 0.67 | 10.10 | 53.09 | 0.28 | 2.93 | 0.84 | 32.18 |
| $Na_2HPO_4$ | 30.07 | 0.20 | 2.02 | 0.80 | 16.01 | 77.68 | 0.22 | 2.58 | 1.18 | 26.14 |
| $NaH_2PO_4$ | 20.44 | 0.19 | 1.01 | 0.63 | 3.50 | 19.75 | 0.30 | 1.22 | 0.70 | 12.07 |
| $Na_3PO_4$ | 19.90 | 0.24 | 1.29 | 0.64 | 5.36 | - | - | - | - | - |
| Urea | 33.68 | 0.23 | 2.16 | 0.66 | 10.45 | 46.21 | 0.26 | 1.98 | 0.78 | 3.83 |
| Trehalose | 37.65 | 0.21 | 2.60 | 0.66 | 38.32 | 159.25 | 0.20 | 6.07 | 0.90 | 73.50 |

Almost all flow curves containing GG and SH are well fitted by the BCY model with the exception of SH in the presence of $Na_3PO_4$, which shows a very low viscosity and an inappreciable shear thinning behaviour. SA dispersions exhibit minor changes in the viscosity profile upon the addition of the different salts in the whole shear range examined, and all the extrapolated $\eta_0$values are very close to the value of pure SA dispersion. This behaviour originates from the peculiar gelation mechanism of sodium alginate, which is strictly dependent on the presence of divalent cations. The gelling capacity is directly correlated to the amount of a-L-guluronic acid (G) blocks present along the polysaccharide chain, because only the a-L-guluronic acid has an active role in the formation of crosslinks in the hydrogel. The G blocks of the polymer chain form cavities, which work as a binding site for the bivalent cations and then arrange themselves all around creating a structure comparable to an "egg box".[172,173] Monovalent ions like sodium may be capable of stabilizing intermolecular "egg-box" junctions analogous to those formed with divalent cations but of considerably shorter time-scale and much lower binding energy.[174,175] For this reason we do not observe any remarkable variation in the dispersion properties by changing the nature of the anion of the sodium salt, and the results obtained from the flow curves experiments are not listed in Table 3.6.

Figure 3.11 illustrates the effect of trehalose, $Na_2SO_4$ and NaF on the profile of the flow curve of SH and GG. For SH the presence of trehalose led to an increase of the strength of the tridimensional network, as indicated by the increase of $\eta_0$ (from 44.66 up to 159.25 Pa·s) and by a shift of the yield value of $\dot{\gamma}$, $\lambda$. On the other hand, sulfate and fluoride lower both the $\eta_0$ (21.01 and 28.05 Pa·s respectively) and the $\lambda$ values. Indeed, trehalose is known as a kosmotrope or water-structure maker: this disaccharide is able to break the tetrahedral HB network of water and re-order the water molecules in the hydration layer.[176,177] However, experiments conducted by us on a 0.5 M solution of trehalose in water show neither an increase in the viscosity, nor a modification in the rheological response.

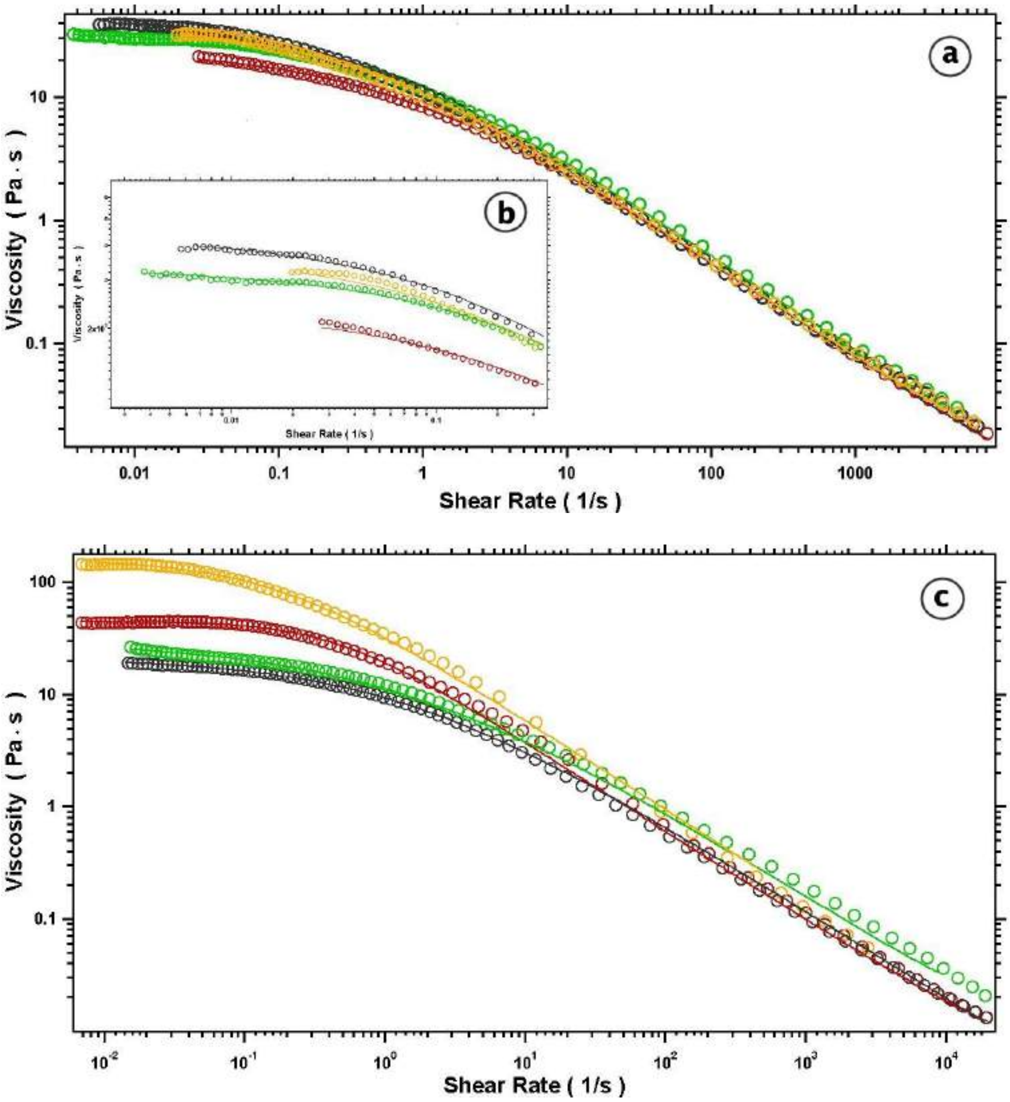

Figure 3.11 - Flow curves of (a) GG and SH (c) 1% w/w mixtures (red) and in the presence of 0.5 M trehalose (yellow), NaF (green) and $Na_2SO_4$ (grey). The inset (b) shows the flow curves of GG zoomed at low shear stress. The solid lines represent the fitting of the experimental curves.

The competition for water molecules between trehalose and the polysaccharide chains leads to partial de-hydration of the macromolecules.[178] It has been shown that trehalose can modify the hydration layer of biomolecules,[179,180] stabilizing their HB network. This picture, commonly known as *preferential exclusion theory*. The *water replacement theory* instead argues that the hydration layer of the macromolecules is substituted by trehalose, which directly forms HB and stabilizes the structure. A third approach, the *vitrification theory*, can be applied only at higher concentration of trehalose and envisages that it creates a glassy matrix which acts as a protective cocoon, shielding and stabilizing the macromolecules from external stresses.[178] Since in our case the concentration of trehalose is relatively low, we can exclude the latter hypothesis. In the case of sulphate we propose two different mechanisms, depending on the investigated polysaccharide. The $SO_4^{2-}$ ion is a kosmotrope, which subtracts water from the macromolecule hydration layer. In the case of SH, where negatively charged -$COO^-$ groups are distributed along the chains, the addition of sulfate brings about a weakening in the polymeric network, that results in a decrease of the strength of the polymeric network. Conversely for GG the reduction of water molecules in the hydration layer promotes the formation of interchain interactions, due to the non-ionic nature of the polysaccharide. Therefore, the strength of the polymeric network increases, as indicated by the trend of both the viscosity and the $\lambda$ values. Moreover, also the effect of fluoride supports this argument. Indeed, kosmotropic ions like fluoride and sulfate strongly modify the rheology of the systems. At the same time, the addition of the other halides to GG and SH does not affect significantly the values of $\eta_0$ and $\lambda$.

A further peculiar case concerns the three phosphate anions (Figure 3.12). In fact, the rheological profiles show that $HPO_4^{2-}$ increases the viscosity of the SH solution to 77.68 Pa·s, while $H_2PO_4^-$ lowers (19.75) and $PO_4^{3-}$ dramatically breaks down the flow curves.

We recall that the rheological properties of hyaluronate strongly depend on the pH in a non-linear correlation.[62,65,66,181] In particular for hyaluronic acid the complex viscosity reaches a maximum value at about pH = 2.5, sided by two remarkable drops in acid (pH = 1.6) and mid-acid conditions (pH = 3.34).[142] The stiffening of the hyaluronic network is attributed to a critical balance between attractive and repulsive forces. These forces that involve ionized or neutral carboxylic and amino groups are mainly electrostatic.[140] Moreover, above pH = 12 the viscosity dramatically breaks down, leading to a Newtonian-like behaviour.

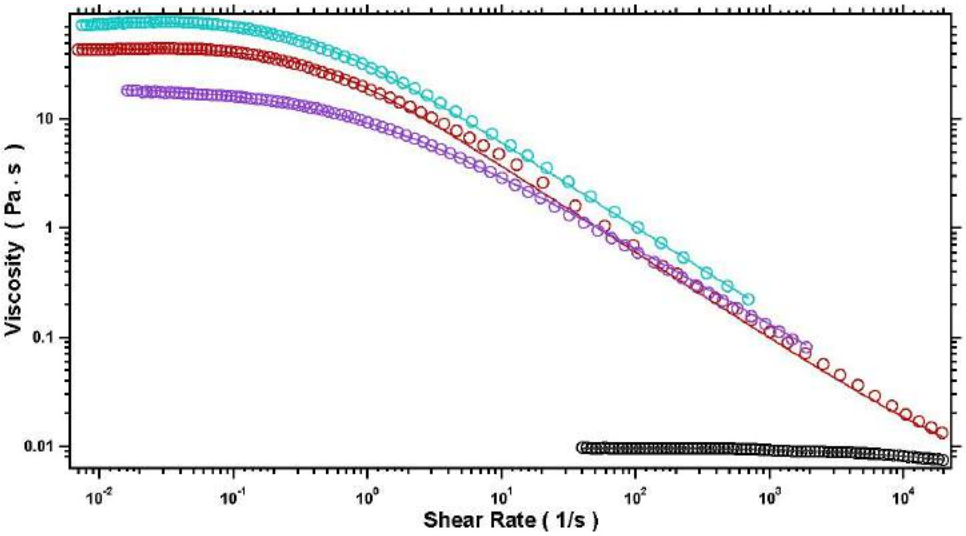

Figure 3.12 – Flow curves of SH 1% w/w pure solution (red), in the presence of 0.5 M $NaH_2PO_4$ (violet), $Na_2HPO_4$ (turquoise) and $Na_3PO_4$ (black). The solid lines represent the fitting of the experimental curves.

Finally, in a wide range of pH (between 2.8 and 12) the rheological properties and viscosity remain unchanged.[142] Furthermore, Maleki investigated the dilute (0.05% w/w) and semi-dilute (0.5% w/w) regimes of HA solutions, with the pH set between 1 and 13 by adding 0.1 M phosphate buffers.[144] The results show that the presence of these buffers does not affect the pH responsivity.

The 0.5 M $Na_3PO_4$ solution provides an extremely high pH (13) that can at least partly deprotonate the –OH groups of the hyaluronate chain, breaking the cooperative HB network of the polysaccharide chains. On the other hand, our results for 0.5 M $NaH_2PO_4$ and $Na_2HPO_4$ solutions (pH = 4.7 and 9.9, respectively) differ from those reported in the literature. Presumably in these pH conditions mono-hydrogenphosphate acts as a soft cross-linker, strengthening the HB network and increasing the viscosity. We argue that the increment in viscosity is due to a combination of two cooperating effects: the basic pH promotes the deprotonation, enhancing the HB network, and at the same time the higher SH concentrations shrink the polysaccharide network where $HPO_4^{2-}$ anions bridge different chains and re-enforce the HB network.

In the presence of dihydrogenphosphate the pH is lower. The mid-acid environment weakens the network by reducing the number of active sites available for HB. Moreover, in $H_2PO_4^-$ the number of acceptor sites for hydrogen bonding is reduced and thus the ion contribution to the strengthening of the system is reduced.

Moreover, the power law index parameter $n$ reflects how the systems respond to an applied stress. Indeed, both GG dispersions and SH solutions exhibit only small fluctuations of $n$ around the value of 0.2 for all samples. Thus, the scalar law that describes the shear thinning behaviour above the $\lambda$ critical value, is almost independent on the chemical nature of the added salt. After the disruption of the HB network in both cases we observed the same shear thinning effect.

DSC experiments were  conducted on SH, GG, SA formulations in order to investigate the effect of the different salts on the thermal properties of the fluids. The thermograms of GG in the presence of different 0.5 M solutions of sodium halides are shown in Figure 3.13.

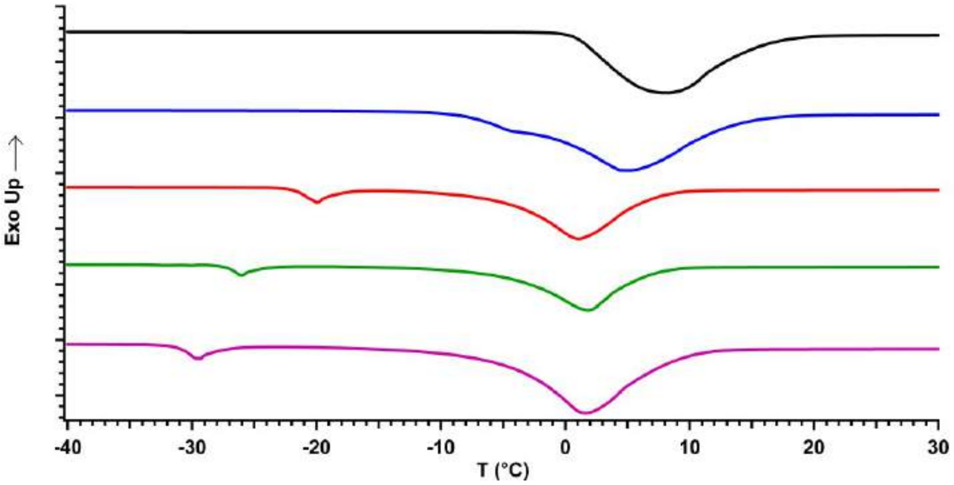

Figure 3.13 – DSC heating curves of 1% aqueous mixtures of GG pure (black) and in the presence of 0.5 M solutions of NaF (blue), NaCl (red), NaBr (green) and NaI (magenta). Curves have been offset for graphical purposes..

In the case of NaF the endothermic peak shows a bimodal behaviour. The curve was deconvoluted by using an exponentially modified Gaussian function (EMG) according to Equation (2.3). The fitting procedure provides the two $T_0$ values corresponding to the centers of the two Gaussian curves used for the deconvolution. $T_0$ are found to be 5.07 and -4.45 °C. This bimodal behaviour is increased with increasing halide atomic number: in the case of

NaCl, NaBr and NaI two distinct peaks appear in the DSC curve whose distance increases moving down in the group. The higher temperature peak corresponds to the melting of free water ($T_{mf}$) and is similar to the peak produced by the salt-free GG dispersion. The lower temperature peak located between –30 and -5 °C relates to the melting of freezable bound water ($T_{mb}$), that freezes below 0 °C and has a reduced enthalpy of fusion.[150]

For the samples containing pure GG, SA and SH the peak related to the melting of freezable bound water is not observed, probably because it overlaps with the free water melting peak giving rise to a broad endothermic signal (see Section 3.1.1). The addition of a salt modifies the interactions between water and the polysaccharide chains and changes the distribution of water between the two states, inducing a separation of the two overlapping peaks which is strictly dependent on the salt nature. The melting temperatures and enthalpy changes of free water ($T_{mf}$ and $\Delta H_{mf}$, in ° C and J/g) and of the freezable bound water ($T_{mb}$ and $\Delta H_{mb}$, in ° C and J/g) are listed in Table 3.7.

The melting point and the enthalpy change for the bound freezable water depend on the interactions between the polymer chains and water.[151] As proposed by De Andres-Santos for 1% aqueous solutions of sodium hyaluronate, we assume that the lower $T_{mb}$, the higher the number of water and polysaccharide molecules that remain closely associated to each other, i.e., the more hydrated the chains.[182] On the other hand, a higher $T_{mb}$ indicates an increment in the interchain hydrogen bonding (HB) interactions within the polysaccharide, thus suggesting a sort of de-hydration of the polymer.

Table 3.7 - Melting temperature and enthalpy change of free water ($T_{mf}$ and $\Delta H_{mf}$, in ° C and J/g) and of the freezable bound water ($T_{mb}$ and $\Delta H_{mb}$, in ° C and J/g) in 1% aqueous mixtures of guar gum, sodium alginate, and sodium hyaluronate, in the presence of different salts or neutral cosolutes. The concentration of all cosolutes is always 0.5 M, unless otherwise specified.

| additive | $T_{mf}$ | $\Delta H_{mf}$ | $T_{mb}$ | $\Delta H_{mb}$ | $T_{mf}$ | $\Delta H_{mf}$ | $T_{mb}$ | $\Delta H_{mb}$ | $T_{mf}$ | $\Delta H_{mf}$ | $T_{mb}$ | $\Delta H_{mb}$ |
|---|---|---|---|---|---|---|---|---|---|---|---|---|
| | Guar Gum 1% | | | | Sodium Alginate 1% | | | | Sodium Hyaluronate 1% | | | |
| none | 7.88 | 307.3 | | | 5.36 | 336.4 | | | 2.18 | 353.0 | | |
| NaF | 5.07 | 155.5 | -4.45 | 125.8 | 1.16 | 273.7 | -4.11 | 56.39 | 0.66 | 300.8 | -5.23 | 40.46 |
| NaCl | 1.05 | 245.2 | -19.9 | 22.11 | 1.33 | 241.8 | -19.8 | 21.50 | -0.03 | 260.1 | -20.4 | 23.77 |
| NaBr | 1.80 | 249.7 | -26.0 | 16.58 | 0.05 | 267.3 | -26.3 | 17.78 | -0.16 | 268.8 | -26.7 | 19.18 |
| NaI | 1.62 | 256.2 | -29.6 | 15.07 | 0.07 | 267.6 | -29.7 | 16.40 | -0.57 | 272.4 | -29.9 | 16.54 |
| $Na_2SO_4$ | 4.24 | 318.4 | | | 2.61 | 334.1 | | | 2.49 | 331.8 | | |
| NaSCN | 1.54 | 282.7 | | | -0.22 | 276.3 | | | -0.13 | 289.4 | | |
| $NaClO_4$ | 2.58 | 278.2 | | | -0.35 | 293.6 | -33.2 | 12.28 | -0.22 | 299.6 | -33.2 | 5.678 |
| $Na_3PO_4$ | 1.28 | 58.88 | | | 4.42 | 294.8 | | | 0.64 | 317.6 | | |
| $Na_2HPO_4$ | 5.13 | 293.5 | | | 1.50 | 331.9 | | | 1.79 | 274.5 | | |
| $NaH_2PO_4$ | 3.00 | 291.5 | | | -0.23 | 295.8 | | | -0.32 | 307.5 | | |
| Urea | 3.48 | 247.9 | -10.6 | 8.342 | 2.03 | 254.1 | -11.1 | 11.68 | 0.00 | 268.8 | -11.8 | 13.67 |
| Trehalose | 1.56 | 255.2 | | | 0.59 | 279.9 | | | 0.07 | 261.9 | | |

The results obtained for the samples containing the sodium halides show no remarkable variation in $T_{mf}$ and $\Delta H_{mf}$ with the exception of NaF. Instead, the values of $T_{mb}$ decrease from -4.45 (NaF) to -29.65 °C (NaI), while $\Delta H_{mb}$ decreases from 125.8 (NaF) to 15.07 J/g (NaI). These trends suggest the presence of a specific anion effect on the conformational structure and intermolecular interactions of GG. In particular, the more chaotropic the anion, the lower the value of $T_{mb}$ and hence the lower the number of interacting sites between the polysaccharide chains. We argue that strongly hydrated kosmotropic anions like fluoride and sulfate compete with the polysaccharide chains for water molecules, thus lowering the hydration of the chains.[183] This effect promotes the formation of interchain HB and eventually leads to the aggregation of polysaccharide molecules.

On the other hand, the presence of chaotropic anions, like iodide, modifies the dimensions of the polysaccharide coils and increases their solvent-accessible surface area (ASA).[184] These ion hydration effects that lead to the salting-in processes induced by chaotropes and salting-out by kosmotropes on proteins has been extensively studied.[185] The ruling mechanism by which chaotropes increase the solvation of the polymer surface seems to be a direct interaction of the ions with the weakly hydrated portions of the polysaccharide chain, as already found and reported in the case of.[186–188]

The presence of urea produces a second endothermic peak in the thermogram, related to the melting of freezable bound water. At this concentration urea usually acts as an enhancer of the solvation of the polysaccharide chains by promoting their unfolding.[189]

In the case of the other additives ($Na_2SO_4$, NaSCN, $NaClO_4$, $Na_3PO_4$, $Na_2HPO_4$, $NaH_2PO_4$ and trehalose) only a broad endothermic peak around 0 °C is clearly detected (see Table 3.7, and 0). The presence of these co-solutes does not induce a separation between the freezable bound and the free water melting peaks, resulting in a DSC profile which is similar to those of pure GG, SA and SH samples (see Paragraph 3.1.1). The case of $Na_2SO_4$ is peculiar as it shows a value of $\Delta H_{mf}$ (318.4 J/g) which is close to that of pure water (333.5 J/g). The sulfate ions strongly interact with the water molecules inducing a de-hydration of the polysaccharide chains, reducing the amount of freezable bound water in favour of the free water, and resulting in an overlap of the two DSC signals.

The effect induced by $Na_2HPO_4$ is peculiar and deserves an in-depth analysis. The DSC curve (see 0) shows a shoulder at about 20°C. This phenomenon can be related to a liquid crystalline-to-isotropic liquid state transition.[190,191] Since this transition is observed both for GG and SA samples, we argue that the presence of $Na_2HPO_4$ preserves the liquid crystalline phase in the guar and sodium alginate network, whereas all the other examined salts and co-solutes destabilize this state.

In order to separate the two endothermic contributions and calculate the enthalpy for this transition, EMG deconvolution was performed and the fitting parameters ($T_{ph}$ and $\Delta H_{ph}$) are shown in Table 3.8. For GG the liquid crystalline-to-isotropic liquid state transition occurs at $T_{ph} = 19.3$ ° C, with a corresponding enthalpy change of 24.68 J/g.

Table 3.8 – Temperature and enthalpy change for the transition between the liquid crystalline and the isotropic liquid state in the presence of $Na_2HPO_4$ 0.5 M for the three investigated polysaccharides..

| polysaccharide | $T_{ph}$ (°C) | $\Delta H_{ph}$ (J/g) |
|---|---|---|
| guar gum 1% | 19.32 | 24.68 |
| sodium alginate 1% | 14.41 | 7.10 |
| sodium hyaluronate 1% | 19.02 | 67.14 |

Aqueous solutions of SA and SH in the presence of salts and cosolutes show an identical thermal behaviour to that previously described for GG dispersions. The values of $T_{mf}$, $\Delta H_{mf}$, $T_{mb}$ and $\Delta H_{mb}$ extracted from the thermograms are reported in Table 3.7. SH and SA samples show analogous DSC curves to the corresponding GG samples, with the exception of perchlorate. For both SA and SH systems, the thermograms of perchlorate containing sample shows two peaks instead of one, as in the GG/perchlorate sample. An extra peak appears at about -33 °C and can be ascribed to the freezable bound water melting. This peak may reflect polymer-salt interactions similar to those occurring with other chaotropic ions. In the GG sample this peak is not shown, indicating that a different mechanism occurs. It is worthwhile to mention that $ClO_4^-$ may act as an oxidizer and it is extensively used as gel breaker in guar-based formulations.[192–194] Presumably perchlorate partially oxidizes the polysaccharide chains, inducing a structural modification and a change in the polymer-water interactions, and the peak for the melting of freezing bound water disappears. This mechanism does not take place with the partially anionic chains of SA and SH.

In order to correlate the rheological and thermal behaviours to the thermodynamic properties of the investigated salts, we report in Figure 3.14 the viscosities for GG, SH and water (top panel) and the $T_{mb}$ values for GG and SH (bottom panel) in the presence of $Na_2SO_4$, NaF, NaCl, NaBr, NaSCN, NaI, $NaClO_4$ as functions of the $\Delta G_{hydration}$ of the anion.
The viscosity values of aqueous salt solutions and $\Delta G_{hydration}$ are taken from literature (for further details see Paper I in 0).[195–201] In the case of $T_{mb}$, the samples containing $Na_2SO_4$, NaSCN and $NaClO_4$ (only for GG) are not reported since no bound freezable water melting peak was detected in the DSC thermograms.

The viscosity plot shows that the addition of a salt to GG (black) and to water (red) produces a similar trend, in agreement to the direct Hofmeister sequence:

$Na_2SO_4$ > NaF > NaCl > NaBr > NaSCN > NaI > $NaClO_4$.

Thus, we conclude that the addition of a salt induces a similar modification in the viscosity for both pure water and GG dispersion. On the other hand, the trend recorded for SH differs remarkably, showing the opposite behaviour and following a reverse Hofmeister series.

The added salt produces an identical effect on the $T_{mb}$ for the two polysaccharides, resulting in a decrease of the freezable bound water melting temperature moving along the series:

NaF > NaCl > NaBr > NaI > $NaClO_4$.

These results confirm that the salt affects in the same way the hydration of the GG and SH by modifying the interactions between the water molecules and the polysaccharides, regardless of the different charge of their chains. Despite this, the GG dispersions and SH solutions show a diametrically opposite trend in terms of viscosities.

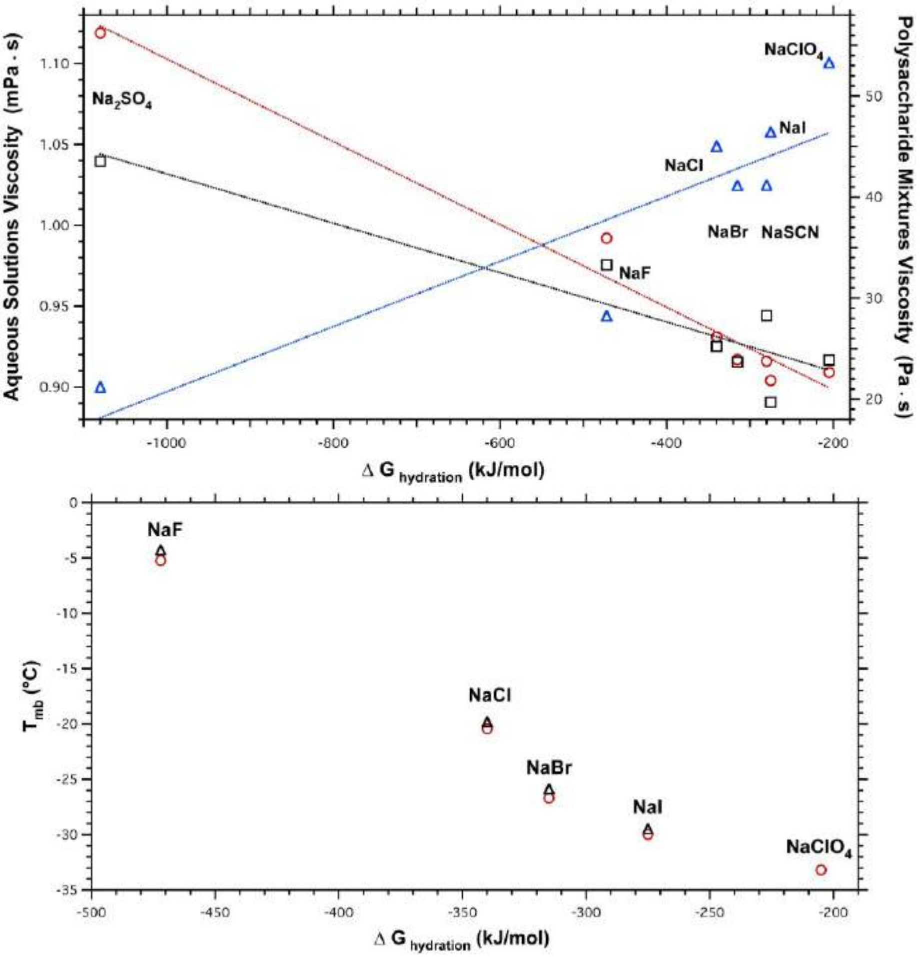

Figure 3.14 – Top panel: viscosity values for GG (black), SH (blue) and water (red) in the presence of the different sodium salts as a function of the $\Delta G_{hydration}$ of the anion. The left axis refers to the red line, while the right axis refers to black and blue lines. The dotted lines are only a guide for the eye. Bottom panel: $T_{mb}$ for GG (black) and SH (red) in the presence of different sodium salts as a function of the $\Delta G_{hydration}$ of the anion.

Kosmostropic anions induce a partial de-hydration of the polysaccharide chains, while the less hydrated chaotropic ions adsorb to the polymer chains, promote their unfolding and enhance the polymer-water interactions. The magnitude of the anion effect, both on the thermal and the rheological behaviours, is considerably higher in the case of the kosmotropic ions, whereas in the presence of chaotropic ions the behaviours are practically the same as those of the pure polysaccharide solutions.

These findings apparently point out that the degree of hydration of the polymer chains is the crucial factor that leads to a significant variation in the strength of the polysaccharide network, and that this phenomenon is ion specific. In the case of a neutral polysaccharide (guar gum) the decrease in the number of the water molecules that interact with the polysaccharide chains leads to a strengthening of the network, due to stronger inter-chain interactions. Vice versa, for a charged polysaccharide (sodium hyaluronate), electrostatic repulsive forces come into play with a greater impact, as a result of the reduced number of water molecules that can screen the charges. The overall effect is a weakening of the chain-chain interactions and, consequently the softening of the network.

From these evidences we conclude that the viscosity of the polysaccharide network can be remarkably modified by the presence of different salts, that perturb the hydration of the chains and change their intermolecular interactions. The effect of the ions is apparently related to their hydration properties and their propensity to adsorb at the polymer interface. GG and SH exhibit an opposite response to the addition of the different solutes, which make them very versatile base ingredients for the formulation of hydraulic fracturing for specific shale gas formations. On the other hand, the viscosity of SA dispersions is not affected by the addition of the different anions. In addition, the gelation of SA water mixtures occurs almost instantaneously in the presence of divalent cations in solution,[172] originating very hard gels which can obstruct the pipelines during the shale gas extraction. For these reasons we decided to exclude SA from the list of potential candidates for the formulation of green hydraulic fracturing fluids, and replaced it with a more versatile polysaccharide, hydroxypropylcellulose (HPC).

HPC water dispersions were characterized via rheological and DSC experiments analogously to GG and SH, and the main results are listed in Table 3.9.

Table 3.9 – Main physico-chemical parameters of HPC 1 % water mixtures obtained from rheological and DSC experiments.

| Experimental Technique | Property | HPC 1%<br>Water mixture |
|---|---|---|
| Rheology - Flow Curves | $\eta_0$(Pa·s) | 27.65 |
| | $n$ | 0.47 |
| | $\lambda$ (s) | 1.63 |
| | $a$ | 0.77 |
| DSC | $T_{mf}$ (°C) | 2.45 |
| | $\Delta H_{mf}$ (J/g) | 323.5 |

### 3.2.2 Polysaccharide formulations in “Shale Water”

After the investigation on the specific effect of single salts, we tested the rheological behaviours of the polysaccharide formulations in a high salinity solution, named “shale water”, which mimics the real operative salinity conditions (see Paragraph 2.2.3). In the perspective of optimizing the formulation performances and limiting the impact of the fluid, for this set of experiments we decreased the concentration of the polysaccharide down to 0.5 % w/w, which is the usual gelling agent concentration in commercial fracfluid formulations. In Figure 3.15 the flow curves for GG, SH and HPC 0.5 % w/w dispersions in shale water are reported.

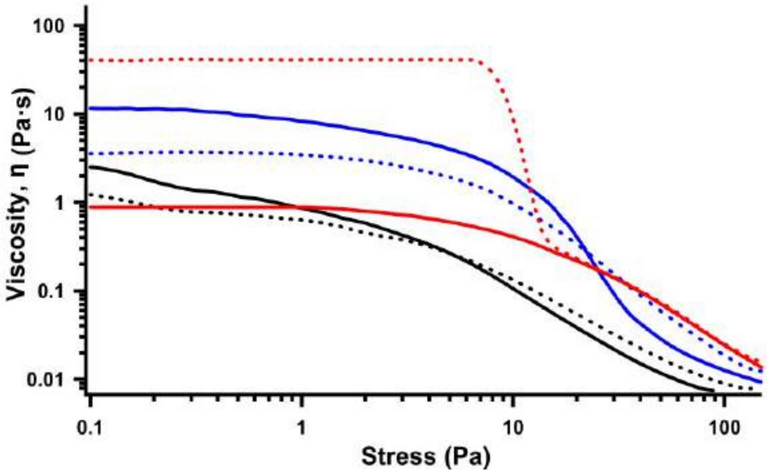

Figure 3.15 – Flow curves of 0.5% w/w GG (black), HPC (red), and SH (blue) dispersions in water (solid lines) and in shale water (dotted lines).

All the investigated polysaccharide formulations exhibit a good salt tolerance. In particular, sodium hyaluronate and guar gum are only marginally affected by the mix of salts present in the shale water. In the case of GG dispersions $\eta_0$decreases from 1.28 to 0.785 Pa·s, while for SH the zero-shear viscosity decreases from 11.5 to 3.58 Pa·s. The effect of salts on the viscosity is presumably due to a modification in the molecular conformation of the polysaccharide chains. The formulations in pure water exhibit higher viscosities due to highly expanded molecules in the medium. As the salt concentration increases, the electrostatic screening effect of salts around the polysaccharide chains limits the polymer extension, which collapses to a more compact coil.[202] This leads to a decrease in the hydrodynamic volume of the polysaccharide and in the electrostatic repulsion among the polymer chains, resulting in a reduction of the formulation viscosity. The effect is more pronounced in the case of SH, where negatively charged −COO− groups are distributed along the chains, while for GG the viscosity decrease is less evident, due to the non-ionic nature of the polysaccharide.

On the other hand, hydroxypropyl cellulose shows a completely different behaviour in high salinity conditions. For HPC dispersions the zero-shear viscosity increases from 0.884 to 39.9 Pa·s in the presence of shale water, highlighting a remarkable stiffening of the polymer network. This effect is related to the peculiar phase behaviour of hydroxypropylcellulose/water systems: HPC exhibits a lower critical solution temperature

(LCST), and it is known to form a liquid-crystalline phase in a concentrated solution. After phase separation, the phase-separated polymer-rich phase forms an anisotropic liquid-crystalline phase.[164] The balance between hydrophilic and hydrophobic interactions of inter- and intra- polymer chains essentially drives this phase transition in the HPC network.[203,204] The addition of salts to HPC dispersions alters the interactions between water molecules and polymer chains, leading to polymer association and to the collapse of the swollen network.[205] The formation of polymer-rich aggregates brings about an increase of the formulation viscosity, as evidenced by the flow curve experiments (Figure 3.15).

These experiments provided useful information about the salt resistance of the different systems, and their potential applications in real operating conditions. As a matter of fact, by considering the different behaviours in response to the specific salts, it possible to select the proper formulation which better fits the salt composition originating from the rock formation.

### 3.2.3 Polysaccharide formulations – Salt toleration thresholds

After assessing the formulation response to an high salt content which mimics the salinity conditions in real shale gas extraction basins, we performed additional experiments overstressing the salt concentration to extremely high values in order to qualitatively determine the resistance threshold of our fluids. Sodium chloride is the most abundant salt present in the European flowback water,[206] thus we carried out our experiments by simply varying the concentration of NaCl from 0.1 to 5 M and visually inspecting the changes on the polysaccharide formulations. In Figure 3.16 the images of the GG, SH and HPC formulations at different NaCl concentrations are reported.

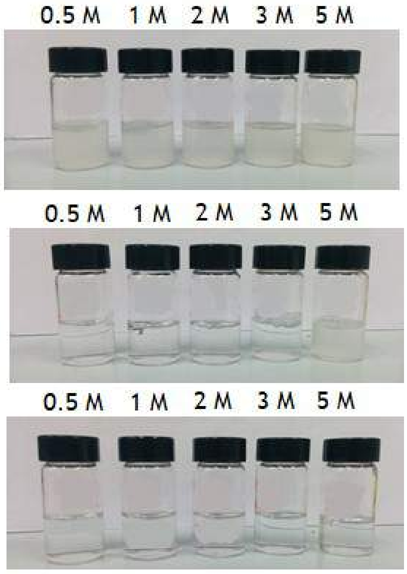

Figure 3.16 – From top to bottom: GG, HPC and SH 0.5 % w/w formulations in the presence on NaCl at different concentrations (0.5, 1, 2, 3 and 5 M)

For GG and SH dispersions no remarkable modifications in the viscosity and formulation texture are observed by increasing salt concentration, confirming a very good resistance to high salinity conditions. SH dispersions appear clear and transparent, while GG mixtures have an opaque brownish coloration due to the presence of insoluble residues deriving from the industrial processing.[207]

HPC dispersions show a good resistance up to a concentration of 2 M. The formulations are transparent and no remarkable variations are observed. By increasing the salt concentration the sample shows a phase separation (3 M), and when NaCl reaches a concentration of 5 M HPC can’t be dispersed anymore. These findings can be explained in terms of salt-induced phase separation and modification of the LCST, as explained in Paragraph 3.2.2.

Further studies, including rheological and DSC experiments, are necessary to quantitatively evaluate the effect of NaCl at these concentrations on the viscosity and thermal properties of the formulations.

### 3.2.4 Effect of different salts on VES formulations

Following a similar approach as in the case of the polysaccharide-based formulations, we perform preliminary studies on the effect of simple salts on the properties of the VES fluids. In these experiments potassium chloride was replaced by the other potassium halides, *i.e.* KF, KBr and KI at a concentration of 0.5 M, and the samples are visually inspected to detect macroscopic changes in the texture of the formulation. The concentration of the surfactant was fixed at 13 % w/w.

For all the examined salts the samples appear as transparent yellowish viscoelastic gels, indicating that the potassium halides can effectively screen the electrostatic repulsion between the oleate headgroups, promoting the formation of a wormlike micellar entangled network. By tilting the glass vial containing the samples we obtained useful information about the firmness of the gel texture: in the presence of fluoride, a kosmotropic anion, NaOL forms a very stiff gel which does not flow inside the tube, while in the case of chaotropic anions like iodide (and to a lesser extent bromide) the gel is softer and starts flowing after few seconds of observation. These very qualitative and preliminary results suggest a potential specific ion effect on the rheological properties of the VES formulations; anyway a deeper and more accurate study is necessary to clarify how and to which extent the salt affects the fluid properties.

The stability of the VES formulations was also tested in shale water in order to assess their resistance and effectiveness in salinity conditions similar to those of real shale formations. For the NaOL 13 % formulation in shale water we do not observe the formation of a viscoelastic gel: the dispersion appears as an inhomogeneous slurry with a very low viscosity, presumably due to the very high ionic strength of the mixed salt solution which prevents the formation and the entanglement of the wormlike micelles. These preliminary results are very promising in the perspective of controlling the formulation viscosity over the entire extraction process. During the initial stage of the fracturing operations, NaOL and a simple salt (e.g. KCl) can be mixed in water in appropriate concentrations to reach the optimal fluid viscosity for proppant carriage. Hence the fluid is pumped downhole together with the sand (proppant) to initiate new fractures and propagate the existing ones. When the fluid comes into contact with the rock formation the salt content increases, causing the collapse of the wormlike viscoelastic network and a breakdown in the viscosity. This facilitates the extraction of the trapped gas and allows a simple and secure recovery of the fluid, which can be regenerated by the addition of fresh water and re-used in future fracturing operations.

## 3.3 Effect of Temperature and Pressure

Alongside salinity, also pressure and temperature play a crucial role in the chemistry and performances of hydraulic fracturing fluids. These two parameters may be extremely variable, and even wells drilled in the same formation may be incredibly different, exposing the fracfluid formulations to a wide variety of downhole conditions.[208,209] For example, the Marcellus shale, which is present from 1200 to 2600 m in the subsurface,[210] typically falls within a temperature range of 40−100 °C but can reach temperatures of 100−125 °C in the southwestern region,[211] with downhole pressures typically ranging from 275 to 414 bar. In deeper shales, such as the Haynesville in Texas/Louisiana (3200 to 4100 m underground), the downhole temperature can reach almost 200 °C and corresponding pressures may be over 690 bar.[208] European shale gas reservoirs like the Bowland Basin in UK demonstrates similarities to North American shale gas plays, whereas relatively few regions have been drilled until now: despite the high potential of European formations, there is currently a lack of data about their geochemical and petrophysical properties, as well as the pressure-temperature conditions downhole.[212]

For this reason, after evaluating the effect of different salts on the main physico-chemical properties of the formulations, we investigated how the variation of T and P affects the fluid behaviour. The results are included in Paper II, “Carbon Black-Induced Electrical Responsiveness in Viscoelastic Formulations” (in preparation) which is attached in 0.

First, we checked the effect of temperature on the rheological properties of the fluid by performing flow curve experiments on the polysaccharide and VES formulations at increasing temperatures up to 60 °C. For GG, SH and HPC formulations the polysaccharide concentration was fixed at 0.5 % w/w, while for the VES fracfluid we tested the sample containing NaOL 13 % + KCl 4%. The results are shown in Figure 3.17, Figure 3.18, Figure 3.19 and Figure 3.20.

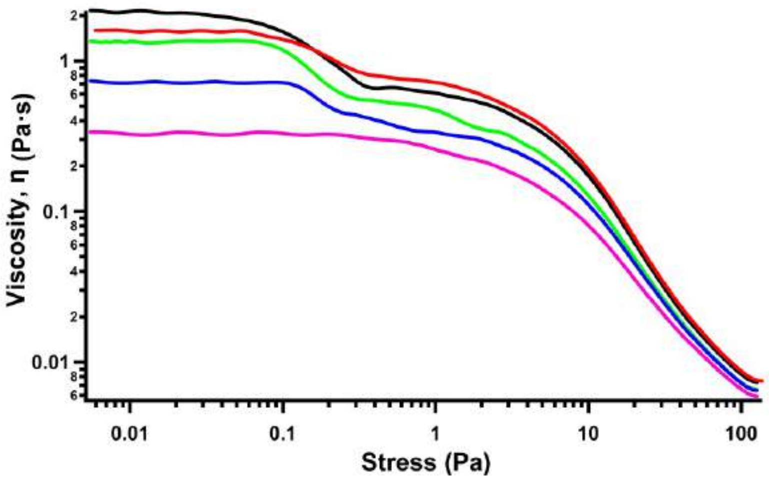

Figure 3.17 – Flow curves for GG 0.5 % at different temperatures: 25 (black), 30 (red), 40 (green), 50 (blue) and 60 °C (pink).

For GG dispersion the raise in temperature causes a downward shift in the polysaccharide flow curve, with a progressive lowering of the zero shear-viscosity value moving from 25 to 60 °C (Figure 3.17). As temperature increases the intermolecular interactions between polymer chains are weakened, resulting in a softer network where the chains slide one over the other with a progressively lower friction. No remarkable changes are observed in the curve profile, confirming the weakening of the network without any structural modification/degradation.

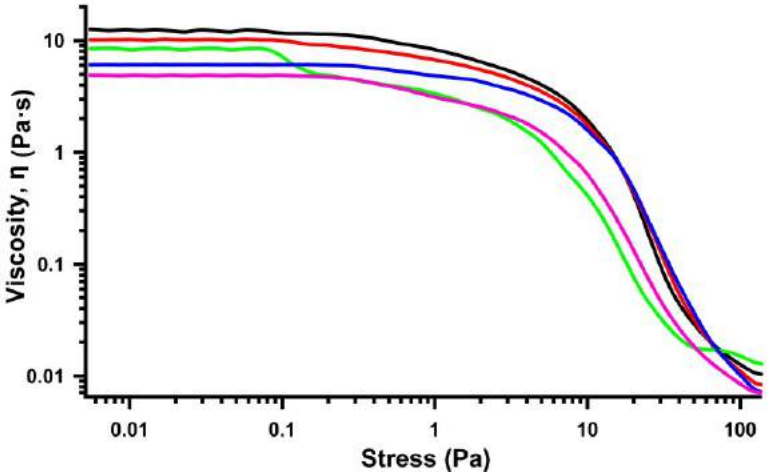

Figure 3.18 – Flow curves for SH 0.5 % at different temperatures: 25 (black), 30 (red), 40 (green), 50 (blue) and 60 °C (pink).

For SH dispersion we recorded a similar rheological behaviour (Figure 3.18): the formulation exhibits the same trend observed for guar gum with a progressive lowering of the zero-stress plateau as temperature increases. However, the viscosity variation is very narrow (from 12 to 5 Pa·s), indicating a marginal effect of temperature in the investigated range.

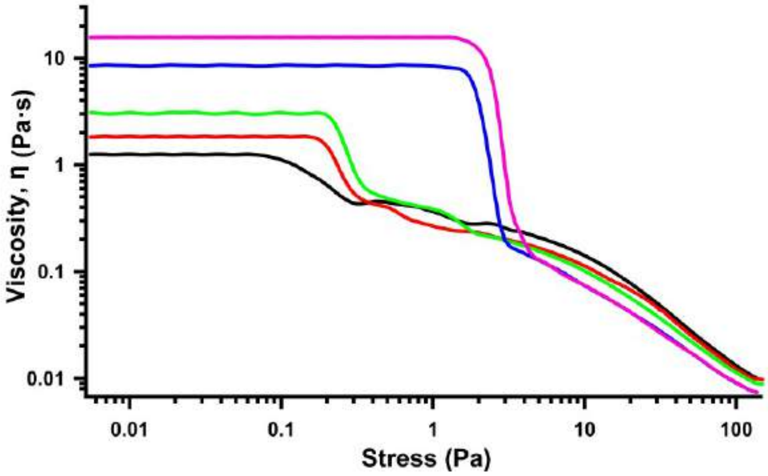

Figure 3.19 – Flow curves for HPC 0.5 % at different temperatures: 25 (black), 30 (red), 40 (green), 50 (blue) and 60 °C (pink).

The HPC-based formulation shows an opposite trend, as reported in Figure 3.19. The zero-shear viscosity increases with temperature, as the polysaccharide network becomes more viscous and rigid. Moreover, also the critical stress values corresponding to the collapse of the network are shifted to higher rates. This counterintuitive response to temperature variation is consistent with the peculiar phase behaviour of HPC/water systems and it is widely reported in literature. Indeed, a similar case concerns another cellulosic derivative, the extracellular polysaccharide produced by some bacterial strains of Xanthomonas Campestris.[213,214] This biomolecule shows a viscosity trend that follows in parallel the temperature profile: the higher the temperature, the greater the zero stress viscosity of the system. In our case, this response to the thermal stress is presumably due to the partially hydrophobic nature of the HPC side-chain. When temperature is raised the hydrating water molecules are depleted from the hydroxypropyl side groups, and lead to the formation of ”stronger aggregation of interpolymer complexes” stabilized by hydrogen bonding and hydrophobic interactions.[215] The final result is an increase in the network crosslinking degree and a strengthening in the viscosity and stiffness of the system.

Regarding the NaOL-based formulations, Figure 3.20 shows the flow curves acquired at the different temperatures.

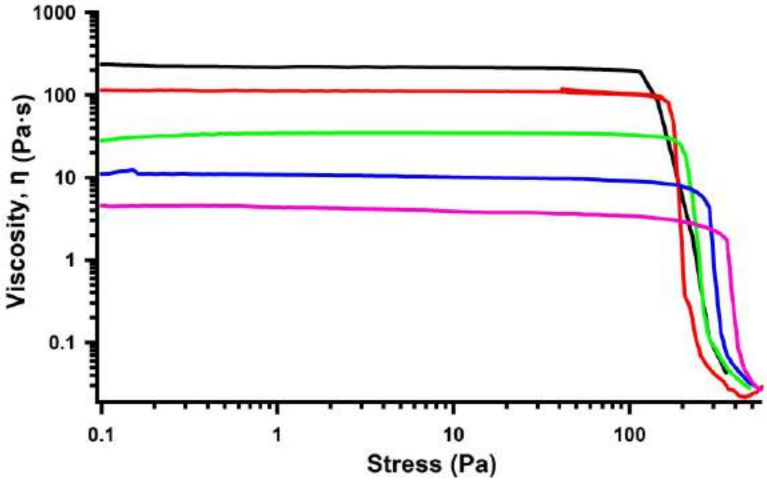

Figure 3.20 – Flow curves for NaOL 13 % + KCl 4% at different temperatures: 25 (black), 30 (red), 40 (green), 50 (blue) and 60 °C (pink).

The temperature increase induces the breaking in the entangled micellar network with progressive lowering of the zero-stress plateau. The viscosity breakdown is quite considerable, as the zero shear-viscosity decreases from 228 to 5 Pa·s, indicating a strong temperature-dependence of this system.

The low-stress plateau region can be analysed as a function of temperature according to a modified Arrhenius equation to obtain the Gibbs free energy of activation representing the strength of flow objects in solution:[216]

$$\eta = \eta_\infty \, exp \left(\frac{\Delta G^{\neq}}{RT}\right) \tag{3.6}$$

$$RT \ln (\eta) = \mathrm{RT} \ln(\eta_\infty) + \Delta G^{\neq} \tag{3.7}$$

where $\eta$ is the viscosity, $\Delta G^{\neq}$ the Gibbs free energy of activation representing the strength of flow obstacles, $\eta_\infty$ a constant corresponding to the viscosity at ‘‘infinite’’ temperature which, in a simple fluid, is a function of the molecular size together with a pre-exponential factor associated with the diffusion coefficient, $R$ is the universal gas constant and $T$ the absolute temperature. Plotting ln (η) versus $1/T$ we obtain $\ln(\eta_\infty)$ as the intercept and $\Delta G^{\neq}/R$ as the slope respectively, from which the value of Gibbs free energy of activation can be extrapolated. Table 3.10 reports the values of $\eta_0$ and $\Delta G^{\neq}$ for the different investigated formulations.

Table 3.10 – Zero-stress viscosity $\eta_0$ (Pa·s) and the Gibbs free energy of activation $\Delta G^{\neq}$ at 25, 30, 40, 50 and 60 °C for GG, SH, HPC 0.5 % w/w and for NaOL 13 % + KCl 4 % (VES) formulations.

| $T$ | $\eta_0$(Pa·s) | | | |
|---|---|---|---|---|
| | GG | SH | HPC | VES |
| 25° C | 2.1 | 13 | 1.3 | 228 |
| 30° C | 1.6 | 10 | 1.8 | 150 |
| 40° C | 1.3 | 8.4 | 3.1 | 36 |
| 50° C | 0.7 | 6.1 | 8.4 | 11 |
| 60° C | 0.3 | 4.9 | 15 | 4.1 |
| $\Delta G^{\neq}$ (kJ mol$^{-1}$) | 41 | 22 | - | 98 |

The extracted Gibbs free energy of activation $\Delta G^{\neq}$ for the pure VES formulation is about 98 kJ mol$^{-1}$, reflecting a tight entanglement of the chains that hinders the flow. The obtained value is in line with those reported in the literature for worm-like micelles network.[217,218] In the case of SH and GG dispersions, we obtained values for $\Delta G^{\neq}$ of about 22 and 41 kJ mol$^{-1}$, respectively. The calculated $\Delta G^{\neq}$ values of the two polysaccharide dispersions fall in the range reported in literature for polymers.[219] A similar analysis cannot be extended to HPC because of the temperature-induced phase separation and stiffening of the polymer network. The strong difference between the activation energies found for GG and the hyaluronate dispersion is simply explained by the much higher intrinsic viscosities of SH as compared with guar gum. At a given concentration, the overlap between macromolecules and the interactions between polymer chains are larger in the case of hyaluronate, than for GG.

After investigating the thermal response of the formulations in this range of low-to-moderate temperatures, we performed high pressure and high temperature experiments in collaboration with the Chemical Engineering Department of the University of Huelva to provide a deeper and more accurate description of the fluid behaviour in harsh conditions, which mimics the P-T conditions of the shale play. Flow curve experiments on two formulations, namely HPC 0.5 % and NaOL 13 % + KCl 4 %, were carried out at increasing temperature (from 25 to 120

°C) and pressure (1, 50, 200 and 390 bar). Figure 3.21 shows the flow curves for HPC 0.5 % dispersion at 25 ° C and increasing pressure.

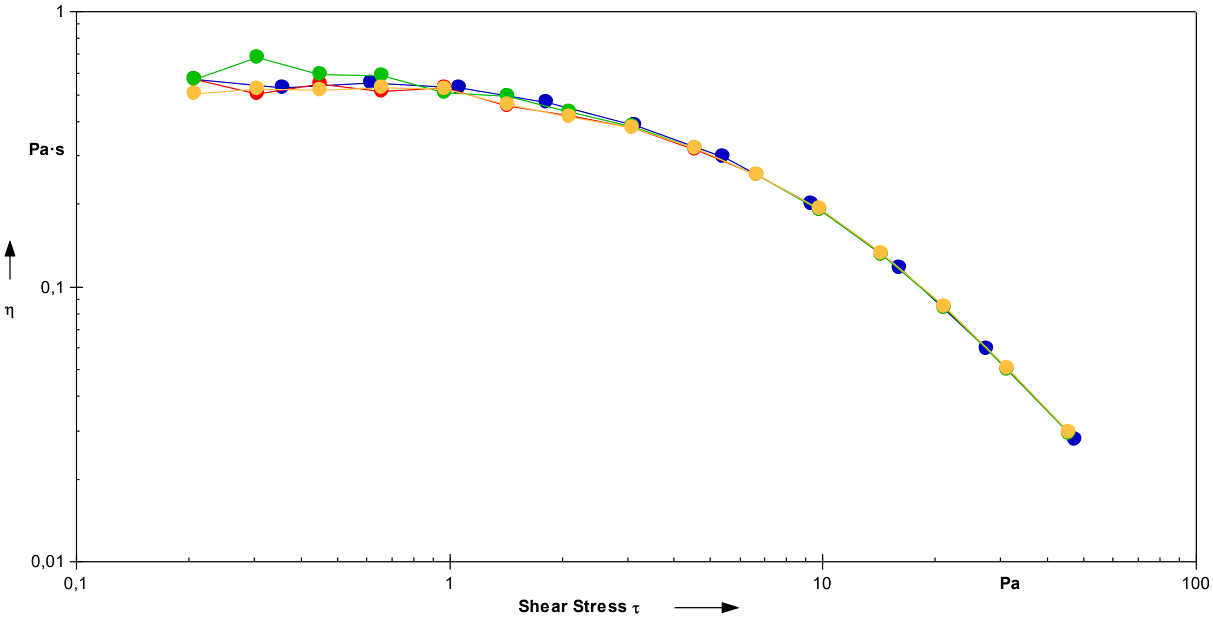

Figure 3.21 – Flow curves for HPC 0.5 % dispersion at 25 ° C and different pressures: 1 (blue), 50 (red), 200 (green), and 390 (yellow) bar.

All the examined samples exhibit the typical shear-thinning behaviour of HPC/water systems: no remarkable variations in the profile or in the zero-stress plateau are observed, indicating that the rheological behaviour of this formulation is not affected by pressure, even when it reaches very high values.

The effect of high temperature on the HPC-based formulation is shown in Figure 3.22, which reports the flow curves for the HPC 0.5 % dispersion at 25 and 120°C. For the experiment at 120 °C, the pressure is increased up to 50 bar to prevent water evaporation.

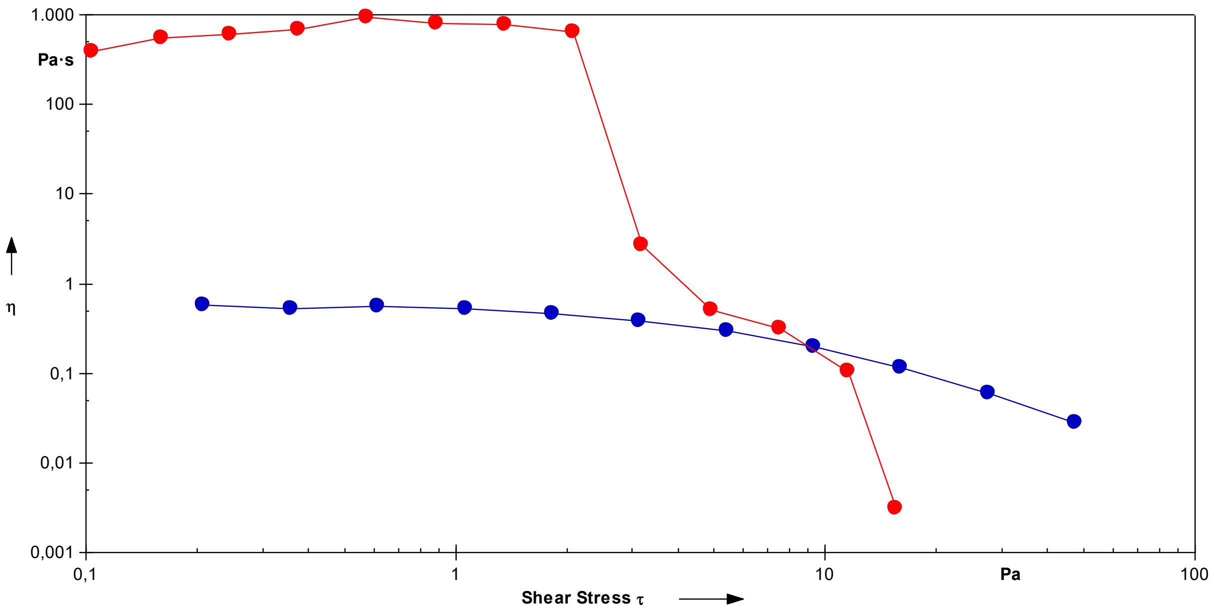

Figure 3.22 – Flow curves for HPC 0.5 % dispersion at increasing temperatures: 25 (blue), 60 (red) and 120 (green) °C. The sample at 120 °C was pressurized at 50 bar to prevent water evaporation.

The raise in temperature brings about an upward shift in the polysaccharide flow curve, with a remarkable increase of the zero shear-viscosity: these results are consistent with the viscosity trend observed in the range 25 – 60 °C (see Figure 3.19) and demonstrate that no degradation/decomposition of the polysaccharide matrix occurs even when the temperature reaches very high values.

Considering the complex temperature-dependent phase behaviour of the HPC formulation, we performed a flow temperature ramp experiment in order to better understand the rheological response of the polysaccharide dispersion. This test consists in imposing a temperature ramp from 25 to 120 °C and measuring the viscosity at a fixed torque (120 μNm) and pressure (1 bar). The results are shown in Figure 3.23.

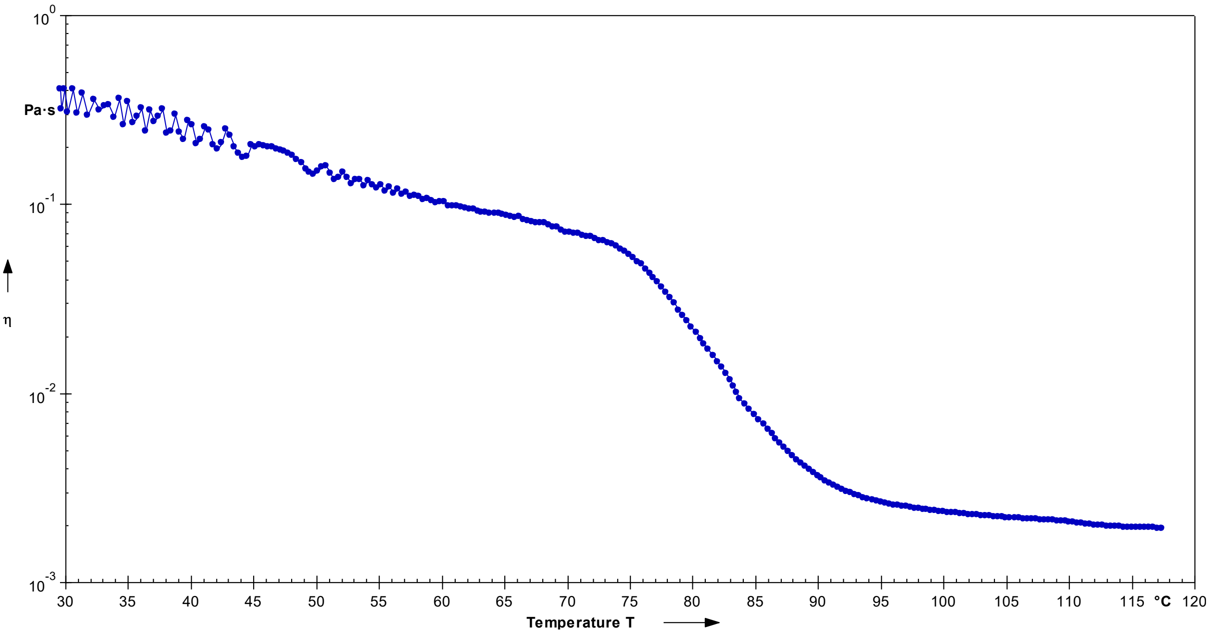

Figure 3.23 – Viscosity-temperature dependence for the HPC 0.5 % dispersion at fixed torque (120 μNm) and pressure (1 bar).

As temperature increases, the fluid viscosity progressively decreases under a constant applied shear. This result may seem counterintuitive if compared with the viscosity data obtained in static conditions: the apparent divergence is due to the external shear stress, which induces the alignment of the polymer chains and prevents them from building up association complexes.

The effect of high pressure on the VES formulation is shown in Figure 3.24, which reports the flow curves for the NaOL 13 % + KCl 4 % at increasing values of P, from 1 to 390 bar. For this set of measurements the temperature was fixed at 25 °C.

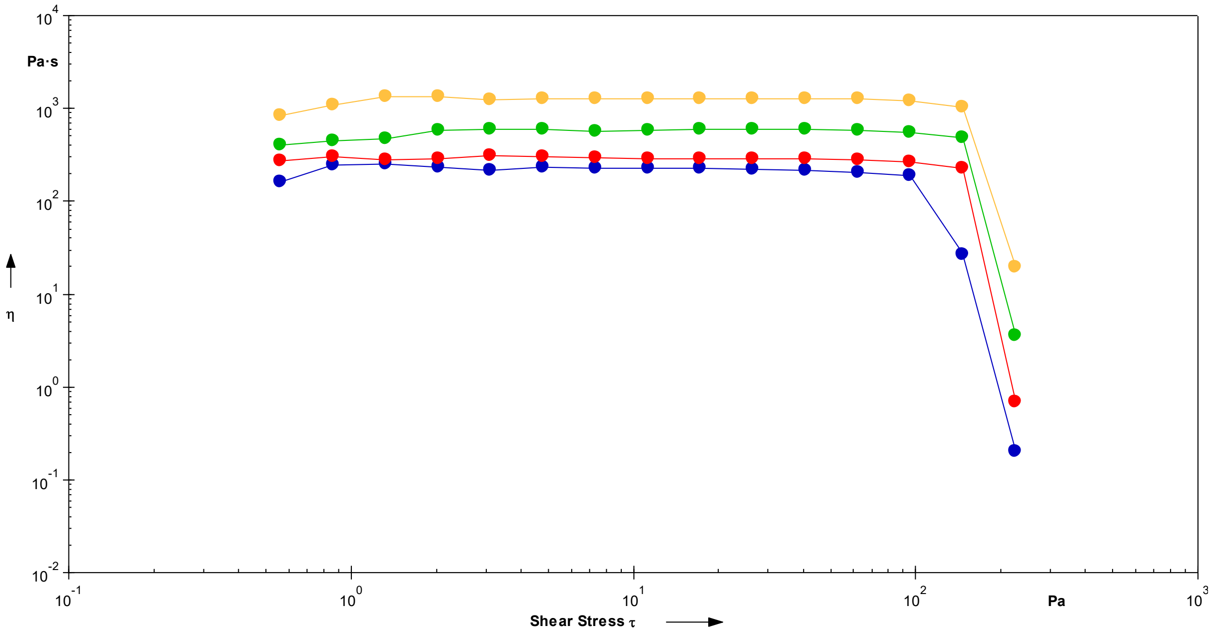

Figure 3.24 – Flow curves for the NaOL 13 % + KCl 4 % formulation at 25 ° C and different pressures: 1 (blue), 50 (red), 200 (green), and 390 (yellow) bar.

The pressure increase induces an upward shift in the flow curves with a progressive increase of the zero-stress plateau. The viscosity increment is absolutely remarkable, as the zero-shear viscosity increase from 230 to 1270 Pa·s, demonstrating a strong dependence of the formulation fluid behaviour on pressure. The same trend is observed also at 60 °C, although to a lesser extent, with a zero-shear viscosity increasing from 4.70 to 10 Pa·s. Other experiments (not reported) showed that this behaviour is completely reversible. To the best of our knowledge this is the first experimental evidence of the effect of high pressures on the rheological properties of sodium oleate-based viscoelastic systems. A possible explanation for these outstanding viscosity increase could be the enhancement of the micellar entanglement due to the applied external pressure which promotes the interactions between the wormlike structures. Presumably the presence of dissolved gases within the matrix plays a crucial role in the viscosity modification under high pressures. Nevertheless further experiments are necessary to clearly define the driving force which regulates this pressure-dependent rheological behaviour.

Figure 3.25 show the effect of high temperature (up to 120 °C) on the fluid behaviour of the NaOL 13 % + KCl 4 % formulation. All the experiments were performed at 50 bar in order to prevent water evaporation.

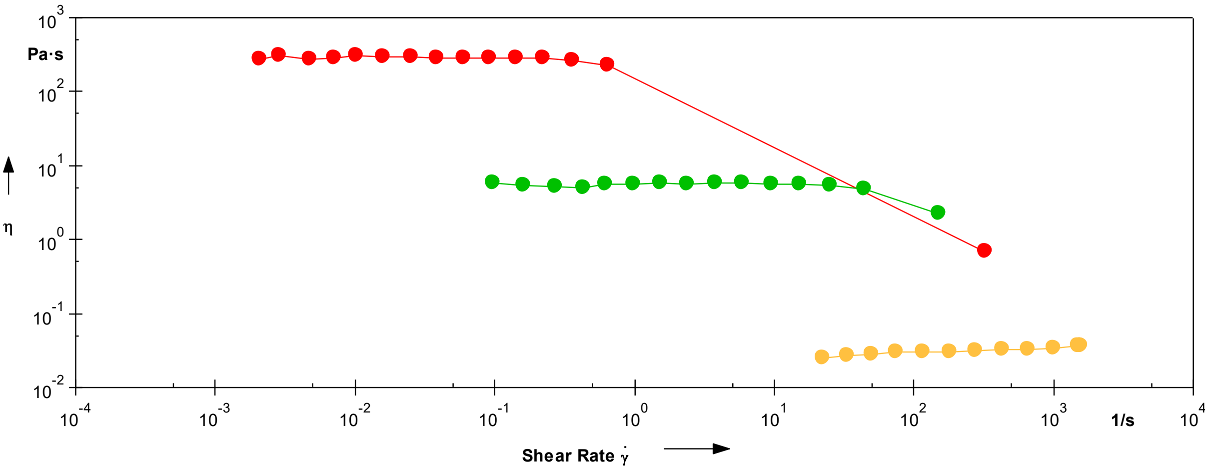

Figure 3.25 – Flow curves for the NaOL 13 % + KCl 4 % formulation at 50 bar and different temperatures: 25 (red), 60 (green), and 120 °C (yellow).

The results are consistent with the viscosity trend observed in the range 25 – 60 °C (see Figure 3.19): the temperature increase induces a weakening in the entangled micellar network with the progressive lowering of the zero-stress plateau. At very high T (120 °C) the shear thinning region disappears and the formulation shows a pure Newtonian behaviour, indicating the complete rupture of the micellar entanglement. All the temperature-dependent viscosity variations are fully reversible, demonstrating that no degradation occurs even at very high temperatures.

## 3.4 *Stimuli*-Responsive Formulations

In this section we provide an extensive characterization of the rheological and thermal properties of the stimuli-responsive fluids we developed starting from the polysaccharide and VES-based formulations. The effect of the two responsive additives, namely Carbon Black (CB) and Azorubine, on the fluid behaviour is studied by means of rheological experiments (flow curves, oscillatory measurements), optical microscopy, DSC and SAXS measurements. The results are included in Paper II and III, which are attached in 0.

### 3.4.1 Electro-responsive formulations - Effect of Carbon Black

Optical micrographs of CB dispersions in saponin and sodium oleate were acquired to assess the homogeneity of CB dispersions as a function of the CB amount and in the presence of different dispersing agents (saponin, for the polysaccharide formulations, or sodium oleate). Indeed, it was proved that the structure of carbon black, the nature of the polymer, and the processing history of the sample affect the electrical conductivity of the composite system.[220,221] The results are shown in Figure 3.26.

For all the examined samples stable aqueous dispersions of CB were obtained, either with saponin and sodium oleate. The formation of carbonaceous aggregates occur when the amount of carbon black increases from 1% to 3% w/w; anyway, the carbonaceous particulate appears homogeneously dispersed also in the presence of the higher amount of CB. Therefore, any effect on the electro-responsiveness due to samples inhomogeneity can be disregarded.

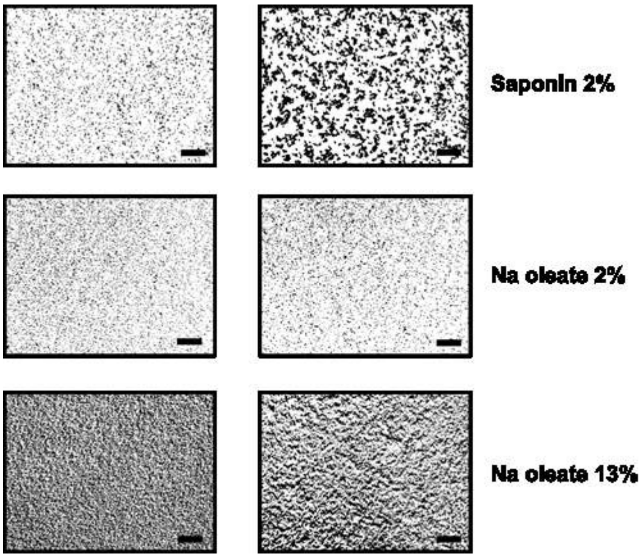

Figure 3.26 – Optical images of carbon black 1% (left) and 3% w/w (right) dispersions in saponin 2% and sodium oleate 2% and 13% w/w. Scale bar: 300 μm..

This result is of particular interest for practical applications since several efforts were made to find an easy way to disperse hydrophobic carbonaceous materials, such as fullerenes or carbon nanotubes in aqueous media, especially for biomedical applications.[222,223] Some works report the encapsulation of CB in silica,[213,224] or polymer particles,[225] while others suggest the use of surfactant molecules, such as sodium oleate and saponin, that can provide both electrostatic and steric stabilization, depending on the nature of the hydrophilic head.[113,226] In particular, saponin can adsorb by exposing its hydrophobic triterpene or steroid moiety to the CB surface, while the glucoside hydrophilic head faces the aqueous phase.[226] In the case of sodium oleate, we expect that its adsorption on the CB surface occurs through the C=C double bond in the chain, as suggested by Wang,[227] while the negatively charged carboxylates provide an electrostatic stabilization to the composite structure.

Once the homogeneity of the CB-enriched dispersions was assessed, we performed flow curve experiments to study the effect of CB on the fluid behaviour of the polysaccharide and VES formulations. The results are shown in Figure 3.27.

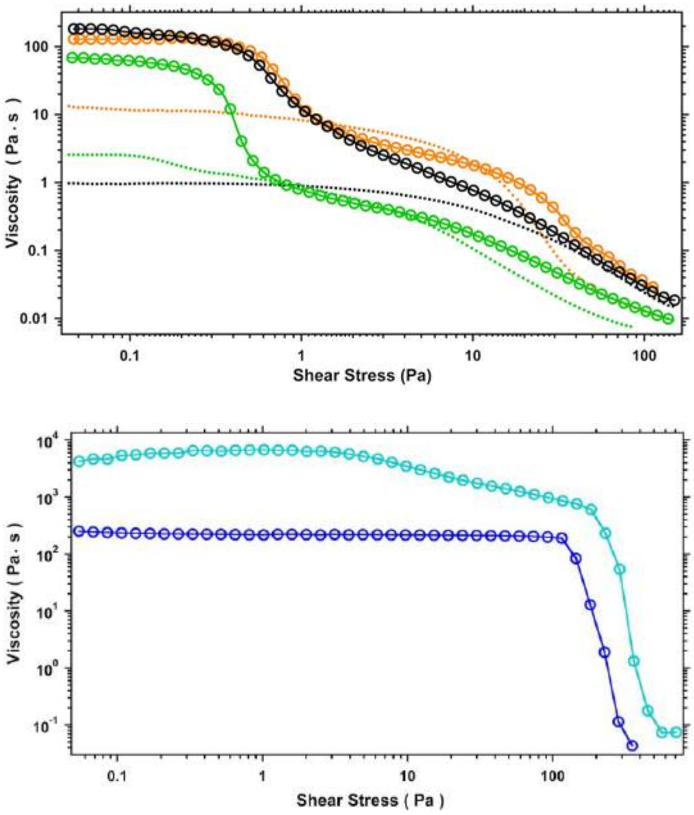

Figure 3.27 – Top: Flow curves of 0.5% w/w pure (dotted lines) and containing 3% w/w of CB (empty circles) GG (green), HPC (black), and SH (orange) dispersions. Bottom: Flow curves of NaOL 13% + KCl 4% (dark blue) and NaOL 13% + KCl 4% + CB 10% (light blue).

The different rheological profiles reflect the viscosity changes and network stiffening induced by CB. For the polysaccharide dispersions the addition of CB leads to an increase in the viscosity of at least an order of magnitude. This result is in line with the well-known thickening effect of CB,[228] and reflects the effective inclusion of the additive in the polysaccharide matrices. Moreover, in the presence of CB the rheological profiles are significantly modified with respect to the pure polysaccharides. In fact, besides the Newtonian region with a high viscosity value at low shear rate, a marked change in the slope of the curves is observed, for shear stress ranging between 0.3 and 3 Pa, especially for GG and SH based samples. This behaviour is probably related to the viscous drag between the polymer chains adsorbed on the CB particles and the bulk polymer, as described in the case of the interaction between CB and an acrylic resin.[229]

When CB is added to the VES formulation up to 10% w/w, we observed a strong increase in the zero-stress viscosity, from 234 to 5373 Pa s, indicating that the carbonaceous particulate acts as a reinforcing agent for the network. Furthermore, we observed that the shear-thinning behaviour starts at a higher value of the critical stress, suggesting a structuring effect for the CB particles. Despite the addition of CB strongly affects the stiffness of the VES network, the rheological profile with or without CB remains essentially unaltered. We argue that the structure of the NaOL micellar network is not significantly modified by the presence of the carbonaceous particles. In order to understand the effect of CB on the mechanical properties of NaOL dispersions and to obtain insights on their relaxation dynamics, oscillatory frequency sweep tests were carried out on VES systems after the addition of 10% of carbon black. The results are compared with the data obtained for the NaOL 13% + KCl 4% formulation without CB (see Figure 3.28).

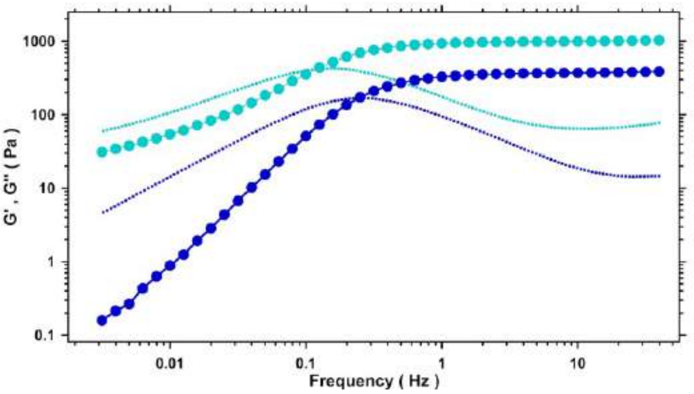

Figure 3.28 – Storage (circles) and loss (dotted lines) moduli of pristine (dark blue) and 10% w/w CB-enriched (light blue) NaOL 13% + KCl 4% VES formulations. All the measurements were carried out in the linear viscoelastic regime (strain amplitude = 1.0 %).

At high frequency the samples behave as elastic systems ($G'$ shows a plateau and dominates over $G''$), whereas at low frequency they show a viscous behaviour ($G'' > G'$). As observed for the other NaOL/KCl formulations (see Section 3.1.2) the dynamics of the studied systems cannot be described according to the single-element Maxwell model, hence $G'$ and $G''$ are used to calculate the time-weighted relaxation spectra $H(\tau)$, which are reported in Figure 3.29.

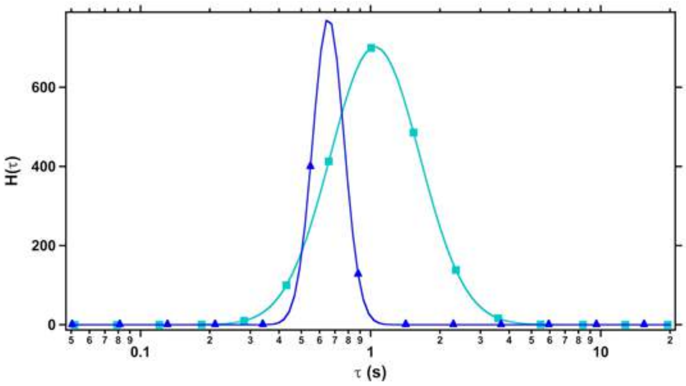

Figure 3.29 – *H(τ)* relaxation spectra of pristine (dark blue) and CB-enriched (light blue) NaOL 13% + KCl 4% VES formulations.

The CB-enriched VES formulation shows a higher relaxation time, confirming the reinforcing role of the particulate in the stabilization of the matrix. Moreover, considering that the numbers of interconnections between the worm-like micelles is directly linked to the values of the elastic plateaus in the oscillatory frequency sweep tests,[139] we argue that carbon black leads to the formation of a more entangled micellar network, as suggested by the higher value of the *G'* modulus associated to the CB-enriched sample.

A further confirmation of the negligible effect of CB on the micellar structure of NaOL arises from the SAXS data analysis (Figure 3.30). The scattering curves of the samples before and after the addition of CB are similar, except for the strong contribution to the scattering intensity in the low *q*-region ($q < 0.005$ Å$^{-1}$) due to the CB particles. This result indicates that the addition of CB does not affect the size and the intermicellar interactions among the charged aggregates. According to the literature,[74,222] the observed scattering profile is associated to the presence of polydispersed core-shell elongated objects interacting via a screened Coulomb potential in solution.

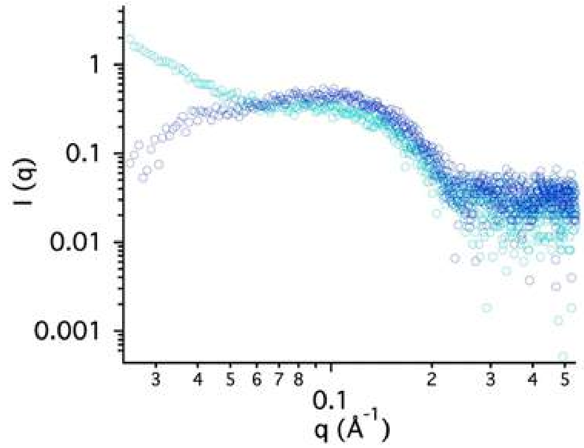

Figure 3.30 – SAXS curves of VES formulations: NaOL 13 % + KCl 4 % (dark blue) and 10 % CB enriched samples (light blue).

In order to evaluate the electrical responsivity of the CB-enriched formulations, electrical stimulation experiments were carried out by applying a 30 V voltage for 1 hour to the polysaccharide and the VES systems (see Paragraph 2.4.1.6). The electro-responsivity of polymers is a widely known phenomenon that involves a large set of biomolecules.[230–232] The application of a voltage to our formulations produces electrophoretic, polarization and osmotic effects, that result in the separation of a liquid and easy-flowing phase on one electrode, and of a viscous and sticky phase that concentrates at the opposite side. Taking advantage of their different viscosities, the two phases can be easily separated and recovered. The measured weight gives a rough estimation of the percentage of recovered liquid phase squeezed out from the sample after the electrostimulation (Table 3.11).

Table 3.11 - Zero stress viscosities ($\eta_0$ ± 5%, in Pa s) and mass percentage of liquid (L, %) and sticky (S, %) phases recovered after the application of a voltage (30 V for 1 hour).

| Sample | $\eta_0$ | L | $\eta_0$(L) | S | $\eta_0$(S) |
|---|---|---|---|---|---|
| GG | 2.1 | - | 1.1 | - | 1.1 |
| HPC | 1.3 | 61 | 0.55 | 39 | 40 |
| SH | 13 | 53 | 0.15 | 48 | 43 |
| NaOL 13% + KCl 4% | 234 | 34 | 390 | 66 | 4.4 |
| GG+CB 3% | 67 | - | 22 | - | 22 |
| HPC+CB 3% | 118 | 50 | 20 | 50 | 4482 |
| SH+CB 3% | 129 | 28 | 63 | 72 | 975 |
| NaOL13% + KCl 4% + CB 10% | 5373 | - | 356900 | - | 356900 |

All pure polysaccharide dispersions, except for guar gum, exhibit this behaviour in response to the electrical stimulus. The electrical stimulus effect on the flow curves for the GG, SH and HPC dispersions are reported in the Figure 3.31. By comparing the profiles of the pristine SH sample (black) and those of the “liquid” and “sticky” phases (red and green, respectively), we figured out that the rheological response is affected by the application of the voltage. Indeed, the red profile shows a two order of magnitude lower $\eta_0$, whereas the green curve shows a noticeable increase in $\eta_0$. Despite this difference in the viscosity values, the three rheological profiles are similar.

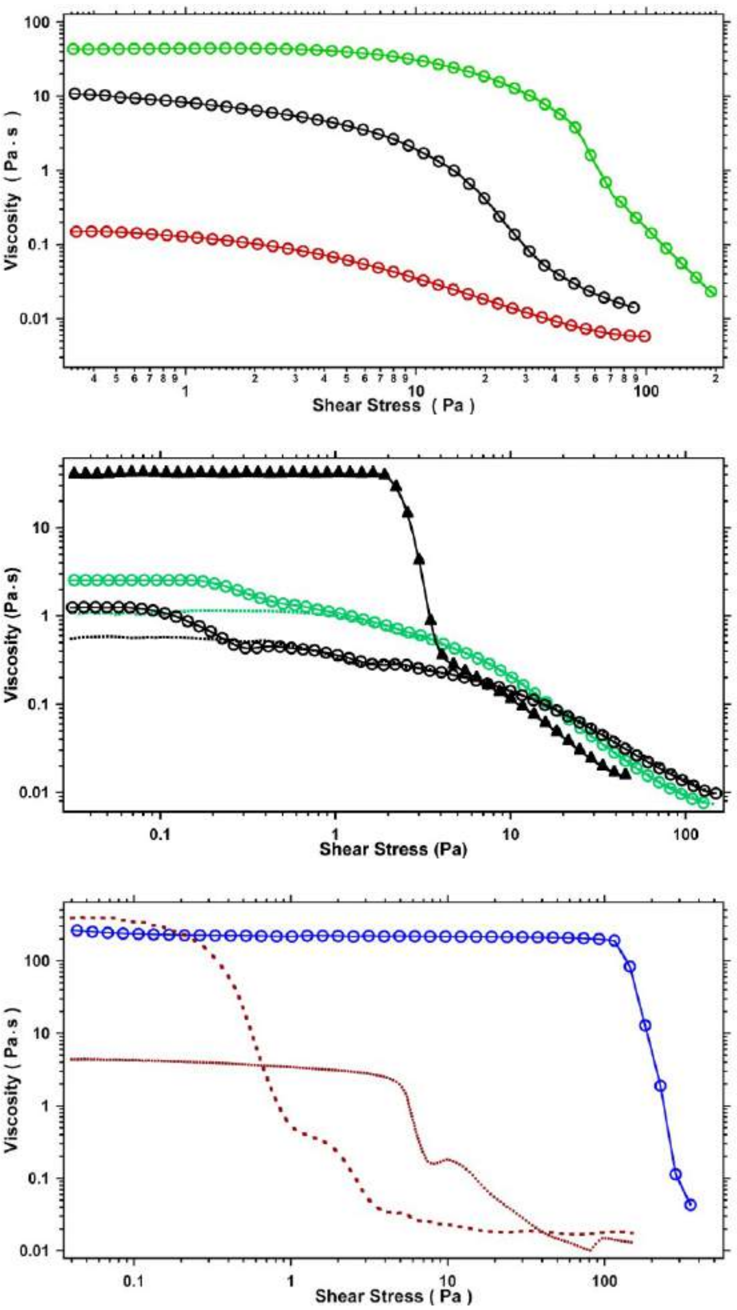

Figure 3.31 – Top: Flow curves of 0.5% w/w SH dispersion before the application of the electrical stimulus (black) and of the two phases separated at the end of the process (viscous phase in green, fluid phase in red). Mid: Flow curves on HPC (black) and GG (green) before (circles) and after the electrical stimulus. The liquid and sticky portions obtained after the application of the voltage are indicated by dotted lines and triangles, respectively. Bottom: Flow curves of NaOL 13% + KCl 4% VES formulation before the application of the electrical stimulus (blue circles) and of the two phases separated at the end of the process (brown lines).

This suggests that all the samples possess the same structure and no modification in the polysaccharide network is induced by the electrical stimulation. Thus we argue that the changes in viscosity are simply due to the electrically induced differences in the polysaccharide/water ratio. Indeed, the applied voltage leads to the contraction of both SH and HPC networks and results in the reduction of the mesh size and in the partial removal of water from the polysaccharidic network. As expected the amount of the liquid portion recovered at the end of the electrical stimulus depends on the nature of the polysaccharide. The electrical stimulus imparts an effect also on the NaOL-based formulations, leading to the formation of two phases with different flow curves. Both phases show lower profiles and the curve obtained from the sticky and more viscous portion is not shown. Moreover, unlike the case of polysaccharide formulations, the two collected phases exhibit a rheological profile significantly different from that of the sample before the stimulus. This result suggests that the application of the voltage partially breaks the micellar entanglement and the homogeneity of the sample, leading to irregular and more indented profiles in comparison to the typical VES flow curve.

Considering that both pure VES and polysaccharides show a remarkable response upon the application of a voltage, their electro-responsiveness was checked after the addition of the conducting CB in different amounts: from 1 to 3% for the polysaccharides and up to a maximum of 10% for the VES formulation. The flow curves of the two phases collected after the application of the electrical stimulus in the presence of CB are reported in Figure 3.32. Since the pure GG dispersion does not exhibit a significant response to the electric voltage, the flow curves for the GG+CB sample are not shown.

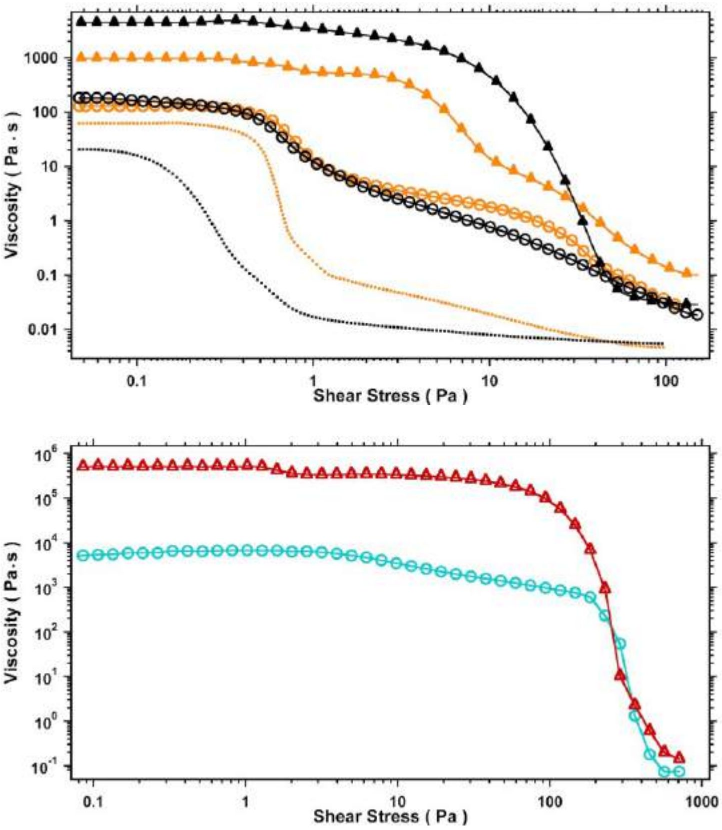

Figure 3.32 – Top: Flow curves of 0.5% w/w HPC (black) and SH (orange) dispersion containing CB 3 wt% before the application of the electrical stimulus (empty circles) and of the two phases separated at the end of the process (viscous, triangles and liquid, dotted lines). Bottom: Flow curves of sodium oleate 13% + KCl 4% VES formulation containing CB 10 % before the application of the electrical stimulus (light blue circles) and at the end of the process (red triangles).

For the polysaccharide matrices, we recorded different responses to the electrical stimulus depending on the nature of the investigated polysaccharide. However, in all cases with the exception of guar gum, the change in the zero-shear viscosities of the different phases after the stimulus is enhanced compared to the pure polysaccharides. This result suggests that CB can be successfully used as an additive to tune the response of polysaccharide formulations to an external stimulus, such as the application of a voltage.

When the CB-enriched VES formulation is electrically stimulated, the zero-stress viscosity of the formulation increases of about two orders of magnitude, indicating the formation of a more rigid network, probably due to the shrinking of the worm-like micelle network.

However, as for the pristine formulation before the addition of CB, we did not observe the formation of two different phases, presumably because CB acts as a reinforcing agent. In addition, the rheological profile of the sample before and after the stimulus does not change significantly, showing the typical non-Newtonian behaviour of the VES formulations. This result confirms the view that, in the presence of carbon black, the electrical stimulus can be used as a trigger to effectively increase the strength and stiffness of the matrix without changing the viscoelastic network of sodium oleate-based formulations.

To evaluate the increased thermal resistance of our formulations after the addition of carbon black, the flow curves were acquired at 25, 30, 40, 50, and 60 °C. Figure 3.33 shows the rheological behaviour of GG, SH and HPC dispersions before and after the addition of CB (3% w/w). As expected, for GG the raise in temperature causes a downward shift in the polysaccharide flow curve, with a progressive lowering of the zero shear-viscosity value moving from 25 to 60 °C. The GG+CB samples exhibit a wider and higher viscosity drop ( from 67 to 10 Pa s) in comparison to the pure GG sample, indicating that the presence of CB enhances the thermal resistance of the polysaccharide network. Moreover, the two systems exhibit quite different profiles in the lower stress region, while they flow in the same way at higher stress. This feature seems to suggest that an additional structural order is granted by the carbonaceous particles, that are responsible for the higher viscosity in the GG+CB system. However, when the applied stress increases, this higher structuring breaks down and the difference vanishes.

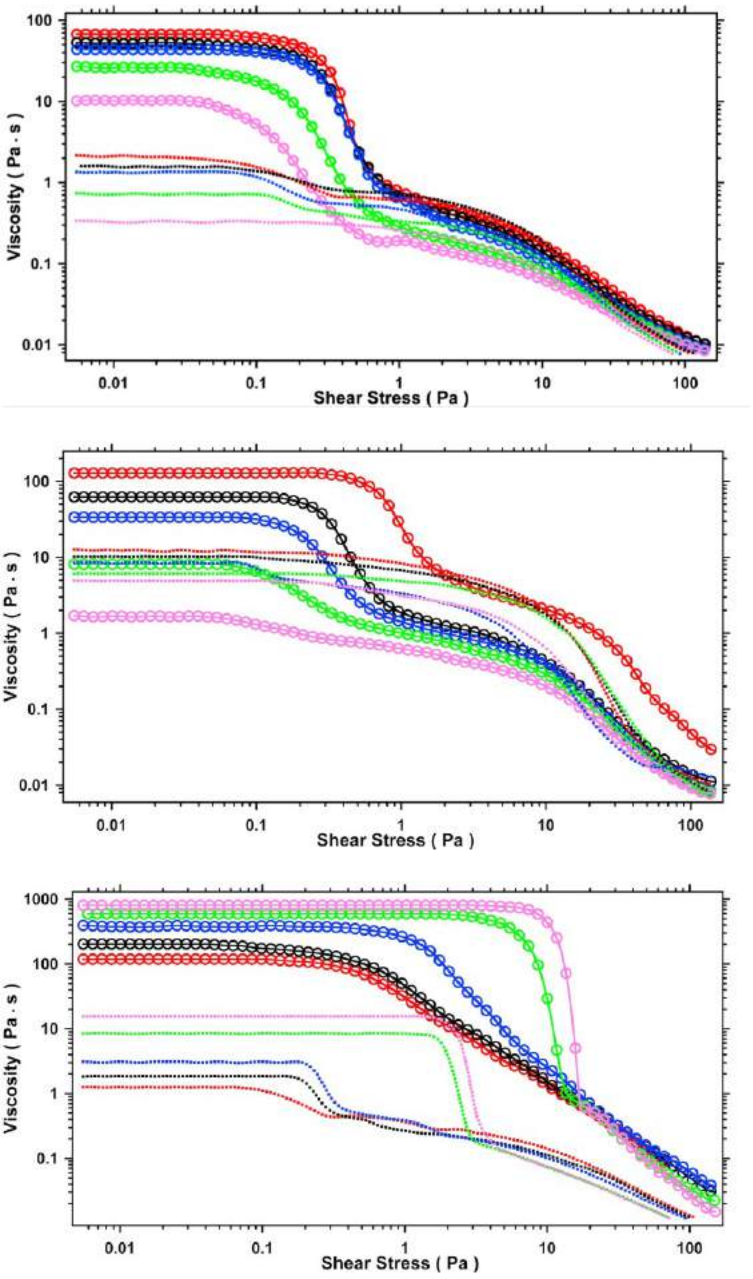

Figure 3.33 – Top: Flow curves of GG 0.5% (dotted lines) and GG 0.5% + CB 3% (circles) at 25 (red), 30 (black), 40 (blue), 50 (green) and 60 (pink) °C. Mid: Flow curves of SH 0.5% (dotted lines) and SH 0.5% + CB 3% (circles) at 25 (red), 30 (black), 40 (blue), 50 (green) and 60 (pink) °C. Bottom: Flow curves of HPC 0.5% (dotted lines) and HPC 0.5% + CB 3% (circles) at 25 (red), 30 (black), 40 (blue), 50 (green) and 60 °C (pink).

Despite this effect, the flow curves remain unchanged within each series, confirming that the structures of the network are only weakened but not modified in different arrangements.

For SH and SH+CB we recorded a similar rheological behaviour. The presence of CB does not modify this behaviour but the response to the increase in temperature is enhanced. More in detail, the pristine SH system shows only a limited decrease in the viscosity, while the SH+CB sample shows a wider gap, from 129 to 2 Pa s. In comparison to guar gum the addition of carbonaceous particles affects the SH network thermal resistance in a slightly different manner: the system is strengthened below 50 °C, while at higher temperatures the presence of CB seems to promote the chains disentanglement. As with guar gum, the CB-enriched system shows a double plateau and a double drop in its profile. Instead, the pure polysaccharide exhibits a single plateau associated to a single fall in viscosity. This difference reflects the second level structure, originating from the reinforcement of the polysaccharide network due to the CB particles, that is responsible for the overall increased rigidity and viscosity. Moving along the temperature series, we note the shift of the critical stress at which the higher viscosity plateau starts to decrease. The highly ordered structure loses its stability: in fact, passing from 25 to 50 °C, the gap between the first and the second plateau progressively becomes less pronounced, until it is barely visible in the profile recorded at 60 °C.

The HPC+CB dispersion shows an opposite trend: as in the case of the pure HPC formulation (see also Paragraph 3.3) the zero-shear viscosity increases with temperature, indicating a remarkable stiffening of the polysaccharide network. Moreover the shifting of the critical stress at which the fluid starts to flow toward higher values is clearly observable also in the presence of CB. These evidences indicate that CB effectively enhances the thermal stability of the HPC formulations without affecting the structure of the polymer matrix, since no appreciable variations in the rheological profiles are observed after the addition of the carbonaceous particles.

Regarding the NaOL-based formulations, Figure 3.34 shows the flow curves acquired at the different temperatures on both systems before and after the addition of CB.

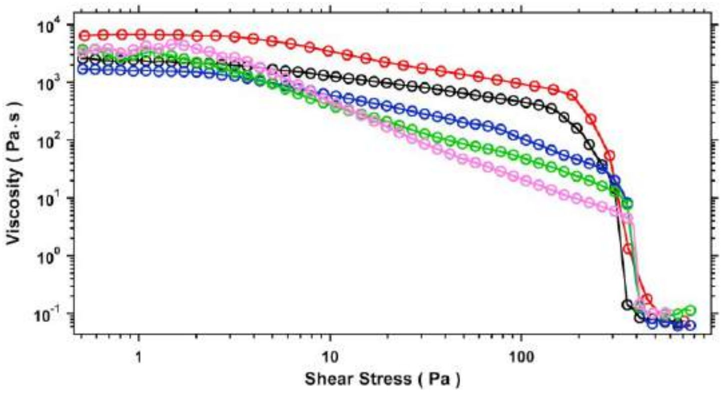

Figure 3.34 – Flow curves of the NaOL 13 % + KCl 4 % system containing CB 10% w/w at different temperatures: 25 (red), 30 (black), 40 (blue), 50 (green) and 60 (pink) °C.

In the absence of CB, the temperature increase induces the breaking in the entangled micellar network with a rapid drop in the viscosity of the system (see Paragraph 3.3). In the case of the CB-enriched formulations, the zero-shear viscosities are about two orders of magnitude higher, confirming the reinforcement of the network due the addition of CB. Furthermore, the rheological profile is quite different if compared to the pristine samples, with two different regions before the shear-thinning behaviour. We argue that for low values of the shear stress both the entangled micelles and the CB particles move together with the typical Newtonian behaviour already observed for worm-like micellar phases. When higher shear stresses are applied to the system, the viscous force between sodium oleate micelles and the carbonaceous particles arises, producing a second region where the system behaves as a shear-thinning material.[229] It is worth noting that the system seems to have a more pronounced shear-thinning behaviour as the temperature increases, as suggested by the value of critical stress that corresponds to the onset of the second region. For shear stresses higher than 100 Pa, the rapid drop of viscosity is similar to that observed for the pristine samples without CB, indicating the total break of the entangled micellar network even in the presence of the reinforcing agent.

The trend of the low-stress plateau region can be interpreted accordingly to Equation (3.6) to obtain the Gibbs free energy of activation ($\Delta G^{\neq}$ ) representing the strength of flow objects in solution, as in the case of pure polysaccharide and VES formulations (Paragraph 3.3). The results are shown in Table 3.12.

Table 3.12 - Zero-stress viscosity values ($\eta_0$, in Pa·s) and the extracted Gibbs free energy of activation ($\Delta G^{\neq}$) for polysaccharide and VES formulations before and after the addition of CB at 25, 30, 40, 50 and 60 °C.

| | $\eta_0$(Pa·s) | | | | | | | |
|---|---|---|---|---|---|---|---|---|
| T | GG | | SH | | HPC | | VES | |
| | No CB | CB | No CB | CB | No CB | CB | No CB | CB |
| 25 | 2.1 | 67 | 13 | 129 | 1.3 | 118 | 228 | 6741 |
| 30 | 1.6 | 53 | 10 | 65 | 1.8 | 203 | 150 | 2421 |
| 40 | 1.3 | 44 | 8.4 | 34 | 3.1 | 390 | 36 | 1627 |
| 50 | 0.7 | 26 | 6.1 | 8 | 8.4 | 594 | 11 | 2985 |
| 60 | 0.3 | 10 | 4.9 | 1.7 | 15 | 805 | 4 | 3914 |
| $\Delta G^{\neq}$ (kJ/mol) | 41 | 41 | 22 | 97 | - | - | 98 | - |

In the presence of the carbonaceous additive, the VES system exhibits a different response to the temperature raise. Indeed, the viscosity decreases in the range between 25 and 40 °C, as observed in the case of pure VES, whereas it shows a higher plateau when the temperature is further increased up to 50 and 60 °C. Thus, in this case $\Delta G^{\neq}$ cannot be estimated with an Arrhenius plot.

When CB is added to the polysaccharide systems, we observed different responses to a temperature increment. In the case of GG (a neutral polymer), we calculated the same $\Delta G^{\neq}$ value obtained before the addition of CB (41 kJ mol$^{-1}$). Instead in the case of the anionic SH, the addition of CB induces a significant change in $\Delta G^{\neq}$, that increases from 22 to 97 kJ mol$^{-1}$.

The HPC-based formulation cannot be analyzed according to this model because of the temperature-induced phase separation and stiffening of the polymer network.

The CB-polymer intermolecular interactions are usually interpreted in terms of a tunnelling effect,[233] a percolation phenomenon[234] or through a combination of the two models.[235,236] Both models assume a close contact between the chains and the CB particles. Probably, the different charge on the polysaccharide chains is the key factor that affects the CB-polymer interaction mechanism and how the system answers in response to the application of various stimuli. Anyway, the obtained results seem to indicate a complex behaviour of the mixed CB-polysaccharide systems and further experiments are needed in order to describe the different mechanisms of interactions.

In conclusion, the addition of carbon black to viscoelastic or polysaccharide aqueous formulations brings about a greater viscosity and a larger threshold of the network collapse, an improvement in the thermal properties, and imparts a remarkable electrical responsiveness to an external voltage. All these features make CB a very versatile additive which could be potentially used to modulate in a remote and controlled way the rheological and flow properties of fracfluid formulations.

### 3.4.2 Light-responsive formulations – Effect of Azorubine

As described in Paragraph 1.6.2, we include azorubine in a dispersion on sodium oleate in the presence of KCl in order to enable the modification of the formulation rheological properties through an external UV light stimulus. The UV treatment brings about the *trans-cis* isomerization of azorubine, which is incorporated within the surfactant cylindrical aggregates, resulting in a modification of the wormlike micellar structure of NaOL and in a variation of the formulation fluid behaviour.

First, we investigated the effect of UV irradiation on the flow properties of NaOL-based formulations at increasing KCl concentration (from 0 to 4 % w/w) in the absence of azorubine. Figure 3.35 shows the flow curves obtained before and after UV irradiation from the dispersions of NaOL, 13% w/w in the presence of KCl at different concentrations (0, 0.5, 2 and 3% w/w). For the curves at other KCl concentrations see Paper III in 0.

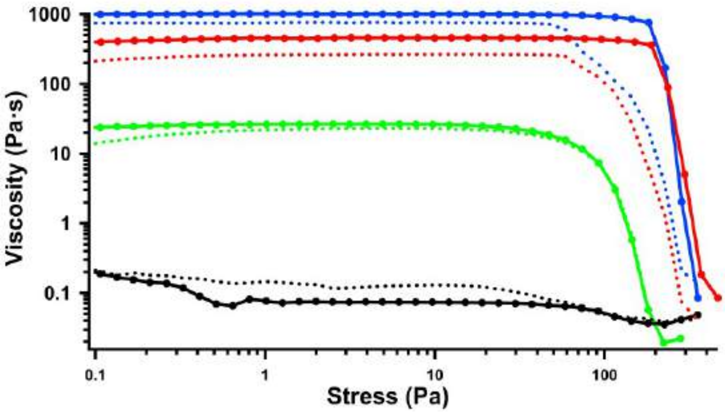

Figure 3.35 – Flow Curves before (solid lines) and after (dashed lines) UV irradiation for 13% w/w NaOL (0.43 M, black) and in the presence of KCl at 0.5% (green), 2% (blue) and 3% w/w (red).

The flow profiles are in good agreement with the data obtained for the VES formulations in Paragraph 3.1.2: after UV irradiation all the samples exhibit a Newtonian plateau at low shear stress, followed by a shear-thinning region as the shear stress increases. The viscosity drop at high shear stress is very sharp, due to the shear-induced alignment of the wormlike micelles.

The UV irradiation does not affect the flow properties of the formulations: the profiles, as well as the values of $\eta_0$ exhibit minor fluctuations within the experimental uncertainty before and after the UV treatment. For this reason any effect due to UV irradiation on the NaOL micellar structure can be disregarded.

The flow curves for the NaOL samples at different KCl concentration (0, 0.1%, 0.5% and 4%) in the presence of 0.18% w/w (3.6 $10^{-3}$M) azorubine are reported in Figure 3.36. For the curves at other KCl concentrations see Paper III in 0.

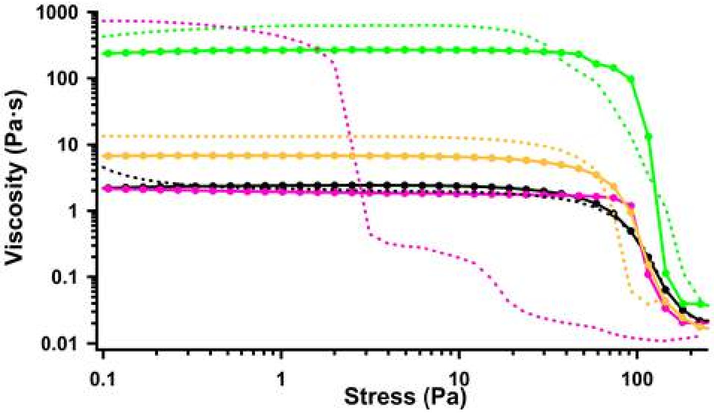

Figure 3.36 – Flow curves before (solid lines) and after (dashed lines) UV irradiation for NaOL 0.43 M mixture in the presence of 0.18% w/w azorubine ($3.6 \cdot 10^{-3}$ M) at different KCl concentration: 0 (black), 0.1% (orange), 0.5% (green) and 4% w/w (pink).

In the presence of azorubine all the formulations exhibit a shear-thinning behaviour that is similar to that found for the pure NaOL-KCl systems. The results obtained from the fitting of the experimental data with the Cross model are reported in Table 3.13.

Table 3.13 – Zero-shear rate viscosity $\eta_0$ (Pa·s) obtained by fitting the experimental viscosity data with the Cross model.

| | $\eta_0$(Pa·s) | | | | | | | |
|---|---|---|---|---|---|---|---|---|
| KCl % (w/w) | 0 % | 0.1 % | 0.5 % | 1 % | 2 % | 3 % | 3.5 % | 4 % |
| No UV | 2.50 | 6.94 | 278.8 | 951.8 | 57.98 | 5.72 | 2.66 | 1.85 |
| UV Irradiation | 2.07 | 13.6 | 728.3 | 736.7 | 53.44 | 5.21 | 2.01 | 730.1 |

After UV irradiation the viscosity of the samples with 0.1%, 0.5% and 4% KCl increases from 6.94 to 13.6, from 278.8 to 728.3 and from 1.85 to 730.1 Pa·s, respectively. For the other KCl concentrations no significant variations in the formulation viscosity are observed after the UV treatment, except for the sample containing KCl 1 % which shows a relatively small decrease. These findings lead to two important conclusions: (i) Azorubine has a remarkable effect as photo-active molecule in modifying the viscosity of the fluids after UV irradiation. A similar light-modulated viscosity change is reported for binary mixtures of

NaOL and a light-responsive cationic azobenzene dye (1-[2-(4-phenylazophenoxy)-ethyl]-3-methylimidazolium bromide).[96] In the work of Lu *et al.* the UV irradiation and the resulting *trans*-to-*cis* isomerization of the azo dye induces a decrease in the viscosity of the system, with a transition from a gel-like structure to a Newtonian fluid. In our case the opposite effect on the viscosity and the strengthening of the wormlike three-dimensional network may be attributed to the different chemical structure of the azo dye and its negative charge.(ii) The presence of KCl plays a key role in modulating the effect of azorubine. The experimental data reported in Table S1 show that the *trans*-to-*cis* isomerization of azorubine induces an increase in the formulation viscosity when KCl concentration is lower than 1% w/w. Between 1% and 3.5% no remarkable changes are observed before and after the UV irradiation, suggesting that the major contribution to the strength of the system is provided by the salt. The behaviour of the sample containing azorubine and 4% KCl is peculiar and deserves a deeper analysis. The viscosity increases by two orders of magnitude, but the rheological profile shows some differences after the UV treatment. A first Newtonian plateau appears in the low stress regime, then the viscosity rapidly decreases at a critical shear stress which is considerably lower than the viscosity breakdown point before the irradiation. After this initial decrease the flow curve shows a second, less pronounced plateau, followed by the typical shear-thinning region at high stress values. A similar behaviour was reported by Barrie *et al.* in 2004 for carbon black particles dispersed in an acrylic polymeric matrix.[229] In this case the presence of an intermediate (secondary) Newtonian plateau is attributed to the interaction between the polymer layer and the polymer matrix, in particular to the viscous drag between the polymer chains adsorbed on the particles with the polymer in solution. In a more recent work Sochi depicts this intermediate region as a characteristic feature of viscoelastic fluids in porous media flow, that may be attributed to the time-dependent nature of the viscoelastic fluid when the relaxation time of the fluid and the characteristic time of the flow become comparable.[237] In our system the appearance of this secondary Newtonian plateau may reflect the formation of ordered structures with a different degree of organization. We will return to this issue later in the section dedicated to SAXS results. To the best of our knowledge this is the first time that such behaviour is found and reported for wormlike micellar dispersions. As a matter of fact the cited literature sources deal with polymeric blends[238] or to a more general viscoelastic behaviour in porous media flow.[239] Further work is necessary to deepen and clarify this phenomenon. The high salt concentration may be responsible for the formation of complex, more entangled structures after UV exposure. These structures are responsible for the remarkable increase in the viscosity of the formulation and exhibit a low resistance to the applied stress, as confirmed by the low critical stress value. This hypothesis is also confirmed by the fact that during the sample preparation the azorubine solution becomes turbid at this salt concentration, suggesting the formation of aggregated structures. The same salt-induced behaviour is observed in pure azorubine solutions, without sodium oleate, and presumably reflects the formation of piled up structures stabilized by π-stacking interactions.[240]

Figure 3.37 reports the values of $\eta_0$ as a function of KCl concentration before and after the UV treatment.

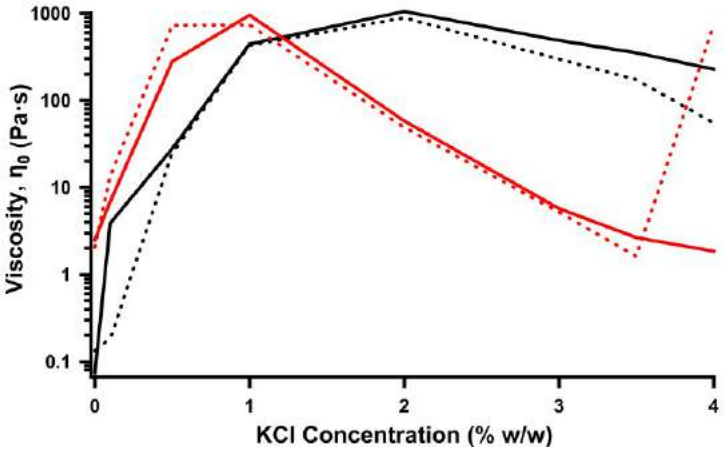

Figure 3.37 – Zero-shear viscosity ($\eta_0$) for the formulations containing 0.18% w/w azorubine (red) and the reference samples without the dye (black) as a function of the salt concentration (a) before (solid line) and after (dashed line) UV irradiation.

For the two sets of samples the viscosity steeply increases in the dilute regime, then it reaches a maximum and progressively decreases at higher concentrations of salt. The experimental results show that azorubine induces two distinct effects on the salt curves (see also Paragraph 3.1.2). The first effect is the shift of the peak maximum to lower KCl concentrations. Azorubine is an amphiphilic molecule that can penetrate across the micellar interface at least partially. This results in a flattening of the micelle/water interface with a significant lowering in the surface curvature. Moreover the electrostatic repulsion between different tubular micelles is screened and the viscosity increases even at lower concentration of salt.

The second effect is the modification of the salt curve shape after the maximum. In the presence of azorubine the viscosity decreases more rapidly, as a consequence of the increased branching density. Rogers *et al.* reported that for several mixed surfactant/salt viscoelastic systems, the branching effect is more evident with sodium salicylate, a hydrotropic salt that can penetrate more efficiently underneath the water/micellar interface salt respect to a simple inorganic salt like KCl.[241] This effect due to branched structures is quite common and found also in nonionic or zwitterionic systems.[93]

The effect of UV irradiation on the viscoelastic properties of wormlike systems are investigated by means of oscillatory shear measurements as a function of KCl concentration in the presence of azorubine. Figure 3.38 reports the storage and loss moduli obtained in the frequency sweep experiments before and after UV irradiation for the samples containing azorubine in the presence of KCl at different concentrations (0, 0.5% and 2%). The frequency sweep curves for other KCl concentrations are reported in Paper III in 0.

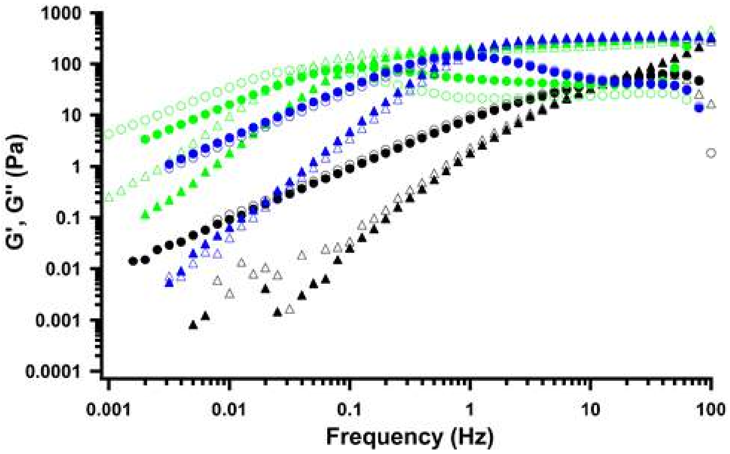

Figure 3.38 – Storage (triangles) and loss (circles) moduli before (filled markers) and after (hollow markers) UV irradiation for NaOL 0.43 M + azorubine 0.18 % mixture in the presence of KCl at 0 (black), 0.5 % (green) and 2 % (blue).

The formulations exhibit a viscoelastic behaviour with curves that look similar to those reported in Paragraph 3.1.2, indicating that the two frequency-dependent regimes are present. The crossover frequency decreases when KCl concentration is increased from 0 to 0.5%, then it progressively shifts to higher values upon further increase in the salt concentration. The UV treatment has a very minor effect on the viscoelastic properties of the formulations, with the exception of the sample containing KCl 4% (see Paper III). In this case before the UV irradiation the storage and loss moduli show a crossover in the high-frequency region, followed by a remarkable drop at medium and low frequencies, which indicates a predominantly viscous behaviour. After the UV treatment $G'$ and $G''$ overlap for the most part of the whole frequency range and after a slight decrease at high frequencies they levels off to a relatively high constant value in the medium and low-frequency regime. This results is consistent with the remarkable viscosity increase observed after the irradiation (Figure 3.36) due to the presence of light-induced ordered structures.

As in the case of pure and CB-enriched VES formulations, we use both $G'$ and $G''$ to calculate the time-weighted relaxation spectrum $H(\tau)$. The relaxation times extracted from the spectra are reported as a function of KCl concentration in Figure 3.39.

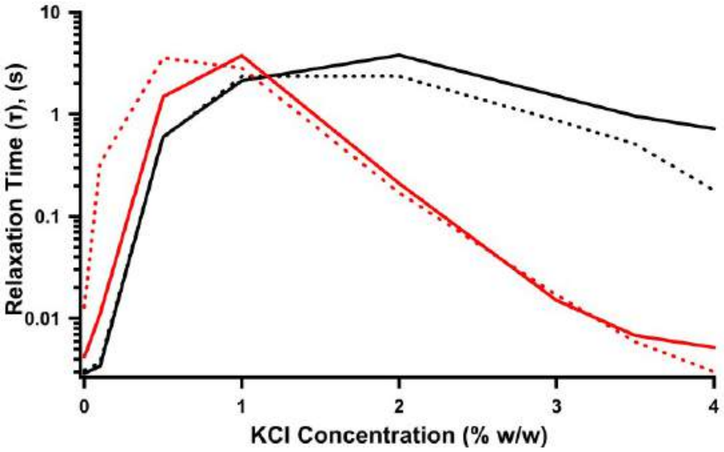

Figure 3.39 – Relaxation time ($\tau$) for the formulations containing azorubine (red) and the reference samples without the dye (black) as a function of the salt concentration before (solid line) and after (dashed line) the UV irradiation.

All the relaxation spectra shows a broad primary peak from which we estimate the relaxation times. For most samples multiple secondary peaks are observed, indicating the presence of different relaxation mechanisms (reptation, breaking and recombination, Rouse, etc.). The relaxation times follow the same trend of the viscosity as the salt concentration increases. This behaviour confirms the strengthening effect of azorubine on the entangled micellar network after the UV irradiation, which induces similar changes in the viscosity and in the dynamic rheological properties of the formulations.

The only exception is represented by NaOL + KCl 4% in the presence of azorubine: in this case the relaxation time after the UV treatment is very close to the value of the non-irradiated sample. As we mentioned in the previous section, the remarkable increase in the viscosity observed at this salt concentration is probably due to the presence of aggregated structures.

After evaluating the effect of UV irradiation on the rheological and flow properties of our VES formulations we performed DSC measurements to study how the UV treatment in the presence of azorubine affects the thermal behaviour of the systems. The investigated samples were the NaOL/KCl dispersions after UV irradiation and the NaOL/KCl formulations in the presence of azorubine before and after the UV treatment. The melting peak temperatures, the corresponding enthalpy changes and amount (%) of the free and interfacial water ($T_{mf}$, $\mathit{\Delta} H_{mf}$, $W_f$ $T_{mi}$, $\Delta H_{mi}$and $W_i$ respectively) obtained from the DSC thermograms are listed in Table 3.14 and Table 3.15Table 3.5. For the DCS curves see Paper III in 0.

Table 3.14 - Melting temperature, the relative enthalpy change and amount (%) of free water ($\Delta H_{mf}$, $T_{mf}$ and $W_f$), interfacial water ($\Delta H_{mi}$, $T_{mi}$and $W_i$) and freezable bound water ($\Delta H_{mb}$, $T_{mb}$and $W_b$) for the NaOL 13 % + KCl 4 % dispersion after UV irradiation

| | | **$\Delta H_{mf}$ (J/g)** | **$T_{mf}$ (°C)** | **$W_f$ (%)** | **$\Delta H_{mi}$ (J/g)** | **$T_{mi}$ (°C)** | **$W_I$ (%)** | **$\Delta H_{mb}$ (J/g)** | **$T_{mb}$ (°C)** | **$W_b$(%)** |
|---|---|---|---|---|---|---|---|---|---|---|
| **NaOL 13 % After UV Irradiation** | No KCl | 314.7 | 1.85 | 94.3 | - | - | - | - | - | |
| | KCl 0.1 % | 305.2 | 1.54 | 91.4 | - | - | - | - | - | |
| | KCl 0.5 % | 288.0 | 1.57 | 86.3 | 2.899 | -15.44 | 0.9 | - | - | |
| | KCl 1 % | 269.4 | 0.14 | 81.0 | 8.0296 | -13.53 | 2.6 | - | - | |
| | KCl 2 % | 231.2 | -0.39 | 69.2 | 18.39 | -12.25 | 5.9 | - | - | |
| | KCl 3 % | 178.2 | -0.72 | 53.4 | 25.52 | -11.54 | 8.2 | - | - | |
| | KCl 3.5 % | 161.7 | -1.16 | 48.4 | 26.78 | -11.52 | 8.6 | - | - | |
| | KCl 4 % | 153.2 | -1.06 | 45.9 | 19.85 | -12.06 | 6.4 | 2.433 | -23.90 | 0.78 |

Table 3.15 - Melting temperature, the relative enthalpy change and amount (%) of free water ($\Delta H_{mf}$, $T_{mf}$ and $W_f$), interfacial water ($\Delta H_{mi}$, $T_{mi}$and $W_i$) and freezable bound water ($\Delta H_{mb}$, $T_{mb}$and $W_b$) for the NaOL 13 % + KCl 4 % dispersion in the presence of azorubine before and after UV irradiation.

| | | $\Delta$H$_{mf}$ (J/g) | T$_{mf}$ (°C) | W$_f$ (%) | $\Delta$H$_{mi}$ (J/g) | T$_{mi}$ (°C) | W$_I$ (%) | $\Delta$H$_{mb}$ (J/g) | T$_{mb}$ (°C) | W$_b$ (%) |
|---|---|---|---|---|---|---|---|---|---|---|
| **NaOL 13 %<br>Azorubine 0.18 %<br>Before<br>UV Irradiation** | No KCl | 312.4 | 2.33 | 93.6 | - | - | - | - | - | - |
| | KCl 0.1 % | 310.1 | 1.54 | 92.9 | - | - | - | - | - | - |
| | KCl 0.5 % | 288.5 | 1.18 | 86.4 | 2.112 | -17.61 | 0.68 | - | - | - |
| | KCl 1 % | 266.4 | 0.46 | 79.8 | 6.545 | -14.54 | 2.10 | - | - | - |
| | KCl 2 % | 209.0 | 1.79 | 62.6 | 11.05 | -12.08 | 3.54 | - | - | - |
| | KCl 3 % | 183.4 | -0.12 | 54.9 | 17.24 | -11.99 | 5.52 | 1.7 | -23.70 | 1.72 |
| | KCl 3.5 % | 163.2 | -0.65 | 48.9 | 19.95 | -11.69 | 6.39 | 0.73 | -25.81 | 0.73 |
| | KCl 4 % | 167.4 | -1.28 | 50.2 | 23.64 | -12.16 | 7.57 | 3.67 | -24.01 | 3.67 |
| **NaOL 13 %<br>Azorubine 0.18 %<br>After<br>UV Irradiation** | No KCl | 313.6 | 1.52 | 94.0 | - | - | - | - | - | - |
| | KCl 0.1 % | 312.5 | 0.85 | 93.6 | - | - | - | - | - | - |
| | KCl 0.5 % | 306.8 | 0.72 | 91.9 | - | - | - | - | - | - |
| | KCl 1 % | 271.9 | 0.13 | 81.5 | 6.591 | -14.72 | 2.11 | - | - | - |
| | KCl 2 % | 231.3 | -0.45 | 69.3 | 14.92 | -12.75 | 4.78 | - | - | - |
| | KCl 3 % | 186.1 | -0.46 | 55.8 | 15.70 | -12.16 | 5.03 | 1.8 | -23.94 | 0.59 |
| | KCl 3.5 % | 182.7 | -1.18 | 54.7 | 20.47 | -12.40 | 6.56 | 1.40 | -24.42 | 0.45 |
| | KCl 4 % | 153.2 | -1.06 | 45.9 | 19.85 | -12.06 | 6.36 | 2.43 | -23.90 | 0.78 |

For the NaOL/KCl irradiated samples $W_f$ rapidly decreases, passing from 94% to 45% as the salt concentration increases. Similar values are obtained for the NaOL/KCl systems before the UV irradiation (see Paragraph 3.1.2), demonstrating that the endothermic process (*i.e.* the melting of the free water) is not affected by the UV treatment, as expected. For the samples containing azorubine the presence of the dye does not induce remarkable variations in the amount of free and interfacial water, as well as in the values of peak temperatures and the relative enthalpy changes. The main difference is represented by the freezable bound water melting peak, that appears starting from KCl 3%. As indicated by the viscosity measurements, the negatively charged sulfonate groups in the azorubine molecule have a cooperative effect with KCl in screening the electrostatic repulsion between the micellar surfaces. This synergistic action reduces the amount of salt that is required for the formation of the micellar entangled network (and eventually the branched structures), and affects the thermal transition of the water molecules that closely interacts with the micellar surface, *i.e.* the freezable bound water.

In order to find a correlation between the observed rheological flow curves of the investigated systems and their nanostructure SAXS experiments were performed. Figure 3.40 reports SAXS curves of pure NaOL 13 %, NaOL 13 % in the presence of KCl 4 % and NaOL 13 % + KCl 4 % in the presence of azorubine 0.18 %. The main result from SAXS analysis is that there is a transition from non-interacting spherical micelles in the formulation containing only NaOL to a network of polydispersed core-shell elongated objects interacting via a screened Coulomb potential upon the addition of salt. This behaviour is already reported in the literature[74,78,111] and the formation of a network of interacting long micelles is in good agreement with the rheological data of sodium oleate in the presence of different KCl concentrations (Paragraph 3.1.2). The appearance of the interaction contribution in the low-q region of the SAXS curve of the sample containing both oleate and KCl can be ascribed to the screening of the electrostatic charges on the surface of oleate micelles thanks to salt addition.

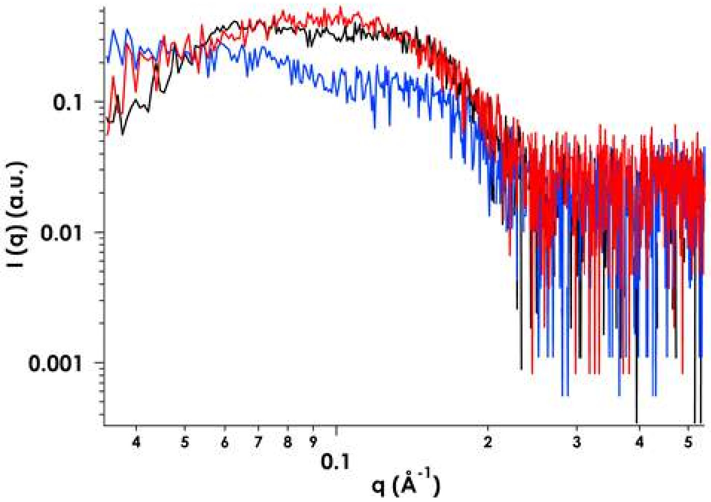

Figure 3.40 – SAXS curves of NaOL 13 % (blue), NaOL 13 % + KCl 4 % (red) and NaOL 13 % + KCl 4 % in the presence of azorubine 0.18 % (black). All curves are offset along y-axes.

A very similar behaviour can be observed upon the addition of azorubine since the SAXS profile of the formulation containing the dye is similar to that of the sample with KCl. This result is consistent with the rheological experiments reported in this Section: in the presence of azorubine the formation of micellar branched structures occurs more rapidly than in the case of the single KCl addition, determining a decrease in the formulation viscosity. Nevertheless, the wormlike structure is maintained, as demonstrated by the similar SAXS profiles. Finally, the effect of the UV irradiation on the nanostructure of the viscoelastic formulations is investigated acquiring the SAXS scattering profiles reported in Figure 3.41 on NaOL formulations containing the azo dye and KCl 0.1 % and 4 %. SAXS curves of the samples after UV irradiation show the presence of a sharp peak centred at 0.15 $q^{-1}$ (corresponding to a dimension of about 8 nm) independently from KCl concentration. Since this feature is not visible in the SAXS profiles of the samples before UV exposure, we can argue the formation of a light-induced ordered phase. This result represents a further confirmation of what we observed by means of the rheological experiments, where the remarkable increase of viscosity observed after the UV treatment of the samples was ascribed to the strengthening of the micellar network and the formation of ordered structures, especially in the sample containing the higher amount of KCl.

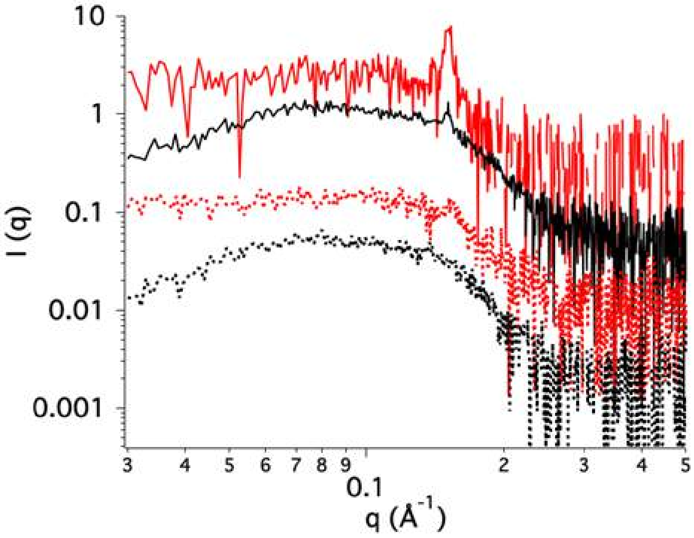

Figure 3.41 – SAXS curves of NaOL 13 % + azorubine containing KCl 0.1 % (black curves) and 4 % (red curves) before (dotted lines) and after (continuous line) UV irradiation. All curves are offset along y-axes.

In conclusion we illustrated a simple and inexpensive procedure for the formulation of a green photo-responsive viscoelastic fluids starting from non-toxic, biocompatible, commercially available materials. The addition azorubine to a dispersion on sodium oleate in the presence of KCl enables the effective modification of the formulation rheological properties through an external UV light stimulus. This approach could be easily implemented in a real shale gas extraction site by simple introducing optical fibres inside the well to propagate the light input.

## 3.5 NORM REDUCTION STRATEGIES

In this Section we provide an extensive overview of the possible approaches that can be used to limit the amount of NORM extracted in the flowback water during shale gas operation or that can be employed for the treatment of wastewaters after gas extraction. Starting from the current state of the art on the water treatment techniques and the most commonly used additives together with the geochemical data found in the literature for the currently exploited formations in US and Europe (see Paragraph 1.6.3), we propose two green strategies for NORM reduction. The first takes advantage of a physical method that is the magnetic water treatment, while the second one is based on the use of NORM-reducing chemical additives.

In the latter case, different chemicals which are completely safe in terms of composition are proposed and their performances are evaluated also by adding these additives to the green formulations developed in order to mimic their behaviour in complex formulations, thus simulating real operative conditions.

### 3.5.1 Magnetic Water Treatment

For the study of magnetic water treatment, the size and the morphology of $CaCO_3$, $BaCO_3$ and $SrCO_3$ crystals were assessed by means of optical microscopy at two different temperatures, 25 and 60 °C. From the comparison of optical micrographs acquired at the different conditions (temperature, magnetic treatment, chemical nature of the magnetically treated ions), we qualitatively predicted the efficacy of the magnetic treatment in the presence of different salts and we gain info on the effect of both temperature and chemical nature of the treated ions on the magnetic effect. Regarding calcium carbonate, fluorescence and XRD experiments were also performed to monitor the conversion between the two main polymorphs of $CaCO_3$ upon magnetic treatment. The results are included in “The effect of temperature and magnetic field on the precipitation of insoluble salts of alkaline earth metals”, submitted, which is reported in 0 as Paper IV.

Our study started from the investigation of the effect of temperature on the precipitation of calcium, barium and strontium carbonates. Figure 3.42 shows the comparison between the optical micrographs obtained after 60 min from the mixing of the starting solutions at 25 and 60 °C.

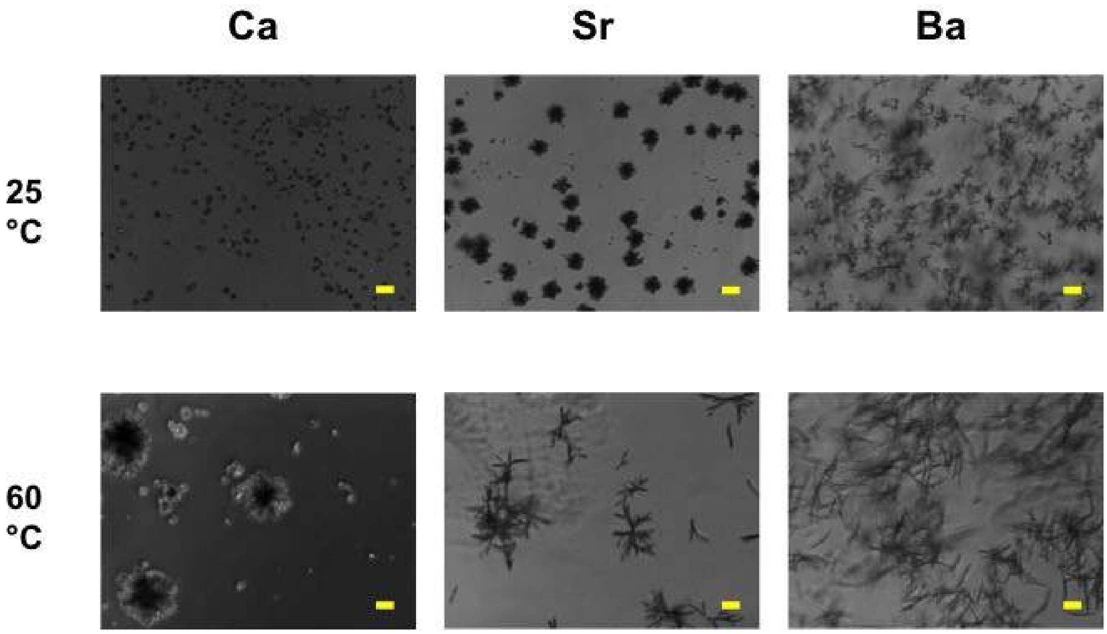

Figure 3.42 – Optical micrographs of calcium, strontium and barium carbonates precipitated after 60 min from the mixing of non magnetized solutions at 25 and 60 °C. Scale bar: 100 μm.

The optical micrographs recorded at room temperature on calcium carbonate reveal the formation of calcite (rhombohedral crystals) and vaterite (spherical crystals). This result is in line with previous studies on $CaCO_3$ polymorphs formed from highly super-saturated solutions: it was found that vaterite and calcite are formed at low temperature (14−30 °C), while the conversion into aragonite (orthorombic structure, often in form of needle-like crystals) is favoured at higher temperatures (60−80 °C) and becomes the predominant form at about 70 °C.[242] Accordingly, optical microscopy at 60 °C shows the presence of aragonite together with calcite and hexagonal plate vaterite crystals. Similar results were obtained by means of fluorescence (Figure 3.43).

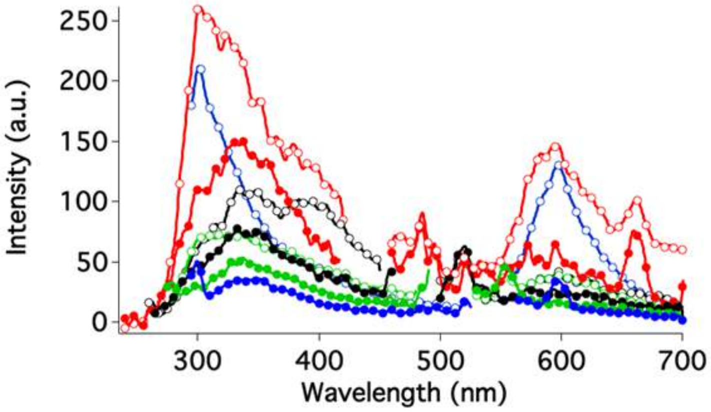

Figure 3.43 – Fluorescence excitation spectra of $CaCO_3$ crystals in solution at 25 (empty circles) and 60 °C (filled circles) in the absence of magnetic field. Red: $\lambda_{exc} = 220$ nm, black: $\lambda_{exc} = 238$ nm, green: $\lambda_{exc} = 254$ nm, blue: $\lambda_{exc} = 272$ nm.

The sample investigated at 25 °C shows strong emission signals centred at about 300 ($\lambda_{exc} = 272$ nm) and 600 ($\lambda_{exc} = 238$ and 254 nm), while the sample at 60 °C shows a significant broad peak at about 350 nm ($\lambda_{exc} = 272$ nm) and an emission peak centred at 555 nm ($\lambda_{exc} = 254$ nm). Since the signals at 300 and 600 nm are particularly intense only in the sample obtained at 25 °C, we can infer that they are related to calcite, and that this is the most abundant polymorph at such temperature. This agrees with the observations obtained from the optical images. Instead the signals centred at 350 and 555 nm are mainly visible in the sample at 60 °C, so they are probably due to aragonite crystals. This observation, together with a reduction in the intensity of calcite emission bands (300 and 600 nm), indicates a partial conversion of calcite into aragonite at higher temperature, in agreement with previous literature works and with our optical microscopy experiments. The temperature-induced formation of aragonite is also confirmed by XRD measurements reported in Figure 3.44, where the peaks at 26.3, 27.3, 41 and 46° associated with aragonite appear in the pattern of the sample precipitated at 60 °C.

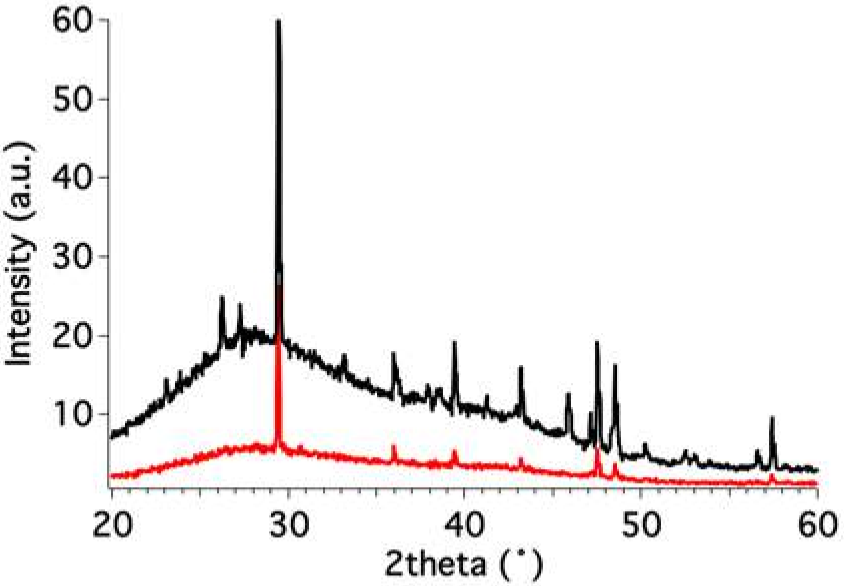

Figure 3.44 – XRD patterns of $CaCO_3$ crystals precipitated at 25 (red) and 60 (black) °C. Spectra are offset along y-axes.

Regarding strontium and barium carbonates, no different allotropic forms exist in the temperature range investigated: optical micrographs show that the morphology of crystals remains the same for both samples at 25 and 60 °C (for further details see Paper IV in 0). In particular, strontianite ($SrCO_3$) crystals possess a dendritic structure, while witherite ($BaCO_3$) precipitates forming floc crystals. However, the size of the crystals increases as temperature is raised up to 60 °C.

The obtained results reveal that temperature strongly affects crystal dimension causing an increase in their size, especially in the case of strontium and barium carbonates. This is in agreement with previous studies on the precipitation of carbonate-scaling minerals as a function of T and P, where it is reported that the alkali earth carbonates are less soluble at temperatures above 25 °C.[243] This is a good result for applicative purposes because we expect a similar behaviour also for NORM ions: the formation of larger scales makes the extraction of NORM more difficult in real operative conditions. On the other hand, the formation of larger scales at high T could be a problem in the case of calcium carbonate, since it is the most abundant scaling mineral so its enhanced precipitation is responsible for pipelines obstruction: however, we have demonstrated that aragonite formation is favoured at

60 °C. Since aragonite is less densely packed with respect to calcite, aragonite scales are softer and more soluble with respect to calcite deposits.

After evaluating how temperature affects the salt precipitation, we studied the effect of magnetic field. Figure 3.45 shows the optical images obtained at 25 °C on precipitates from solutions exposed to the static magnetic field and compared to those obtained from untreated solutions.

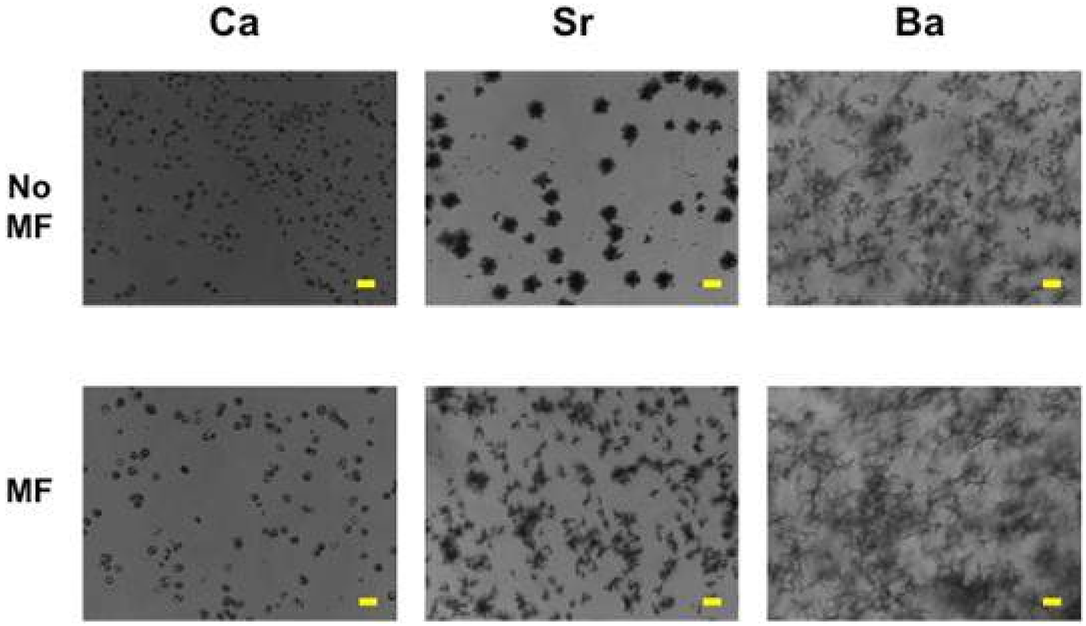

Figure 3.45 – Optical micrographs of calcium, strontium and barium carbonates precipitated at 25 °C after 60 minutes from the mixing of non magnetized (top) and magnetized (bottom) solutions. Scale bar: 100 µm.

In the case of calcium carbonate, according to the results found in the literature,[115] the magnetic exposure of the starting solutions leads to a suppression of the nucleation and an acceleration of the growth that results in the decrease of the number of crystals and an increase of their size. Fluorescence spectra reported in Figure 3.46 show a strong decrease in the intensity of the magnetized sample in agreement with a lower amount of crystals in solution.

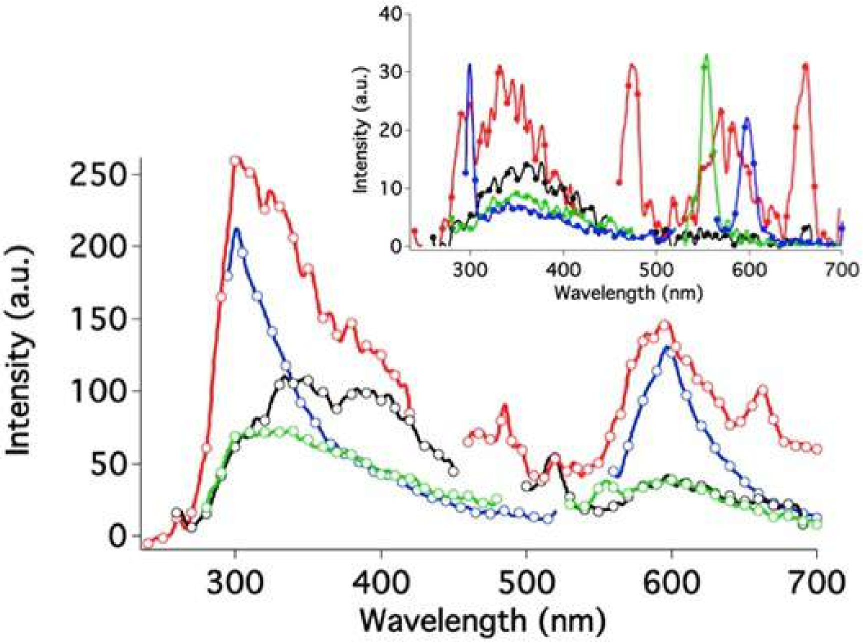

Figure 3.46 – Fluorescence excitation spectra of $CaCO_3$ crystals in solution at 25 °C starting from non magnetized (empty circles) and magnetized (inset) solutions. Red: $\lambda_{exc} = 220$ nm, black: $\lambda_{exc} = 238$ nm, green: $\lambda_{exc} = 254$ nm, blue: $\lambda_{exc} = 272$ nm.

Regarding Sr(II) and Ba(II) carbonates, there is no effect of the magnetic field on the crystal morphology. However, the suppression of nuclei and the formation of few larger crystals occur for witherite. Instead, in the case of strontianite, the exposure to the static MF has the opposite effect, inducing the precipitation of smaller crystals.

Our experimental results suggest that the application of an external MF is an effective method to reduce the amount of precipitate not only in the case of $CaCO_3$, as already extensively reported in previous works, but also in the case of other insoluble salts.

The effect of MWT on calcium sulfate scales was investigated as well, since gypsum ($CaSO_4 \cdot 2H_2O$) is another of the main components of mineral scales. From optical micrographs (Figure 3.47), we have found that there are no significant changes in the crystalline structure of the precipitate after magnetic treatment of the reactants: needle-like crystals are visible in the case of both magnetized and non magnetized solutions. Regarding the size of the precipitated crystals, we can observe the opposite effect of MF with respect to calcium carbonate: $CaSO_4$ crystals obtained from magnetized solutions are smaller than those precipitated from untreated solutions. However, it seems that the magnetic treatment reduces the amount of precipitate, as observed for calcium carbonate. The different behaviour observed for carbonate and sulfate can be ascribed to the different chemical properties of the two ions, in particular their diamagnetic/paramagnetic nature. However, this issue needs to be further considered and more experiments have to be acquired, for example using an alternating magnetic field.

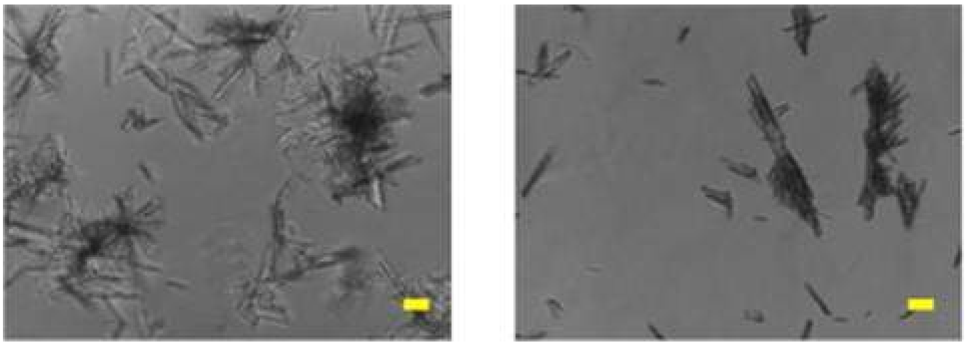

Figure 3.47 – Optical micrographs of calcium sulfate precipitated at 25 °C immediately after the mixing of non magnetized (left) and magnetized (right) solutions. Scale bar: 100 µm

Considering the strong effect of both high T and static MF on insoluble salts precipitation, we decided to assess what happens when both high temperature and magnetic treatment are combined together. The idea was to understand if scale formation during shale gas operations can be limited by pumping down hole formulations previously exposed to the magnetic field. Considering that temperature in real operative conditions is around 100 °C, tests on magnetically treated solutions were performed at  60 °C to assess if they retain their behaviour against salts precipitation in real conditions.

Figure 3.48 shows the comparison of the optical micrographs of Ca(II), Sr(II) and Ba(II) carbonates precipitating from magnetized solutions at 25 and 60 °C.

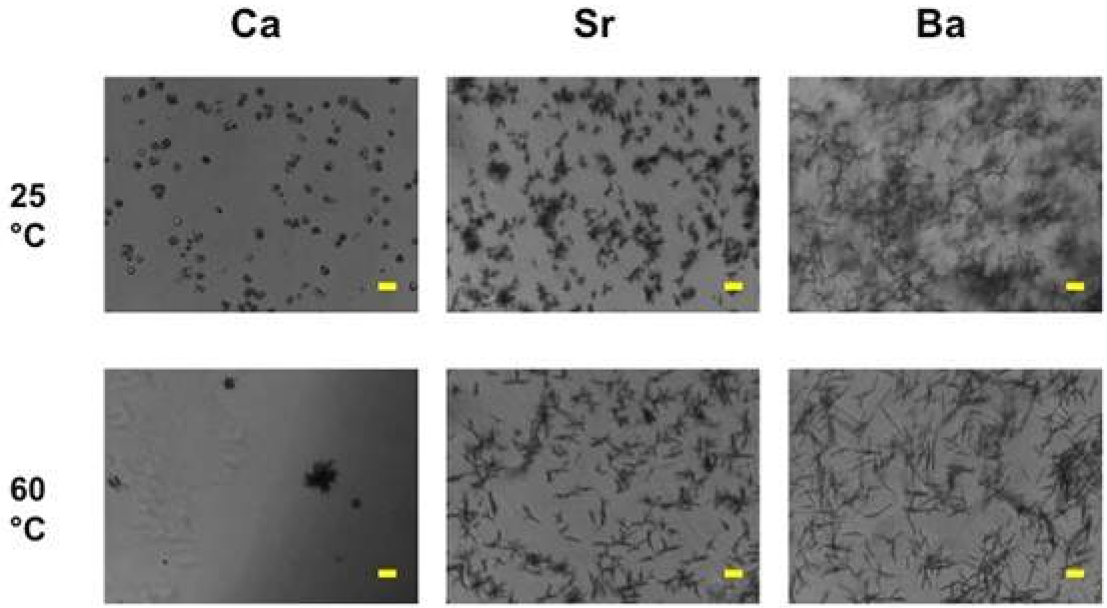

Figure 3.48 – Optical micrographs of calcium, strontium and barium carbonates precipitated at 25 (top) and 60 (bottom) °C after 60 minutes from the mixing of magnetized solutions. Scale bar: 100 µm.

In the case of $CaCO_3$, the optical images reveal that the combination of high T and MF leads to: i) a good conversion of calcite into aragonite and ii) a strong suppression of the number of crystals in solution. XRD measurements in Figure 3.49 show a strong decrease in the signals associated with calcite compared to those obtained after the treatment with the magnetic field at 25 °C where a significant contribution of aragonite peaks appears.

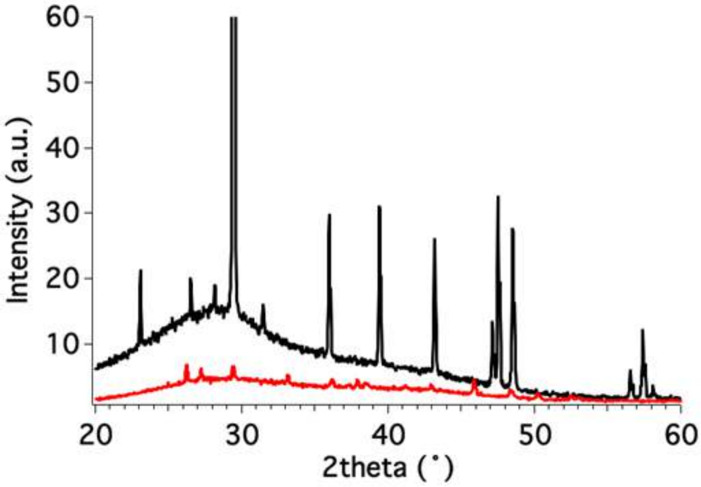

Figure 3.49 – XRD patterns of $CaCO_3$ crystals precipitated after the magnetic treatment at 25 (black) and 60 (red) °C. Spectra are offset along y-axes.

The fluorescence spectra shown in Figure 3.50 indicate an enhancement in the emission peaks of aragonite when $CaCO_3$ is precipitated at high T from magnetized solutions. The sample obtained at 60 °C in the presence of MF produces emission signals roughly twice as intense as those obtained at 25 °C after magnetization of the solutions, indicating the presence of larger amounts of small crystals. The comparison of these results with those obtained from the sample precipitated at 60 °C without any magnetic treatment suggest that the kind of polymorph in solution depends mainly on the temperature. There is an increase in the aragonite content at higher temperatures, while the magnetization prior to mixing the reactants can reduce the amount of precipitate.

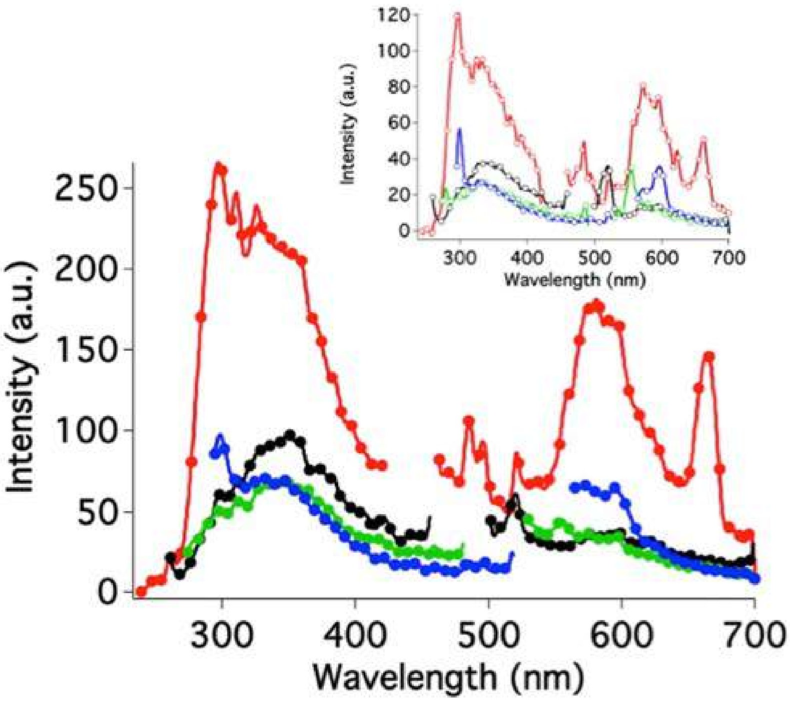

Figure 3.50 – Fluorescence excitation spectra of $CaCO_3$ crystals in solution at 25 (inset) and 60 °C (filled circles) in the case of magnetized solutions. Red: $\lambda_{exc} = 220$ nm, black: $\lambda_{exc} = 238$ nm, green: $\lambda_{exc} = 254$ nm, blue: $\lambda_{exc} = 272$ nm.

Similar results were obtained for witherite and strontianite from optical images. As in the previous cases the crystal morphology remains unchanged, while the formation of fewer larger crystals is favoured (see Paper IV in 0).

The experimental results suggest that the crystal growth is favoured with respect to the nucleation step when high T and MF are combined together during the precipitation of the alkaline earth insoluble salts, thus leading to the formation of a smaller amount of larger crystals. In addition, regarding $CaCO_3$, the combination of these two parameters promotes the formation of aragonite. With this in mind, we can conclude that the combined application of high T and external magnetic fields can be an easy and feasible way to control scale formation and limit the problem of pipes obstruction. Furthermore, the formation of fewer scales of larger dimensions limits the likelihood of NORM extraction in the flowback water at the end of operation.

## 3.5.2 Use of Antiscaling Agents

In this section, we discuss the qualitative results obtained on the precipitation of calcium and strontium sulfates in the presence of different green scale inhibitors. It is worth noting that, differently from what we have done in the study of magnetic water treatment, the role of antiscalants was assessed on the precipitation of sulfates instead of carbonates: the choice was done on the basis of crystals morphology. In fact, sulfates precipitate forming larger crystals with respect to carbonates so it is easier to observe possible morphological variations induced by the addition of antiscalants by means of optical microscopy. For the same reason, we do not report results on barium salts in the presence of antiscalants since it precipitates immediately due to its very low solubility in water forming very small crystals that are difficult to observe with a good resolution using our optical microscope.

First of all, the performances of the studied antiscalants were assessed in pure water. Figure 3.51 shows $CaSO_4$ precipitates without and with the different studied antiscalants and the corresponding optical micrographs. In particular, we can observe a strong reduction of the amount of precipitated salt especially in the case of PAS, PG-low $M_w$ and PAC-medium and high $M_w$.

Optical images reveal that, differently from the big floc crystals obtained when calcium sulfate is precipitated in neat water, the addition of the additives leads to the formation of less compact crystals for all the investigated molecules; however, the most remarkable effect on gypsum morphology is obtained for PAS and PAC-medium and high $M_w$.

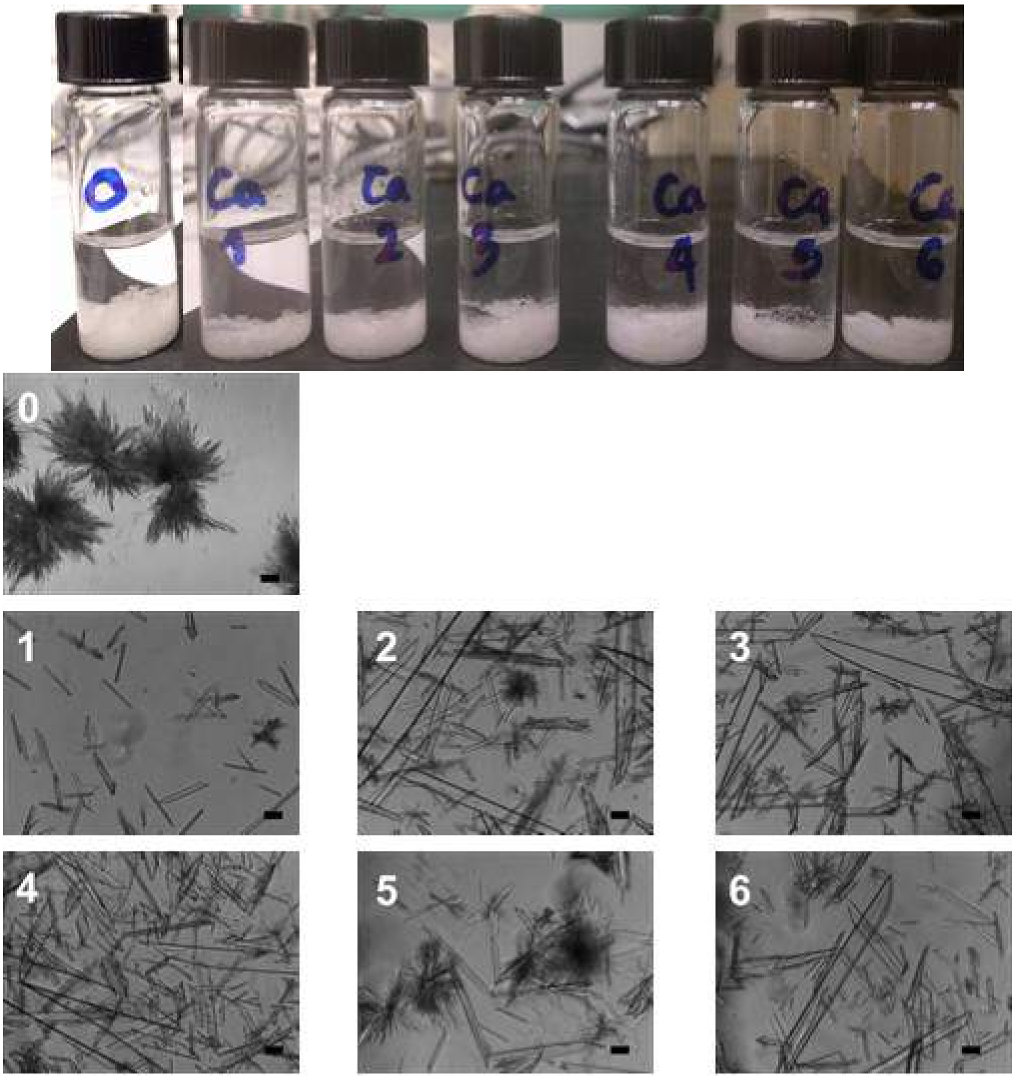

Figure 3.51 – Effect of different antiscalants on the precipitation of calcium sulfate in water at 25 °C. Top: picture of the precipitates; bottom: corresponding optical micrographs. Scale bar: 100 µm. (0) no antiscalant; (1) PAS; (2) PG-low $M_w$; (3) PG-high $M_w$; (4) PAC-low $M_w$; (5) PAC-medium $M_w$; (6) PAC-high $M_w$.

Similar results were found in the case of $SrSO_4$ (see Figure 3.52).

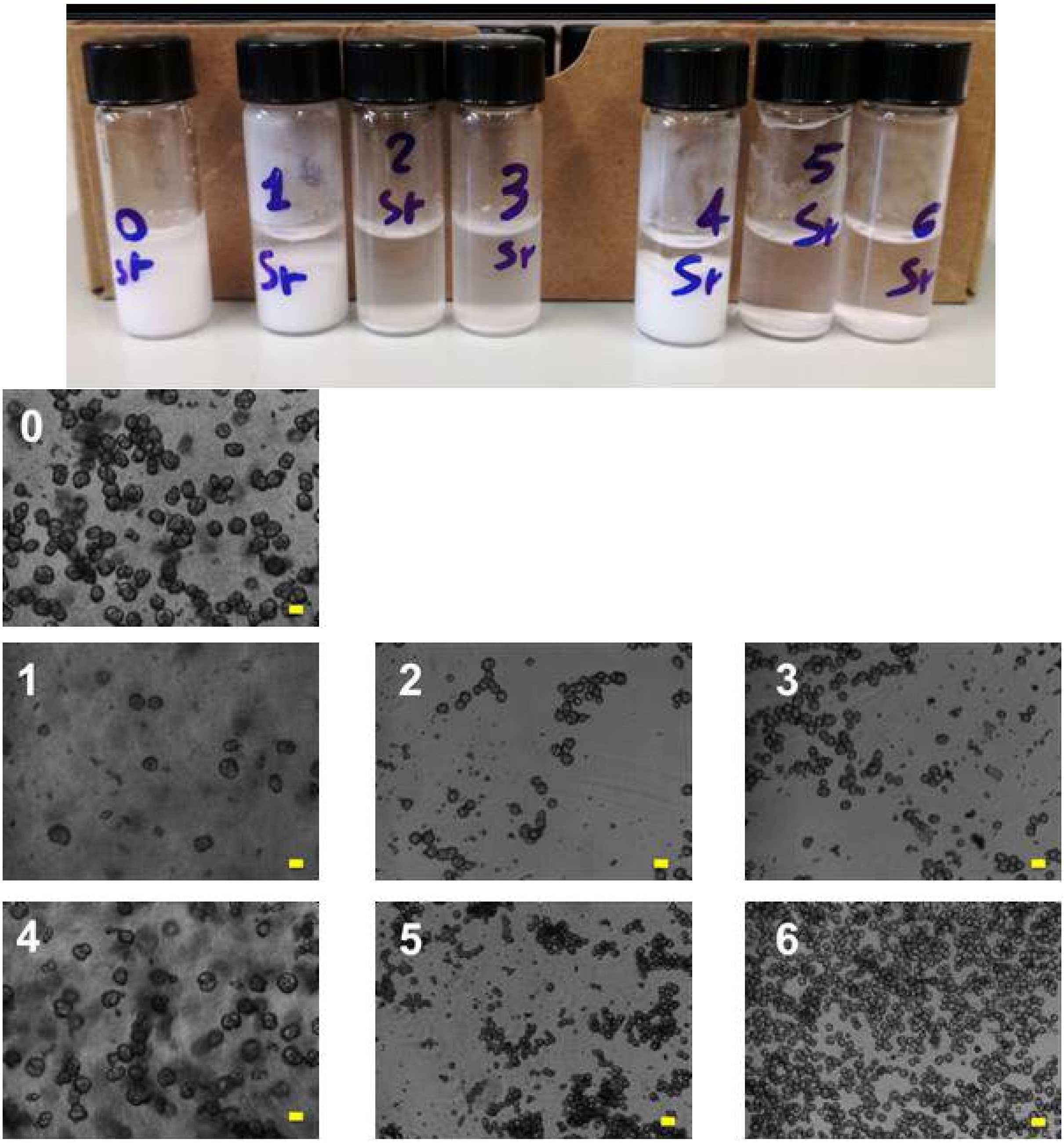

Figure 3.52 – Effect of different antiscalants on the precipitation of strontium sulfate in water at 25 °C. Top: picture of the precipitates; bottom: corresponding optical micrographs. Scale bar: 100 µm. (0) no antiscalant; (1) PAS; (2) PG-low $M_w$; (3) PG-high $M_w$; (4) PAC-low $M_w$; (5) PAC-medium $M_w$; (6) PAC-high $M_w$.

Considering that scale inhibitors are added in very small amount far from the stoichiometric concentration of the scaling species, scale suppression can be ascribed to physical mechanisms: the adsorption of antiscalant molecules on active growth sites of crystals leads to reduced nucleation and crystal growth rates and to the formation of distorted crystal structures. The crystal distortion weakens the tenacity of the scale and the highly irregular stressed crystals tend to slough off as crystal growth occurs.[244] In addition, all the tested scale inhibitors possess negative charges in their chemical structure: the electrostatic repulsion between approaching crystals is another possible mechanism to prevent the crystal growth. Considering that PAS possesses two negative charges while the other additives are monovalent salts, it is not surprising that it is one of the most performing agents.

Regarding the use of antiscalants with different molecular weights, the choice was done on the basis of previous literature reports. Indeed, it was proved that a minimum number of monomer units is required to have effective binding to the crystal surface that differs from mineral to mineral: for example, in the case of calcium sulfate in the presence of polyacrylates, it was found the optimum effectiveness with molecular weight of ~2000 Da.[245] In another study on polyaspartate scale inhibitors, Ross et al. proved that polyaspartates in the range of 3000-4000 Da are the most effective for inhibition of calcium carbonate and barium sulfate, while, for calcium sulfate inhibition, the optimum molecular weight was found to be in the range of 1000-2000 Da.[246]

In general, as the molecular weight increases, there might not be a proportional increase in binding effectiveness for a polymer. Additionally, the number of molecules in a given weight of polymer decreases, resulting in decreased activity. Finally, it has to be considered that larger molecules move in solution slower than smaller ones at the same temperature, as the adsorption on the surface of growing crystals is dependent on their diffusion coefficient in solution. Accordingly, the precipitation of larger crystals both in the case of $CaSO_4$ and $SrSO_4$ is observed in the case of the formulations containing high $M_w$ PG and PAC.

The effect of high temperature (60 °C as in the case of MWT) on the performances of antiscaling agents was also investigated. Tests were carried out just on calcium sulfate in water as an example and the obtained optical micrographs are shown in Figure 3.53.

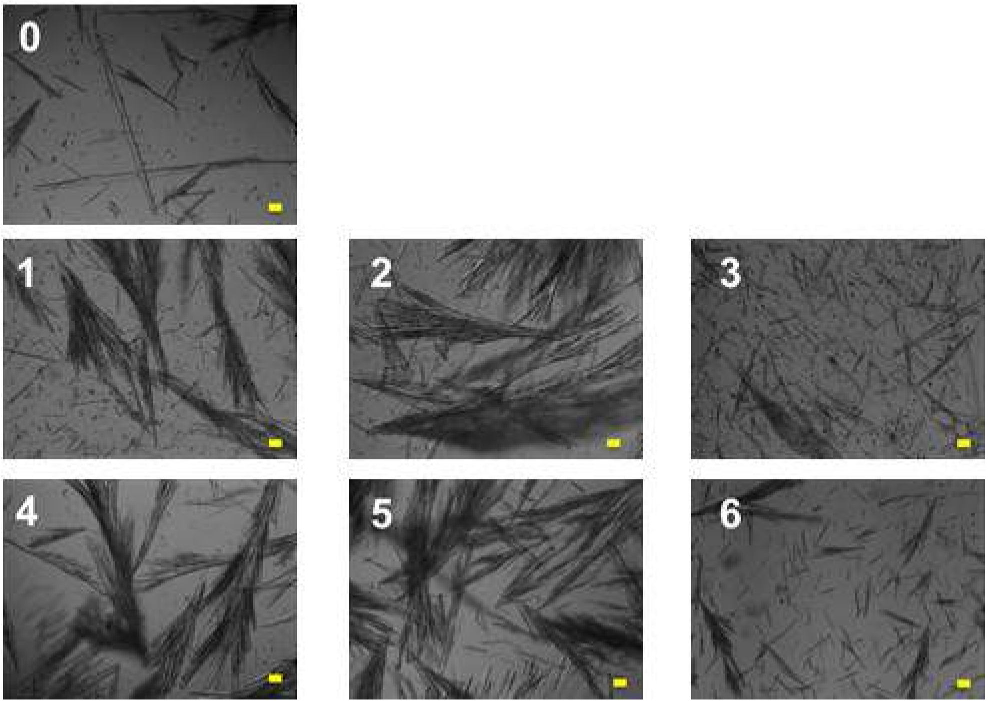

Figure 3.53 – Optical micrographs showing the effect of different antiscalants on the precipitation of calcium sulfate in water at 60 °C. Scale bar: 100 µm. (0) no antiscalant; (1) PAS; (2) PG-low $M_w$; (3) PG-high $M_w$; (4) PAC-low $M_w$; (5) PAC-medium $M_w$; (6) PAC-high $M_w$.

Increasing temperature, the formation of bigger crystals is favoured also in the presence of scale inhibitors since calcium sulfate solubility in water decreases with respect to room temperature. The worst performances of all the studied additives at 60 °C with respect to those observed at room temperature can be explained considering that, due to a decrease of salt solubility at high T, the scale layer forms more rapidly and becomes thicker thus reducing the scale inhibition efficiency. The same behaviour is reported in the literature on calcium carbonate scales precipitated at high temperature in high salinity wastewater.[247] Another possible factor that reduces the efficacy of antiscalants at high T could be an enhancement of the thermal motion of antiscalant molecules, which probably reduces the rate of their adsorption on the forming crystalline nuclei. However, PG-low $M_w$ and PAC-high $M_w$ show very good performances in the reduction of precipitate amount.

In the final part of the work, the effectiveness of antiscaling agents was evaluated in the final polysaccharides-based formulations developed in these years. It is worth noting that antiscalants performances were evaluated only in polysaccharidic formulations and VES formulations were not considered for these tests since in the presence of a viscoelastic surfactant salts interact with the surfactant rather than with the scale inhibitor. Figure 3.54 shows calcium sulfate precipitates and the corresponding optical micrographs in the presence of scale inhibitors added to sodium hyaluronate-based formulation.

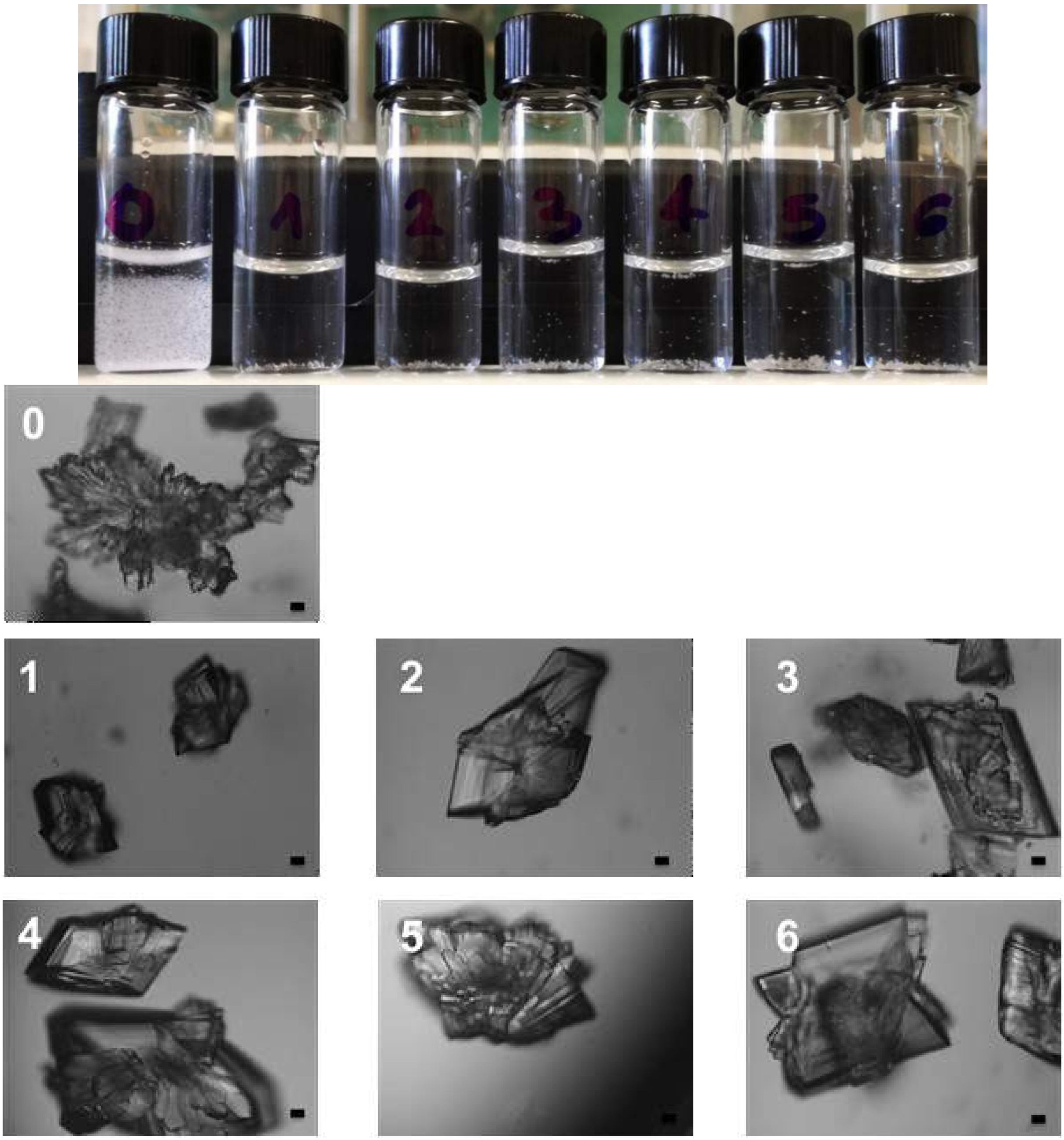

Figure 3.54 – Effect of different antiscalants on the precipitation of calcium sulfate in SH-based formulation at 25 °C. Top: picture of the precipitates; bottom: corresponding optical micrographs. Scale bar: 100 µm. (0) no antiscalant; (1) PAS; (2) PG-low $M_w$; (3) PG-high $M_w$; (4) PAC-low $M_w$; (5) PAC-medium $M_w$; (6) PAC-high $M_w$.

We can observe that crystal morphology is completely different from that observed in pure water, also without additives. The formation of more ordered crystals with shorter needles suggests that probably the polysaccharide matrix acts as "templating agent": considering the high viscosity of polysaccharides-based systems, we can argue that crystalline nuclei move slower with respect to neat water. In addition, we observe that the differences among the studied antiscalants are less remarkable with respect to what was observed in pure water: the amount of precipitate and the crystals morphology are more or less the same for all samples. However, all antiscalants show very good performances, even better than those observed in water. We might explain this unexpected result considering that sodium hyaluronate is negatively charged so the polysaccharide itself acts as a scale inhibitor. This, combined with the presence of antiscalant additives, ensures the stop of crystallites growth, thus significantly decreasing the amount of precipitate.

The obtained results are of great interest for real applications since we have demonstrated that scaling minerals precipitation can be inhibited by adding very small concentrations of green additives whose effectiveness is enhanced in the final polysaccharidic formulations developed for the extraction of the shale gas. In addition, it is possible to tune the effectiveness of these completely safe and degradable additives against scales of different chemical composition simply varying the kind and molecular weight of the additives.

# Chapter 4 Conclusions

In this work we developed two completely safe and eco-compatible model fracturing fluids specific for the shale gas formations found in Europe. These formulations must meet very strict requirements in order to minimize the environmental impact while maintaining optimal operative performances: they must contain no controlled or toxic substances and possess an appropriate viscosity for proppant transport. In addition they must be effective in high pressure, temperature and salinity conditions, and contain specific additives to limit NORM extraction. The first formulation we proposed is a linear gel based on four different green polysaccharides, namely guar gum (GG), sodium hyaluronate (SH), sodium alginate (SA) and hydroxpropylcellulose (HPC). The second is a viscoelastic surfactant-based (VES) fluid, composed by an eco-compatible surfactant, sodium oleate (NaOL), and a inorganic salt, KCl, which is commonly used in fracfluid formulations as clay stabilizer. From rheological and DSC experiments we observed that at ambient conditions these fluids show a very high viscosity (optimal to avoid proppant sedimentation) even at very low concentrations, and a high shear resistance, which prevents viscosity loss upon high shearing during the pumping operations. In particular for the VES formulation the viscosity can be effectively modulated by varying the NaOL/KCl ratio. Moreover, all the fluids exhibit a good thermal stability. These key physico-chemical parameters were then assessed in T, P and salinity conditions which mimic the real operative conditions in shale gas extraction wells. From the experimental results we demonstrated that the viscosity and fluid behaviour of both the polysaccharides and VES formulations can be modified by changing the nature and concentration of simple inorganic salts or using a mixed salt solution which reproduces the high salinity conditions of flowback water in European shale formations. High temperatures (tested up to 120 °C) heavily affect the rheological properties of the formulations, determining a remarkable decrease in the viscosity of the systems. The only exception is represented by HPC, which shows a viscosity increase at high temperature due to its peculiar phase behaviour. Considering the effect of high pressures, the VES formulation shows a strong dependence of the fluid behaviour on P: interestingly, when the pressure is increased up to very high values (390 bar) the formulation viscosity remarkably decreases, and the effect is completely reversible.

From these evidences we demonstrated how the variation in the specific physico-chemical properties of a shale formation (i.e. temperature, pressure and salinity conditions) can be effectively used to modulate the viscosity and the rheological behaviour of the formulations. This approach has a major advantage: no additional chemicals or modifications in the fluid pumping operations are required in order to control the fluid behaviour. Nevertheless, the intrinsic high variability of P, T and salinity conditions within the well may limit the application of our fracfluids. For this reason in the second part of this work we explored two innovative strategies to formulate responsive fluids whose rheological and thermal properties can undergo controlled and reversible changes in response to an external stimulus. We studied the effect of the inclusion of two different additives, Carbon Black (CB) and Azorubine, both on the polysaccharide and VES formulations in order to impart a responsiveness to an applied electrical voltage and UV light respectively. From the experimental results we observed that the addition of CB brings about an increase in the fluid viscosity and a higher threshold for viscosity loss upon high shearing. Moreover the presence of CB determines an improvement in the thermal properties, and imparts a remarkable electrical responsiveness to an external voltage, which results in the formulation phase separation with a consequent potential fluid recovery. The addition of Azorubine to the VES formulation leads to a photo-responsive fluid whose rheological behaviour can be efficiently and reversibly triggered from remote by using UV light. The UV irradiation gives rise to a remarkable increase in the formulation viscosity which reflects a strengthening of the NaOL micellar network induced by the *trans-cis* isomerization of Azorubine. This effect is reversible and mediated by the presence of salts. The obtained results demonstrated that the use of CB and Azorubine is avery promising strategy for the development of innovative formulations based on biocompatible, commercially available materials. These systems can be effectively used during the fracturing operations, where a quick change in the physico-chemical features of the fluid is required but very difficult to be performed.

In the last part of the work we developed two completely safe and environmental friendly approaches that can be successfully used to limit the amount of NORM in the flowback water and/or for the treatment of wastewaters after the extraction of the shale gas. The first method is a physical treatment consisting in the exposure of the fracfluid to a weak static magnetic field before being pumped in the pipelines (Magnetic Water Treatment, MWT). This treatment leads to a suppression of the nucleation and an acceleration of the growth of different scale-forming minerals, like $CaCO_3$, $SrCO_3$, $BaCO_3$ and $CaSO_4$, resulting in the decrease of the number of crystals and an increase of their size. The formation of a smaller amount of larger crystals is enhanced by the combination between the exposure of the fracfluid to an external MF and the high temperature that can be found in the wells during extraction operations. In addition, in the case of $CaCO_3$, the combination of MF and high T promotes the formation of aragonite, which is less densely packed and thus more soluble with respect to the other polymorph of calcium carbonate usually formed at room temperature and in the absence of magnetic treatments. The obtained results show that MWT can be an easy and feasible method to reduce insoluble alkali earth metals scales and thus the likelihood of pipelines obstruction. In addition, the method can be also applied to reduce the problem of NORM extraction since the formation of fewer scales of larger dimensions makes more difficult the extraction of NORM ions in the flowback water at the end of the operations.

The second method is based on the use of green innovative scale inhibitors, in particular polyglutammate (PG) and polyaspartate (PAS) sodium salts, which can potentially replace the non-environmentally friendly polyacrilates in fracfluid formulations. We assessed their effectiveness against the precipitation of both $CaSO_4$ and $SrSO_4$ evaluating their performances in terms of reduction of precipitate and/or control of crystals size. We demonstrated that these additives are effective at very low concentrations and that their performances are even enhanced when added to the polysaccharide-based formulation. All the experiments were conducted both at 25 and 60 °C to assess if the studied molecules retain their effectiveness against scales formation at high temperatures, thus simulating real operative conditions in the extraction wells. The obtained results show that some scale inhibitors exhibit a remarkable tolerance towards high temperature, so they can be effectively used in real applications. Furthermore, we have seen that, depending on the chemical composition of mineral scales, the effectiveness of scale inhibitors can be tuned simply varying the kind and molecular weight of the additive. Good results were obtained also in the case of strontium salts: the use of very small amounts of green antiscalants could be a simple way to limit the formation of mineral scales, also in the presence of radioactive materials, such as radium salts.

# References

[1] A. G. Bell, *Natl. Geogr.* **1917**.

[2] J. J. Siirola, *AIChE J.* **2014**, *60*, 810–819.

[3] World Energy Council 2010, World Energy Council, London, UK, **2010**.

[4] *A Guide to Shale Gas*, Energy Institute, **2015**.

[5] V. Kuuskraa, S. H. Stevens, K. D. Moodhe. *Technically recoverable shale oil and shale gas resources: an assessment of 137 shale formations in 41 countries outside the United States*. US Energy Information Administration, US Department of Energy, 2013**.**

[6] European Commission, **2014**.

[7] G. E. King, Society Of Petroleum Engineers, **2010**.

[8] R. B. Jackson, A. Vengosh, T. H. Darrah, N. R. Warner, A. Down, R. J. Poreda, S. G. Osborn, K. Zhao, J. D. Karr, *Proc. Natl. Acad. Sci.* **2013**, 201221635.

[9] R. Davies, G. Foulger, A. Bindley, P. Styles, *Mar. Pet. Geol.* **2013**, *45*, 171–185.

[10] W.-Y. Kim, *J. Geophys. Res. Solid Earth* **2013**, *118*, 3506–3518.

[11] R. W. Howarth, R. Santoro, A. Ingraffea, *Clim. Change* **2011**, *106*, 679.

[12] L. M. Cathles, L. Brown, M. Taam, A. Hunter, *Clim. Change* **2012**, *113*, 525–535.

[13] L. Gandossi. "An overview of hydraulic fracturing and other formation stimulation technologies for shale gas production." *Eur. Commisison Jt. Res. Cent. Tech Reports* 26347 , **2013** (Update 2015).

[14] F. P. Carvalho, *Food Energy Secur.* **2017**, *6*, 61–77.

[15] American Petroleum Institute, "Hydraulic Fracturing Operations-Well Construction and Integrity Guidelines." *American Petroleum Institute, Report Number HF1*, **2009**.

[16] B. Koppelman, A. Walker, E. Woods. "Shale gas extraction in the UK: a review of hydraulic fracturing." *London: RS-RAENG*, **2012**.

[17] US Environmental Protection Agency, **2011**.

[18] J. B. Clark, *J. Pet. Technol.* **1949**, *1*, 1–8.

[19] J. B. Clark, C. R. Fast, American Petroleum Institute, **1952**.

[20] J. C. Padgett, World Petroleum Congress, **1951**.

[21] W. L. Grossman, Society Of Petroleum Engineers, **1951**.

[22] C. Montgomery, *Eff. Sustain. Hydraul. Fract.* **2013**, DOI 10.5772/56192.

[23] J. L. Gidley, *Recent Advances in Hydraulic Fracturing*, Richardson, Texas: Monograph Series, SPE., **1988**.

[24] R. Caenn, H. C. H. Darley, G. R. Gray, *Composition and Properties of Drilling and Completion Fluids*, Gulf Professional Publishing, **2017**.

[25] R. Barati, J.-T. Liang, *J. Appl. Polym. Sci.* **2014**, *131*, n/a-n/a.

[26] W. a. M. Wanniarachchi, P. G. Ranjith, M. S. A. Perera, *Environ. Earth Sci.* **2017**, *76*, 91.

[27] E. C. Donaldson, W. Alam, N. Begum, in *Hydraul. Fract. Explain.*, Gulf Publishing Company, **2013**, pp. 77–93.

[28] P. C. Harris, *J. Pet. Technol.* **1988**, *40*, 1.277-1.279.

[29] R. Whistler, *Industrial Gums: Polysaccharides and Their Derivatives*, Elsevier, **2012**.

[30] L. Li, G. A. Al-Muntasheri, F. Liang, *Petroleum* **2016**, *2*, 313–323.

[31] N. Goel, S. N. Shah, B. P. Grady, *J. Pet. Sci. Eng.* **2002**, *35*, 59–81.

[32] O. US Environmental Protection Agency, in *US EPA*, **2015**.

[33] G. A. Kahrilas, J. Blotevogel, P. S. Stewart, T. Borch, *Environ. Sci. Technol.* **2015**, *49*, 16–32.

[34] C. G. Struchtemeyer, M. D. Morrison, M. S. Elshahed, *Int. Biodeterior. Biodegrad.* **2012**, *71*, 15–21.

[35] M. S. Al-Anazi, M. Alkhaldi, A. B. Fuseni, K. M. Marshad, Society Of Petroleum Engineers, **2014**.

[36] T. W. Teklu, X. Li, Z. Zhou, N. Alharthy, L. Wang, H. Abass, *J. Pet. Sci. Eng.* **2018**, *162*, 367–377.

[37] K. M. Heyob, J. Blotevogel, M. Brooker, M. V. Evans, J. J. Lenhart, J. Wright, R. Lamendella, T. Borch, P. J. Mouser, *Environ. Sci. Technol.* **2017**, *51*, 13985–13994.

[38] Z. J. Zhou, W. O. Gunter, R. G. Jonasson, Petroleum Society Of Canada, **1995**.

[39] G. A. Al-Muntasheri, Society Of Petroleum Engineers, **2014**.

[40] F. O'Sullivan, S. Paltsev, *Environ. Res. Lett.* **2012**, *7*, 044030.

[41] D. V. S. V. Gupta, P. S. Carman, R. Venugopal, Society Of Petroleum Engineers, **2012**.

[42] S. Kakadjian, J. Thompson, R. Torres, Society Of Petroleum Engineers, **2015**.

[43] "Find out! (What are the risks?): SHIP - Shale Gas Information Plattform," can be found under http://www.shale-gas-information-platform.org/what-are-the-risks/, **n.d.**

[44] A. Vengosh, R. B. Jackson, N. Warner, T. H. Darrah, A. Kondash, *Environ. Sci. Technol.* **2014**, *48*, 8334–8348.

[45] A. Vengosh, N. Warner, R. Jackson, T. Darrah, *Procedia Earth Planet. Sci.* **2013**, *7*, 863–866.

[46] A. W. Nelson, A. W. Knight, D. May, E. S. Eitrheim, M. K. Schultz, in *Hydraul. Fract. Environ. Issues*, American Chemical Society, **2015**, pp. 89–128.

[47] M. F. Attallah, M. M. Hamed, E. M. El Afifi, H. F. Aly, *J. Environ. Radioact.* **2015**, *139*, 78–84.

[48] P. T. Benavides, B. H. Gebreslassie, U. M. Diwekar, *Chem. Eng. Sci.* **2015**, *137*, 977–985.

[49] C. He, T. Zhang, X. Zheng, Y. Li, R. D. Vidic, *Energy Technol.* **2014**, *2*, 968–976.

[50] J. A. López-Comino, S. Cesca, J. Jarosławski, N. Montcoudiol, S. Heimann, T. Dahm, S. Lasocki, A. Gunning, P. Capuano, W. L. Ellsworth, *Sci. Rep.* **2018**, *8*, 8653.

[51] S. Talebi, R. P. Young, L. Vandamme, W. J. McGaughey, American Rock Mechanics Association, **1991**.

[52] A. Yousefzadeh, Q. Li, R. Aguilera, Society Of Petroleum Engineers, **2015**.

[53] J. J. Bommer, H. Crowley, R. Pinho, *J. Seismol.* **2015**, *19*, 623–646.

[54] D. R. Caulton, P. B. Shepson, M. O. L. Cambaliza, D. McCabe, E. Baum, B. H. Stirm, *Environ. Sci. Technol.* **2014**, *48*, 9548–9554.

[55] C. E. Clark, A. J. Burnham, C. B. Harto, R. M. Horner, *Environ. Pract.* **2012**, *14*, 249–261.

[56] Clark, C. E. Burnham, A. J., Harto, C. B., & Horner, R. M., **2012**.

[57] C. F. Mason, L. A. Muehlenbachs, S. M. Olmstead, *Annu. Rev. Resour. Econ.* **2015**, *7*, 269–289.

[58] Gandossi Luca, **2013**.

[59] M. Oblonšek, S. Šostar-Turk, R. Lapasin, *Rheol. Acta* **2003**, *42*, 491–499.

[60] D. Tatini, F. Sarri, P. Maltoni, M. Ambrosi, E. Carretti, B. W. Ninham, P. Lo Nostro, *Carbohydr. Polym.* **2017**, *173*, 344–352.

[61] J. A. Burdick, M. M. Stevens, in *Biomater. Artif. Organs Tissue Eng.* (Eds.: L.L. Hench, J.R. Jones), Woodhead Publishing, **2005**, pp. 107–115.

[62] D. A. Gibbs, E. W. Merrill, K. A. Smith, E. A. Balazs, *Biopolymers* **1968**, *6*, 777–791.

[63] S. Fujii, N. Sasaki, M. Nakata, *J. Polym. Sci. Part B Polym. Phys.* **2001**, *39*, 1976–1986.

[64] J. Fink, *Hydraulic Fracturing Chemicals and Fluids Technology*, Gulf Professional Publishing, **2013**.

[65] I. Gatej, M. Popa, M. Rinaudo, *Biomacromolecules* **2005**, *6*, 61–67.

[66] A. Maleki, A.-L. Kjøniksen, B. Nyström, *Macromol. Symp.* **2008**, *274*, 131–140.

[67] Y. A. Mørch, M. Qi, P. O. M. Gundersen, K. Formo, I. Lacik, G. Skjåk-Bræk, J. Oberholzer, B. L. Strand, *J. Biomed. Mater. Res. A* **2012**, *100*, 2939–2947.

[68] K. Y. Lee, D. J. Mooney, *Prog. Polym. Sci.* **2012**, *37*, 106–126.

[69] A. S. Hoffman, *Adv. Drug Deliv. Rev.* **2012**, *64*, *Supplement*, 18–23.

[70] X. Liu, Y. Zhou, W. Nie, L. Song, P. Chen, *J. Mater. Sci.* **2015**, *50*, 6113–6123.

[71] C. Chang, L. Zhang, *Carbohydr. Polym.* **2011**, *84*, 40–53.

[72] N. V. Thampi, R. P. John, K. Ojha, U. G. Nair, *Ind. Eng. Chem. Res.* **2016**, *55*, 5805–5816.

[73] Q. Cao, L. Yu, L.-Q. Zheng, G.-Z. Li, Y.-H. Ding, J.-H. Xiao, *Colloids Surf. Physicochem. Eng. Asp.* **2008**, *312*, 32–38.

[74] C. A. Dreiss, *Soft Matter* **2007**, *3*, 956–970.

[75] P. A. Hassan, S. R. Raghavan, E. W. Kaler, *Langmuir* **2002**, *18*, 2543–2548.

[76] G. Chauhan, K. Ojha, A. Baruah, G. Chauhan, K. Ojha, A. Baruah, *Braz. J. Chem. Eng.* **2017**, *34*, 241–251.

[77] P. Koshy, V. K. Aswal, M. Venkatesh, P. A. Hassan, *J. Phys. Chem. B* **2011**, *115*, 10817–10825.

[78] C. Flood, C. A. Dreiss, V. Croce, T. Cosgrove, G. Karlsson, *Langmuir* **2005**, *21*, 7646–7652.

[79] S. Khandavalli, J. Hendricks, C. Clasen, J. P. Rothstein, *J. Rheol.* **2016**, *60*, 1331–1346.

[80] J. Huang, S. Zhang, Y. Feng, J. Li, H. Yan, F. He, G. Wang, Y. Liu, L. Wang, *Colloids Surf. Physicochem. Eng. Asp.* **2016**, *500*, 222–229.

[81] G. C. Kalur, S. R. Raghavan, *J. Phys. Chem. B* **2005**, *109*, 8599–8604.

[82] M. Wei, Y. Gao, X. Li, M. J. Serpe, *Polym. Chem.* **2016**, *8*, 127–143.

[83] S. Guragain, B. P. Bastakoti, V. Malgras, K. Nakashima, Y. Yamauchi, *Chem. – Eur. J.* **n.d.**, *21*, 13164–13174.

[84] P. J. F. Harris, *Crit. Rev. Solid State Mater. Sci.* **2005**, *30*, 235–253.

[85] Y. Quan, Q. Liu, S. Zhang, S. Zhang, *Appl. Surf. Sci.* **2018**, *445*, 335–341.

[86] M. Liu, A. R. Horrocks, *Polym. Degrad. Stab.* **2002**, *75*, 485–499.

[87] J. Zhao, K. Dai, C. Liu, G. Zheng, B. Wang, C. Liu, J. Chen, C. Shen, *Compos. Part Appl. Sci. Manuf.* **2013**, *48*, 129–136.

[88] G. Wypych, *PVC Degradation and Stabilization*, Elsevier, **2015**.

[89] H. S. Katz, J. V. Mileski, *Handbook Of Fillers For Plastics*, Springer Science & Business Media, **1987**.

[90] Q. Cao, Y. Song, Y. Tan, Q. Zheng, *Carbon* **2010**, *48*, 4268–4275.

[91] J. König, in *Colour Addit. Foods Beverages* (Ed.: M.J. Scotter), Woodhead Publishing, Oxford, **2015**, pp. 35–60.

[92] H. M. D. Bandara, S. C. Burdette, *Chem. Soc. Rev.* **2012**, *41*, 1809–1825.

[93] R. Dąbrowski, P. Kula, J. Herman, *Crystals* **2013**, *3*, 443–482.

[94] D. Statman, I. Jánossy, *J. Chem. Phys.* **2003**, *118*, 3222–3232.

[95] H. Rau, in *Photochromism* (Eds.: H. Dürr, H. Bouas-Laurent), Elsevier Science, Amsterdam, **2003**, pp. 165–192.

[96] Y. Lu, T. Zhou, Q. Fan, J. Dong, X. Li, *J. Colloid Interface Sci.* **2013**, *412*, 107–111.

[97] H. Oh, A. M. Ketner, R. Heymann, E. Kesselman, D. Danino, D. E. Falvey, S. R. Raghavan, *Soft Matter* **2013**, *9*, 5025–5033.

[98] Y. Lin, X. Cheng, Y. Qiao, C. Yu, Z. Li, Y. Yan, J. Huang, *Soft Matter* **2010**, *6*, 902–908.

[99] D. Wang, R. Dong, P. Long, J. Hao, *Soft Matter* **2011**, *7*, 10713–10719.

[100] R. Kumar, S. R. Raghavan, *Soft Matter* **2009**, *5*, 797–803.

[101] J. Li, M. Zhao, H. Zhou, H. Gao, L. Zheng, *Soft Matter* **2012**, *8*, 7858–7864.

[102] H. Sakai, S. Taki, K. Tsuchiya, A. Matsumura, K. Sakai, M. Abe, *Chem. Lett.* **2012**, *41*, 247–248.

[103] N. S. Zaidi, J. Sohaili, K. Muda, M. Sillanpää, *Sep. Purif. Rev.* **2014**, *43*, 206–240.

[104] K. W. Busch, M. A. Busch, *Desalination* **1997**, *109*, 131–148.

[105] K. Higashitani, J. Oshitani, *J. Colloid Interface Sci.* **1998**, *204*, 363–368.

[106] D. J. K. Ross, R. M. Bustin, *AAPG Bull.* **2008**, *92*, 87–125.

[107] D. Hasson, H. Shemer, A. Sher, *Ind. Eng. Chem. Res.* **2011**, *50*, 7601–7607.

[108] I. Couillet, T. Hughes, *Aqueous Fracturing Fluid*, **2003**, CA2471340A1.

[109] R. M. Kelly, S. A. Khan, P. Leduc, A. Tayal, R. K. Prud'homme, *Methods and Compositions for Fracturing Subterranean Formations*, **1995**, US5421412A.

[110] Q. Jiang, J. Rentschler, R. Perrone, K. Liu, *J. Membr. Sci.* **2013**, *431*, 55–61.

[111] M. M. Michel, L. Reczek, M. Granops, P. Rudnicki, A. Piech, *Desalination Water Treat.* **2016**, *57*, 10222–10231.

[112] A. Carrero-Parreño, V. C. Onishi, R. Salcedo-Díaz, R. Ruiz-Femenia, E. S. Fraga, J. A. Caballero, J. A. Reyes-Labarta, *Ind. Eng. Chem. Res.* **2017**, *56*, 4386–4398.

[113] D. Das, S. Panigrahi, P. K. Senapati, P. K. Misra, *Energy Fuels* **2009**, *23*, 3217–3226.

[114] D. Das, S. Panigrahi, P. K. Misra, A. Nayak, *Energy Fuels* **2008**, *22*, 1865–1872.

[115] K. Higashitani, A. Kage, S. Katamura, K. Imai, S. Hatade, *J. Colloid Interface Sci.* **1993**, *156*, 90–95.

[116] L. Hołysz, M. Chibowski, E. Chibowski, *Colloids Surf. Physicochem. Eng. Asp.* **2002**, *208*, 231–240.

[117] R. A. Barrett, S. A. Parsons, *Water Res.* **1998**, *32*, 609–612.

[118] J. Oshitani, D. Yamada, M. Miyahara, K. Higashitani, *J. Colloid Interface Sci.* **1999**, *210*, 1–7.

[119] H. A. Barnes, J. F. Hutton, K. Walters, *An Introduction to Rheology*, Elsevier, **1989**.

[120] T. Osswald, N. Rudolph, in *Underst. Plast. Rheol.*, Hanser, **2015**, pp. I–XI.

[121] M. P. Escudier, R. J. Poole, F. Presti, C. Dales, C. Nouar, C. Desaubry, L. Graham, L. Pullum, *J. Non-Newton. Fluid Mech.* **2005**, *127*, 143–155.

[122] W. Lertwimolnun, B. Vergnes, *Polym. Eng. Sci.* **2006**, *46*, 314–323.

[123] S. J. Haward, A. Jaishankar, M. S. N. Oliveira, M. A. Alves, G. H. McKinley, *Biomicrofluidics* **2013**, *7*, DOI 10.1063/1.4816708.

[124] M. P. Escudier, I. W. Gouldson, A. S. Pereira, F. T. Pinho, R. J. Poole, *J. Non-Newton. Fluid Mech.* **2001**, *97*, 99–124.

[125] M. C. García, M. C. Alfaro, N. Calero, J. Muñoz, *Carbohydr. Polym.* **2014**, *105*, 177–183.

[126] P. J. Carreau, *Trans. Soc. Rheol.* **1972**, *16*, 99–127.

[127] K. Yasuda, R. C. Armstrong, R. E. Cohen, *Rheol. Acta* **1981**, *20*, 163–178.

[128] M. M. Cross, *J. Colloid Sci.* **1965**, *20*, 417–437.

[129] F. E. Antunes, L. Coppola, D. Gaudio, I. Nicotera, C. Oliviero, *Colloids Surf. Physicochem. Eng. Asp.* **2007**, *297*, 95–104.

[130] Z. Mitrinova, S. Tcholakova, N. Denkov, *Colloids Surf. Physicochem. Eng. Asp.* **2018**, *537*, 173–184.

[131] D. Tatini, P. Tempesti, F. Ridi, E. Fratini, M. Bonini, P. Baglioni, *Colloids Surf. B Biointerfaces* **2015**, *135*, 400–407.

[132] T. N. Blanton, T. C. Huang, H. Toraya, C. R. Hubbard, S. B. Robie, D. Louër, H. E. Göbel, G. Will, R. Gilles, T. Raftery, *Powder Diffr.* **1995**, *10*, 91–95.

[133] E. R. Morris, *Carbohydr. Polym.* **1990**, *13*, 85–96.

[134] E. R. Morris, A. N. Cutler, S. B. Ross-Murphy, D. A. Rees, J. Price, *Carbohydr. Polym.* **1981**, *1*, 5–21.

[135] B. A. Harper, S. Barbut, L.-T. Lim, M. F. Marcone, *J. Food Sci.* **n.d.**, *79*, E562–E567.

[136] A. D. Patel, Society Of Petroleum Engineers, **2009**.

[137] J. Parnell, C. Brolly, S. Spinks, S. Bowden, *Appl. Geochem.* **2016**, *66*, 82–87.

[138] T. Prasenjit, G. S. Borgohain, *Int. J. Res. Eng. Appl. Sci.* **2015**, *5*, 16–38.

[139] B. A. Schubert, E. W. Kaler, N. J. Wagner, *Langmuir* **2003**, *19*, 4079–4089.

[140] T. Shikata, H. Hirata, T. Kotaka, *Langmuir* **1987**, *3*, 1081–1086.

[141] T. Shikata, H. Hirata, T. Kotaka, *Langmuir* **1988**, *4*, 354–359.

[142] N. Garti, A. Aserin, S. Ezrahi, I. Tiunova, G. Berkovic, *J. Colloid Interface Sci.* **1996**, *178*, 60–68.

[143] M. Ambrosi, P. L. Nostro, L. Fratoni, L. Dei, B. W. Ninham, S. Palma, R. H. Manzo, D. Allemandi, P. Baglioni, *Phys. Chem. Chem. Phys.* **2004**, *6*, 1401–1407.

[144] P. C. Schulz, *J. Therm. Anal. Calorim.* **1998**, *51*, 135–149.

[145] M. Fernandez-Tarrio, C. Alvarez-Lorenzo, A. Concheiro, *J. Therm. Anal. Calorim.* **2007**, *87*, 171–178.

[146] P. C. Schulz, J. E. Puig, *Colloids Surf. Physicochem. Eng. Asp.* **1993**, *71*, 83–90.

[147] N. Garti, *Thermal Behaviour of Dispersed Systems*, CRC Press, **2000**.

[148] K. Nakamura, T. Hatakeyama, H. Hatakeyama, *Polymer* **1983**, *24*, 871–876.

[149] D. Senatra, G. Gabrielli, G. G. T. Guarini, *EPL Europhys. Lett.* **1986**, *2*, 455.

[150] Chaplin, Martin, "Polysaccharide hydration," can be found under http://www1.lsbu.ac.uk/water/polysaccharide_hydration.html, **n.d.**

[151] L. Guan, H. Xu, D. Huang, *J. Polym. Res.* **2010**, *18*, 681–689.

[152] T. Hatakeyama, M. Tanaka, H. Hatakeyama, *J. Biomater. Sci. Polym. Ed.* **2010**, *21*, 1865–1875.

[153] H. Hoffmann, in *Struct. Flow Surfactant Solut.*, American Chemical Society, **1994**, pp. 2–31.

[154] S. J. Candau, E. Hirsch, R. Zana, *J. Colloid Interface Sci.* **1985**, *105*, 521–528.

[155] T. M. Clausen, P. K. Vinson, J. R. Minter, H. T. Davis, Y. Talmon, W. G. Miller, *J. Phys. Chem.* **1992**, *96*, 474–484.

[156] L. J. Magid, Z. Han, Z. Li, P. D. Butler, *Langmuir* **2000**, *16*, 149–156.

[157] R. D. Koehler, S. R. Raghavan, E. W. Kaler, *J. Phys. Chem. B* **2000**, *104*, 11035–11044.

[158] M. In, G. G. Warr, R. Zana, *Phys. Rev. Lett.* **1999**, *83*, 2278–2281.

[159] A. Parker, W. Fieber, *Soft Matter* **2012**, *9*, 1203–1213.

[160] C. Rodriguez-Abreu, K. Aramaki, Y. Tanaka, M. A. Lopez-Quintela, M. Ishitobi, H. Kunieda, *J. Colloid Interface Sci.* **2005**, *291*, 560–569.

[161] N. Naito, D. P. Acharya, J. Tanimura, H. Kunieda, *J. Oleo Sci.* **2004**, *53*, 599–606.

[162] R. G. Shrestha, C. Rodriguez-Abreu, K. Aramaki, *J. Oleo Sci.* **2009**, *58*, 243–254.

[163] D. Balzer, S. Varwig, M. Weihrauch, *Colloids Surf. Physicochem. Eng. Asp.* **1995**, *99*, 233–246.

[164] K. Penfield, *Int. J. Cosmet. Sci.* **2005**, *27*, 300–300.

[165] H. Rehage, H. Hoffmann, *Mol. Phys.* **1991**, *74*, 933–973.

[166] S. J. Candau, R. Oda, *Colloids Surf. Physicochem. Eng. Asp.* **2001**, *183–185*, 5–14.

[167] P. L. Nostro, S. Murgia, M. Lagi, E. Fratini, G. Karlsson, M. Almgren, M. Monduzzi, B. W. Ninham, P. Baglioni, *J. Phys. Chem. B* **2008**, *112*, 12625–12634.

[168] M. Buchanan, M. Atakhorrami, J. F. Palierne, F. C. MacKintosh, C. F. Schmidt, *Phys. Rev. E* **2005**, *72*, 011504.

[169] H. Rehage, H. Hoffmann, *J. Phys. Chem.* **1988**, *92*, 4712–4719.

[170] J. Honerkamp, J. Weese, *Rheol. Acta* **1993**, *32*, 65–73.

[171] E. Carretti, C. Matarrese, E. Fratini, P. Baglioni, L. Dei, *Soft Matter* **2014**, *10*, 4443–4450.

[172] S. Vicini, M. Mauri, J. Wichert, M. Castellano, *Polym. Eng. Sci.* **2017**, *57*, 531–536.

[173] P. Sikorski, F. Mo, G. Skjåk-Bræk, B. T. Stokke, *Biomacromolecules* **2007**, *8*, 2098–2103.

[174] R. Seale, E. R. Morris, D. A. Rees, *Carbohydr. Res.* **1982**, *110*, 101–112.

[175] C. Karakasyan, M. Legros, S. Lack, F. Brunel, P. Maingault, G. Ducouret, D. Hourdet, *Biomacromolecules* **2010**, *11*, 2966–2975.

[176] C. Branca, S. Maccarrone, S. Magazù, G. Maisano, S. M. Bennington, J. Taylor, *J. Chem. Phys.* **2005**, *122*, 174513.

[177] A. Lerbret, P. Bordat, F. Affouard, Y. Guinet, A. Hédoux, L. Paccou, D. Prévost, M. Descamps, *Carbohydr. Res.* **2005**, *340*, 881–887.

[178] N. K. Jain, I. Roy, *Protein Sci. Publ. Protein Soc.* **2009**, *18*, 24–36.

[179] H. Kawai, M. Sakurai, Y. Inoue, R. Chûjô, S. Kobayashi, *Cryobiology* **1992**, *29*, 599–606.

[180] S. Magazù, P. Migliardo, A. M. Musolino, M. T. Sciortino, *J. Phys. Chem. B* **1997**, *101*, 2348–2351.

[181] E. Gura, M. Hückel, P.-J. Müller, *Polym. Degrad. Stab.* **1998**, *59*, 297–302.

[182] A. I. De Andres-Santos, A. Velasco-Martin, E. Hernández-Velasco, J. Martín-Gil, F. J. Martín-Gil, *Thermochim. Acta* **1994**, *242*, 153–160.

[183] W. Yin, H. Zhang, L. Huang, Katsuyoshi Nishinari, *Carbohydr. Polym.* **2008**, *74*, 68–78.

[184] R. A. Curtis, C. Steinbrecher, M. Heinemann, H. W. Blanch, J. M. Prausnitz, *Biophys. Chem.* **2002**, *98*, 249–265.

[185] L. López-Arenas, S. Solís-Mendiola, J. Padilla-Zúñiga, A. Hernández-Arana, *Biochim. Biophys. Acta BBA - Proteins Proteomics* **2006**, *1764*, 1260–1267.

[186] T. Arakawa, S. N. Timasheff, *Biochemistry* **1982**, *21*, 6545–6552.

[187] K. D. Collins, *Methods* **2004**, *34*, 300–311.

[188] P. Lo Nostro, B. W. Ninham, *Chem. Rev.* **2012**, *112*, 2286–2322.

[189] C. G. Winkworth-Smith, W. MacNaughtan, T. J. Foster, *Carbohydr. Polym.* **2016**, *149*, 231–241.

[190] T. Hatakeyama, S. Naoi, H. Hatakeyama, *Thermochim. Acta* **2004**, *416*, 121–127.

[191] K. Nakamura, T. Hatakeyama, H. Hatakeyama, *Seni Gakkaishi* **1991**, *47*, 421–423.

[192] B. E. Hall, C. A. Szemenyei, D. V. S. Gupta, *Breaker System for Aqueous Fluids Containing Xanthan Gums*, **1991**, US5054552 A.

[193] E. A. SCHNOOR, D. SINGH, A. G. RUSSELL, *Aldehydes as a Catalyst for an Oxidative Breaker*, **2016**, WO2016099502 A1.

[194] N. C. Schultheiss, *Multi-Component Materials for Breaker Activity Control*, **2015**, WO2015020670 A1.

[195] I. M. Abdulagatov, A. A. Zeinalova, N. D. Azizov, *J. Chem. Eng. Data* **2004**, *49*, 1444–1450.

[196] D. E. Goldsack, R. C. Franchetto, *Can. J. Chem.* **1978**, *56*, 1442–1450.

[197] M. V. Galmarini, R. Baeza, V. Sanchez, M. C. Zamora, J. Chirife, *LWT - Food Sci. Technol.* **2010**, *44*, 186–190.

[198] G. R. Hood, *Physics* **1933**, *4*, 211–214.

[199] G. J. Janz, B. G. Oliver, G. R. Lakshminarayanan, G. E. Mayer, *J. Phys. Chem.* **1970**, *74*, 1285–1289.

[200] Y. Marcus, *J. Chem. Soc. Faraday Trans.* **1991**, *87*, 2995–2999.

[201] F. L. Rodkey, *Clin. Chem.* **1966**, *12*, 517–518.

[202] E. Hosseini, H. R. Mozafari, M. Hojjatoleslamy, E. Rousta, E. Hosseini, H. R. Mozafari, M. Hojjatoleslamy, E. Rousta, *Food Sci. Technol.* **2017**, *37*, 437–443.

[203] X. Lu, Z. Hu, J. Gao, *Macromolecules* **2000**, *33*, 8698–8702.

[204] Mithra K., Santripti Khandai, Sidhartha S. Jena, *AIP Conf. Proc.* **2016**, *1728*, 020220.

[205] Y. Nishio, R. Chiba, Y. Miyashita, K. Oshima, T. Miyajima, N. Kimura, H. Suzuki, *Polym. J.* **2002**, *34*, 149–157.

[206] Roger Olsen, Carlos Claros, Lorraine Gaston, Dawn Keating, Henning Moe, *UGEE Final Report 4: Impacts and Mitigation Measures*, Environmental Protection Agency (EPA), Ireland, **2016**.

[207] A. M. Pegg, in *Nat. Food Addit. Ingred. Flavour.* (Eds.: D. Baines, R. Seal), Woodhead Publishing, **2012**, pp. 175–196.

[208] G. A. Kahrilas, J. Blotevogel, E. R. Corrin, T. Borch, *Environ. Sci. Technol.* **2016**, *50*, 11414–11423.

[209] T. L. Tasker, P. K. Piotrowski, F. L. Dorman, W. D. Burgos, *Environ. Eng. Sci.* **2016**, *33*, 753–765.

[210] Hobart M. King, "Marcellus Shale - Appalachian Basin Natural Gas Play. A resource that moved from 'marginal' to 'spectacular' as a result of new drilling technology.," can be found under https://geology.com/articles/marcellus-shale.shtml, **retrieved on 25/10/2018.**

[211] D. L. Shaffer, L. H. Arias Chavez, M. Ben-Sasson, S. Romero-Vargas Castrillón, N. Y. Yip, M. Elimelech, *Environ. Sci. Technol.* **2013**, *47*, 9569–9583.

[212] A. L. Fauchille, A. P. van den Eijnden, L. Ma, M. Chandler, K. G. Taylor, K. Madi, P. D. Lee, E. Rutter, *Mar. Pet. Geol.* **2018**, *92*, 109–127.

[213] E. R. Morris, D. A. Rees, G. Young, M. D. Walkinshaw, A. Darke, *J. Mol. Biol.* **1977**, *110*, 1–16.

[214] G. Holzwarth, *Biochemistry* **1976**, *15*, 4333–4339.

[215] D. Filip, D. Macocinschi, E. Paslaru, B. S. Munteanu, R. P. Dumitriu, M. Lungu, C. Vasile, *J. Nanoparticle Res.* **2014**, *16*, 2710.

[216] H. D. Chandler, *J. Colloid Interface Sci.* **2013**, *409*, 98–103.

[217] D. Angelescu, A. Khan, H. Caldararu, *Langmuir* **2003**, *19*, 9155–9161.

[218] D. A. Kuryashov, O. E. Philippova, V. S. Molchanov, N. Y. Bashkirtseva, I. N. Diyarov, *Colloid J.* **2010**, *72*, 230–235.

[219] J. Desbrieres, *Biomacromolecules* **2002**, *3*, 342–349.

[220] J.-C. Huang, *Adv. Polym. Technol.* **2002**, *21*, 299–313.

[221] D. M. Bigg, *J. Rheol.* **1984**, *28*, 501–516.

[222] F. Liang, B. Chen, "A Review on Biomedical Applications of Single-Walled Carbon Nanotubes", **2010**.

[223] F. Cataldo, T. da Ros, *Medicinal Chemistry and Pharmacological Potential of Fullerenes and Carbon Nanotubes*, Springer Science & Business Media, **2008**.

[224] F. Tiarks, K. Landfester, M. Antonietti, *Langmuir* **2001**, *17*, 5775–5780.

[225] F. Tiarks, K. Landfester, M. Antonietti, *Macromol. Chem. Phys.* **2001**, *202*, 51–60.

[226] H. Sis, M. Birinci, *Colloids Surf. Physicochem. Eng. Asp.* **2009**, *341*, 60–67.

[227] W. Wang, S. Efrima, O. Regev, *Langmuir* **1998**, *14*, 602–610.

[228] S.-Y. Yang, W.-N. Lin, Y.-L. Huang, H.-W. Tien, J.-Y. Wang, C.-C. M. Ma, S.-M. Li, Y.-S. Wang, *Carbon* **2011**, *49*, 793–803.

[229] C. L Barrie, P. C. Griffiths, R. J. Abbott, I. Grillo, E. Kudryashov, C. Smyth, *J. Colloid Interface Sci.* **2004**, *272*, 210–217.

[230] B. Nasri-Nasrabadi, A. Kaynak, Z. Komeily Nia, J. Li, A. Zolfagharian, S. Adams, A. Z. Kouzani, *Chem. Eng. J.* **2018**, *334*, 1775–1780.

[231] C. Alvarez-Lorenzo, B. Blanco-Fernandez, A. M. Puga, A. Concheiro, *Adv. Drug Deliv. Rev.* **2013**, *65*, 1148–1171.

[232] S. Kennedy, S. Bencherif, D. Norton, L. Weinstock, M. Mehta, D. Mooney, *Adv. Healthc. Mater.* **2014**, *3*, 500–507.

[233] E. K. Sichel, J. I. Gittleman, P. Sheng, *Phys. Rev. B* **1978**, *18*, 5712–5716.

[234] J.-P. Reboul, G. Moussalli, *Int. J. Polym. Mater. Polym. Biomater.* **1976**, *5*, 133–146.

[235] I. Balberg, *Carbon* **2002**, *40*, 139–143.

[236] F. Carmona, C. Mouney, *J. Mater. Sci.* **1992**, *27*, 1322–1326.

[237] T. Sochi, *Polymer* **2010**, *51*, 5007–5023.

[238] M. Samuel, D. Polson, D. Graham, W. Kordziel, T. Waite, G. Waters, P. S. Vinod, D. Fu, R. Downey, Society Of Petroleum Engineers, **2000**.

[239] C. Moitzi, N. Freiberger, O. Glatter, *J. Phys. Chem. B* **2005**, *109*, 16161–16168.

[240] M. F. Nazar, S. Murtaza, B. Ijaz, M. Asfaq, M. A. Mohsin, *J. Dispers. Sci. Technol.* **2015**, *36*, 18–27.

[241] S. A. Rogers, M. A. Calabrese, N. J. Wagner, *Curr. Opin. Colloid Interface Sci.* **2014**, *19*, 530–535.

[242] T. Ogino, T. Suzuki, K. Sawada, *Geochim. Cosmochim. Acta* **1987**, *51*, 2757–2767.

[243] A. V. García, K. Thomsen, E. H. Stenby, *Geothermics* **2006**, *35*, 239–284.

[244] H. Füredi-Milhofer, S. Sarig, *Prog. Cryst. Growth Charact. Mater.* **1996**, *32*, 45–74.

[245] Z. Amjad, *J. Colloid Interface Sci.* **1988**, *123*, 523–536.

[246] R. J. Ross, K. C. Low, J. E. Shannon, *Mater. Perform.* **1997**, *36*.

[247] X. Li, B. Gao, Q. Yue, D. Ma, H. Rong, P. Zhao, P. Teng, *J. Environ. Sci.* **2015**, *29*, 124–130.

# Appendix A - List of Papers

PAPER I - D. Tatini, F. Sarri, P. Maltoni, M. Ambrosi, E. Carretti, B. W. Ninham, P. Lo Nostro. Specific ion effects in polysaccharide dispersions. *Carbohydrate Polymers*, **2013**, *173*, 344–352.

PAPER II - F. Sarri, D. Tatini, M. Raudino, M. Ambrosi, E. Carretti, P. Lo Nostro. Carbon Black-Induced Electrical Responsiveness in Viscoelastic Formulations. *In preparation*, **2018**.

PAPER III - D. Tatini, F. Sarri, A. Dalle Vaglie, M. Raudino, M. Ambrosi, E. Carretti, , B. W. Ninham, P. Lo Nostro. Light-modulated rheological properties in green innovative formulations. *In preparation*, **2018**.

PAPER IV - M. Raudino F. Sarri, D. Tatini, M. Ambrosi, G. D. Aloisi, W. Ninham, L. Dei, P. Lo Nostro. The effect of temperature and magnetic field on the precipitation of insoluble salts of alkaline earth metals. *Submitted*, **2018**.

Carbohydrate Polymers 173 (2017) 344–352

Contents lists available at ScienceDirect

Carbohydrate Polymers

journal homepage: www.elsevier.com/locate/carbpol

# Specific ion effects in polysaccharide dispersions

Duccio Tatini[a], Filippo Sarri[a], Piefrancesco Maltoni[a], Moira Ambrosi[a], Emiliano Carretti[a], Barry W. Ninham[a,b], Pierandrea Lo Nostro[a,*]

[a] Department of Chemistry "Ugo Schiff" and CSGI, University of Florence, 50019 Sesto Fiorentino, Firenze, Italy
[b] Department of Applied Mathematics, Research School of Physical Sciences and Engineering, Australian National University, Canberra, ACT 2600, Australia

ARTICLE INFO

*Article history:*
Received 17 March 2017
Received in revised form 22 May 2017
Accepted 24 May 2017
Available online 27 May 2017

*Keywords:*
Polysaccharide(s)
Guar gum
Sodium hyaluronate
Specific ion effect
Viscosity
Thermal properties

ABSTRACT

The specific effects induced by some strong electrolytes or neutral co-solutes on aqueous mixtures of guar gum (GG), sodium alginate (SA) and sodium hyaluronate (SH) were studied through rheology and DSC experiments. The results are discussed in terms of changes in the polymer conformation, structure of the network and hydration properties. This study is also aimed at controlling the viscosity of the aqueous mixtures for application in green formulations to be used as fracturing fluids for shale gas extraction plants.

## 1. Introduction

Hofmeister, or specific ion effects consist in changes induced in a measurable phenomenon or physico-chemical property by the addition of a specific salt. These effects usually take place at moderately high concentrations, e.g. above 10 mM. They occur in a large variety of systems and practically in all realms of nature: in bulk solutions, aqueous and non-aqueous systems, at interfaces and in self-assembled structures (Lo Nostro & Ninham, 2012; Lo Nostro & Ninham, 2016).

Compared to the pristine sequence found by Hofmeister in his studies on the precipitation of albumin dispersions, other systems may exhibit a different order. However, in general it is observed that as the ion changes, the measured properties are affected. Recently it has been found that the charge and polarity of the involved species and surfaces are crucial factors in determining whether the effectiveness of the salts follows the direct or reverse Hofmeister series (Schwierz, Horinek, Sivan, & Netz, 2016). In a dilute regime, electrostatics dominates the picture of ionic interactions, and Coulomb potential describes the behavior of the solution, with a substantial correct prediction of the ionic activity coefficient. However, electrostatic interactions are non ion-specific, while the surface charge density depends on the ion size. At high salt concentrations, non-electrostatic forces come into play, Coulomb interactions are screened, and ion specificity emerges.

The rheology and thermal behaviors of solutions and dispersions of biopolymers such as polysaccharides are examples of specific ion effects, in fact such features can be tuned by the proper choice of electrolytes at a suitable concentration. This topic has been fully investigated in the literature (see Hatakeyama, Tanaka, & Hatakeyama, 2010; Guan, Xu, & Huang, 2010; Kupská, Lapcík, Lapcíková, Záková, & Juríková, 2014, and references therein). One of the more interesting insights is the mechanism through which such effects take place. Norton studied the disorder-order transition and the helix–helix aggregation in κ-carrageenan in the presence of different salts, and concluded that these phenomena depend on the salt-induced modification of the solvent quality of water, and not on direct salt-polyelectrolyte interactions (Norton, Morris, & Rees, 1984). Along the same line, Xu explained the effect of salts on the sol-gel transition of methylcellulose in terms of the ability of individual ions to change water structure and of the strength of the interactions between water molecules (Xu, Wang, Tam, & Li, 2004).

As a final point regarding the application of the above theoretical model to salting-in and salting-out phenomena, we return to the fact that, in general, the surface of a macromolecule exposes sites

---

* Corresponding author at: Department of Chemistry Ugo Schiff, Via della Lastruccia 3, 50019 Sesto Fiorentino, Firenze, Italy.

*E-mail addresses:* duccio.tatini@unifi.it (D. Tatini), filippo.sarri@unifi.it (F. Sarri), pierfrancesco.maltoni@stud.unifi.it (P. Maltoni), moira.ambrosi@unifi.it (M. Ambrosi), emiliano.carretti@unifi.it (E. Carretti), barry.ninham@anu.edu.au (B.W. Ninham), pierandrea.lonostro@unifi.it (P. Lo Nostro).

http://dx.doi.org/10.1016/j.carbpol.2017.05.078
0144-8617/

(functional groups) which differ in their relative affinities to the components of the mixed solvent. (Piculell & Nilsson, 1989).

A more relevant study is that by Yin on the gelation of konjac glucomannan (KGM) and in particular on its rheological behavior in the presence of different salts. The increase in the viscosity upon addition of salting-out salts is explained in terms of (i) the modification of the water structure or (ii) by the change in the interactions between the ions and specific sites on the polymer chains (Yin, Zhang, Huang, & Nishinari, 2008). Finally, Singh investigated the gelling behaviour of agarose with $Na_2SO_4$, and found that the release of water from the gel is due to the water withdrawing action of sulfate ions (Singh, Meena, & Kumar, 2009).

In the present contribution we report a study on the effect induced by some strong electrolytes and neutral cosolutes on the rheology and thermal behavior of some polysaccharide aqueous dispersions and solutions. The results are discussed in terms of the Hofmeister series, ion-polymer and polymer-water interactions.

This investigation is relevant for the application of polysaccharides in green formulations for fracturing fluids used in shale gas extraction (Barati & Liang, 2014; Kelly, Khan, Leduc, Tayal, & Prud'homme, 2001; Legemah, Qu, Sun, Beall, & Zhou, 2013).

The basic ingredients that are commonly used in fracturing fluids comprise water, more or less chemically modified polysaccharides as gelling agents (guar gum, cellulose, xanthan gum and their derivatives), a large number of salts as formulation stabilizers or clay control agents, acids (e.g. HCl, $H_3BO_3$ and citric acid) and bases to adjust the pH, cross-linker initiators (potassium borate or metaborate, complexes of zirconium or titanium with organic chelators), naphtha derivatives and surfactants (Barati & Liang, 2014; Gandossi & Von Estorff, 2015; Li, Al-Muntasheri, & Liang, 2016; Montgomery, 2013).

Several scientists have discussed a number of possible environmental risks related to the production of shale gas. These include the accidental release of fracturing fluids, leaks of hydrocarbons, the uptake of Naturally Occurring Radioactive Materials (NORM), the introduction of foreign bacterial strains to the subsurface, and induced micro-seismicity (Arthur, Bohm, Coughlin, Layne, & Cornue, 2009; Holloway & Rudd, 2013, Chapter 11; Osborn, Vengosh, Warner, & Jackson, 2011; Vengosh, Jackson, Warner, Darrah, & Kondash, 2014). To limit some of these risks, we focus on "greener" formulations, which employ biocompatible and non-toxic ingredients.

## 2. Hypotheses

This study is aimed at demonstrating that the thermal and rheological properties of aqueous mixtures containing guar gum, sodium alginate and sodium hyaluronate can be significantly modified by using strong electrolytes, and that salt specific effects show up, following the Hofmeister series. The ions exhibit particular effects related to their structure and particularly to their capability to interfere with the polymer hydrogen bonding network and with the solvent properties of water. The results support our effort to formulate green alternatives to the currently used hydraulic fracturing fluids.

## 3. Experimental

### 3.1. Materials

All chemicals were reagent grade (≥99%) and used as received. NaF, NaI, NaSCN, $NaClO_4 \cdot H_2O$, $NaH_2PO_4$ were purchased from Fluka (Milan, Italy). NaCl, NaBr, $Na_2SO_4$, $Na_3PO_4 \cdot 3H_2O$, $Na_2HPO_4 \cdot 7H_2O$, trehalose and sodium alginate (average molecular mass 240 kDa; mannuronate/guluronate ratio 0.44) were supplied by Sigma-Aldrich (Milan, Italy). Urea was purchased from Riedel de Haen (Germany). Guar gum (average molecular mass 2000 kDa) was supplied by Lamberti S.p.A. (Milan, Italy); high molecular weight (1800–2000 kDa) sodium hyaluronate was purchased from Stanford Chemicals Company (Fairbanks, CA). All solutions and dispersions were prepared with bidistilled Milli-Q water (resistivity>18 MΩ·cm at 25 °C).

### 3.2. Sample preparation

In general gelling agents for fracturing formulations are used up to 1% w/w (Couillet & Hughes, 2008; Kelly et al., 2001). The addition of a crosslinker lowers the concentration to 0.1–0.5% (Goel, Shah, & Grady, 2002). We chose a polysaccharide concentration of 1% to avoid the addition of a crosslinker; in this way we can focus exclusively on the effect of the salt on the polymer chains.

GG, SA and SH 1% w/w water mixtures were prepared by slowly adding a weighted amount of polysaccharide powder to water under constant stirring at room temperature. In these conditions complete dissolution occurs in about one hour for all the investigated biopolymers. The samples containing the different salts or co-solutes were prepared following the same procedure, replacing water with 0.5 M aqueous solutions of the salts or neutral co-solutes.

### 3.3. Rheology

Rheological measurements were performed on a Paar Physica UDS 200 rheometer working in the controlled shear-stress mode. For all samples a plate–plate geometry (diameter, 2.5 cm; gap, 300 μm) was used. Under these conditions the total amount of the sample in the cell was about 0.4 mL. All measurements were performed at 25.0 °C (Peltier control system). For each sample the flow curve was acquired in a torque range between $10^{-3}$ and 2000 mN m, after a 15 min soaking time to equilibrate at the set temperature.

### 3.4. Thermal properties

Differential Scanning Calorimetry (DSC) was performed by means of a DSC-Q2000 by TA Instruments (Philadelphia, PA). The samples were first cooled from 20° to −60 °C at 10 °C/min, then heated up to 50 °C at 5 °C/min. Measurements were conducted in $N_2$ atmosphere, with a flow rate of 50 mL/min. For the samples prepared with NaF and $Na_2HPO_4$ the deconvolution of endothermic peaks was performed by means of the Igor Pro 6.36 software, using a summation of exponentially modified Gaussian (EMG) functions (Tatini et al., 2015). The single EMG function is defined as:

$$f(T) = \sqrt{\frac{\pi}{2}}\frac{hw}{|s|}\exp\left[\frac{w^2}{2s^2}\left(\frac{T_0 - T}{s}\right)\right]\operatorname{erf}\left[\frac{T_0 - T}{2\left(w + \frac{w}{|s|}\right)}\right] \quad (1)$$

where $h$ is the height, $T_0$ the center, $w$ the width of the peak and $s$ is the distortion factor (shape). For the deconvoluted peaks, the peak temperatures correspond to $T_0$, while the enthalpy changes are calculated using the total area under the peak.

## 4. Results and discussion

The thermal and rheological properties of the investigated polysaccharides were studied in their pure aqueous mixtures and after the addition of some sodium salts or neutral co-solutes (trehalose and urea). It may sound trivial, but it is important to underline that in the two experimental techniques used in this study the sample is treated in totally different manners. In DSC the specimen remains still and is heated/cooled above and below room temperature. On the other hand, during the acquisition of the

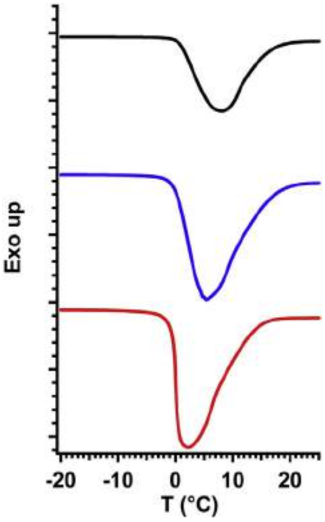

**Fig. 1.** From top to bottom: DSC heating curves of 1% aqueous mixtures of GG (black), SA (blue), and SH (red). Curves have been offset for graphical purposes. (For interpretation of the references to colour in this figure legend, the reader is referred to the web version of this article.)

flow curve the sample is mechanically stressed at constant temperature, its supramolecular texture is modified and its reaction to this perturbation recorded. The thermal behavior (studied through DSC) reflects the interactions between the cosolutes, the polymer chains and water; while the rheological behavior depends on the interactions between the polymer chains, and their distribution and entanglement in the matrix.

### *4.1. Thermal behavior*

The thermograms of 1% aqueous mixtures of GG, SA and SH are reported in Fig. 1.

The endothermic peak, due to the melting of free water, is always centered slightly above 0 °C, presumably because of a kinetic effect (Hatakeyama et al., 2010; Naoi, Hatakeyama, & Hatakeyama, 2002). The melting peak temperatures ($T_{mf}$) and the corresponding enthalpy changes ($\Delta H_{mf}$, in J/g) are listed in Table 1. GG shows the highest melting temperature, associated to the lowest melting enthalpy, while SH possesses the lowest peak temperature and the largest melting enthalpy. SA shows intermediate values.

The thermograms of GG in the presence of different 0.5 M solutions of sodium halides are shown in Fig. 2.

In the case of NaF the endothermic peak shows a bimodal behavior. The curve was deconvoluted by using an exponentially modified Gaussian function (EMG) according to Eq. (1). This approach is commonly implemented in the analysis of overlapping DSC peaks in drugs (Elsabee & Prankerd, 1992), paraffins (Anghel, Georgiev, Petrescu, Popov, & Constantinescu, 2014) and polymer composites characterization (Tatini et al., 2015). The fitting procedure provides the two $T_0$ values corresponding to the centers of the two Gaussian curves used for the deconvolution. $T_0$ are found to be 5.07 and −4.45 °C. This bimodal behavior is increased with increasing halide atomic number: in the case of NaCl, NaBr and NaI two distinct peaks appear in the DSC curve whose distance increases moving down in the group. The higher temperature peak corresponds to the melting of free water ($T_{mf}$ in Table 1) and is similar to the peak produced by the salt-free GG dispersion. The lower temperature peak located between −30 and −5 °C relates to the melting of freezable bound water ($T_{mb}$ in Table 1), that freezes below 0 °C and has a reduced enthalpy of fusion (Chaplin, 2012).

For the samples containing pure GG, SA and SH the peak related to the melting of freezable bound water is not observed. Presumably the freezable bound and the free water melting peaks overlap together in the broad endothermic signal which is centered around 0 °C in the heating scans (see Fig. 1). A similar behavior was reported by Nakamura in the case of cellulose with different amounts of adsorbed water (Nakamura et al., 1981). The addition of a salt modifies the interactions between water and the polysaccharide chains, and changes the distribution of water between the two states: freezable bound and free water. This effect induces a separation of the two overlapping peaks, which is strictly dependent on the salt nature.

The melting point and the enthalpy change for the bound freezable water depend on the interactions between the polymer chains and water (Guan et al., 2011).

As proposed by De Andres-Santos for 1% aqueous solutions of sodium hyaluronate, we assume that the lower $T_{mb}$, the higher the number of water and polysaccharide molecules that remain closely associated to each other, i.e., the more hydrated the chains (De Andres-Santos, Velasco-Martin, Hernández-Velasco, Martín-Gil, & Martín-Gil, 1994). On the other hand, a higher $T_{mb}$ indicates an increment in the interchain hydrogen bonding (HB) interactions within the polysaccharide, thus suggesting a sort of de-hydration of the polymer.

The results obtained for the samples containing the sodium halides show no remarkable variation in $T_{mf}$ and $\Delta H_{mf}$ with the exception of NaF. Instead, the values of $T_{mb}$ decrease from −4.45 (NaF) to −29.65 °C (NaI), while $\Delta H_{mb}$ decreases from 125.8 (NaF) to 15.07 J/g (NaI). These trends suggest the presence of a specific anion effect on the conformational structure and intermolecular interactions of GG. In particular, the more chaotropic the anion, the lower the value of $T_{mb}$ and hence the lower the number of interacting sites between the polysaccharide chains. We argue that strongly hydrated kosmotropic anions like fluoride and sulfate compete with the polysaccharide chains for water molecules, thus lowering the hydration of the chains (Yin et al., 2008). This effect promotes the formation of interchain HB and eventually leads to the aggregation of polysaccharide molecules.

On the other hand, the presence of chaotropic anions, like iodide, modifies the dimensions of the polysaccharide coils and increases their solvent-accessible surface area (ASA) (Curtis, Steinbrecher, Heinemann, Blanch, & Prausnitz, 2002). These ion hydration effects that lead to the salting-in processes induced by chaotropes and salting-out by kosmotropes on proteins have been extensively studied (López-Arenas, Solís-Mendiola, Padilla-Zúñiga, & Hernández-Arana, 2006). The ruling mechanism by which chaotropes increase the solvation of the polymer surface seems to be a direct interaction of the ions with the weakly hydrated portions of the polysaccharide chain, as already found and reported in the case of proteins (Arakawa & Timasheff, 1982; Collins, 2004; Lo Nostro & Ninham, 2012).

The presence of urea produces a second endothermic peak in the thermogram, related to the melting of freezable bound water. At this concentration urea usually acts as an enhancer of the solvation of the polysaccharide chains (Winkworth-Smith, MacNaughtan, & Foster, 2016) by promoting their unfolding.

In the case of the other additives ($Na_2SO_4$, NaSCN, $NaClO_4$, $Na_3PO_4$, $Na_2HPO_4$, $NaH_2PO_4$ and trehalose) only a broad endothermic peak around 0 °C is clearly detected (see Table 1, and Figs. S1 and S2 in Supplementary material). The presence of these cosolutes does not induce a separation between the freezable bound and the free water melting peaks, resulting in a DSC profile which is similar to those of pure GG, SA and SH samples (Fig. 1). The case of $Na_2SO_4$ is peculiar as it shows a value of $\Delta H_{mf}$ (318.4 J/g) which is close to that of pure water (333.5 J/g). The sulfate ions strongly interact with the water molecules inducing a de-hydration of the polysaccharide

**Table 1**
Melting temperature and enthalpy change of free water ($T_{mf}$ and $\Delta H_{mf}$, in °C and J/g) and of the freezable bound water ($T_{mb}$ and $\Delta H_{mb}$, in °C and J/g) in 1% aqueous mixtures of guar gum, sodium alginate, and sodium hyaluronate, in the presence of different salts or neutral cosolutes. The concentration of all cosolutes is always 0.5 M, unless otherwise specified.

| additive | $T_{mf}$ | $\Delta H_{mf}$ | $T_{mb}$ | $\Delta H_{mb}$ | $T_{mf}$ | $\Delta H_{mf}$ | $T_{mb}$ | $\Delta H_{mb}$ | $T_{mf}$ | $\Delta H_{mf}$ | $T_{mb}$ | $\Delta H_{mb}$ |
|---|---|---|---|---|---|---|---|---|---|---|---|---|
| Guar Gum 1% | | | | | Sodium Alginate 1% | | | | Sodium Hyaluronate 1% | | | |
| none | 7.88 | 307.3 | | | 5.36 | 336.4 | | | 2.18 | 353.0 | | |
| NaF | 5.07 | 155.5 | −4.45 | 125.8 | 1.16 | 273.7 | −4.11 | 56.39 | 0.66 | 300.8 | −5.23 | 40.46 |
| NaCl | 1.05 | 245.2 | −19.98 | 22.11 | 1.33 | 241.8 | −19.82 | 21.50 | −0.03 | 260.1 | −20.43 | 23.77 |
| NaBr | 1.80 | 249.7 | −26.03 | 16.58 | 0.05 | 267.3 | −26.34 | 17.78 | −0.16 | 268.8 | −26.71 | 19.18 |
| NaI | 1.62 | 256.2 | −29.65 | 15.07 | 0.07 | 267.6 | −29.73 | 16.40 | −0.57 | 272.4 | −29.99 | 16.54 |
| $Na_2SO_4$ | 4.24 | 318.4 | | | 2.61 | 334.1 | | | 2.49 | 331.8 | | |
| NaSCN | 1.54 | 282.7 | | | −0.22 | 276.3 | | | −0.13 | 289.4 | | |
| $NaClO_4$ | 2.58 | 278.2 | | | −0.35 | 293.6 | −33.23 | 12.28 | −0.22 | 299.6 | −33.19 | 5.678 |
| $Na_3PO_4$ | 1.28 | 58.88 | | | 4.42 | 294.8 | | | 0.64 | 317.6 | | |
| $Na_2HPO_4$ | 5.13 | 293.5 | | | 1.50 | 331.9 | | | 1.79 | 274.5 | | |
| $NaH_2PO_4$ | 3.00 | 291.5 | | | −0.23 | 295.8 | | | −0.32 | 307.5 | | |
| Urea | 3.48 | 247.9 | −10.62 | 8.342 | 2.03 | 254.1 | −11.11 | 11.68 | 0.00 | 268.8 | −11.83 | 13.67 |
| Trehalose | 1.56 | 255.2 | | | 0.59 | 279.9 | | | 0.07 | 261.9 | | |

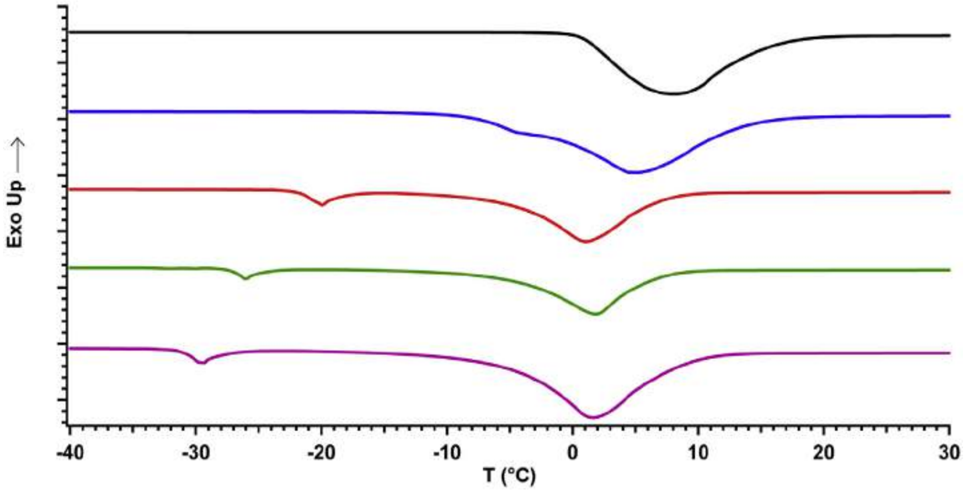

**Fig. 2.** From top to bottom: DSC heating curves of 1% aqueous mixtures of GG pure (black) and in the presence of 0.5 M solutions of NaF (blue), NaCl (red), NaBr (green) and NaI (magenta). Curves have been offset for graphical purposes. (For interpretation of the references to colour in this figure legend, the reader is referred to the web version of this article.)

chains, reducing the amount of freezable bound water in favour of the free water, and resulting in an overlap of the two DSC signals.

The effect induced by $Na_2HPO_4$ is peculiar and deserves an in-depth analysis. The DSC curve (Fig. S3 in Supplementary material) shows a shoulder at about 20 °C. This phenomenon can be related to a liquid crystalline-to-isotropic liquid state transition (Hatakeyama, Naoi, & Hatakeyama, 2004; Nakamura, Hatakeyama, & Hatakeyama, 1991). Since this transition is observed both for GG and SA samples, we argue that the presence of $Na_2HPO_4$ preserves the liquid crystalline phase in the guar and sodium alginate network, whereas all the other examined salts and co-solutes destabilize this state.

In order to separate the two endothermic contributions and calculate the enthalpy for this transition, EMG deconvolution was performed and the fitting parameters ($T_{ph}$ and $\Delta H_{ph}$) are shown in Table S1 (see the Supplementary material). For GG the liquid crystalline-to-isotropic liquid state transition occurs at $T_{ph} = 19.3°$ C, with a corresponding enthalpy change of 24.68 J/g.

Aqueous solutions of SA and SH in the presence of salts and cosolutes show an identical thermal behavior to that previously described for GG dispersions. The values of $T_{mf}$, $\Delta H_{mf}$, $T_{mb}$ and $\Delta H_{mb}$ extracted from the thermograms are reported in Table 1. SH and SA samples show analogous DSC curves to the corresponding GG samples, with the exception of perchlorate. For both SA and SH systems, the thermograms of perchlorate containing sample show two peaks instead of one, as in the GG/perchlorate sample. An extra peak appears at about −33 °C and can be ascribed to the freezable bound water melting. This peak may reflect polymer-salt interactions similar to those occurring with other chaotropic ions. In the GG sample this peak is not shown, indicating that a different mechanism occurs. It is worthwhile to mention that $ClO_4^-$ may act as an oxidizer and it is extensively used as gel breaker in guar-based formulations (Hall, Szemenyei, & Gupta, 1991; Schnoor, Singh, & Russel, 2016; Schultheiss, 2015). Presumably perchlorate partially oxidizes the polysaccharide chains, inducing a structural modification and a change in the polymer-water interactions, and the peak for the melting of freezing bound water disappears. This mechanism does not take place with the partially anionic chains of SA and SH.

## 4.2. Rheology

### 4.2.1. Fitting of the flow curves

All the flow curves show a similar profile (see Fig. 3). At low shear rate all mixtures exhibit a Newtonian plateau. For stronger perturbations a shear thinning region is shown.

We applied the Bird–Carreau–Yasuda (BCY) rheological model to the flow curves. This model, sometimes referred to as Carreau–Yasuda or Carreau model (Barnes, Hutton, & Walters, 1989), was empirically developed to describe the mechanical

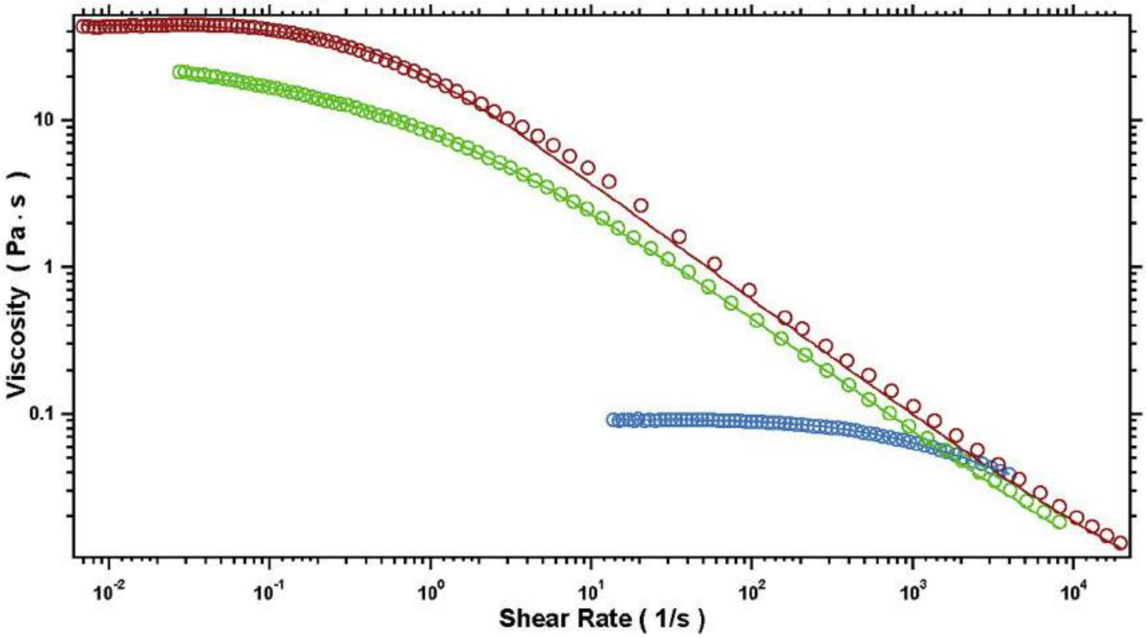

**Fig. 3.** From bottom to top: Flow curves for 1% w/w SA (light blue), GG (green), and SH mixtures (red). The solid lines represent the fitting of the experimental curves. (For interpretation of the references to colour in this figure legend, the reader is referred to the web version of this article.)

behavior of systems that exhibit both a Newtonian and a shear thinning region (Osswald & Rudolph, 2015). In particular it is used to study the rheology of polymeric water-based dispersions and solutions, e.g. those from polyacrylamide (Escudier et al., 2005), polypropylene (Lertwimolnun & Vergnes, 2006), and polysaccharides such as SH (Haward, Jaishankar, Oliveira, Alves, & McKinley, 2013), GG (Nandhini Venugopal & Abhilash, 2010), xanthan gum and carboxymethylcellulose (Escudier, Gouldson, Pereira, Pinho, & Poole, 2001; Escudier et al., 2005; García, Alfaro, Calero, & Muñoz, 2014).

In the BCY model the following equation describes the dependence of the viscosity value η:

$$\eta = \eta_\infty + (\eta_0 - \eta_\infty) \cdot [1 + (\lambda\dot{\gamma})^a]^{(n-1)/a} \tag{2}$$

where $\eta$, $\eta_0$, $\eta_\infty$, $\dot{\gamma}$, $\lambda$, $n$, and $a$ are the viscosity, the zero shear rate viscosity, the viscosity at infinite shear, the applied shear rate, the yield of shear rate above which the system shows a shear thinning behavior, the power law index, and the Yasuda parameter indicating the width of the transition region between $\eta_0$ and $\eta_\infty$, respectively (Carreau, 1972; Osswald & Rudolph, 2015; Yasuda, Armstrong, & Cohen, 1981).

Almost all flow curves containing GG and SH are well fitted (as shown by the $\chi^2$, see Table 2) by the BCY model with the sole exceptions of SH in the presence of $Na_3PO_4$ and of the SA solutions, which show a very low variability in the whole shear range examined. Table 2 lists the values of $\boldsymbol{\eta}_0$, $\boldsymbol{\lambda}$, $a$ and $n$ extracted from the fitting of the flow curves, according to Eq. (2).

### 4.2.2. *Flow curves*

In order to check the effect of different salts on the viscosity of polysaccharide mixtures, we mainly focussed our attention on the trend of $\eta_0$ value.

Fig. 3 shows the flow curves for the 1% aqueous mixtures of SA, GG and SH. All samples exhibit a specific non-Newtonian behavior: the zero shear viscosity of SH and GG water-based systems are in the order of tens of Pa s ($\eta_0$ = 44.66 and 24.41 Pa s, respectively), while the alginate system shows a low value, about 0.11 Pa s in the whole explored torque range. On the other hand, the addition of salts or neutral co-solutes induces remarkable changes in the rheological properties of GG and SH (see Table 2).

Fig. 4 illustrates the effect of trehalose, $Na_2SO_4$ and NaF on the profile of the flow curve of SH and GG. For SH the presence of trehalose led to an increase of the strength of the tridimensional network, as indicated by the increase of $\eta_0$ (from 44.66 up to 159.25 Pa s) and by a shift of the yield value of $\dot{\gamma}$, $\lambda$. On the other hand, sulfate and fluoride lower both the $\eta_0$ (21.01 and 28.05 Pa s respectively) and the $\lambda$ values.

A similar trend is obtained for trehalose and GG, while the addition of $Na_2SO_4$ and NaF to GG induces an opposite effect, as indicated by the raise in the zero shear viscosity (from 24.41 up to 43.53 and 33.30 Pa s, respectively), and by the shift of $\lambda$ to higher values. These results suggest a synergistic interaction between trehalose and the polysaccharide molecules, which is more significant for SH. We argue that trehalose establishes crosslinking intra- and intermolecular interactions, resulting in a strengthening of the system.

Indeed, trehalose is known as a kosmotrope or water-structure maker: this disaccharide is able to break the tetrahedral HB network of water and re-order the water molecules in the hydration layer (Branca et al., 2005; Lerbret et al., 2005). However, experiments conducted by us on a 0.5 M solution of trehalose in water show neither an increase in the viscosity, nor a modification in the rheological response.

The competition for water molecules between trehalose and the polysaccharide chains leads to partial de-hydration of the macromolecules (Jain & Roy 2008). It has been shown that trehalose can modify the hydration layer of biomolecules (Kawai, Sakurai, Inoue, Chujo, & Kobayashi, 1992; Magazù, Migliardo, Musolino, & Sciortino, 1997), stabilizing their HB network. This picture is commonly known as *preferential exclusion theory*. The *water replacement theory* instead argues that the hydration layer of the macromolecules is substituted by trehalose, which directly forms HB and stabilizes the structure. A third approach, the *vitrification theory*, can be applied only at higher concentration of trehalose and envisages that it creates a glassy matrix which acts as a protective cocoon, shielding and stabilizing the macromolecules from external stresses (Jain & Roy 2008). Since in our case the concentration of tre-

**Table 2**
The zero shear rate viscosity ($\eta_0$, in Pa s), power law index ($n$), the reciprocal of the critical shear rate at which the viscosity begins to drop down ($\lambda$, in s), the width of the transition region between $\eta_0$ and $\eta_\infty$ ($a$), and the $\chi^2$ extracted from the fitting of the flow curves for 1% aqueous mixtures of guar gum and sodium hyaluronate, in the presence of different salts or neutral cosolutes. The concentration of all cosolutes is always 0.5 M, unless otherwise specified.

| additive | $\eta_0 \pm 2.5\%$ | $n \pm 4\%$ | $\lambda \pm 5\%$ | $a \pm 3\%$ | $\chi^2$ | $\eta_0 \pm 1.5\%$ | $n \pm 15\%$ | $\lambda \pm 9\%$ | $a \pm 4\%$ | $\chi^2$ |
|---|---|---|---|---|---|---|---|---|---|---|
| | | Guar Gum 1% | | | | | | Sodium Hyaluronate 1% | | |
| none | 24.41 | 0.20 | 1.36 | 0.58 | 6.96 | 44.66 | 0.20 | 2.22 | 1.21 | 51.71 |
| NaF | 33.30 | 0.19 | 1.64 | 0.65 | 13.29 | 28.05 | 0.19 | 0.87 | 0.57 | 7.12 |
| NaCl | 25.23 | 0.22 | 1.19 | 0.58 | 7.28 | 44.84 | 0.21 | 2.14 | 1.00 | 72.92 |
| NaBr | 23.68 | 0.22 | 1.24 | 0.57 | 3.64 | 40.95 | 0.26 | 2.07 | 0.93 | 98.98 |
| NaI | 19.70 | 0.24 | 1.11 | 0.51 | 6.88 | 46.23 | 0.15 | 1.22 | 0.55 | 6.25 |
| $Na_2SO_4$ | 43.53 | 0.21 | 3.14 | 0.67 | 32.67 | 21.01 | 0.22 | 0.76 | 0.59 | 3.75 |
| NaSCN | 28.27 | 0.16 | 1.12 | 0.42 | 7.05 | 40.96 | 0.27 | 2.11 | 0.68 | 39.50 |
| $NaClO_4$ | 23.87 | 0.22 | 1.47 | 0.67 | 10.10 | 53.09 | 0.28 | 2.93 | 0.84 | 32.18 |
| $Na_2HPO_4$ | 30.07 | 0.20 | 2.02 | 0.80 | 16.01 | 77.68 | 0.22 | 2.58 | 1.18 | 26.14 |
| $NaH_2PO_4$ | 20.44 | 0.19 | 1.01 | 0.63 | 3.50 | 19.75 | 0.30 | 1.22 | 0.70 | 12.07 |
| $Na_3PO_4$ | 19.90 | 0.24 | 1.29 | 0.64 | 5.36 | | | | | |
| Urea | 33.68 | 0.23 | 2.16 | 0.66 | 10.45 | 46.21 | 0.26 | 1.98 | 0.78 | 3.83 |
| Trehalose | 37.65 | 0.21 | 2.60 | 0.66 | 38.32 | 159.25 | 0.20 | 6.07 | 0.90 | 73.50 |

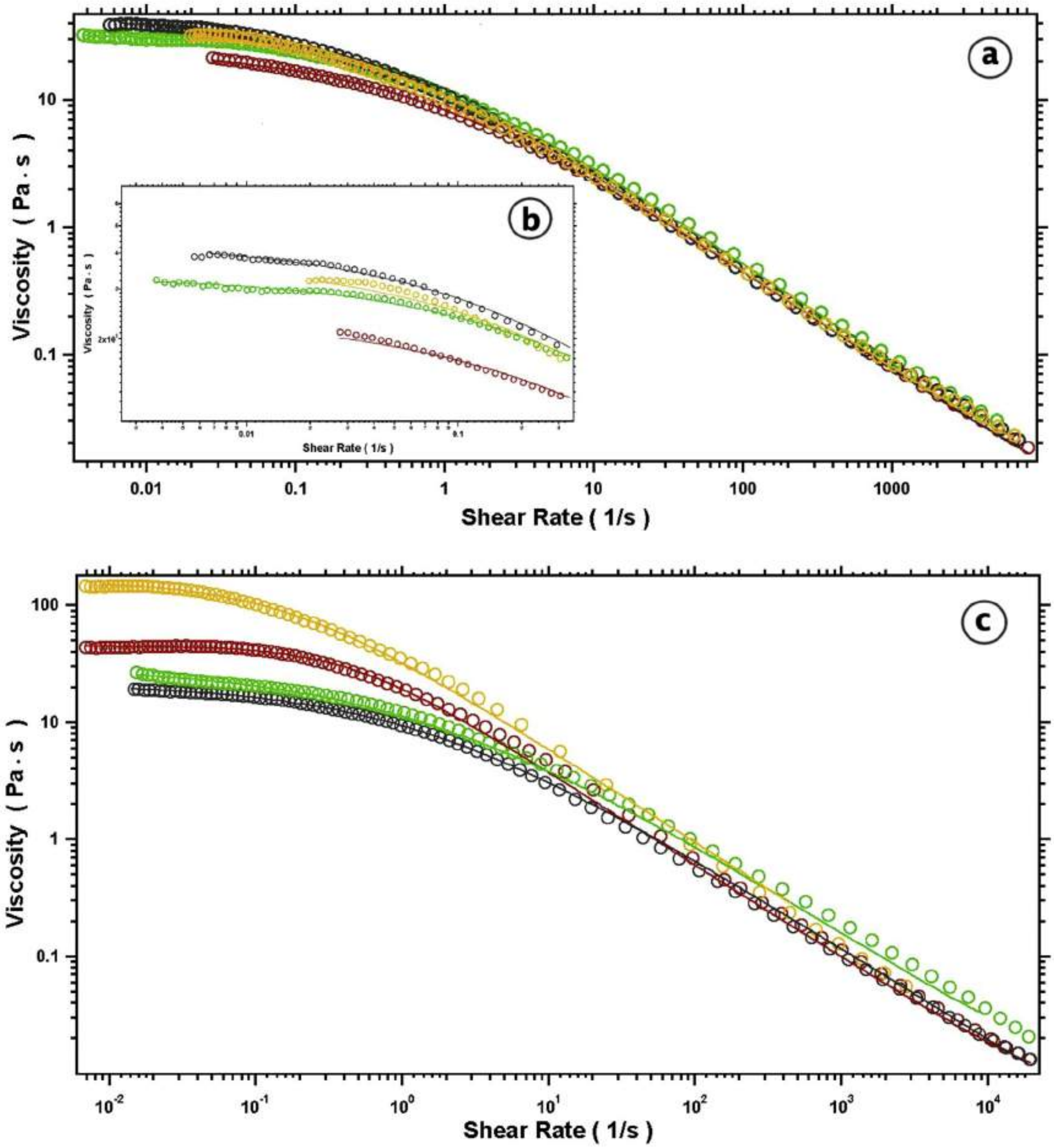

**Fig. 4.** Flow curves of (a) GG and SH (c) 1% w/w mixtures (red) and in the presence of 0.5 M trehalose (yellow), NaF (green) and $Na_2SO_4$ (grey). The inset (b) shows the flow curves of GG zoomed at low shear stress. The solid lines represent the fitting of the experimental curves. (For interpretation of the references to colour in this figure legend, the reader is referred to the web version of this article.)

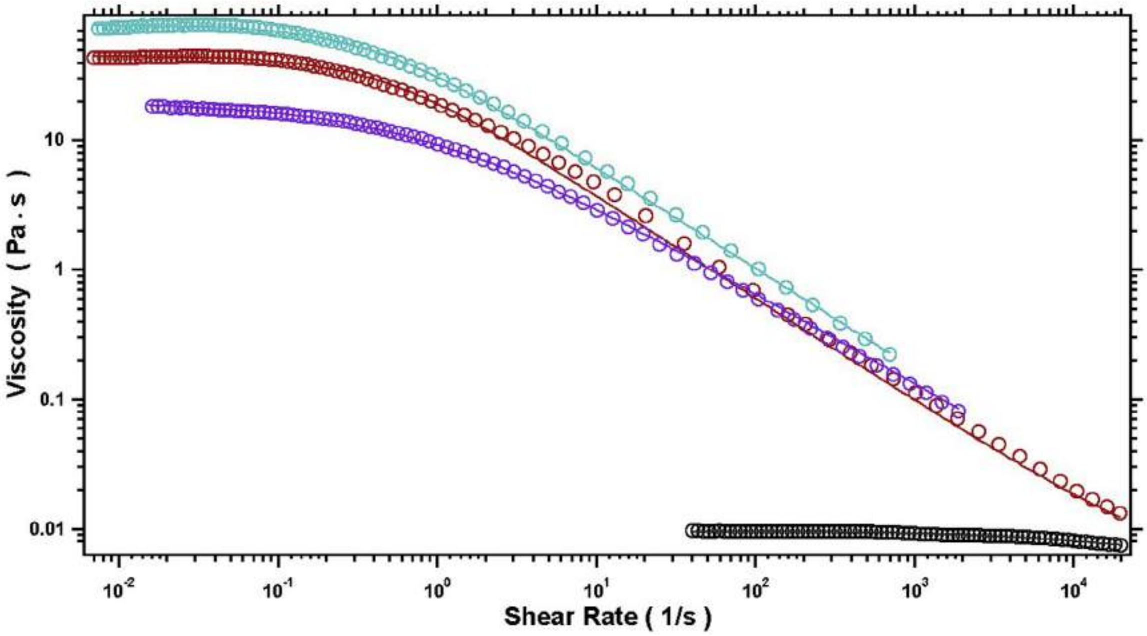

**Fig. 5.** Flow curves of SH 1% w/w pure solution (red), in the presence of 0.5 M $NaH_2PO_4$ (violet), $Na_2HPO_4$ (turquoise) and $Na_3PO_4$ (black). The solid lines represent the fitting of the experimental curves. (For interpretation of the references to colour in this figure legend, the reader is referred to the web version of this article.)

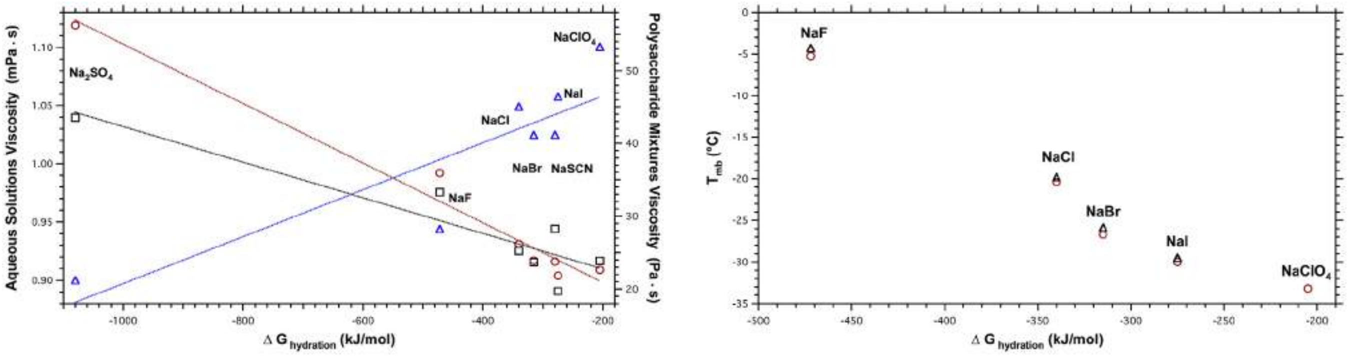

**Fig. 6.** Left panel: viscosity values for GG (black), SH (blue) and water (red) in the presence of the different sodium salts as a function of the $\Delta G_{hydration}$ of the anion. The left axis refers to the red line, while the right axis refers to black and blue lines. The dotted lines are only a guide for the eye. Right panel: $T_{mb}$ for GG (black) and SH (red) in the presence of different sodium salts as a function of the $\Delta G_{hydration}$ of the anion. (For interpretation of the references to colour in this figure legend, the reader is referred to the web version of this article.)

halose is relatively low, we can exclude the latter hypothesis. In the case of sulphate we propose two different mechanisms, depending on the investigated polysaccharide. The $SO_4^{2-}$ ion is a kosmotrope, which subtracts water from the macromolecule hydration layer. In the case of SH, where negatively charged $-COO^-$ groups are distributed along the chains, the addition of sulfate brings about a weakening in the polymeric network, that results in a decrease of the strength of the polymeric network. Conversely for GG the reduction of water molecules in the hydration layer promotes the formation of interchain interactions, due to the non-ionic nature of the polysaccharide. Therefore, the strength of the polymeric network increases, as indicated by the trend of both the viscosity and the λ values.

Moreover, also the effect of fluoride supports this argument. Indeed, kosmotropic ions like fluoride and sulfate strongly modify the rheology of the systems. At the same time, the addition of the other halides to GG and SH does not affect significantly the values of $\eta_0$ and λ.

A further peculiar case concerns the three phosphate anions (Fig. 5). In fact, the rheological profiles show that $HPO_4^{2-}$ increases the viscosity of the SH solution to 77.68 Pa·s, while $H_2PO_4^-$ lowers (19.75) and $PO_4^{3-}$ dramatically breaks down the flow curves.

We recall that the rheological properties of hyaluronate strongly depend on the pH in a non-linear correlation (Gatej, Popa, & Rinaudo, 2005; Gibbs, Merrill, & Smith, 1968; Gura, Hückel, & Müller, 2003; Maleki, Kjøniksen, & Nyström, 2008). In particular for hyaluronic acid the complex viscosity reaches a maximum value at about pH = 2.5, sided by two remarkable drops in acid (pH = 1.6) and mid-acid conditions (pH = 3.34) (Gatej et al., 2005). The stiffening of the hyaluronic network is attributed to a critical balance between attractive and repulsive forces. These forces that involve ionized or neutral carboxylic and amino groups are mainly electrostatic (Gibbs et al., 1968). Moreover, above pH = 12 the viscosity dramatically breaks down, leading to a Newtonian-like behavior. Finally, in a wide range of pH (between 2.8 and 12) the rheological properties and viscosity remain unchanged (Gatej et al., 2005; Maleki, 2008). Furthermore, Maleki investigated the dilute (0.05% w/w) and semi-dilute (0.5% w/w) regimes of HA solutions, with the pH set between 1 and 13 by adding 0.1 M phosphate buffers (Maleki et al., 2008).

The results show that the presence of these buffers does not affect the pH responsivity.

The 0.5 M $Na_3PO_4$ solution provides an extremely high pH (13) that can at least partly deprotonate the —OH groups of the hyaluronate chain, breaking the cooperative HB network of the polysaccharide chains. On the other hand, our results for 0.5 M $NaH_2PO_4$ and $Na_2HPO_4$ solutions (pH = 4.7 and 9.9, respectively) differ from those reported in the literature. Presumably in these pH conditions mono-hydrogenphosphate acts as a soft cross-linker, strengthening the HB network and increasing the viscosity. We argue that the increment in viscosity is due to a combination of two cooperating effects: the basic pH promotes the deprotonation, enhancing the HB network, and at the same time the higher SH concentrations shrink the polysaccharide network where $HPO_4^{2-}$ anions bridge different chains and re-enforce the HB network.

In the presence of di-hydrogenphosphate the pH is lower. The mid-acid environment weakens the network by reducing the number of active sites available for HB. Moreover, in $H_2PO_4^-$ the number of acceptor sites for hydrogen bonding is reduced and thus the ion contribution to the strengthening of the system is reduced.

Moreover, the power law index parameter $n$ reflects how the systems respond to an applied stress. Indeed, both GG dispersions and SH solutions exhibit only small fluctuations of $n$ around the value of 0.2 for all samples. Thus, the scalar law that describes the shear thinning behavior above the $\lambda$ critical value, is almost independent on the chemical nature of the added salt. After the disruption of the HB network in both cases we observed the same shear thinning effect.

In order to correlate the rheological and thermal behaviors to the thermodynamic properties of the investigated salts, we report in Fig. 6 the viscosities for GG, SH and water (on the left) and the $T_{mb}$ values for GG and SH (on the right) in the presence of $Na_2SO_4$, NaF, NaCl, NaBr, NaSCN, NaI, $NaClO_4$ as functions of the $\Delta G_{hydration}$ of the anion.

The viscosity values of aqueous salt solutions and $\Delta G_{hydration}$ are taken from literature and reported in Table S2 in the Supplementary Material (Abdulagatova et al., 2005; Goldsack & Franchetto, 1977; Galmarini et al., 2011; Hood, 1933; Janz et al., 1969; Marcus, 1991; Wolf, 1966). In the case of $T_{mb}$, the samples containing $Na_2SO_4$, NaSCN and $NaClO_4$ (only for GG) are not reported since no bound freezable water melting peak was detected in the DSC thermograms.

The viscosity plot (left panel in Fig. 6) shows that the addition of a salt to GG (black) and to water (red) produces a similar trend, in agreement to the direct Hofmeister sequence: $Na_2SO_4 > NaF > NaCl > NaBr > NaSCN > NaI > NaClO_4$. Thus, we conclude that the addition of a salt induces a similar modification in the viscosity for both pure water and GG dispersion. On the other hand, the trend recorded for SH differs remarkably, showing the opposite behavior and following a reverse Hofmeister series.

The added salt produces an identical effect on the $T_{mb}$ for the two polysaccharides, resulting in a decrease of the freezable bound water melting temperature moving along the series: $NaF > NaCl > NaBr > NaI > NaClO_4$.

These results confirm that the salt affects in the same way the hydration of the GG and SH by modifying the interactions between the water molecules and the polysaccharides, regardless of the different charge of their chains. Despite this, the GG dispersions and SH solutions show a diametrically opposite trend in terms of viscosities.

Kosmostropic anions induce a partial de-hydration of the polysaccharide chains, while the less hydrated chaotropic ions adsorb to the polymer chains, promote their unfolding and enhance the polymer–water interactions. The magnitude of the anion effect, both on the thermal and the rheological behaviors, is considerably higher in the case of the kosmotropic ions, whereas in the presence of chaotropic ions the behaviors are practically the same as those of the pure polysaccharide solutions.

These findings apparently point out that the degree of hydration of the polymer chains is the crucial factor that leads to a significant variation in the strength of the polysaccharide network, and that this phenomenon is ion specific. In the case of a neutral polysaccharide (guar gum) the decrease in the number of the water molecules that interact with the polysaccharide chains leads to a strengthening of the network, due to stronger inter-chain interactions. Vice versa, for a charged polysaccharide (sodium hyaluronate), electrostatic repulsive forces come into play with a greater impact, as a result of the reduced number of water molecules that can screen the charges. The overall effect is a weakening of the chain–chain interactions and, consequently the softening of the network.

## 5. Conclusions

The thermal and rheological behavior of 1% aqueous mixtures of guar gum (GG), sodium hyaluronate (SH) and sodium alginate (SA) were investigated in the presence of different salts or neutral co-solutes at constant concentration. The results suggest that the added solutes can remarkably modify the texture of the polysaccharide network by perturbing the hydration of the chains and changing their intermolecular interactions. The effect of the ions is apparently related to their hydration properties and their propensity to adsorb at the polymer interface. As a matter of fact a strongly hydrated (kosmotropic) ion is expected to deprive the polysaccharide chain of water, remain confined in the bulk solution, and enhance the interchain interaction in the case of the neutral GG. This results in a remarkable strenghtening of the system. On the other hand with the negatively charged SH, kosmotropes induce a weakening in the interactions. The chaotropes (bromide, iodide, thiocyanate) do not change the rheological properties of the mixtures. Being almost unhydrated, these ions are assumed to adsorb at the polymer surface and partially deplete some water from the hydration layer. This phenomenon is supposed to favor the unfolding of the chain, increase its hydration and reduce the interchain interactions. Phosphate ions deserve a special comment, in fact $PO_4^{3-}$ and $H_2PO_4^-$ lower the viscosity, while $HPO_4^{2-}$ produces a significant increment in the viscosity, both for GG and SH. Such behavior is probably related to a delicate balance between the different pH properties and the capacity of the three ions to strengthen the HB network.

These results are relevant for the formulation of greener frac fluids to be used in shale gas exploitation. More work is necessary to modify the behavior of more diluted polysaccharide solutions and dispersions (e.g. 0.5%), to study the effect of more concentrated salt solutions, to check the effect of temperature and pressure, and of other physico-chemical triggers for controlling the viscosity of the frac fluid in the different stages of the life of a basin.

## Acknowledgments

The authors acknowledge funding from the European Union Horizon 2020 research and innovation programme under grant agreement No. 640979.

## Appendix A. Supplementary data

Supplementary data associated with this article can be found, in the online version, at http://dx.doi.org/10.1016/j.carbpol.2017.05.078.

## References

Anghel, E. M., Georgiev, A., Petrescu, S., Popov, R., & Constantinescu, M. (2014). Thermo-physical characterization of some paraffins used as phase change materials for thermal energy storage. *Journal of Thermal Analysis and Calorimetry*, *117*, 557–566.

Arakawa, T., & Timasheff, S. N. (1982). Preferential interactions of proteins with salts in concentrated solutions. *Biochemistry*, *21*, 6545–6552.

Arthur, J. D., Bohm, B. K., Coughlin, B. J., Layne, M. A., & Cornue, D. (2009). Evaluating the environmental implications of hydraulic fracturing in shale gas reservoirs. *Society of Petroleum Engineers*, *121038*, 1–15.

Barati, R., & Liang, J.-T. (2014). A review of fracturing fluid systems used for hydraulic fracturing of oil and gas wells. *Journal of Applied Polymer Science*, *131*(16)

Barnes, H. A., Hutton, J. F., & Walters, K. (1989). *An introduction to rheology*. Elsevier.

Branca, C., Maccarrone, S., Magazù, S., Maisano, G., Bennington, S. M., & Taylor, J. (2005). Tetrahedral order in homologous disaccharide-water mixtures. *The Journal of Chemical Physics*, *122*, 174513.

Carreau, P. J. (1972). Rheological equations from molecular network theories. *Journal of Rheology*, *16*(1), 99–127.

Chaplin, M. (n.d.). *Polysaccharide hydration*. Retrieved March 16, 2017, from http://www1.lsbu.ac.uk/water/polysaccharide_hydration.html.

Collins, K. D. (2004). Ions from the Hofmeister series and osmolytes: Effects on proteins in solution and in the crystallization process. *Methods*, *34*, 300–311.

Couillet, I., & Hughes, T. (2008). Aqueous fracturing fluid. US Patent 7,427,583B2, Retrieved: March 16, 2017.

Curtis, R. A., Steinbrecher, C., Heinemann, M., Blanch, H. W., & Prausnitz, J. M. (2002). Hydrophobic forces between protein molecules in aqueous solutions of concentrated electrolyte. *Biophysical Chemistry*, *98*(3), 249–265.

De Andres-Santos, A. I., Velasco-Martin, A., Hernández-Velasco, E., Martín-Gil, J., & Martín-Gil, F. J. (1994). Thermal behaviour of aqueous solutions of sodium hyaluronate from different commercial sources. *Thermochimica Acta*, *242*, 153–160.

Elsabee, M., & Prankerd, R. J. (1992). Solid-state properties of drugs. II: Peak shape analysis and deconvolution of overlapping endotherms in differential scanning calorimetry of chiral mixtures. *International Journal of Pharmaceutics*, *86*, 211–219.

Escudier, M. P., Gouldson, I. W., Pereira, A. S., Pinho, F. T., & Poole, R. J. (2001). On the reproducibility of the rheology of shear-thinning liquids. *Journal of Non-Newtonian Fluid Mechanics*, *97*, 99–124.

Escudier, M. P., Poole, R. J., Presti, F., Dales, C., Nouar, C., Desaubry, C., et al. (2005). Observations of asymmetrical flow behaviour in transitional pipe flow of yield-stress and other shear-thinning liquids. *Journal of Non-Newtonian Fluid Mechanics*, *127*, 143–155.

Gandossi, L., & Von Estorff, U. (2015). *An overview of hydraulic fracturing and other formation stimulation technologies for shale gas production—Update 2015. JRC technical report*. EUR 26347.

García, C., Alfaro, C., Calero, N., & Muñoz, J. (2014). Influence of polysaccharides on the rheology and stabilization of α-pinene emulsions. *Carbohydrate Polymers*, *105*, 177–183.

Gatej, I., Popa, M., & Rinaudo, M. (2005). Role of the pH on hyaluronan behavior in aqueous solution. *Biomacromolecules*, *6*, 61–67.

Gibbs, D. A., Merrill, E. W., & Smith, K. A. (1968). Rheology of hyaluronic acid. *Biopolymers*, *6*, 777–791.

Goel, N., Shah, S. N., & Grady, B. P. (2002). Correlating viscoelastic measurements of fracturing fluid to particles suspension and solids transport. *Journal of Petroleum Science and Engineering*, *35*(1–2), 59–81.

Guan, L., Xu, H., & Huang, D. (2010). The investigation on states of water in different hydrophilic polymers by DSC and FTIR. *Journal of Polymer Research*, *18*, 681–689.

Gura, E., Hückel, M., & Müller, P.-J. (2003). Specific degradation of hyaluronic acid and its rheological properties. *Polymer Degradation and Stability*, *59*, 297–302.

Hall, B. E., Szemenyei, C. A., & Gupta, D. V. S. (1991). *Breaker system for aqueous fluids containing xanthan gums*.. Retrieved: March 16, 2017, from http://www.google.ch/patents/US5054552.

Hatakeyama, T., Naoi, S., & Hatakeyama, H. (2004). Liquid crystallization of glassy guar gum with water. *Thermochimica Acta*, *416*, 121–127.

Hatakeyama, T., Tanaka, M., & Hatakeyama, H. (2010). Thermal properties of freezing bound water restrained by polysaccharides. *Journal of Biomaterials Science, Polymer Edition*, *21*, 1865–1875.

Haward, S. J., Jaishankar, A., Oliveira, M. S. N., Alves, M. A., & McKinley, G. H. (2013). Extensional flow of hyaluronic acid solutions in an optimized microfluidic cross-slot device. *Biomicrofluidics*, *7*(4).

Holloway, M. D., & Rudd, O. (2013). *Fracking: The operations and environmental consequences of hydraulic fracturing*. John Wiley & Sons.

Jain, K. N., & Roy, I. (2008). Effect of trehalose on protein structure. *Protein Science*, *18*, 24–36.

Kawai, H., Sakurai, M., Inoue, Y., Chujo, R., & Kobayashi, S. (1992). Hydration of oligosaccharides: Anomalous hydration ability of trehalose. *Cryobiology*, *29*, 599–606.

Kelly, R. M., Khan, S. A., Leduc, P., Tayal, A., & Prud'homme, R. K. (2001). *Methods and compositions for fracturing subterranean formations*.. Retrieved: March 16, 2017, from http://www.google.com/patents/US5421412.

Kupská, I., Lapcík, L., Lapcíková, B., Záková, K., & Juríková, J. (2014). The viscometric behaviour of sodium hyaluronate in aqueous and KCl solutions. *Colloids and Surfaces A: Physicochemical and Engineering Aspects*, *454*, 32–37.

López-Arenas, L., Solís-Mendiola, S., Padilla-Zúñiga, J., & Hernández-Arana, A. (2006). Hofmeister effects in protein unfolding kinetics: Estimation of changes in surface area upon formation of the transition state. *Biochimica Et Biophysica Acta (BBA): Proteins and Proteomics*, *1764*, 1260–1267.

Legemah, M., Qu, Q., Sun, H., Beall, B., & Zhou, J. (2013). Alternative polysaccharide fracturing fluids for harsh reservoir conditions. *Presented at the SPE unconventional resources conference and exhibition-Asia pacific, society of petroleum engineers*.

Lerbret, A., Bordat, P., Affouard, F., Guinet, Y., Hedoux, A., Paccou, L., et al. (2005). Influence of homologous disaccharides on the hydrogen-bond network of water: complementary Raman scattering experiments and molecular dynamics simulations. *Carbohydrate Research*, *340*, 881–887.

Lertwimolnun, W., & Vergnes, B. (2006). Effect of processing conditions on the formation of polypropylene/organoclay nanocomposites in a twin screw extruder. *Polymer Engineering and Science*, *46*, 314–323.

Li, L., Al-Muntasheri, G. A., & Liang, F. (2016). A review of crosslinked fracturing fluids prepared with produced water. *Petroleum*, *2*(4), 313–323.

Lo Nostro, P., & Ninham, B. W. (2012). Hofmeister phenomena: An update on ion specificity in biology. *Chemical Reviews*, *112*, 2286–2322.

Lo Nostro, P., & Ninham, B. W. (2016). Editorial: Electrolytes and specific ion effects. New and old horizons. *Current Opinion in Colloid & Interface Science*, *23*, A1–A5.

Magazù, S., Migliardo, P., Musolino, A. M., & Sciortino, M. T. (1997). α,α-Trehalose-water solutions. 1. Hydration phenomena and anomalies in the acoustic properties. *Journal Physical Chemistry B*, *101*, 2348–2351.

Maleki, A., Kjøniksen, A.-L., & Nyström, B. (2008). Effect of pH on the behavior of hyaluronic acid in dilute and semidilute aqueous solutions. *Macromolecular Symposia*, *274*, 131–140.

Marcus, Y. (1991). Thermodynamics of solvation of ions. Part 5. Gibbs free energy of hydration at 298.15 K. *Journal of the Chemical Society, Faraday Transactions*, *87*(18), 2995–2999.

Montgomery, C. (2013). Fracturing fluid components. In R. Jeffrey (Ed.), *Effective and sustainable hydraulic fracturing* (pp. 25–45). InTech.

Nakamura, K., Hatakeyama, T., & Hatakeyama, H. (1991). Formation of the liquid crystalline state in the water–sodium alginate system. *Sen'i Gakkaishi*, *47*, 421–423.

Nandhini Venugopal, K., & Abhilash, M. (2010). Study of hydration kinetics and rheological behaviour of guar gum. *International Journal of Pharma Sciences and Research*, *1*(1), 28–39.

Naoi, S., Hatakeyama, T., & Hatakeyama, H. (2002). Phase transition of locust bean gum-, tara gum- and guar gum-water systems. *Journal of Thermal Analysis and Calorimetry*, *70*, 841–852.

Norton, I. T., Morris, E. R., & Rees, D. A. (1984). Lyotropic effects of simple anions on the conformation and interactions of kappa-carrageenan. *Carbohydrate Research*, *134*, 89–101.

Osborn, S. G., Vengosh, A., Warner, N. R., & Jackson, R. B. (2011). Methane contamination of drinking water accompanying gas-well drilling and hydraulic fracturing. *Proceedings of the National Academy of Sciences*, *108*(20), 8172–8176.

Osswald, T., & Rudolph, N. (2015). Polymer rheology. In *Understanding plastics rheology*. Hanser.

Piculell, L., & Nilsson, S. (1989). Anion-specific salt effects in aqueous agarose systems. 1. Effects on the coil-helix transition and gelation of agarose. *Journal of Physical Chemistry*, *93*, 5596–5601.

Schnoor, E. A., Singh, D., & Russel, A. G. (2016). *Aldehydes as a catalyst for an oxidative breaker*. Retrieved: March 16, 2017, from http://www.google.it/patents/WO2016099502A1.

Schultheiss, N. C. (2015). *Multi-component materials for breaker activity control*.. Retrieved: March 16, 2017, from http://www.google.it/patents/WO2015020670A1.

Schwierz, N., Horinek, D., Sivan, U., & Netz, R. R. (2016). Reversed Hofmeister series—The rule rather than the exception. *Current Opinion in Colloid & Interface Science*, *23*, 10–18.

Singh, T., Meena, R., & Kumar, A. (2009). Effect of sodium sulfate on the gelling behavior of agarose and water structure inside the gel networks. *Journal of Physical Chemistry B*, *113*, 2519–2525.

Tatini, D., Tempesti, P., Ridi, F., Fratini, E., Bonini, M., & Baglioni, P. (2015). Pluronic/gelatin composites for controlled release of actives. *Colloids and Surfaces B: Biointerfaces*, *135*, 400–407.

Vengosh, A., Jackson, R. B., Warner, N., Darrah, T. H., & Kondash, A. (2014). A critical review of the risks to water resources from unconventional shale gas development and hydraulic fracturing in the United States. *Environmental Science & Technology*, *48*(15), 8334–8348.

Winkworth-Smith, C. G., MacNaughtan, W., & Foster, T. J. (2016). Polysaccharide structures and interactions in a lithium chloride/urea/water solvent. *Carbohydrate Polymers*, *149*, 231–241.

Xu, Y., Wang, C., Tam, K. C., & Li, L. (2004). Salt-assisted and salt-duppressed sol–gel transitions of methylcellulose in water. *Langmuir*, *20*, 646–652.

Yasuda, K., Armstrong, R. C., & Cohen, R. E. (1981). Shear flow properties of concentrated solutions of linear and star branched polystyrenes. *Rheologica Acta*, *20*(2), 163–178.

Yin, W., Zhang, H., Huang, L., & Nishinari, K. (2008). Effects of the lyotropic series salts on the gelation of konjac glucomannan in aqueous solutions. *Carbohydrate Polymers*, *74*, 68–78.

# Carbon Black-Induced Electrical Responsiveness in Viscoelastic Formulations

Filippo Sarri[a], Duccio Tatini[a], Martina Raudino[a], Moira Ambrosi[a], Emiliano Carretti[a],
and Pierandrea Lo Nostro[a,b,*]

a: Department of Chemistry "Ugo Schiff" and CSGI, University of Florence, 50019 Sesto Fiorentino (Firenze), Italy
b: Enzo Ferroni Foundation, 50019 Sesto Fiorentino (Firenze), Italy

---

[*] Corresponding author. Tel: +39 055 4573010. E-mail: pierandrea.lonostro@unifi.it (P. Lo Nostro)

## Abstract

Carbon black (CB) is an interesting material that is commonly added to different kinds of materials such as rubber, rubber and polymeric blends in order to impart desired functionalities. For example the addition of CB extends the lifetime of a rubber, improves its stability and makes it more resistant against abrasion and mechanical stresses. In this work, carbon black is added to aqueous viscoelastic dispersions based on sodium oleate, or guar gum, sodium hyaluronate or hydroxypropyl cellulose gels, in order to obtain higher viscosities and conductivities, enhance the thermal properties and provide electrical responsiveness to the final formulations. Rheology, optical microscopy, SAXS and conductivity measurements are performed to test and compare the properties of CB-enriched samples to the original dispersions. The results indicate that even small amounts of carbon black lead to an enhanced stability against mechanical and thermal stresses, and imparts a significant electrical responsiveness to an external voltage.

This work shows that the addition of carbon black to viscoelastic systems or to polysaccharide gels imparts interesting technological features that significantly expand the horizon of their potential applications, for example in situations where the remote control of their physico-chemical properties is necessary and not easily obtained with other systems.

## 1. Introduction

The use of carbon black (CB) as an additive in the manufacturing of plastic, rubber and various polymeric blends currently applies to many industrial areas [1]. This wide use is related to the peculiar properties that the carbon powder imparts to the rubber blend. For example CB enriched tires show a longer lifetime, a lower thermal degradation and a higher resistance to abrasion and mechanical stresses [2,3].

Another remarkable fraction of the annual CB production, close to 20%, is used in the rubber industry, where CB is added as a filler to improve mechanical, thermal and tensile properties of natural rubbers and elastomers [4-6]. The addition of carbon black in a rubber matrix deeply affects its mechanical properties. However the rubber's mechanical responses can be further modified through an appropriate functionalization of the carbonaceous particles with, e.g., phenol, carboxyl or lactone functional groups as reported by Park [7].

CB also finds a remarkable use in the polymer industry, especially in the production of polypropylene, polyester and polyethylene [8,9]. In fact, CB is able to capture the UV wavelengths that largely contribute to the polymer degradation [10]. The benefits of CB for plastics are not limited just to the UV shielding effect. The presence of carbonaceous particles grants the plastic matrix a greater electric conductivity and an increased resistance to thermal degradation, abrasion and tear [11,12]. Moreover, the addition of CB brings about another advantage, i.e. the reduction of polymeric materials with no significant modification of their mechanical properties.

More recently, CB has attracted some attention for the production of specifically designed nanocomposites. According to Bagavathi, CB can be combined to $Fe_3O_4$ and used in dye-sensitized solar cells (DSSC) as a better performing and low cost alternative material to conventional platinum counter electrodes [13]. Battista reports on the coupling of CB and $LiNbO_3$ crystals for the production of devices for the accumulation of solar power based on the pyroelectric effect [14]. The coupling of polyaniline and CB leads to the production of microwave absorbing materials [15], while the combination of CB and a suitable polymer can lead to the production of a portable sensor for the detection of volatile organic compounds (VOCs), i.e. a portable electronic nose system [16].

Although CB is mainly used in solids such as plastics and rubbers, its addition to liquid matrices is considerably increasing. This trend is related to the use of CB as pigment in paints and inks, particularly those for ink-jet printing [17-20].

In this contribution we explore the potential use of carbon black in liquid systems such as polysaccharide dispersions or viscoelastic surfactants (VES) based formulations for the control and improvement of their thermal properties, rheological behavior, conductivity and electrical responsiveness. The investigation was conducted through rheology, electrical conductivity, optical microscopy and small angle X-ray scattering (SAXS) experiments. The results suggest that CB improves the performances of such water-based dispersions without affecting the 3D ordered network and its rheological behavior. CB was added in small amounts, 3% and 10% w/w for polysaccharides and VES, respectively. Such contents are much lower than those usually necessary to modify the properties of most composites (around 20% w/w) [21]. The formation of fluid systems that contain relatively moderate amounts of CB paves the way to new potential applications in so far unexplored fields, such as the formulation of fluids for hydraulic fracturation involved in the extraction of shale gas.

## 2. Materials and Methods

### 2.1. Materials

Sodium oleate (NaOL, ACS grade) was purchased from Riedel-De Haën (Seelze, Germany). Carbon Black VULCAN® XC-72R was provided by Cabot Corporation (Boston, USA), KCl (≥ 99%) and saponin (≥ 99%) were purchased from Sigma-Aldrich (Milan, Italy), guar gum and hydroxypropyl cellulose (average molecular mass 2000 and 1600-1800 kDa, respectively) were supplied by Lamberti S.p.A. (Milan, Italy), and high molecular weight (1800 – 2000 kDa) sodium hyaluronate was purchased from Stanford Chemicals Company (Fairbanks, CA). All solutions and dispersions were prepared with Milli-Q water (resistivity > 18 MΩ cm at 25 °C).

Preparation of the Polysaccharide Dispersions: 0.5% w/w water dispersions of guar gum (GG), hydroxypropyl cellulose (HPC) and sodium hyaluronate (SH) were prepared by slowly adding a weighted amount of the polysaccharide powder to MilliQ water under constant stirring at room temperature. In these conditions homogeneous dissolution occurs in about 30 minutes for all the investigated biopolymers.

### *2.2. Sample preparation*

### *2.2.1. Preparation of the VES dispersions*

2% and 13% w/w VES samples were prepared by dissolving under magnetic stirring the proper amount of sodium oleate in MilliQ water or in a 0.5 M KCl aqueous solution.

### *2.2.2. Addition of carbon black*

Carbon black was added to the polysaccharide or to the VES samples following two different procedures: a) To effectively include CB in the polysaccharide matrices, a 2% w/w saponin solution was first prepared. This solution was added to a weighted amount of CB in order to obtain a final CB concentration of either 1% or 3% w/w and magnetically stirred for a few minutes. The mixture was sonicated for 1 hour at 40 kHz and the polysaccharide was added under magnetic stirring. b) In the case of the VES systems, no additive was necessary for the dispersion of CB, as sodium oleate itself is able to disperse the carbonaceous particulate. Hence, the VES solution was simply added to a weighted amount of CB (1, 3 or 10% w/w), then the mixture was sonicated for 30 minutes.

### *2.3. Optical microscopy*

Nikon Eclipse Ti-S Inverted Microscope was used to obtain optical images of CB dispersions in saponin and sodium oleate. All experiments were performed in automatic mode using an objective with a 10x magnification at room temperature. At least three different regions for each sample were analyzed in order to obtain a statistically meaningful result.

### *2.4. Rheology*

Rheology measurements were performed by a Paar Physica UDS 200 rheometer working in the controlled shear-stress mode. For all samples a plate–plate geometry (diameter 4.0 cm; gap 300 $\mu$m) was used. In these operating conditions, the total amount of the sample in the cell was about 0.5 mL. Rheological measurements were performed at 25, 30, 40, 50 and 60 °C (Peltier control system). For each sample, the flow curve was acquired in a torque range between $10^{-3}$ and 2000 mN m, after a 15 min soaking time to equilibrate at the set temperature. Frequency sweep measurements were carried out within the linear viscoelastic range determined by means of an amplitude sweep test. The storage (*G'*) and loss (*G"*) moduli were measured over the frequency range of 0.001 to 100 Hz.

### *2.5. Conductivity*

Conductivities of both polysaccharide and VES systems were measured through a sensION™ +EC7 conductivity platinum cell (HACH, error ≤ 5% in the measuring range between 0.2 and $2 \cdot 10^5$ mS $cm^{-1}$). For each sample at least five measurements were performed and averaged.

### *2.6. Electrical responsiveness*

The electrical responsiveness of VES and polysaccharide-based systems was assessed by applying a 30 V voltage for 1 hour through a Hewlett Packard Harrison 6112 A DC power supply. Two platinum wires of 1.0 mm diameter (Sigma-Aldrich) were dipped into the dispersions and used as electrodes.

### *2.7. Small angle X-ray Scattering*

SAXS experiments were carried out using a HECUS S3-Micro (Kratky camera) equipped with two position-sensitive detectors (PSD-50M) containing 1024 channels of 54-μm width. Cu Kα radiation of wavelength 1.542 Å was provided by a GeniX X-ray generator (Xenocs, Grenoble) working with a microfocus sealed-tube operating at 50 W. The sample to detector distance was 281 mm. The volume between the sample and the detector was kept under vacuum during the measurements to minimize scattering from the air. The Kratky camera was calibrated using silver behenate, which is known to have a well-defined lamellar structure ($d$ = 58.38 Å) [22]. Scattering curves were monitored in a $q$-range from 0.02 to 0.55 $Å^{-1}$. Liquid samples were analyzed in a borosilicate glass capillary tube. For all measurements the temperature was kept constant at 25 °C controlled by a Peltier element, with an accuracy of ± 0.1 °C. All scattering curves were corrected for the empty capillary contribution considering the relative transmission factors. Desmearing of the SAXS curves was not necessary because of the sophisticated point microfocusing system.

## 3. Results and Discussion

### *3.1. Homogeneity of carbon black dispersions*

Optical micrographs of CB dispersions in saponin and sodium oleate (see Figure 1) were acquired to assess the homogeneity of CB dispersions as a function of the CB amount and in the presence of different dispersing agents (saponin or sodium oleate). Indeed, it was proved that the structure of carbon black, the nature of the polymer, and the processing history of the sample affect the electrical conductivity of the composite [23,24].

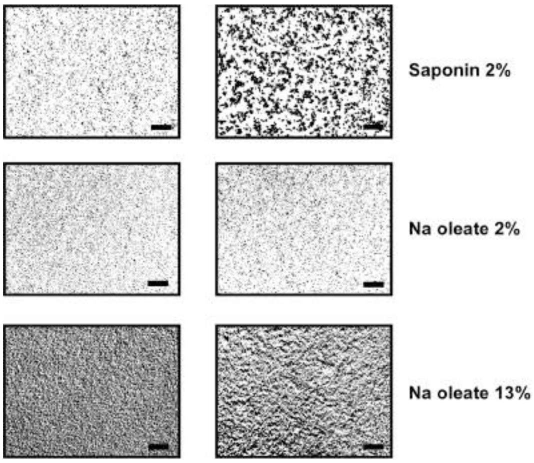

**Fig. 1.** Optical micrographs of carbon black 1% (left) and 3% w/w (right) dispersions in saponin 2% and sodium oleate 2% and 13% w/w. Scale bar: 300 μm.

Our results show that stable aqueous dispersions of CB with saponin or sodium oleate were obtained. Carbonaceous aggregates form when the amount of carbon black increases from 1% to 3% w/w. The carbonaceous particulate appears homogeneously dispersed also in the presence of the higher amount of CB. Therefore, any effect on the electro-responsiveness due to samples inhomogeneity can be disregarded.

This result is of particular interest for practical applications since several efforts were made in the past to find an easy way to disperse hydrophobic carbonaceous materials, such as fullerenes or carbon nanotubes in aqueous media, especially for biomedical applications [25,26]. Some works report the encapsulation of CB in silica [27,28], or polymer particles [29], while others suggest the use of surfactant molecules, such as sodium oleate and saponin, that can provide both electrostatic and steric stabilization, depending on the nature of the hydrophilic head [30,31].

In particular, saponin can adsorb by exposing its hydrophobic triterpene or steroid moiety to the CB surface, while the glucoside hydrophilic head faces the aqueous phase [32]. In the case of sodium oleate, we expect that its adsorption on the CB surface occurs through the C=C double bond in the chain, as suggested by Wang [33], while the negatively charged carboxylates stabilize the structure electrostatically.

*3.2. Flow curves of VES and polysaccharides systems*

Rheological flow curves were acquired on both pure and carbon black-enriched polysaccharides or VES formulations. The different rheological profiles shown in Figure 2 reflect the viscosity changes and network stiffening induced by CB. For the sake of brevity, we discuss the results obtained for the samples showing the most significant changes, i.e. polysaccharides and VES formulations containing 3 and 10% of CB, respectively.

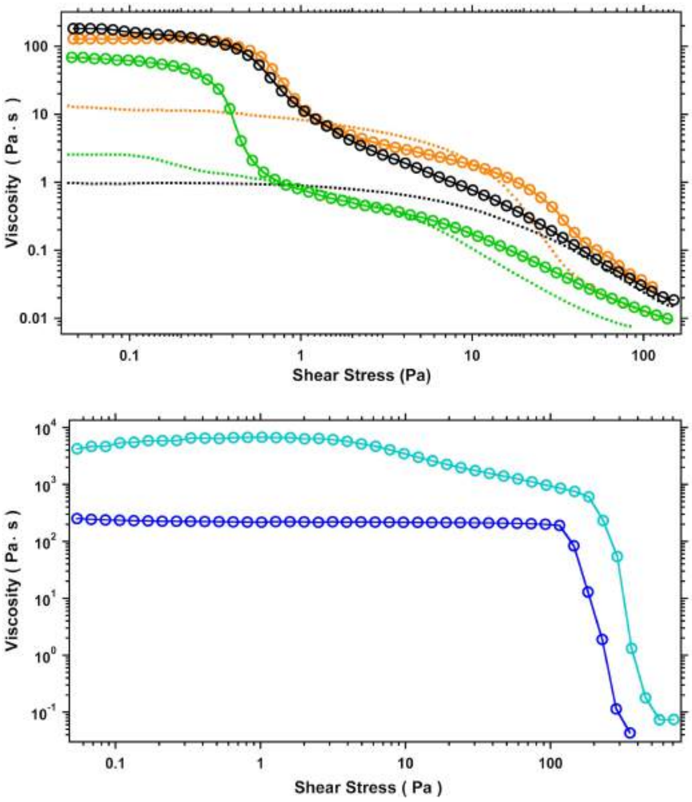

**Fig. 2.** Top: Flow curves of 0.5% w/w pure (dotted lines) and containing 3% w/w of CB (empty circles) GG (green), HPC (black), and SH (orange) dispersions. Bottom: Flow curves of NaOL 13% + KCl 4% (dark blue) and NaOL 13% + KCl 4% + CB 10% (light blue).

The pure polysaccharide dispersions exhibit a non-Newtonian behavior with the zero stress viscosity ranging between 1 and 12 Pa s moving from HPC to SH [34]. The addition of CB leads to an increase in the viscosity of at least an order of magnitude. This result is in line with the well known thickening effect of CB [35], and reflects the effective inclusion of the additive in the polysaccharide matrices. Moreover, in the presence of CB the rheological profiles are significantly modified with respect to the pure polysaccharides. In fact, besides the Newtonian region with a high viscosity value at low shear rate, a marked change in the slope of the curves is observed, for shear stress ranging between 0.3 and 3 Pa, especially for GG and SH based samples. This behavior is probably related to the viscous drag between the polymer chains adsorbed on the CB particles and the bulk polymer, as described by Barrie in the study of the interaction between CB and an acrylic resin [36].

Regarding the VES formulations (Figure 2), the pristine system NaOL 13% + KCl 4% shows the typical non-Newtonian behavior of worm-like micelles of ionic surfactants: in particular, the sample displays a Newtonian plateau with a high viscosity value ($\eta_0$ = 234 Pa s) followed by a shear-thinning region above a critical stress (around 115 Pa) that reflects the alignment of the worm-like chains in the shear flow direction [37,38]. When CB is added to the VES system up to 10% w/w, we observed a strong increase in the zero-stress viscosity, from 234 to 5373 Pa s, indicating that the carbonaceous particulate acts as a reinforcing agent for the network. Furthermore, we observed that the shear-thinning behavior starts at a higher value of the critical stress, suggesting a structuring effect for the CB particles. Despite the addition of CB strongly affects the stiffness of the VES network, the rheological profile with or without CB remains essentially unaltered. We argue that the structure of the NaOL micellar network is not significantly modified by the presence of the carbonaceous particles. In order to understand the effect of CB on the mechanical properties of NaOL dispersions and to obtain insights on their relaxation dynamics, oscillatory frequency sweep tests were carried out on VES systems before and after the addition of 10% of carbon black (see Figure 3).

At high frequency the samples behave as elastic systems (G’ shows a plateau and dominates over *G”*), whereas at low frequency they show a viscous behavior (*G”* > *G’*).

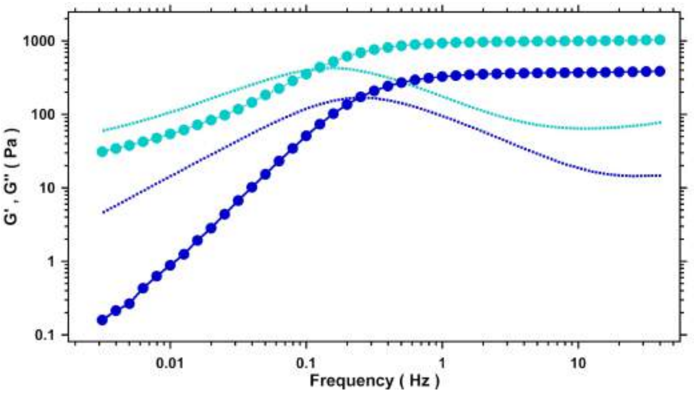

**Fig. 3.** Storage (circles) and loss (dotted lines) moduli of pristine (dark blue) and 10% w/w CB-enriched (light blue) NaOL 13% + KCl 4% VES formulations. All the measurements were carried out in the linear viscoelastic regime (strain amplitude = 1.0 %).

The dynamics of the studied systems cannot be described according to the single-element Maxwell model, hence *G'* and *G"* are used to calculate the time-weighted relaxation spectra *H(τ)* reported in Figure 4 [39]. The CB-enriched VES formulation shows a higher relaxation time, confirming the reinforcing role of the particulate in the stabilization of the matrix. Moreover, considering that the numbers of interconnections between the worm-like micelles is directly linked to the values of the elastic plateaus in the oscillatory frequency sweep tests (Figure 3) [40], we argue that carbon black leads to the formation of a more entangled micellar network, as suggested by the higher value of the *G'* modulus associated to the CB-enriched sample.

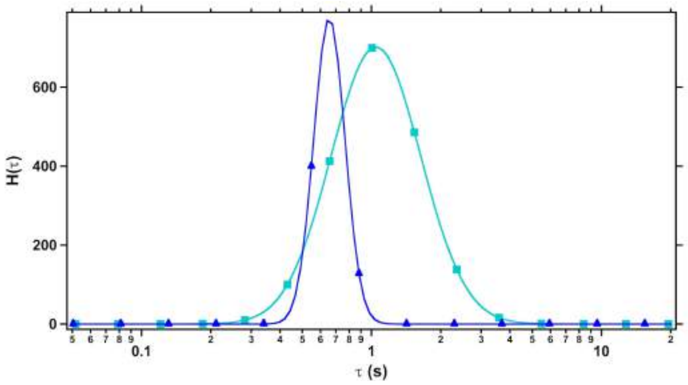

**Fig. 4.** H(τ) relaxation spectra of pristine (dark blue) and CB-enriched (light blue) NaOL 13% + KCl 4% VES formulations.

A further confirmation of the negligible effect of CB on the micellar structure of NaOL arises from the SAXS data analysis (Figure A1 in the Appendix). The scattering curves of the samples before and after the addition of CB are similar, except for the strong contribution to the scattering intensity in the low *q*-region ($q < 0.005$ Å$^{-1}$) due to the CB particles. This result indicates that the addition of CB does not affect the size and the intermicellar interactions among the charged aggregates. According to the literature [41,42], the observed scattering profile is associated to the presence of polydispersed core-shell elongated objects interacting via a screened Coulomb potential in solution.

### *3.3. Electrical stimulus*

The electroresponsivity of polymers is a widely known phenomenon that involves a large set of biomolecules [43-45]. The application of a voltage (30 V for 1 hour) to the formulations produces electrophoretic, polarization and osmotic effects, that result in the separation of a liquid and easy-flowing phase on one electrode, and of a viscous and sticky phase that concentrates at the opposite side. Taking advantage of their different viscosities, the two phases can be easily separated by simply turning the vessel. The measured weight gives a rough estimation of the percentage of recovered liquid phase squeezed out from the sample after the electrostimulation (Table 1).

**Table 1.** Zero stress viscosities ($\eta_0$ ± 5%, in Pa s) and mass percentage of liquid (L, %) and sticky (S, %) phases recovered after the application of a voltage (30 V for 1 hour).

| Sample | $\eta_0$ | L | $\eta_0$(L) | S | $\eta_0$(S) |
|---|---|---|---|---|---|
| GG | 2.1 | - | 1.1 | - | 1.1 |
| HPC | 1.3 | 61 | 0.55 | 39 | 40 |
| SH | 13 | 53 | 0.15 | 48 | 43 |
| NaOL 13% + KCl 4% | 234 | 34 | 390 | 66 | 4.4 |
| GG+CB 3% | 67 | - | 22 | - | 22 |
| HPC+CB 3% | 118 | 50 | 20 | 50 | 4482 |
| SH+CB 3% | 129 | 28 | 63 | 72 | 975 |
| NaOL13% + KCl 4% + CB 10% | 5373 | - | 356900 | - | 356900 |

All pure polysaccharide dispersions, except for guar gum, exhibit this behavior in response to the electrical stimulus. Figure 5 shows the flow curves in the case of sodium hyaluronate. The electrical stimulus effect on the flow curves for the GG and HPC dispersions are reported in the Appendix (Figure A2). By comparing the profiles of the pristine SH sample (black) and those of the “liquid” and “sticky” phases (red and green, respectively), we figured out that the rheological response is affected by the application of the voltage. Indeed, the red profile shows a two order of magnitude lower $\eta_0$, whereas the green curve shows a noticeable increase in $\eta_0$. Despite this difference in the viscosity values, the three rheological profiles are similar. This suggests that all the samples possess the same structure and no modification in the polysaccharide network is induced by the electrical stimulation. Thus we argue that the changes in viscosity are simply due to the electrically induced differences in the polysaccharide/water ratio. Indeed, the applied voltage leads to the contraction of both SH and HPC networks and results in the reduction of the mesh size and in the partial removal of water from the polysaccharidic network. As expected the amount of the liquid portion recovered at the end of the electrical stimulus depends on the nature of the polysaccharide (see Table 1).

The electrical stimulus imparts an effect also on the NaOL-based formulations, leading to the formation of two phases with different flow curves (Figure 5).

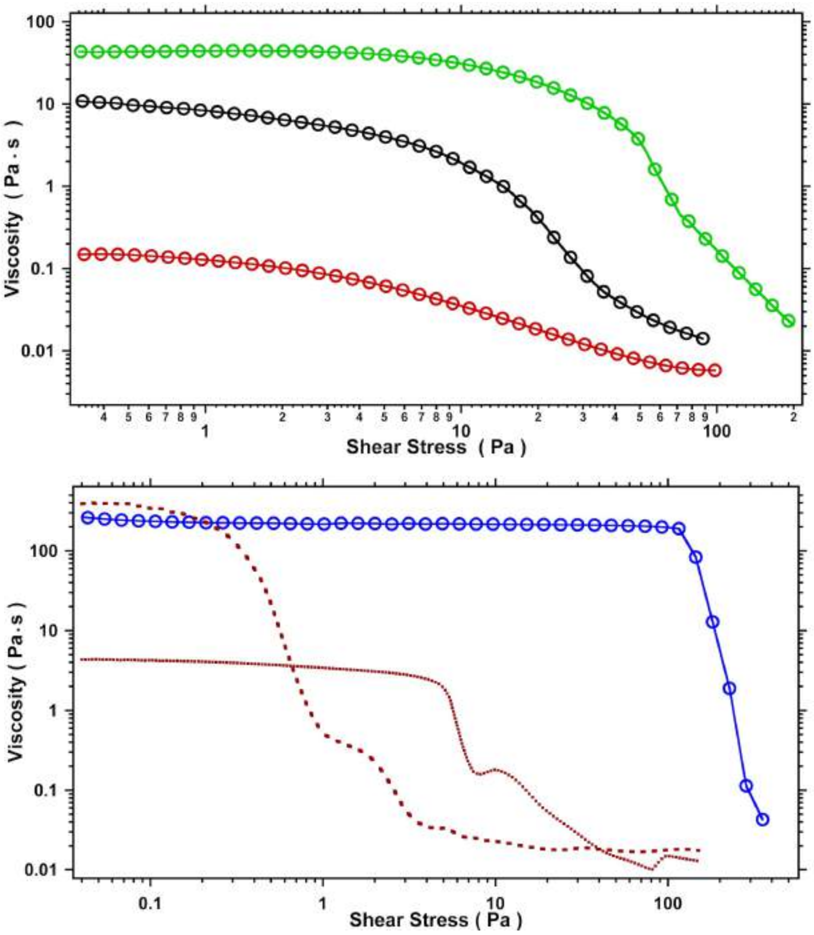

**Fig. 5.** Top: Flow curves of 0.5% w/w SH dispersion before the application of the electrical stimulus (black) and of the two phases separated at the end of the process (viscous phase in green, fluid phase in red). Bottom: Flow curves of NaOL 13% + KCl 4% VES formulation before the application of the electrical stimulus (blue circles) and of the two phases separated at the end of the process (brown lines).

Both phases show lower profiles and the curve obtained from the sticky and more viscous portion is not shown. Moreover, unlike the case of polysaccharide formulations, the two collected phases exhibit a rheological profile significantly different from that of the sample before the stimulus. This result suggests that the application of the voltage partially breaks the micellar entanglement and the homogeneity of the sample, leading to irregular and more indented profiles in comparison to the typical VES flow curve.

Considering that both pure VES and polysaccharides show a remarkable responsiveness upon the application of a voltage, their electro-responsiveness was checked after the addition of the conducting CB in different amounts: from 1 to 3% for the polysaccharides and up to a maximum of 10% for the VES formulation. The flow curves of the two phases collected after the application of the electrical stimulus in the presence of CB are reported in Figure 6.

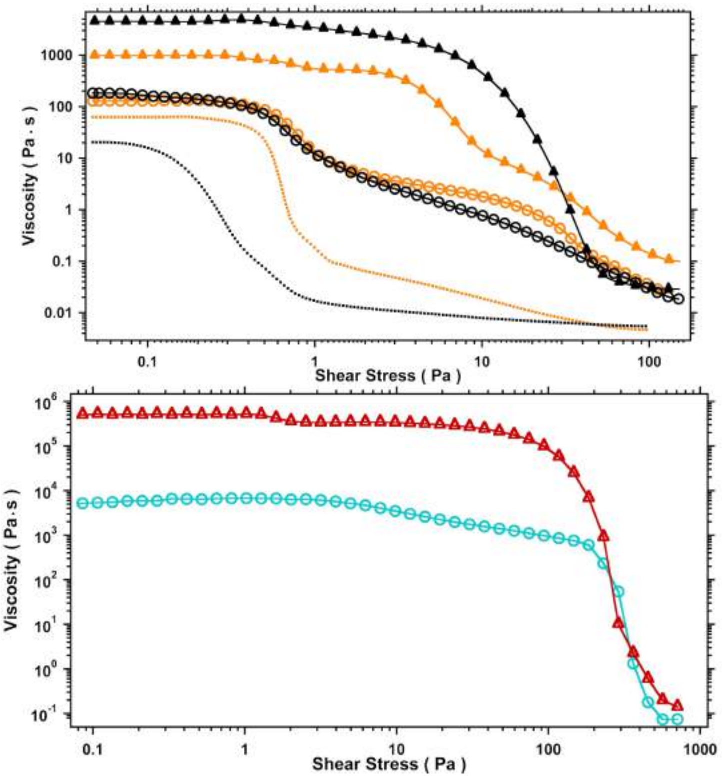

**Fig. 6.** Top: Flow curves of 0.5% w/w HPC (black) and SH (orange) dispersion containing CB 3 wt% before the application of the electrical stimulus (empty circles) and of the two phases separated at the end of the process (viscous, triangles and liquid, dotted lines). Bottom: Flow curves of sodium oleate 13% + KCl 4% VES formulation containing CB 10 % before the application of the electrical stimulus (light blue circles) and at the end of the process (red triangles).

For the polysaccharide matrices, we recorded different responses to the electrical stimulus depending on the nature of the investigated polysaccharide (Figure 6 top).

However, in all cases with the exception of guar gum, the change in the zero-shear viscosities of the different phases after the stimulus is enhanced compared to the pure polysaccharides. This result suggests that CB can be successfully used as an additive to tune the response of polysaccharide formulations to an external stimulus, such as the application of a voltage.

When the CB-enriched VES formulation is electrically stimulated, the zero-stress viscosity of the formulation increases of about two orders of magnitude, indicating the formation of a more rigid network, probably due to the shrinking of the worm-like micelle network. However, as for the pristine formulation before the addition of CB, we did not observe the formation of two different phases, presumably because CB acts as a reinforcing agent. In addition, the rheological profile of the sample before and after the stimulus does not change significantly, showing the typical non-Newtonian behavior of the VES formulations. This result confirms the view that, in the presence of carbon black, the electrical stimulus can be used as a trigger to effectively increase the strength and stiffness of the matrix without changing the viscoelastic network of sodium oleate-based formulations.

### *3.4. Effect of temperature*

To evaluate the increased thermal resistance of our formulations after the addition of carbon black, the flow curves were acquired at 25, 30, 40, 50, and 60 °C. For the sake of comparison, the measurements were performed on polysaccharide- and VES-based formulations both with and without CB powder.

Figure 7 shows the rheological behavior of GG dispersions before and after the addition of CB (3% w/w). As expected, the raise in temperature causes a downward shift in the polysaccharide flow curve, with a progressive lowering of the zero shear-viscosity value moving from 25 to 60 °C. More specifically, the viscosity of pristine polysaccharide system ranges between 2.15 and 0.34 Pa s, while the GG+CB samples exhibit a wider and higher spectrum between 67 and 10 Pa s. Thus, the presence of CB enhances the thermal resistance of the GG polysaccharide network with higher viscosity profiles in comparison to the pure GG sample. Moreover, the two systems exhibit quite different profiles in the lower stress region, while they flow in the same way. This feature seems to suggest that an additional structural order is granted by the carbonaceous particles, that are responsible for the higher viscosity in the GG+CB system. However, when the applied stress increases, this higher structuring breaks down and the difference is canceled out.

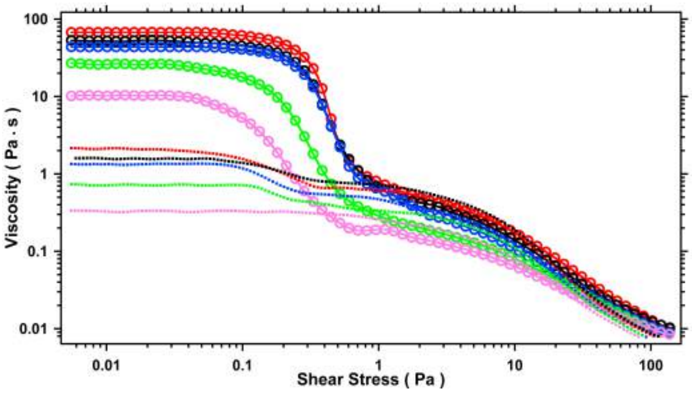

**Fig. 7.** Flow curves of GG 0.5% (dotted lines) and GG 0.5% + CB 3% (circles) at 25 (red), 30 (black), 40 (blue), 50 (green) and 60 (pink) °C.

Despite this effect, the flow curves remain unchanged within each series. Thus, the intermolecular interactions of the two systems are weakened as temperature raises, resulting in a softer network where the chains slide one over the other with a progressively lower friction. However, the similarities among the profiles in each polysaccharide set of curves confirm that the structures of the network are only weakened but not modified in different arrangements.

For SH and SH+CB we recorded a similar rheological behavior (Figure 8). Indeed, sodium hyaluronate exhibits the same trend observed for guar gum with a progressive lowering of the zero-stress plateau as temperature increases.

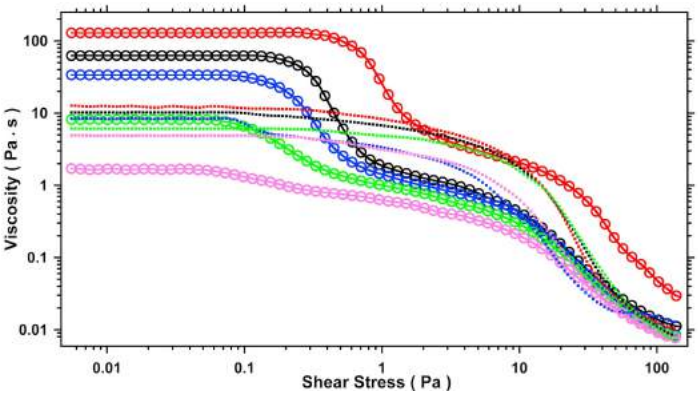

**Fig. 8.** Flow curves of SH 0.5% (dotted lines) and SH 0.5% + CB 3% (circles) at 25 (red), 30 (black), 40 (blue), 50 (green) and 60 (pink) °C.

The presence of CB does not modify this behavior but the response to the increase in temperature is enhanced. More in detail, the pristine SH system shows only a limited decrease in the viscosity, between 12 and 5 Pa s, while the SH+CB sample shows a wider gap, from 129 to 2 Pa s. In comparison to guar gum the addition of carbonaceous particles affects the SH network thermal resistance in a slightly different manner: the system is strengthened below 50 °C, while at higher temperatures the presence of CB seems to promote the chains disentanglement. As with guar gum, the CB-enriched system shows a double plateau and a double drop in its profile. Instead, the pure polysaccharide exhibits a single plateau associated to a single fall in viscosity. This difference reflects the second level structure, originating from the reinforcement of the polysaccharide network due to the CB particles, that is responsible for the overall increased rigidity and viscosity. Moving along the temperature series, we note the shift of the critical stress at which the higher viscosity plateau starts to decrease. The highly ordered structure loses its stability: in fact, passing from 25 to 50 °C, the gap between the first and the second plateau progressively becomes less pronounced, until it is barely visible in the profile recorded at 60 °C.

The last examined polysaccharide dispersion, HPC 0.5 %, shows an opposite trend, as reported in Figure 9. Both in the case of HPC and HPC+CB, the zero-shear viscosity increases with temperature, as the polysaccharide network becomes more viscous and rigid. Moreover, also the critical stress values corresponding to the collapse of the network are shifted to higher rates. This counterintuitive behavior does not represent an absolute novelty in the literature. Indeed, a similar case concerns another cellulosic derivative, the extracellular polysaccharide produced by some bacterial strains of Xanthomonas Campestris [27,46]. This biomolecule shows a viscosity trend that follows in parallel the temperature profile: the higher the temperature, the greater the zero stress viscosity of the system. In our case, this response to the thermal stress is presumably due to the partially hydrophobic nature of the HPC side-chain.

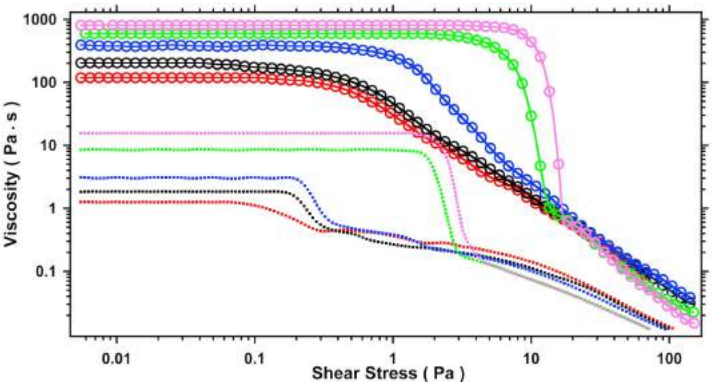

**Fig. 9.** Flow curves of HPC 0.5% (dotted lines) and HPC 0.5% + CB 3% (circles) at 25 (red), 30 (black), 40 (blue), 50 (green) and 60 °C (pink).

When temperature is raised the hydrating water molecules are depleted from the hydroxypropyl side groups, and lead to the formation of ”stronger aggregation of interpolymer complexes” stabilized by hydrogen bonding and hydrophobic interactions [47]. The final result is an increase in the network crosslinking degree and a strengthening in the viscosity and stiffness of the system. A further increase in the temperature up to 120 °C leads to the gelation of HPC.

In summary, the rheological profiles confirm that when CB is added to polysaccharide matrices, the result is an enhancement in the formulation resistance to the temperature increase, while the rheological trend of each polysaccharide remains unchanged.

Regarding the NaOL-based formulations, Figure 10 shows the flow curves acquired at the different temperatures on both systems before and after the addition of CB.

In the absence of CB, the temperature increase induces the breaking in the entangled micellar network with a rapid drop in the viscosity of the system. In the case of the CB-enriched formulations, the zero-shear viscosities are about two orders ofmagnitude higher, confirming the reinforcement of the network due the addition of CB. Furthermore, the rheological profile is quite different if compared to the pristine samples, with two different regions before the shear-thinning behavior.

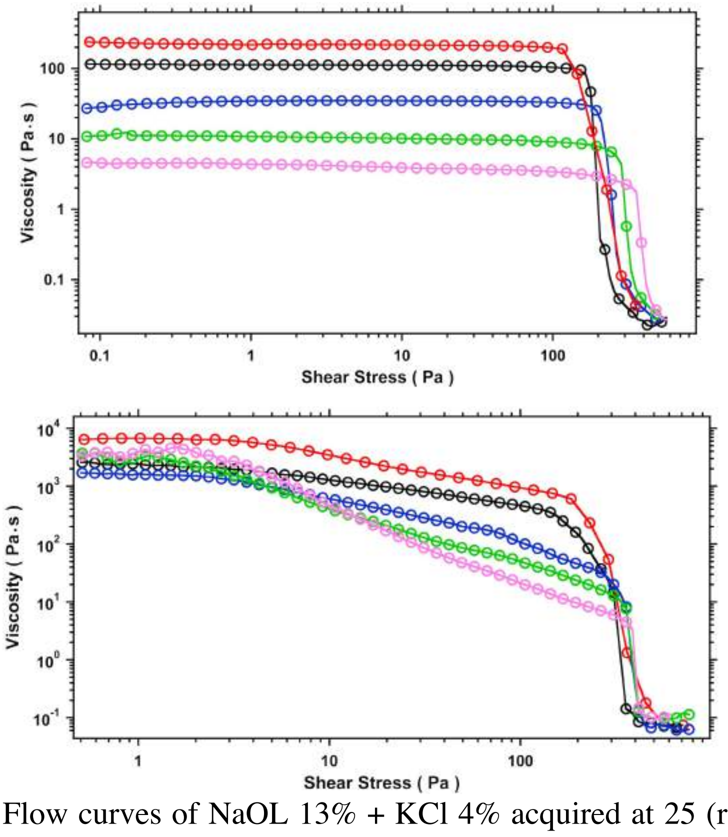

**Fig. 10.** Top: Flow curves of NaOL 13% + KCl 4% acquired at 25 (red), 30 (black), 40 (blue), 50 (green) and 60 (pink) °C. Bottom: Flow curves of the same VES systems containing CB 10% w/w at different temperatures.

We argue that for low values of the shear stress both the entangled micelles and the CB particles move together with the typical Newtonian behavior already observed for worm-like micellar phases. When higher shear stresses are applied to the system, the viscous force between sodium oleate micelles and the carbonaceous particles arises, producing a second region where the system behaves as a shear-thinning material [36]. It is worth noting that the system seems to have a more pronounced shear-thinning behavior as the temperature increases, as suggested by the value of critical stress that corresponds to the onset of the second region. For shear stresses higher than 100 Pa, the rapid drop of viscosity is similar to that observed for the pristine samples without CB, indicating the total break of the entangled micellar network even in the presence of the reinforcing agent.

The low-stress plateau region can be investigated at different temperatures in terms of an activated mechanism that can be interpreted accordingly to a modified Arrhenius equation (see Table A2 and Figure A3 in the Appendix) [48]. The extracted Gibbs free energy of activation ($\Delta G^{\neq}$) for the pure VES formulation is about 98 kJ mol$^{-1}$, reflecting a tight entanglement of the chains that hinders the flow. The obtained value is in line with those reported in the literature for worm-like micelles network [49,50]. In the presence of the carbonaceous additive, the VES system exhibits a different response to the temperature raise. Indeed, the viscosity decreases in the range between 25 and 40 °C, as observed in the case of pure VES, whereas it shows a higher plateau when the temperature is further increased up to 50 and 60 °C. Thus, in this case $\Delta G^{\neq}$ cannot be estimated with an Arrhenius plot.

For the polysaccharide systems the results are listed in the Appendix (Table A3 and Figure A4 and A5). In the case of pure aqueous dispersions of SH and GG, we obtained values for $\Delta G^{\neq}$ of 22 and 41 kJ mol$^{-1}$, respectively. The calculated $\Delta G^{\neq}$ values of the two polysaccharide dispersions fall in the range reported in literature for polymers [51]. A similar analysis cannot be extended to HPC because of the temperature-induced gelation process. As we already noted, when CB is added to the polysaccharide systems, we observed different responses to a temperature increment. In the case of GG (a neutral polymer), we calculated the same $\Delta G^{\neq}$ value obtained before the addition of CB (41 kJ mol$^{-1}$). Instead in the case of the anionic SH, the addition of CB induces a significant change in $\Delta G^{\neq}$, that increases from 22 to 97 kJ mol$^{-1}$.

The CB-polymer intermolecular interactions are usually interpreted in terms of a tunneling effect [52], a percolation phenomenon [53] or through a combination of the two models [54,55]. Both models assume a close contact between the chains and the CB particles. Probably, the different charge on the polysaccharide chains is the key factor that affects the CB-polymer interaction mechanism and how the system answers in response to the application of various stimuli. Anyway, the obtained results seem to indicate a complex behavior of the mixed CB-polysaccharide systems and further experiments are needed in order to describe the different mechanisms of interactions.

## 4. Conclusion

In conclusion, carbon black (CB) was added and dispersed uniformly in different green aqueous polysaccharide or viscoelastic (VES) dispersions stabilized by saponin and sodium oleate. The rheological, thermal and electrical properties of the samples showed significant changes upon the addition of CB. In particular, carbon black brings about a greater viscosity and a larger threshold of the network collapse, an improvement in the thermal properties, and imparts a remarkable electrical responsiveness to an external voltage. Moreover, all these improved performances are achieved at a quite low CB content (3% for the polysaccharide dispersions and 10% for the VES formulations), much lower than the common amounts needed to obtaining significant results [21].

The addition of carbon black to viscoelastic or polysaccharide aqueous formulations can significantly widen the horizon of their potential applications, for example in situations where the remote control of the physico-chemical properties of a water-based gel is necessary and not easily obtained with other systems, as it the case of shale gas downholes.

## Acknowledgements

The authors acknowledge funding from the European Union Horizon 2020 research and innovation program “Shale for Environment” (SXT) under grant agreement Nr. 640979.

## Appendix

### *A.1. Conductivity data*

**Table A1.** Conductivity measurements ($\kappa$, in $\mu$S cm) on polysaccharide (0.5% w/w) and VES (NaOL 13 % + KCl 4%) formulations. Carbon black (CB) is added at 3% w/w for the polysaccharide dispersions and at 10% w/w for the VES systems.

| | $\kappa$ ± Std. Dev. |
|---|---|
| GG | 75.6 ± 1.6 |
| GG + CB | 2964 ± 16 |
| SH | 928 ± 6.6 |
| SH + CB | 2965 ± 16 |
| HPC | 124.9 ± 1.4 |
| HPC + CB | 2440 ± 28 |
| VES | - |
| VES + CB | 5944 ± 234 |

### *A.2. SAXS experiments*

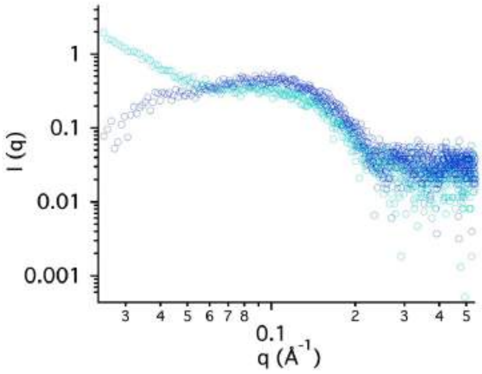

**Fig. A1.** SAXS curves of VES formulations: NaOL 13 % + KCl 4 % (dark blue) and 10 % CB enriched samples (light blue).

### *A.3. Flow curves of electrically stimulated polysaccharides*

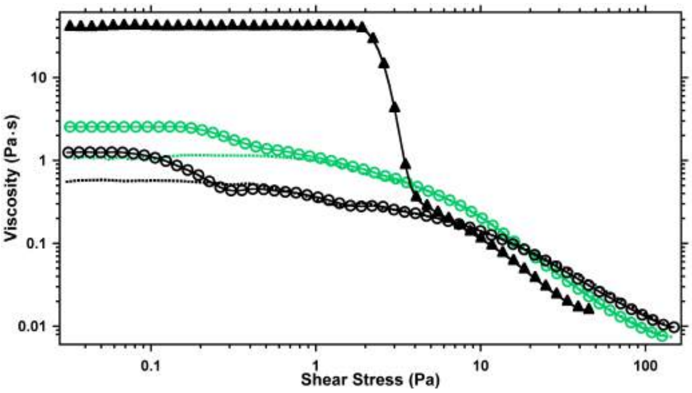

**Fig. A2.** Flow curves on HPC (black) and GG (green) before (circles) and after the electrical stimulus. The liquid and sticky portions obtained after the application of the voltage are indicated by dotted lines and triangles, respectively.

### *A.3. Arrhenius plot of VES and polysaccharide formulations*

The initial plateau region at low stress characteristic of a Newtonian behaviour for the polysaccharide chains and wormlike micelles is analyzed as a function of temperature according to the modified Arrhenius equation reported by Chandler to obtain the Gibbs free energy of activation that reflects the strength of flow in solution [48].

$$\eta_N = \eta_{\infty N}\, exp\,(\frac{\Delta G_N}{RT}) \tag{1}$$

$$RT \ln\,(\eta_N) = \mathrm{RT} \ln(\eta_{\infty N}) + \Delta G_N \tag{2}$$

$\Delta G_N$ is the slope, $RT \ln(\eta_{\infty N})$ is the intercept and $\eta_{\infty N}$ is a constant.

**Table A2.** Zero-stress viscosity values ($\eta_0$, in Pa·s) measured for VES formulations before and after the addition of 10% w/w CB, at 25, 30, 40, 50 and 60 °C.

| T | $\eta_0$ | |
|---|---|---|
| | without CB | with CB |
| 25 | 228 | 6741 |
| 30 | 150 | 2421 |
| 40 | 36 | 1627 |
| 50 | 11 | 2985 |
| 60 | 4 | 3914 |
| *ΔG*≠ (kJ/mol) | 98 | - |

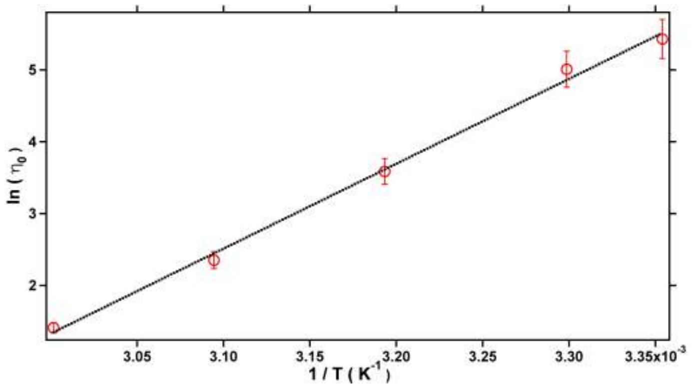

**Fig. A3.** Arrhenius plot for the NaOL 13 % + KCl 4 % sample.

**Table A3.** Zero-stress viscosity values ($\eta_0$, in Pa·s) measured for polysaccharide formulations before and after the addition of 3% w/w CB at 25, 30, 40, 50 and 60 °C.

| T | $\eta_0$ | | | | | |
|---|---|---|---|---|---|---|
| | GG | | SH | | HPC | |
| | before | after | before | after | before | after |
| 25 | 2.1 | 67 | 13 | 129 | 1.3 | 118 |
| 30 | 1.6 | 53 | 10 | 65 | 1.8 | 203 |
| 40 | 1.3 | 44 | 8.4 | 34 | 3.1 | 390 |
| 50 | 0.7 | 26 | 6.1 | 8 | 8.4 | 594 |
| 60 | 0.3 | 10 | 4.9 | 1.7 | 15 | 805 |
| $\Delta G^{\neq}$ (kJ/mol) | 41 | 41 | 22 | 97 | - | - |

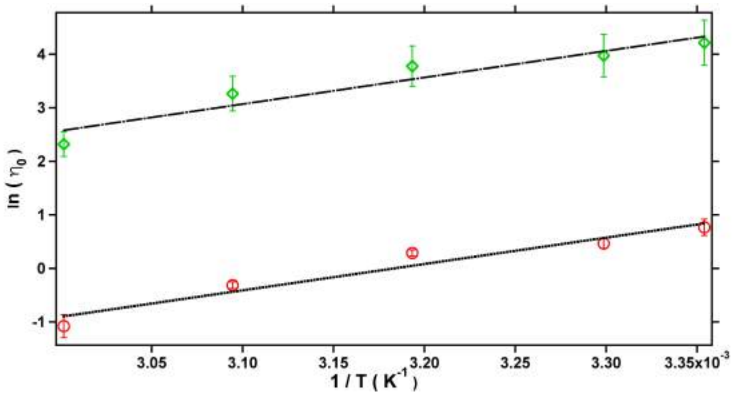

**Fig. A4.** Arrhenius plot for the guar gum dispersions before (red circles) and after (green diamonds) the addition of CB 3% w/w.

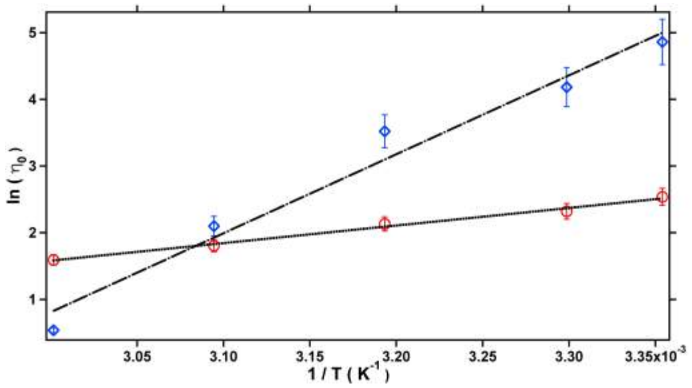

**Fig. A5.** Arrhenius plot for the sodium hyaluronate dispersions before (red circles) and after (blue diamonds) the addition of CB 3 % w/w.

## References

[1] J. G. Speight, Handbook of Petroleum Product Analysis. 2nd ed. Hoboken: John Wiley & Sons, Inc.; 2015.

[2] M. E. Semaan, C. A. Quartes, L. Nikiel, Carbon Black and silica as reinforcers of rubber polymers: Doppler broadening spectroscopy results, Polym. Degrad. Stab. 75 (2) (2002) 259-266.

[3] S.-S. Choi, J.-C. Kim, Lifetime prediction and thermal aging behaviors of SBR and NBR composites using crosslink density changes, J. Ind. Eng. Chem. 18 (3) (2012) 1166-1170.

[4] C. S. Barrera, K. Cornish, High performance waste-derived filler/carbon black reinforced guayule natural rubber composites, Ind. Crop. Prod. 86 (2016) 132-142.

[5] N. Rattanasom, T. Saowapark, C. Deeprasertkul, Reinforcement of Natural Rubber with Silica/Carbon Black Hybrid Filler, Polym. Test. 26 (3) (2007) 369-377.

[6] J. A. C. Harwood, A. R. Payne, Stress Softening in Natural Rubber Vulcanizates. Part III. Carbon Black-filled Vulcanizates, J. Appl. Polym. Sci. 10 (2) (1966) 315-324.

[7] S.-J. Park, K.-S. Cho, S.-K. Ryu, Filler–elastomer Interactions: Influence of Oxygen Plasma Treatment on Surface and Mechanical Properties of Carbon Black/Rubber Composites, Carbon 41 (7) (2003) 1437-1442.

[8] M. Liu, A. R. Horrocks, Effect of Carbon Black on UV Stability of LLDPE Films under Artificial Weathering Conditions, Polym. Degrad. Stab. 75 (3) (2002) 485-499.

[9] J. Zhao, K. Dai, C. Liu, G. Zheng, B. Wang, C. Liu, *et al.*, A Comparison between Strain Sensing Behaviors of Carbon Black/Polypropylene and Carbon Nanotubes/Polypropylene Electrically Conductive Composites, Compos. Part A-Appl. S. 48 (2013) 129-136.

[10] A. R. Horrocks, J. Mwila, M. Miraftab, M. Liu, S. S. Chohan, The Influence of Carbon Black on Properties of Orientated Polypropylene 2. Thermal and Photodegradation, Polym. Degrad. Stab. 65 (1) (1999) 25-36.

[11] H. S. Katz, J. V. Mileski, Handbook Of Fillers For Plastics. Berlin: Springer Science & Business Media; 1987.

[12] N. Hayeemasae, H. Ismail, T. B. Khoon, S. Husseinsyah, H. Harahap, Effect of Carbon Black on the Properties of Polypropylene/ Recycled Natural Rubber Glove Blends, Prog. Rubber Plast. Recycl. Technol. 32 (4) (2015) 241-252.

[13] M. Bagavathi, A. Ramar, R. Saraswathi, $Fe_3O_4$–carbon Black Nanocomposite as a Highly Efficient Counter Electrode Material for Dye-Sensitized Solar Cell, Ceram. Int. 42 (11) (2016) 13190-13198.

[14] L. Battista, L. Mecozzi, S. Coppola, V. Vespini, S. Grilli, P. Ferraro, Graphene and Carbon Black Nano-Composite Polymer Absorbers for a Pyro-Electric Solar Energy Harvesting Device Based on $LiNbO_3$ Crystals, Appl. Energ. 136 (2014) 357-362.

[15] K. H. Wu, T. H. Ting, G. P. Wang, W. D. Ho, C. C. Shih, Effect of Carbon Black Content on Electrical and Microwave Absorbing Properties of Polyaniline/Carbon Black Nanocomposites, Polym. Degrad. Stab. 93 (2) (2008) 483-488.

[16] Y. S. Kim, S.-C. Ha, Y. Yang, Y. J. Kim, Portable Electronic Nose System Based on the Carbon Black–polymer Composite Sensor Array, Sens. Actuators B Chem. 108 (1) (2005) 285-291.

[17] J.-B. Donnet, Carbon Black: Science and Technology. 2nd ed. Boca Raton: CRC Press; 1993.

[18] J. A. Belmont, J. E. Johnson, C. E. Adams (Cabot Corporation), Ink Jet Ink Formulations Containing Modified Carbon Products, Google Patents, March 20, 1997. UStates Patent 5,630,868.

[19] K. Kordás, T. Mustonen, G. Tóth, H. Jantunen, M. Lajunen, C. Soldano, *et al.*, Inkjet Printing of Electrically Conductive Patterns of Carbon Nanotubes, Small 2 (8-9) (2006) 1021-1025.

[20] S. Coppola, L. Mecozzi, V. Vespini, L. Battista, S. Grilli, G. Nenna, *et al.*, Nanocomposite Polymer Carbon-Black Coating for Triggering Pyro-Electrohydrodynamic Inkjet Printing, Appl. Phys. Lett. 106 (26) (2015) 261603.

[21] M. A. Lopez Manchado, L. Valentini, J. Biagiotti, J. M. Kenny, Thermal and Mechanical Properties of Single-Walled Carbon Nanotubes–polypropylene Composites Prepared by Melt Processing, Carbon 43 (7) (2005) 1499-1505.

[22] T. N. Blanton, T. C. Huang, H. Toraya, C. R. Hubbard, S. B. Robie, D. Louër, *et al.*, JCPDS—International Centre for Diffraction Data Round Robin Study of

Silver Behenate. A Possible Low-Angle X-Ray Diffraction Calibration Standard, Powder Diffr. 10 (2) (1995) 91-95.

[23] J.-C. Huang, Carbon Black Filled Conducting Polymers and Polymer Blends, Adv. Polym. Technol. 21 (4) (2002) 299-313.

[24] D. M. Bigg, An Investigation of the Effect of Carbon Black Structure, Polymer Morphology, and Processing History on the Electrical Conductivity of Carbon-Black-Filled Thermoplastics, J. Rheol. 28 (5) (1984) 501-516.

[25] F. Liang, B. Chen, A Review on Biomedical Applications of Single-Walled Carbon Nanotubes, Curr. Med. Chem. 17 (1) (2010) 10-24.

[26] Medicinal Chemistry and Pharmacological Potential of Fullerenes and Carbon Nanotubes. In: F. Cataldo, T. da Ros, editors. Carbon Materials: Chemistry and Physics, Dordrecht: Springer Netherlands; 2008.

[27] E. R. Morris, D. A. Rees, G. Young, M. D. Walkinshaw, A. Darke, Order-Disorder Transition for a Bacterial Polysaccharide in Solution. A Role for Polysaccharide Conformation in Recognition between Xanthomonas Pathogen and Its Plant Host, J. Mol. Biol. 110 (1) (1977) 1-16.

[28] F. Tiarks, K. Landfester, M. Antonietti, Silica Nanoparticles as Surfactants and Fillers for Latexes Made by Miniemulsion Polymerization, Langmuir 17 (19) (2001) 5775-5780.

[29] F. Tiarks, K. Landfester, M. Antonietti, Encapsulation of Carbon Black by Miniemulsion Polymerization, Macromol. Chem. Phys. 202 (1) (2001) 51-60.

[30] H. Sis, M. Birinci, Effect of Nonionic and Ionic Surfactants on Zeta Potential and Dispersion Properties of Carbon Black Powders, Colloids Surf. A 1–3 (341) (2009) 60-67.

[31] D. Das, S. Panigrahi, P. K. Senapati, P. K. Misra, Effect of Organized Assemblies. Part 5: Study on the Rheology and Stabilization of a Concentrated Coal−Water Slurry Using Saponin of the Acacia Concinna Plant, Energy Fuels 23 (6) (2009) 3217-3226.

[32] D. Das, S. Panigrahi, P. K. Misra, A. Nayak, Effect of Organized Assemblies. Part 4. Formulation of Highly Concentrated Coal−Water Slurry Using a Natural Surfactant, Energy Fuels 22 (3) (2008) 1865-1872.

[33] W. Wang, S. Efrima, O. Regev, Directing Oleate Stabilized Nanosized Silver Colloids into Organic Phases, Langmuir 1998, 14 (3) (1998) 602-610.

[34] D. Tatini, F. Sarri, P. Maltoni, M. Ambrosi, E. Carretti, B. W. Ninham, *et al.*, Specific Ion Effects in Polysaccharide Dispersions, Carbohydr. Polym. 173 (2017) 344-352.

[35] S.-Y. Yang, W.-N. Ling, Y.-L. Huang, H.-W. Tien, J.-Y. Wang, C.-C. Ma, *et al.*, Synergetic Effects of Graphene Platelets and Carbon Nanotubes on the Mechanical and Thermal Properties of Epoxy Composites, Carbon 49 (3) (2011) 793-803.

[36] C. L. Barrie, P. C. Griffiths, R. J. Abbott, I. Grillo, E. Kudryashov, C. Smyth, Rheology of Aqueous Carbon Black Dispersions, J. Colloid Interface Sci. 272 (1) (2004) 210-217.

[37] G. C. Kalur, S. R. Raghavan, Anionic Wormlike Micellar Fluids That Display Cloud Points: Rheology and Phase Behavior, J. Phys. Chem. B 109 (18) (2005) 8599-8604.

[38] S. Förster, M. Konrad, P. Lindner, Shear Thinning and Orientational Ordering of Wormlike Micelles, Phys. Rev. Lett. 94 (1) (2005) 017803.

[39] E. Carretti, C. Matarrese, E. Fratini, P. Baglioni, L. Dei, Physicochemical Characterization of Partially Hydrolyzed Poly(Vinyl Acetate)–borate Aqueous Dispersions, Soft Matter 10 (25) (2014) 4443-4450.

[40] B. A. Schubert, E. W. Kaler, N. J. Wagner, The Microstructure and Rheology of Mixed Cationic/Anionic Wormlike Micelles, Langmuir 19 (10) (2003) 4079-4089.

[41] C. Flood, C. A. Dreiss, V. Croce, T. Cosgrove, G. Karlsson, Wormlike Micelles Mediated by Polyelectrolyte, Langmuir 21 (17) (2005) 7646-7652.

[42] C. A. Dreiss, Wormlike Micelles: Where Do We Stand? Recent Developments, Linear Rheology and Scattering Techniques, Soft Matter 3 (8) (2007) 956-970.

[43] B. Nasri-Nasrabadi, A. Kaynak, Z. K. Nia, J. Li, An Electroactive Polymer Composite with Reinforced Bending Strength, Based on Tubular Micro Carbonized-Cellulos, Chem. Eng. J. 334 (2015) 1775-1780.

[44] C. Alvarez-Lorenzo, B. Blanco-Fernandez, A. M. Puga, A. Concheiro, Crosslinked Ionic Polysaccharides for Stimuli-Sensitive Drug Delivery, Adv. Drug Deliv. Rev. 65 (9) (2013) 1148-1171.

[45] S. Kennedy, S. Bencherif, D. Norton, L. Weinstock, M. Mehta, D. Mooney, Rapid and Extensive Collapse from Electrically Responsive Macroporous Hydrogels, Adv. Healthc. Mater. 3 (4) (2014) 500-507.

[46] G. Holzwarth, Conformation of the Extracellular Polysaccharide of Xanthomonas Campestris, Biochemistry 15 (19) (1976) 4333-4339.

[47] D. Filip, D. Macocinschi, E. Paslaru, B. S. Munteanu, R. P. Dumitriu, M. Lungu, *et al.*, Polyurethane Biocompatible Silver Bionanocomposites for Biomedical Applications, J. Nanopart. Res. 2014, 16 (11) (2014) 2710.

[48] H. D. Chandler, Activation Energy and Entropy for Viscosity of Wormlike Micelle Solutions, J. Colloid Interface Sci. 409 (2013) 98-103.

[49] D. A. Kuryashov, O. E. Philippova, V. S. Molchanov, N. Y. Bashkirtseva, I. N. Diyarov, Temperature Effect on the Viscoelastic Properties of Solutions of Cylindrical Mixed Micelles of Zwitterionic and Anionic Surfactants, Colloid J. 72 (2) (2010) 230-235.

[50] D. Angelescu, A. Khan, H. Caldararu, Viscoelastic Properties of Sodium Dodecyl Sulfate with Aluminum Salt in Aqueous Solution, Langmuir 19 (22) (2003) 9155-9161.

[51] J. Desbrieres, Viscosity of Semiflexible Chitosan Solutions: Influence of Concentration, Temperature, and Role of Intermolecular Interactions, Biomacromolecules 3 (2) (2002) 342-349.

[52] E. K. Sichel, J. I. Gittleman, P. Sheng, Transport Properties of the Composite Material Carbon-Poly(Vinyl Chloride), Phys. Rev. B 18 (10) (1978) 5712-5716.

[53] J.-P. Reboul, G. Moussalli, About Some D-C Conduction Processes in Carbon Black Filled Polymers, Int. J. Polym. Mater. 5 (1-2) (1976) 133-146.

[54] I. Balberg, A Comprehensive Picture of the Electrical Phenomena in Carbon Black–polymer Composites, Carbon 40 (2) (2002) 139-143.

[55] F. Carmona, C. Mouney, Temperature-Dependent Resistivity and Conduction Mechanism in Carbon Particle-Filled Polymers, J. Mater. Sci. 27 (5) (1992) 1322-1326.

The addition of carbon black to polysaccharide gels or to viscoelastic aqueous dispersions leads to higher stability and thermal resistance against mechanical stress, and imparts electrical responsiveness to an external applied voltage. The final composite material can be used for different applications where an electrical stimulus triggers a viscosity change in the liquid matrix.

# Light-modulated rheological properties in green innovative formulations

Duccio Tatini,[a] Filippo Sarri,[a] Andrea Dalle Vaglie,[a] Martina Raudino,[a] Moira Ambrosi,[a] Emiliano Carretti,[a] Barry W. Ninham,[b] and Pierandrea Lo Nostro*[a]

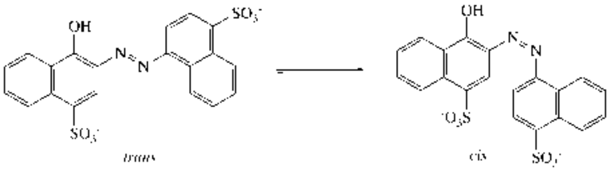

**Figure 1.**Trans-cis isomerization of azorubine.

**Abstract:** The addition of azorubine to a viscoelastic aqueous dispersion of sodium oleate (NaOL, 13% w/w) and KCl (up to 4% w/w) leads to a green gel-like system whose rheological behavior can be efficiently and reversibly triggered from remote by using UV light. Rheology, Differential Scanning Calorimetry (DSC) and Small Angle X-Ray Scattering (SAXS) measurements indicate that the original texture of the NaOL dispersion is significantly hardened upon UV irradiation for 8 hours in the presence of azorubine, showing a seven hundred-fold increase in viscosity. The UV treatment brings about the *trans* to *cis* isomerization of azorubine, which modifies the structure of the NaOL wormlike micellar system, leading to a more entangled, close-textured network. The cooperative effect of KCl on the fluid viscosity is found to be concentration-dependent. The system reverts to its original rheological behaviour after standing for about 1 day. These results are relevant for the development of stimuli-responsive innovative systems based on biocompatible, commercially available materials that can be used in very hardly accessible environments, such as in oil fields, where a quick change in the physico-chemical features of the system is required but very difficult to be performed.

## Introduction

Responsive or “smart” materials are functional materials whose properties can undergo controlled and reversible changes in response to an external stimulus.[1–3] The stimulus or external field applied include thermal, electrical, magnetic, pH, UV/visible light, ionic or metallic interactions or combinations thereof.[4,5]

The formulation of gel-based stimuli-responsive systems with specific performances is crucial for a great number of applications, and particularly when it is impossible or very difficult to switch on/off their properties, and a remotely controlled trigger is necessary.[4,6]

Among these systems, viscoelastic surfactant (VES) solutions have attracted great attention due to their unique features and versatility which can be harnessed in a variety of high-tech and everyday applications.[7–12]

The amphiphilic nature of VES molecules leads to the self-assembly in solution into small aggregates, which display a rich polymorphism, the simplest structure being spherical micelles.[2]

Under certain conditions such as concentration, salinity, temperature, presence of counterions, etc., spherical micelles may undergo uniaxial growth and form elongated and flexible structures, usually referred to as ‘‘wormlike’’ micelles.[13]

Above a critical concentration these wormlike structures form an entangled network, giving rise to a viscoelastic behavior which is reminiscient of that of flexible polymer solutions.[14–17]

Prompted by our ongoing studies on green formulations for frac fluids with suitable responsiveness to physical stimuli such as temperature, pressure, ionic strength, applied voltage and light irradiation, we developed viscoelastic aqueous dispersions of a green surfactant, sodium oleate (NaOL) that, in the presence of minimal amounts of azorubine, a biocompatible dye, undergo a remarkable change in the rheological properties upon irradiation at a specific wavelength.

Sodium oleate is a $C_{18}$-tailed anionic surfactant that self-assemble into wormlike micelles upon addition of simple salts[18] or other surfactants[19]. Several studies have focused on the influence of different additives on the micellar structure and viscoelastic behavior of NaOL solutions.[20–23]

NaOL offers several advantages in many applications, since anionic systems tend to be biodegradable and less toxic compared to cationic ones and are therefore considered to be more environmentally friendly.[24] In particular, anionic surfactants are widely used in enhanced oil recovery because the oil sand in the reservoir possesses negative charges and consequently adsorbs cationic surfactants.[18]

---

[a] D. Tatini, F. Sarri, A. Dalle Vaglie, M. Raudino, Dr. M. Ambrosi, Dr. E. Carretti, Prof. P. Lo Nostro
Department of Chemistry “Ugo Schiff” and CSGI
University of Florence
Via della Lastruccia 3, 50019 Sesto Fiorentino (Firenze), Italy
E-mail: pierandrea.lonostro@unifi.it
[b] Prof. B.W. Ninham
Department of Applied Mathematics, Research School of Physical Sciences and Engineering
Australian National University
Canberra ACT 0200, Australia

Supporting information for this article is given via a link at the end of the document.

Azorubine (Carmoisine, Food red 3 or E 122, disodium 4-hydroxy-3-((4- sulphonatonaphthyl)azo) naphthalenesulfonate), is a synthetic azo dye approved for food decorations and coatings and as drink additive.[25] Its chemical structure is shown in Figure 1. The presence of the azo moiety enables the *trans-cis* isomerization upon irradiation with light at an appropriate wavelength, usually in the UV region.[26–28]

The process may revert spontaneously upon heating since the trans isomer is thermodynamically more stable, or can be induced through irradiation with a visible light.[29]

Previous studies reported on the introduction of different chromophores in VES systems in order to obtain light-responsive fluids with tunable rheological properties. These photo-active molecules include synthetically modified azobenzenes,[30–32] *p*-coumaric acid[33,34] and cinnamic acid derivatives.[35,36] We select azorubine by virtue of its unique advantages in terms of availability, simple manipulation, low cost and complete safety.

This work is a proof-of-concept that shows the efficacy of combining completely biocompatible and non-toxic materials to obtain a versatile formulation with a viscosity and rheological behavior that can be remarkably modified through the irradiation with UV light.

Moreover, all these features make these systems very attractive for a wide range of applications, including agriculture, food industry, cosmetics, "smart" materials, enhanced oil recovery, shale gas extraction, drug delivery and controlled release.

## Results and Discussion

### Flow curve experiments

Figure 2 shows the flow curves obtained before and after UV irradiation from the dispersions of sodium oleate (NaOL, 13% w/w) in the presence of KCl at different concentrations (0, 0.5, 2 and 3% w/w). The curves for other KCl concentrations are reported in Figure S1.

All samples exhibit a Newtonian plateau at low shear stress, followed by a shear-thinning region as the shear stress increases. The viscosity drop at high shear stress is more pronounced in the presence of KCl, while for the pure NaOL dispersion (black line) the shear-thinning is almost negligible. In the literature this rheological behaviour is ascribed to the presence of wormlike micelles,[18] [37] [24] that bring about a rapid drop in the viscosity due to their shear-induced alignment.[2] Moreover, the trend of the viscosity values reported in Figure 1 suggests a structuring effect of KCl on the NaOL micellar network. The experimental curves were fitted according to the Cross model[38] to obtain the zero-shear viscosity, $\eta_0$, and an estimation of the shear relaxation exponent, *m*:

$$\eta = \eta_\infty + \frac{\eta_\infty - \eta_0}{1+(C\dot{\gamma})^m} \qquad \text{Eq. (1)}$$

here $\eta$ is the viscosity, $\eta_\infty$ the infinite-shear viscosity, $\dot{\gamma}$ the shear rate and *C* the consistency. The extracted fitting parameters are listed in Table S1 (see the the Supporting Information). For all samples the *m* exponent is very close to 1, i.e. the theoretical value expected for plastic materials. This result suggests a significant shear-induced modification or alignment of the particles.[39] In several wormlike micellar of ionic surfactants the slope of the power-law region is about 0.9.[40,41] The comparison between the literature data and our results confirms that the shear thinning behaviour of the NaOL-based formulations arises from the anisometric nature of the long, flexible cylindrical aggregates and their orientation in high shear-rate regimes.

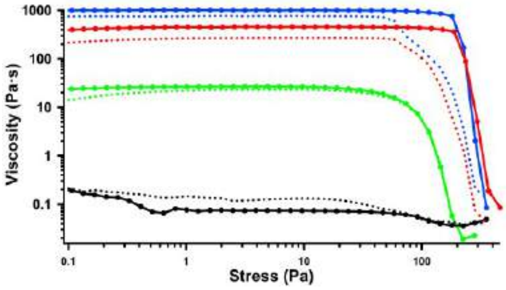

**Figure 2.** Flow Curves before (solid lines) and after (dashed lines) UV irradiation for 13% w/w NaOL (0.43 M, black) and in the presence of KCl at 0.5% (green), 2% (blue) and 3% w/w (red).

The UV irradiation does not affect the flow properties of the formulations: the profiles, as well as the values of $\eta_0$ exhibit minor fluctuations within the experimental uncertainty before and after the UV treatment.

The flow curves for the NaOL samples at different KCl concentration (0, 0.1%, 0.5% and 4%) in the presence of 0.18% w/w (3.6 $10^{-3}$M) azorubine are reported in Figure 3. The flow curves at the other KCl concentrations are shown in Figure S2 (see the Supporting Information).

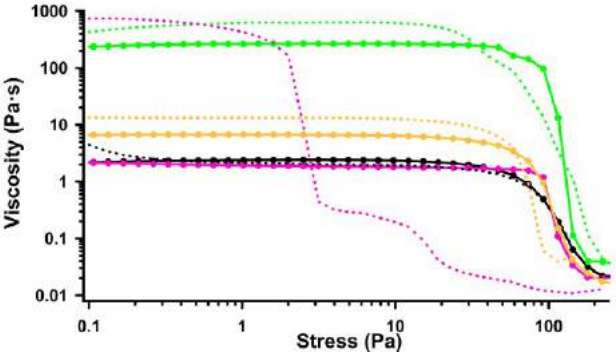

**Figure 3.** Flow curves before (solid lines) and after (dashed lines) UV irradiation for NaOL 0.43 M mixture in the presence of 0.18% w/w azorubine ($3.6{\cdot}10^{-3}$ M) at different KCl concentration: 0 (black), 0.1% (orange), 0.5% (green) and 4% w/w (pink).

In the presence of azorubine all the formulations exhibit a shear-thinning behaviour that is similar to that found for the pure NaOL-KCl systems. The results obtained from the fitting of the experimental data with the Cross model are reported in Table S1 in the Supporting Information. After UV irradiation the viscosity of the samples with 0.1%, 0.5% and 4% KCl increases from 6.94

to 13.6, from 278.8 to 728.3 and from 1.852 to 730.1 Pa·s, respectively. For the other KCl concentrations no significant variations in the formulation viscosity are observed after the UV treatment.

These findings lead to two important conclusions: (i) Azorubine has a remarkable effect as photo-active molecule in modifying the viscosity of the fluids after UV irradiation. A similar light-modulated viscosity change is reported for binary mixtures of NaOL and a light-responsive cationic azobenzene dye (1-[2-(4-phenylazophenoxy)-ethyl]-3-methylimidazolium bromide)[32]. In the work of Lu *et al.* the UV irradiation and the resulting *trans*-to-*cis* isomerization of the azo dye induces a decrease in the viscosity of the system, with a transition from a gel-like structure to a Newtonian fluid. In our case the opposite effect on the viscosity and the strengthening of the wormlike three-dimensional network may be attributed to the different chemical structure of the azo dye and its negative charge.

(ii) The presence of KCl plays a key role in modulating the effect of azorubine. The experimental data reported in Table S1 show that the *trans*-to-*cis* isomerization of azorubine induces an increase in the formulation viscosity when KCl concentration is lower than 1% w/w. Between 1% and 3.5% no remarkable changes are observed before and after the UV irradiation, suggesting that the major contribution to the strength of the system is provided by the salt.

The behaviour of the sample containing azorubine and 4% KCl is peculiar and deserves a deeper analysis. The viscosity increases by two orders of magnitude, but the rheological profile shows some differences after the UV treatment (see Figure 2, pink curves). A first Newtonian plateau appears in the low stress regime, then the viscosity rapidly decreases at a critical shear stress which is considerably lower than the viscosity breakdown point before the irradiation. After this initial decrease the flow curve shows a second, less pronounced plateau, followed by the typical shear-thinning region at high stress values. A similar behaviour was reported by Griffiths *et al.* in 2004 for carbon black particles dispersed in an acrylic polymeric matrix.[42] In this case the presence of an intermediate (secondary) Newtonian plateau is attributed to the interaction between the polymer layer and the polymer matrix, in particular to the viscous drag between the polymer chains adsorbed on the particles with the polymer in solution. In a more recent work Sochi depicts this intermediate region as a characteristic feature of viscoelastic fluids in porous media flow, that may be attributed to the time-dependent nature of the viscoelastic fluid when the relaxation time of the fluid and the characteristic time of the flow become comparable.[43] In our system the appearance of this secondary Newtonian plateau may reflect the formation of ordered structures with a different degree of organization. We will return to this issue later in the section dedicated to SAXS results. To the best of our knowledge this is the first time that such behaviour is found and reported for wormlike micellar dispersions. As a matter of fact the cited literature sources deal with polymeric blends[10] or to a more general viscoelastic behaviour in porous media flow[11]. Further work is necessary to deepen and clarify this phenomenon. The high salt concentration may be responsible for the formation of complex, more entangled structures after UV exposure. These structures are responsible for the remarkable increase in the viscosity of the formulation and exhibit a low resistance to the applied stress, as confirmed by the low critical stress value. This hypothesis is also confirmed by the fact that during the sample preparation the azorubine solution becomes turbid at this salt concentration, suggesting the formation of aggregated structures. The same salt-induced behaviour is observed in pure azorubine solutions, without sodium oleate, and presumably reflects the formation of piled up structures stabilized by $\pi$-stacking interactions.[44]

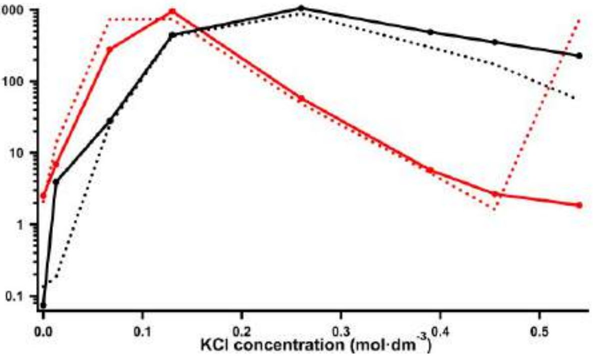

**Figure 4.** Zero-shear viscosity ($\eta_0$) for the formulations containing 0.18% w/w azorubine (red) and the reference samples without the dye (black) as a function of the salt concentration (a) before (solid line) and after (dashed line) UV irradiation.

Figure 4 reports the values of $\eta_0$ as a function of KCl concentration before and after the UV treatment.

In the calculation of the ionic strength, only azorubine (disodium salt) and KCl are taken into account, while the contribution of sodium oleate is overlooked, assuming that its concentration and degree of dissociation remain constant.

For the two sets of samples the viscosity steeply increases in the dilute regime, then it reaches a maximum and progressively decreases at higher concentrations of salt. This behaviour is widely reported for cationic[14,37,45–49], anionic[22,32,50] and non-ionic[48,51–53] surfactant systems that form wormlike micelles, and it is usually referred to as the *salt curve*.[54,55] In the dilute regime the steep increase in the viscosity reflects the one-dimensional growth of the NaOL micelles, resulting in the formation of wormlike structures that overlap and form entangled networks.[50] The presence of a maximum followed by a decrease in the fluid viscosity is usually ascribed to the formation of micellar branched structures.[45,56,57] From a thermodynamic standpoint the increase in the salt concentration results in an increment in the end-cap energy of the linear micelles, which is compensated by the formation of branch points with an opposite curvature.[2] Two further mechanisms contribute to the formation of intermicellar junctions: (i) during the process a partial dehydration of the polar headgroups occurs and some hydrating water molecules are pushed back into the bulk aqueous phase, leading to an increment in entropy, and (ii) as the concentration of branches increases, the semispherical endcaps can fuse together to form a continuous cylindrical bridge that connects different rods.[58] Branched micelles show a lower viscosity compared to linear entangled micelles because they have an additional route for stress relaxation, which involves the sliding of branch points along the micellar body.[2,15]

The experimental results show that azorubine induces two distinct effects on the salt curves (Figure 3). The first effect is the shift of the peak maximum to lower KCl concentrations. Azorubine is an amphiphilic molecule that can penetrate across the micellar interface at least partially. This results in a flattening of the micelle/water interface with a significant lowering in the surface curvature. Moreover the electrostatic repulsion between different tubular micelles is screened and the viscosity increases even at lower concentration of salt.

The second effect is the modification of the salt curve shape after the maximum. In the presence of azorubine the viscosity decreases more rapidly, as a consequence of the increased branching density. Rogers *et al.* reported that for several mixed surfactant/salt viscoelastic systems, the branching effect is more evident with sodium salicylate, a hydrotropic salt that can penetrate more efficiently underneath the water/micellar interface salt respect to a simple inorganic salt like KCl.[59] This effect due to branched structures is quite common and found also in nonionic or zwitterionic systems.[27]

**Oscillatory-shear measurements**

The viscoelastic properties of wormlike systems are investigated by means of oscillatory shear measurements as a function of KCl concentration. Figure 5 shows the storage (*G’*) and loss (*G”*) moduli obtained by frequency sweep experiments before and after UV irradiation for the dispersions of sodium oleate in the presence of KCl at different concentrations. The frequency sweep curves for other KCl concentrations are reported in the Supporting Information.

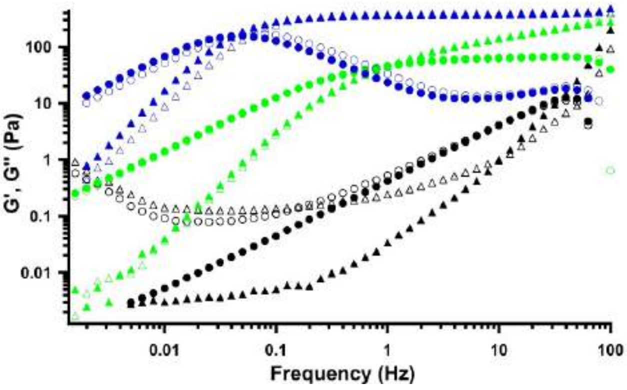

**Figure 5.** Storage (triangles) and loss (circles) moduli before (filled markers) and after (empty markers) UV irradiation for NaOL 0.43 M in the presence of KCl at 0 (black), 0.5% (green) and 2% (blue).

All the samples containing KCl exhibit the typical rheological behaviour of viscoelastic fluids, with two distinct regimes. At low frequencies, when $\omega < \omega_c$ ($\omega_c$ is the crossover frequency between the two moduli) the loss modulus *G”* exceeds the storage modulus *G’*, indicating a predominantly viscous behaviour. At higher frequencies, when $\omega > \omega_c$, *G’* dominates, and the system is mainly elastic. In simple physical terms, this crossover separates the plateau regime of the collective network dynamics from the single-filament regime.[60] The crossover frequency shows a progressive decrease as the salt concentration increases, indicating at first approximation a slower relaxation dynamics of the system due to a more entangled network. No remarkable variations in *G’* and *G”* are observed before and after the UV irradiation with the exception of NaOL alone, that exhibits higher values of the storage and loss moduli in the low frequency region after the UV treatment.

Figure 6 reports the storage and loss moduli obtained in the frequency sweep experiments before and after UV irradiation for the samples containing azorubine in the presence of KCl at different concentrations (0, 0.5% and 2%). The frequency sweep curves for other KCl concentrations are reported in the Supporting Information. The formulations exhibit a viscoelastic behaviour with curves that look similar to those reported in Figure 5, indicating that the two frequency-dependent regimes are present. The crossover frequency decreases when KCl concentration is increased from 0 to 0.5%, then it progressively shifts to higher values upon further increase in the salt concentration.

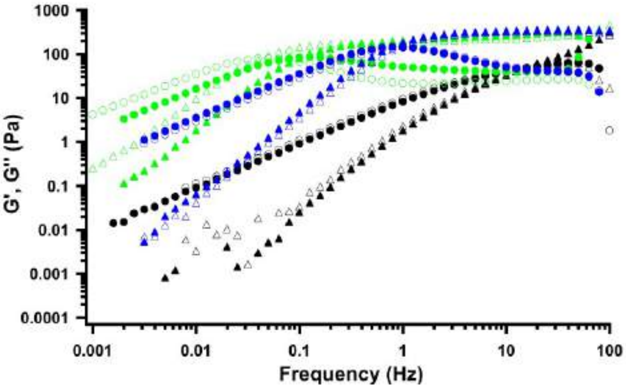

**Figure 6.** Storage (triangles) and loss (circles) moduli before (filled markers) and after (hollow markers) UV irradiation for NaOL 0.43 M + azorubine 0.18 % mixture in the presence of KCl at 0 (black), 0.5 % (green) and 2 % (blue).

The UV treatment has a very minor effect on the viscoelastic properties of the formulations, with the exception of the sample containing KCl 4% (Figure S10 in the Supporting Information). In this case before the UV irradiation the storage and loss moduli show a crossover in the high-frequency region, followed by a remarkable drop at medium and low frequencies, which indicates a predominantly viscous behaviour. After the UV treatment *G’* and *G”* overlap for the most part of the whole frequency range and after a slight decrease at high frequencies they levels off to a relatively high constant value in the medium and low-frequency regime. This results is consistent with the remarkable viscosity increase observed after the irradiation (Figure 2) due to the presence of light-induced ordered structures. The viscoelastic behaviour of entangled wormlike micelles is usually described by the Maxwell model for viscoelastic fluid with a single relaxation time $\tau_R$. If the strain amplitude is small enough the fluid structure is not disturbed by the deformation and the resulting stress is controlled by the rate of spontaneous rearrangements. The storage modulus and the viscous modulus are given by the following equations:[8,56]

$$G' = G_0 \frac{\omega^2 \tau_R^2}{\omega^2 \tau_R^2 + 1} \qquad \text{Eq. (2)}$$

$$G'' = G_0 \frac{\omega \tau_R}{\omega^2 \tau_R^2 + 1} \qquad \text{Eq. (3)}$$

here $\omega$ is the oscillation frequency, $G_0$ the elastic modulus extrapolated to infinite frequency (also referred to as the plateau modulus) and $\tau_R$ the characteristic relaxation time of the system. Combining Eq. (2) and (3), a new expression is obtained:

$$G''^2 + (G' - G_0/2)^2 = (G_0/2)^2 \qquad \text{Eq. (4)}$$

Thus, the plot of $G'$ against $G''$ (the so-called Cole–Cole plot) represents another useful tool to demonstrate the Maxwell behaviour.

In entangled wormlike micelles the overall stress-relaxation dynamics is the result of the competition between two effects. The first is reptation, which is commonly observed in entangled solutions of flexible polymers.[61,62] It consists in a snake-like diffusion of the micelle along its own contour, determined by topological constraints and with a characteristic time $\tau_{rep}$. The second mechanism arises from the breaking and recombination of the micelles, since the surfactant molecules can be exchanged reversibly between different worms, and it is characterized by a relaxation time $\tau_B$.[63] In the so-called “fast breaking limit” (*i.e.* $\tau_B << \tau_R$) several scission/recombination events occur within the reptation time scale, and the Maxwell model accurately predicts the trend of $G'$ and $G''$. As $\tau_B/\tau_R$ increases, the rheological behaviour deviates from the theoretical model at high frequencies, showing an upturn in the viscous modulus. This discrepancy is related to the transition from “slower” reptation to additional faster relaxation processes, such as Rouse (stretching of chains shorter than the entanglement length) or ‘breathing’ modes (tube-length fluctuations).[2] Figures S13 and S14 in the Supporting Information report two examples of the fitting obtained by applying the Maxwell model to the frequency sweep data and the relative Cole-Cole plots. The relaxation dynamic of the NaOL/Azorubine/KCl systems cannot be described by a single-element in the Maxwell model since major discrepancies are observed between the experimental data and the predicted values for most samples. To overcome this problem, we use both $G'$ and $G''$ to calculate the time-weighted relaxation spectrum $H(\tau)$.[64,65] The relaxation times extracted from the spectra are reported as a function of KCl concentration in Figure 7.

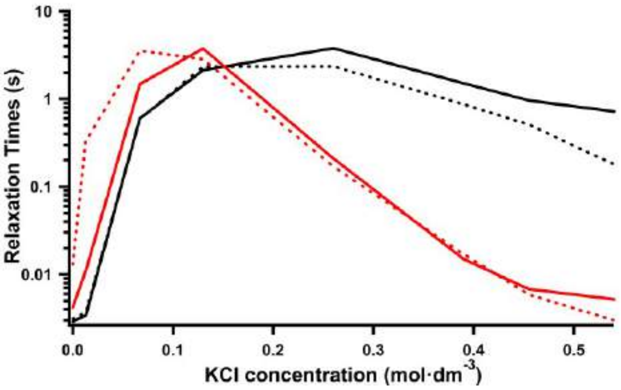

**Figure 7.** Relaxation time ($\tau$) for the formulations containing azorubine (red) and the reference samples without the dye (black) as a function of the salt concentration before (solid line) and after (dashed line) the UV irradiation.

All the relaxation spectra shows a broad primary peak from which we estimate the relaxation times.

For most samples multiple secondary peaks are observed, indicating the presence of different relaxation mechanisms (reptation, breaking and recombination, Rouse, etc.).

The relaxation times follow the same trend of the viscosity as the salt concentration increases (compare Figure 6 and Figure 3). This behaviour confirms the strengthening effect of azorubine on the entangled micellar network after the UV irradiation, which induces similar changes in the viscosity and in the dynamic rheological properties of the formulations.

The only exception is represented by NaOL + KCl 4% in the presence of azorubine: in this case the relaxation time after the UV treatment is very close to the value of the non-irradiated sample. As we mentioned in the previous section, the remarkable increase in the viscosity observed at this salt concentration is probably due to the presence of aggregated structures.

### Differential Scannning Calorimetry

The thermal behavior of the NaOL-based formulations was investigated through Differential Scanning Calorimetry (DSC). The DSC scans for the dispersions of sodium oleate in the presence of KCl at different concentrations (0, 3.5% and 4%) before and after UV irradiation are shown in Figure 8. The thermograms for the other investigated KCl concentrations are reported in the Supporting Information.

All the samples exhibit a broad endothermic peak centered around 0 °C, due to the melting of free water. The melting peak temperatures ($T_{mf}$) and the corresponding enthalpy changes ($\Delta H_{mf}$, in J/g) are listed in Table S2 in the Supporting Information. As the KCl concentration increases both $T_{mf}$ and $\Delta H_{mf}$ decreases, indicating a reduction in the amount of free water in the micellar system.

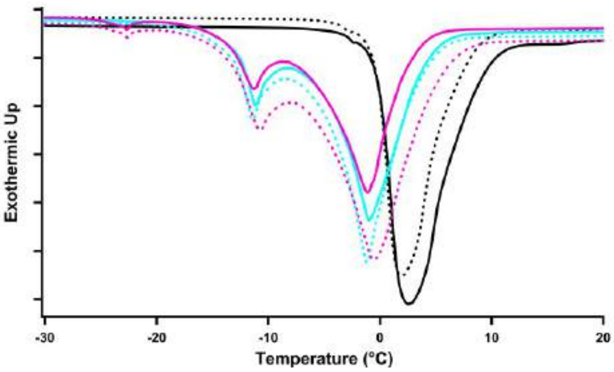

**Figure 8.** DSC heating curves before (solid lines) and after (dashed lines) UV irradiation for NaOL 0.43 M mixture in the presence of KCl at 0 (black), 3.5% (light blue) and 4% (pink).

The concentration of free water ($W_f$ expressed in % w/w) is calculated according to the following equation:[66]

$$W_f = \Delta H_{mf} \cdot 100/\Delta H_{mfw} \qquad \text{Eq. (5)}$$

here $\Delta H_{mf}$ is the experimental enthalpy change, and $\Delta H_{mfw}$ is the heat of fusion of pure water (333.79 J/g in the experimental conditions used in this study).[67]

The values of $W_f$ are listed in Table S2 in the Supporting Information. For the pristine non-irradiated samples $W_f$ rapidly decreases, passing from 96% to 46% as the salt concentration increases. Similar values are obtained for the NaOL-KCl systems after the UV irradiation, demonstrating that the endothermic process (*i.e.* the melting of the free water) is not affected by the UV treatment, as expected.

When KCl concentration exceeds 0.5% a second endothermic peak appears in the thermograms between –15 and –11 °C. This transition is related to the melting of "interfacial" water, *i.e.* the water confined within the region separating the oleate micelles. Due to their wormlike structure the micelles behave like polymer chains and create an entangled network with solvent-rich domains entrapped between the chains. The water molecules confined in these pores interact with the surfactant polar head groups and the counterions at the micellar surface, and exhibit distinctive thermodynamics and dynamic properties, different from those of bulk water.[68] Similar thermal transitions are detected in several surfactant-based systems, such as micellar solutions[69], microemulsions[66] and liquid crystalline phases.[70] The amount of the interfacial water ($W_i$ expressed in % w/w) is calculated as:

$$W_i = \Delta H_{mi} \cdot 100/\Delta H_{miw} \qquad \text{Eq. (6)}$$

where $\Delta H_{mi}$ is the experimental enthalpy change for the melting of interfacial water obtained from the DSC curves and $\Delta H_{miw}$ is the heat of fusion of interfacial water. This enthalpy change depends on the specific polymorphic form of ice produced by the interfacial water.[71] Some authors neglect the polymorphism of ice and use the enthalpy value of water without introducing an appreciable error.[72] We followed Senatra ***et al.***[73] and used the corrected enthalpy value of 312.28 J/g. The values of $\Delta H_{mi}$, $T_{mi}$ and $W_i$ are listed in Table S2 in the Supporting Information.

As KCl concentration increases, a depression of the melting peak temperatures $T_{mi}$ is observed, while $\Delta H_{mi}$ shows an opposite trend, increasing from about 1 J/g in the case of KCl 0.5% to about 27 J/g for KCl 3.5%.

The addition of the salt progressively screens the electrostatic repulsion between the micelles and leads to the formation of a more entangled network. Thus, the number of water molecules confined within the intermicellar domains increases, as indicated by the values of $W_i$, that passes from 0.4% to 8%.

In the case of KCl 4%, the DSC curve shows a third endothermic peak with a small enthalpy change located at about -22 °C. The occurrence of this peak reveals the presence of another type of water, the fraction of interfacial water molecules that are closely associated to the carboxylic moieties of NaOL. The presence of a nearby charged surface alters the thermodynamic properties of these water molecules, leading to remarkably reduced melting temperature and enthalpy of fusion.[66,74] This kind of water is usually referred to as freezable bound water.[73–78]

By comparing the values of the peak temperatures and of the enthalpy changes related to the melting of the interfacial and bound water ($\Delta H_{mb}$, $T_{mb}$ and $W_b$), we conclude that the UV treatment does not alter the hydration state of the NaOL/KCl system.

For the samples containing azorubine the values of $\Delta H_{mf}$, $T_{mf}$, $W_f$, $\Delta H_{mi}$, $T_{mi}$, $W_i$, $\Delta H_{mb}$, $T_{mb}$, and $W_b$ are reported in Table S2 in the Supporting Information.

The presence of the dye does not induce remarkable variations in the amount of free and interfacial water, as well as in the values of peak temperatures and the relative enthalpy changes. The main difference is represented by the freezable bound water melting peak, that appears starting from KCl 3%. As indicated by the viscosity measurements, the negatively charged sulfonate groups in the azorubine molecule have a cooperative effect with KCl in screening the electrostatic repulsion between the micellar surfaces. This synergistic action reduces the amount of salt that is required for the formation of the micellar entangled network (and eventually the branched structures), and affects the thermal transition of the water molecules that closely interacts with the micellar surface, *i.e.* the freezable bound water.

## SAXS

SAXS experiments are performed to find a correlation between the observed rheological flow curves of the investigated systems and their nanostructure. Figure 9 reports SAXS curves of pure NaOL 0.43 M, NaOL 0.43 M in the presence of KCl 4 % and NaOL 0.43 M in the presence of azorubine 0.18 %. The main result from SAXS analysis is that there is a transition from non-interacting spherical micelles in the formulation containing only NaOL to a network of polydispersed core-shell elongated objects interacting via a screened Coulomb potential upon the addition of salt. This behaviour is already reported in the literature [2,20,24] and the formation of a network of interacting long micelles is in good agreement with the rheological data of sodium oleate in the presence of different KCl concentrations shown in Figure 1. The appearance of the interaction contribution in the low-q region of the SAXS curve of the sample containing both oleate

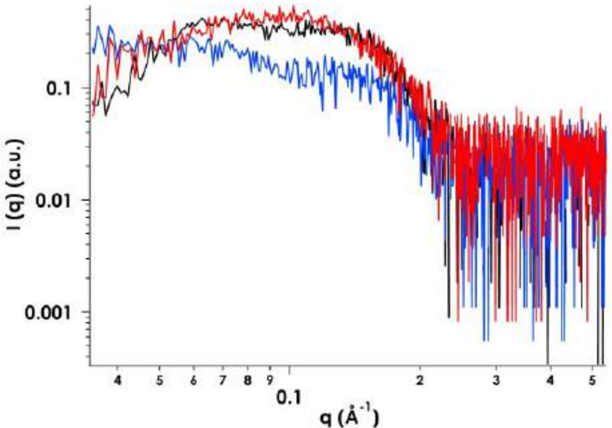

**Figure 9**. SAXS curves of NaOL 0.43 M (blue), NaOL 0.43 M + KCl 4 % (red) and NaOL 0.43 M + azorubine 0.18 % (black). All curves are offset along y-axes

and KCl can be ascribed to the screening of the electrostatic charges on the surface of oleate micelles thanks to salt addition.

A very similar behaviour can be observed upon the addition of azorubine since the SAXS profile of the formulation containing the dye is similar to that of the sample with KCl. This result is consistent with the rheological experiments reported in this Section: in the presence of azorubine the formation of micellar branched structures occurs more rapidly than in the case of the single KCl addition, determining a decrease in the formulation viscosity. Nevertheless, the wormlike structure is retained, as demonstrated by the similar SAXS profiles.

Finally, the effect of the UV irradiation on the nanostructure of the viscoelastic formulations is investigated acquiring the SAXS scattering profiles reported in Figure 10 on the samples exhibiting the most remarkable increase of viscosity after the application of the light stimulus, i.e., NaOL formulations containing the azo dye and KCl 0.1 % and 4 %.

SAXS curves of the samples after UV irradiation show the presence of a sharp peak centred at 0.15 q$^{-1}$ (corresponding to a dimension of about 8 nm) independently from KCl concentration. Since this feature is not visible in the SAXS profiles of the samples before UV exposure, we can argue the formation of a light-induced ordered phase. This result represents a further confirmation of what we observed by means of the rheological experiments shown in Figures 3 and 4, where the remarkable increase of viscosity observed after the photostimulation of the samples was ascribed to the strengthening of the micellar network and the formation of ordered structures, especially in the sample containing the higher amount of KCl.

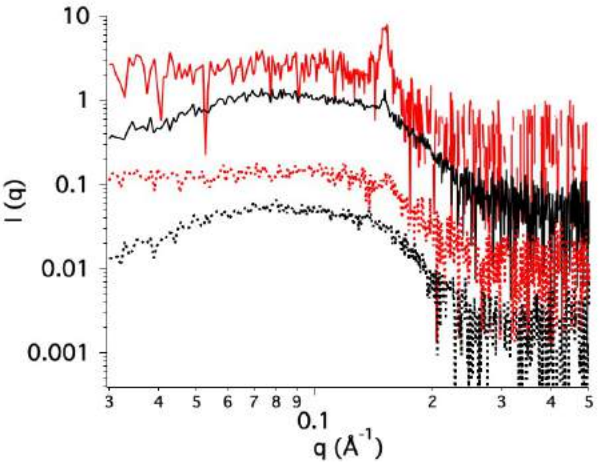

**Figure 10**. SAXS curves of NaOL 0.43 M + azorubine containing KCl 0.1 % (black curves) and 4 % (red curves) before (dotted lines) and after (continuous line) UV irradiation. All curves are offset along y-axes.

## Conclusions

In this work we illustrate a simple and inexpensive procedure for the formulation of green photo-responsive viscoelastic fluids starting from non-toxic, biocompatible, commercially available materials. The addition of a food azo dye, azorubine, to a dispersion on sodium oleate in the presence of KCl enables the modification of the formulation rheological properties through an external UV light stimulus. The UV treatment brings about the *trans-cis* isomerization of azorubine, which is partially intercalated between the surfactant polar heads, resulting in a modification of the wormlike micellar structure of NaOL. This gives rise to a remarkable increase in the formulation viscosity and a variation of the rheological properties, as evidenced by viscosity and oscillatory-shear measurements. The effect of azorubine is mediated by the presence of the salt, since it occurs only in a specific range of KCl concentration. DSC measurements confirm the formation of wormlike micelles above a critical salt concentration, which is lower in the presence of azorubine. The UV treatment does not affect the thermal transitions of the NaOL dispersions, since no significant variation is detected before and after the irradiation. SAXS experiments reveal the formation of light-induced ordered phases after the UV irradiation for the samples containing KCl 01.% and 4 %, providing a structural validation to the results obtained through rheological measurements.

All these features, combined with the complete biocompatibility and non-toxicity break new ground in a wide range of applications, from shale gas extraction to controlled release and drug delivery, where a remote control on the mechanical and physico-chemical properties of the formulation is crucial.

## Experimental Section

### Materials

Sodium oleate (ACS reagent grade, Riedel-De Haën, Seelze, Germany) and potassium chloride (> 99 %, Sigma-Aldrich, Milan, Italy) were used as received without any further purification. Azorubine (E122, food grade quality) was supplied by F.lli Rebecchi S.r.l., Piacenza, Italy. All solutions and dispersions were prepared with bidistilled Milli-Q water (resistivity > 18 MΩ•cm at 25°C).

### Sample Preparation

Sodium oleate viscoelastic formulations were prepared by the addition of a weighted amount of surfactant to KCl aqueous solutions at different concentrations (0, 0.1, 0.5, 1, 2, 3, 3.5, 4 % w/w) under constant stirring at room temperature. The final concentration of NaOL was 0.43 M in all the samples. The azorubine-loaded samples were prepared following a similar procedure: we added different amounts of potassium chloride to a 0.18 5 w/w (3.6 10$^{-3}$M) azorubine aqueous solution to obtain KCl concentrations of 0.1, 0.5, 1, 2, 3, 3.5, 4 % w/w, then we added the surfactant.

### UV Irradiation

About 10 mL of sample was placed in a quartz container and irradiated using a Camag UV lamp (wavelength 254 nm, 8 W, Muttenz, Switzerland) for 8 hours. All the experiments were conducted at 25 °C, and the distance between the sample and light source was fixed at 5 cm.

### Rheology Measurements

Oscillatory shear measurements were carried out on a Paar Physica UDS 200 rheometer using a plate-plate geometry (diameter 40 mm; gap 300 μm). Under these conditions the total amount of the sample in the cell was about 0.4 mL All the measurements were performed at 25.0 ± 0.1 °C (Peltier temperature control system). After being loaded, the samples were equilibrated for 15 min at the set temperature. Frequency sweep measurements were carried out within the linear viscoelastic range at a strain value of 1%, which was previously determined by means of an amplitude sweep test. The storage and loss moduli (G' and G'', respectively) were measured over the frequency range of 0.001 to 100 Hz. The flow curves were acquired in a torque range between 0.1 and 5000 mNm. The intrinsic viscosity ($\eta_0$) values were obtained by fitting the experimental curves with the Cross model (see the Supporting Information).

### Differential Scanning Calorimetry

Differential Scanning Calorimetry (DSC) was performed by means of a DSC-Q2000 by TA Instruments (Philadelphia, PA). The samples were first cooled from 20 °C to − 60 °C at 10 °C/min, then heated up to 50 °C at 5°C/min. Measurements were conducted in $N_2$ atmosphere, with a flow rate of 50 mL/min. For the samples which show overlapping endothermic peaks, the deconvolution of the thermogram was performed by means of the Igor Pro 6.36 software, using a summation of exponentially modified Gaussian (EMG) functions.[77,79] The single EMG function is defined as:

$$f(T) = \sqrt{\frac{\pi}{2}}\frac{hw}{|s|}\exp\left[\frac{w^2}{2s^2}\left(\frac{T_0-T}{s}\right)\right]\operatorname{erf}\left[\frac{T_0-T}{2\left(w+\frac{w}{|s|}\right)}\right]$$

where $h$ is the height, $T_0$ the center, $w$ the width of the peak and $s$ is the distortion factor (shape). For the deconvoluted peaks, the peak temperatures correspond to $T_0$, while the enthalpy changes are calculated using the total area under the peak.

### Small Angle X-Ray Scattering Experiments

SAXS Experiments. SAXS measurements were carried out using a HECUS S3-Micro (Kratky camera) equipped with two position-sensitive detectors (PSD-50M) containing 1024 channels of 54-μm width. Cu Kα radiation of wavelength 1.542 Å was provided by a GeniX X-ray generator (Xenocs, Grenoble) working with a microfocus sealed-tube operating in the power range 12÷50 W. The sample to detector distance was 281 mm. The volume between the sample and the detector was kept under vacuum during the measurements to minimize scattering from the air. The Kratky camera was calibrated using silver behenate, which is known to have a well-defined lamellar structure (d = 58.38 Å) [T. N. Blanton, T. C. Huang, H. Toraya, C. R. Hubbard, S. B. Robie, D. Louër, H. E. Göbel, G. Will, R. Gilles, and T. Raftery, Powder Diffraction 10, 2 ,2013, pp. 91–95]. Scattering curves were monitored in a q-range from 0.01 to 0.55 Å−1. Liquid samples were recorded in a borosilicate glass capillary tube. In all measurements the temperature was kept constant at 25 °C controlled by a Peltier element, with an accuracy of ± 0.1 °C. All the scattering curves were corrected for the empty capillary contribution considering the relative transmission factors. Desmearing of the SAXS curves was not necessary because of the sophisticated point microfocusing system. The scattering length density values were calculated for each component on the basis of its chemical composition (See Supporting Information).

## Acknowledgements

The authors acknowledge the European Union Horizon 2020 research and innovation program under grant agreement Nr. 640979.

**Keywords:** green chemistry • sodium oleate • azorubine • viscosity • stimulus-responsive

## References

[1] M. Wei, Y. Gao, X. Li, M. J. Serpe, *Polym. Chem.* **2016**, *8*, 127–143.

[2] C. A. Dreiss, *Soft Matter* **2007**, *3*, 956–970.

[3] S. Guragain, B. P. Bastakoti, V. Malgras, K. Nakashima, Y. Yamauchi, *Chem. – Eur. J.* **n.d.**, *21*, 13164–13174.

[4] S. Ahn, R. M. Kasi, S.-C. Kim, N. Sharma, Y. Zhou, *Soft Matter* **2008**, *4*, 1151–1157.

[5] D. Wang, G. Wei, R. Dong, J. Hao, *Chem. – Eur. J.* **n.d.**, *19*, 8253–8260.

[6] M. A. C. Stuart, W. T. S. Huck, J. Genzer, M. Müller, C. Ober, M. Stamm, G. B. Sukhorukov, I. Szleifer, V. V. Tsukruk, M. Urban, et al., *Nat. Mater.* **2010**, *9*, 101–113.

[7] J. Yang, *Curr. Opin. Colloid Interface Sci.* **2002**, *7*, 276–281.

[8] H. Rehage, H. Hoffmann, *J. Phys. Chem.* **1988**, *92*, 4712–4719.

[9] H. Shi, Y. Wang, B. Fang, Y. Talmon, W. Ge, S. R. Raghavan, J. L. Zakin, *Langmuir* **2011**, *27*, 5806–5813.

[10] M. Samuel, D. Polson, D. Graham, W. Kordziel, T. Waite, G. Waters, P. S. Vinod, D. Fu, R. Downey, Society Of Petroleum Engineers, **2000**.

[11] C. Moitzi, N. Freiberger, O. Glatter, *J. Phys. Chem. B* **2005**, *109*, 16161–16168.

[12] Z. Zhai, X. Yan, J. Xu, Z. Song, S. Shang, X. Rao, *Chem. – Eur. J.* **n.d.**, *24*, 9033–9040.

[13] Y. Lin, Y. Qiao, Y. Yan, J. Huang, *Soft Matter* **2009**, *5*, 3047–3053.

[14] T. M. Clausen, P. K. Vinson, J. R. Minter, H. T. Davis, Y. Talmon, W. G. Miller, *J. Phys. Chem.* **1992**, *96*, 474–484.

[15] P. A. Hassan, S. R. Raghavan, E. W. Kaler, *Langmuir* **2002**, *18*, 2543–2548.

[16] R. Byron Bird, P. J. Carreau, *Chem. Eng. Sci.* **1968**, *23*, 427–434.

[17] R. H. Colby, *Rheol. Acta* **2010**, *49*, 425–442.

[18] Q. Cao, L. Yu, L.-Q. Zheng, G.-Z. Li, Y.-H. Ding, J.-H. Xiao, *Colloids Surf. Physicochem. Eng. Asp.* **2008**, *312*, 32–38.

[19] P. Koshy, V. K. Aswal, M. Venkatesh, P. A. Hassan, *J. Phys. Chem. B* **2011**, *115*, 10817–10825.

[20] C. Flood, C. A. Dreiss, V. Croce, T. Cosgrove, G. Karlsson, *Langmuir* **2005**, *21*, 7646–7652.

[21] S. Khandavalli, J. Hendricks, C. Clasen, J. P. Rothstein, *J. Rheol.* **2016**, *60*, 1331–1346.

[22] N. V. Thampi, R. P. John, K. Ojha, U. G. Nair, *Ind. Eng. Chem. Res.* **2016**, *55*, 5805–5816.

[23] J. Huang, S. Zhang, Y. Feng, J. Li, H. Yan, F. He, G. Wang, Y. Liu, L. Wang, *Colloids Surf. Physicochem. Eng. Asp.* **2016**, *500*, 222–229.

[24] G. C. Kalur, S. R. Raghavan, *J. Phys. Chem. B* **2005**, *109*, 8599–8604.

[25] J. König, in *Colour Addit. Foods Beverages* (Ed.: M.J. Scotter), Woodhead Publishing, Oxford, **2015**, pp. 35–60.

[26] H. M. D. Bandara, S. C. Burdette, *Chem. Soc. Rev.* **2012**, *41*, 1809–1825.

[27] R. Dąbrowski, P. Kula, J. Herman, *Crystals* **2013**, *3*, 443–482.

[28] D. Statman, I. Jánossy, *J. Chem. Phys.* **2003**, *118*, 3222–3232.

[29] H. Rau, in *Photochromism* (Eds.: H. Dürr, H. Bouas-Laurent), Elsevier Science, Amsterdam, **2003**, pp. 165–192.

[30] H. Oh, A. M. Ketner, R. Heymann, E. Kesselman, D. Danino, D. E. Falvey, S. R. Raghavan, *Soft Matter* **2013**, *9*, 5025–5033.

[31] Y. Lin, X. Cheng, Y. Qiao, C. Yu, Z. Li, Y. Yan, J. Huang, *Soft Matter* **2010**, *6*, 902–908.

[32] Y. Lu, T. Zhou, Q. Fan, J. Dong, X. Li, *J. Colloid Interface Sci.* **2013**, *412*, 107–111.

[33] D. Wang, R. Dong, P. Long, J. Hao, *Soft Matter* **2011**, *7*, 10713–10719.

[34] R. Kumar, S. R. Raghavan, *Soft Matter* **2009**, *5*, 797–803.

[35] J. Li, M. Zhao, H. Zhou, H. Gao, L. Zheng, *Soft Matter* **2012**, *8*, 7858–7864.

[36] H. Sakai, S. Taki, K. Tsuchiya, A. Matsumura, K. Sakai, M. Abe, *Chem. Lett.* **2012**, *41*, 247–248.

[37] B. A. Schubert, E. W. Kaler, N. J. Wagner, *Langmuir* **2003**, *19*, 4079–4089.

[38] M. M. Cross, *J. Colloid Sci.* **1965**, *20*, 417–437.

[39] F. E. Antunes, L. Coppola, D. Gaudio, I. Nicotera, C. Oliviero, *Colloids Surf. Physicochem. Eng. Asp.* **2007**, *297*, 95–104.

[40] T. Shikata, H. Hirata, T. Kotaka, *Langmuir* **1987**, *3*, 1081–1086.

[41] T. Shikata, H. Hirata, T. Kotaka, *Langmuir* **1988**, *4*, 354–359.

[42] C. L. Barrie, P. C. Griffiths, R. J. Abbott, I. Grillo, E. Kudryashov, C. Smyth, *J. Colloid Interface Sci.* **2004**, *272*, 210–217.

[43] T. Sochi, *Polymer* **2010**, *51*, 5007–5023.

[44] M. F. Nazar, S. Murtaza, B. Ijaz, M. Asfaq, M. A. Mohsin, *J. Dispers. Sci. Technol.* **2015**, *36*, 18–27.

[45] S. J. Candau, E. Hirsch, R. Zana, *J. Colloid Interface Sci.* **1985**, *105*, 521–528.

[46] L. J. Magid, Z. Han, Z. Li, P. D. Butler, *Langmuir* **2000**, *16*, 149–156.

[47] R. D. Koehler, S. R. Raghavan, E. W. Kaler, *J. Phys. Chem. B* **2000**, *104*, 11035–11044.

[48] H. Hoffmann, in *Struct. Flow Surfactant Solut.*, American Chemical Society, **1994**, pp. 2–31.

[49] M. In, G. G. Warr, R. Zana, *Phys. Rev. Lett.* **1999**, *83*, 2278–2281.

[50] A. Parker, W. Fieber, *Soft Matter* **2012**, *9*, 1203–1213.

[51] C. Rodriguez-Abreu, K. Aramaki, Y. Tanaka, M. A. Lopez-Quintela, M. Ishitobi, H. Kunieda, *J. Colloid Interface Sci.* **2005**, *291*, 560–569.

[52] N. Naito, D. P. Acharya, J. Tanimura, H. Kunieda, *J. Oleo Sci.* **2004**, *53*, 599–606.

[53] R. G. Shrestha, C. Rodriguez-Abreu, K. Aramaki, *J. Oleo Sci.* **2009**, *58*, 243–254.

[54] D. Balzer, S. Varwig, M. Weihrauch, *Colloids Surf. Physicochem. Eng. Asp.* **1995**, *99*, 233–246.

[55] K. Penfield, *Int. J. Cosmet. Sci.* **2005**, *27*, 300–300.

[56] H. Rehage, H. Hoffmann, *Mol. Phys.* **1991**, *74*, 933–973.

[57] S. J. Candau, R. Oda, *Colloids Surf. Physicochem. Eng. Asp.* **2001**, *183–185*, 5–14.

[58] P. L. Nostro, S. Murgia, M. Lagi, E. Fratini, G. Karlsson, M. Almgren, M. Monduzzi, B. W. Ninham, P. Baglioni, *J. Phys. Chem. B* **2008**, *112*, 12625–12634.

[59] S. A. Rogers, M. A. Calabrese, N. J. Wagner, *Curr. Opin. Colloid Interface Sci.* **2014**, *19*, 530–535.

[60] M. Buchanan, M. Atakhorrami, J. F. Palierne, F. C. MacKintosh, C. F. Schmidt, *Phys. Rev. E* **2005**, *72*, 011504.

[61] P. G. de Gennes, *J. Chem. Phys.* **1971**, *55*, 572–579.

[62] M. Doi, S. F. Edwards, *The Theory of Polymer Dynamics*, Clarendon Press, **1988**.

[63] C. A. Dreiss, *Wormlike Micelles*, **2017**.

[64] J. Honerkamp, J. Weese, *Rheol. Acta* **1993**, *32*, 65–73.

[65] E. Carretti, C. Matarrese, E. Fratini, P. Baglioni, L. Dei, *Soft Matter* **2014**, *10*, 4443–4450.

[66] N. Garti, A. Aserin, S. Ezrahi, I. Tiunova, G. Berkovic, *J. Colloid Interface Sci.* **1996**, *178*, 60–68.

[67] M. Ambrosi, P. L. Nostro, L. Fratoni, L. Dei, B. W. Ninham, S. Palma, R. H. Manzo, D. Allemandi, P. Baglioni, *Phys. Chem. Chem. Phys.* **2004**, *6*, 1401–1407.

[68] P. C. Schulz, *J. Therm. Anal. Calorim.* **1998**, *51*, 135–149.

[69] M. Fernandez-Tarrio, C. Alvarez-Lorenzo, A. Concheiro, *J. Therm. Anal. Calorim.* **2007**, *87*, 171–178.

[70] P. C. Schulz, J. E. Puig, *Colloids Surf. Physicochem. Eng. Asp.* **1993**, *71*, 83–90.

[71] N. Garti, *Thermal Behavior of Dispersed Systems*, CRC Press, **2000**.

[72] K. Nakamura, T. Hatakeyama, H. Hatakeyama, *Polymer* **1983**, *24*, 871–876.

[73] D. Senatra, G. Gabrielli, G. G. T. Guarini, *EPL Europhys. Lett.* **1986**, *2*, 455.

[74] Chaplin, Martin, "Polysaccharide hydration," can be found under http://www1.lsbu.ac.uk/water/polysaccharide_hydration.html, **n.d.**

[75] L. Guan, H. Xu, D. Huang, *J. Polym. Res.* **2010**, *18*, 681–689.

[76] T. Hatakeyama, M. Tanaka, H. Hatakeyama, *J. Biomater. Sci. Polym. Ed.* **2010**, *21*, 1865–1875.

[77] D. Tatini, F. Sarri, P. Maltoni, M. Ambrosi, E. Carretti, B. W. Ninham, P. Lo Nostro, *Carbohydr. Polym.* **2017**, *173*, 344–352.

[78] N. Garti, *Thermal Behavior of Dispersed Systems*, CRC Press, **2000**.

[79] D. Tatini, P. Tempesti, F. Ridi, E. Fratini, M. Bonini, P. Baglioni, *Colloids Surf. B Biointerfaces* **2015**, *135*, 400–407.

# SUPPORTING INFORMATION

## Light-modulated rheological properties in green innovative formulations

Duccio Tatini,[a] Filippo Sarri,[a], Andrea Dalle Vaglie,[a], Martina Raudino,[a] Moira Ambrosi,[a] Emiliano Carretti,[a] Barry W. Ninham,[b] and Pierandrea Lo Nostro*[a]]

### Steady-state Rheology

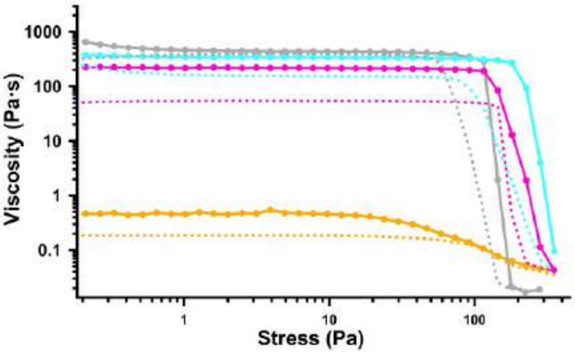

**Figure S1.** Flow Curves before (solid lines) and after (dashed lines) UV irradiation for NaOL 0.43 M mixture in the presence of KCl at 0.1 % (orange), 1% (grey), 3.5 % (light blue) and 4 % (pink).

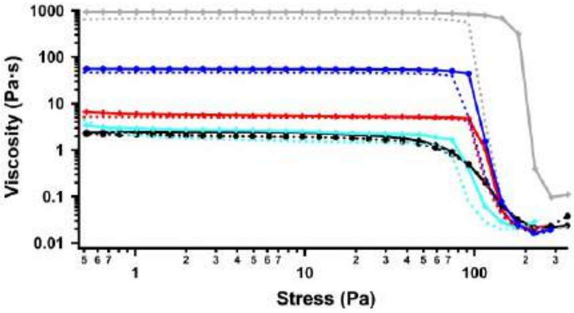

**Figure S2.** Flow Curves before (solid lines) and after (dashed lines) UV irradiation for NaOL 0.43 M mixture in the presence of azorubine 0.18 % at different concentration of KCl: 0 (black), 0.1 % (orange), 1% (grey), 3 % (red) and 3.5 % (light blue).

---

[a] D. Tatini, F. Sarri, A. Dalle Vaglie, M.Raudino, Dr. M. Ambrosi, Dr. E. Carretti, Prof. L. Dei, Prof. P. Lo Nostro
Department of Chemistry “Ugo Schiff”
University of Florence
Via della Lastruccia 3, 50019 Sesto Fiorentino (Firenze), Italy
E-mail: pierandrea.lonostro@unifi.it
[b] Prof. B.W. Ninham
Department of Applied Mathematics, Research School of Physical Sciences and Engineering
Australian National University
Canberra ACT 0200, Australia

Supporting information for this article is given via a link at the end of the document.

**Table S1**. Zero-shear rate viscosity $\eta_0$ , infinite rate viscosity $\eta_\infty$ , Cross time constant *C* (s), shear relaxation exponent *m* and $R^2$ obtained by fitting the experimental viscosity data with the Cross model.

| | | $\eta_0$ (Pa·s) | $\eta_\infty$(Pa·s) | C (s) | m | $R^2$ |
|---|---|---|---|---|---|---|
| NaOL 0.43 M | No KCl | 0.074* | 0.031* | $5.62\cdot10^{-4}$* | 1.91* | 0.998* |
| | KCl 0.1 % | 3.91 | 0.24 | 2.09 | 0.73 | 9.998 |
| | KCl 0.5 % | 27.86 | 0.008 | 0.211 | 0.98 | 0.999 |
| | KCl 1 % | 443.4 | 0.014 | 1.33 | 1.18 | 0.999 |
| | KCl 2 % | 1051 | 0.037 | 2.54 | 1.08 | 0.999 |
| | KCl 3 % | 486.8 | 0.053 | 1.133 | 1.08 | 0.999 |
| | KCl 3.5 % | 351.4 | 0.052 | 0.765 | 1.13 | 0.999 |
| | KCl 4 % | 228.0 | 0.025 | 0.813 | 1.05 | 0.998 |
| NaOL 0.43 M UV Irradiation | No KCl | 0.134* | 0.036* | 0.002* | 1.40* | 0.996* |
| | KCl 0.1 % | 0.185* | 0.029* | 0.001* | 1.35* | 0.999* |
| | KCl 0.5 % | 24.74 | 0.005 | 0.185 | 0.97 | 0.999 |
| | KCl 1 % | 427.0 | 0.011 | 3.6 | 1.03 | 0.999 |
| | KCl 2 % | 886.7 | 0.024 | 7.01 | 0.918 | 0.999 |
| | KCl 3 % | 297.8 | 0.014 | 1.78 | 0.965 | 0.999 |
| | KCl 3.5 % | 172.9 | 0.021 | 0.963 | 0.995 | 0.999 |
| | KCl 4 % | 55.01 | 0.034 | 0.101 | 1.31 | 0.999 |
| NaOL 0.43 M Azorubine 0.18 % | No KCl | 2.501 | 0.014 | 0.020 | 1.03 | 0.999 |
| | KCl 0.1 % | 6.935 | 0.012 | 0.060 | 1.01 | 0.998 |
| | KCl 0.5 % | 278.8 | 0.022 | 1.83 | 1.05 | 0.999 |
| | KCl 1 % | 951.8 | 0.038 | 2.50 | 1.08 | 0.999 |
| | KCl 2 % | 57.98 | 0.012 | 0.251 | 1.13 | 0.998 |
| | KCl 3 % | 5.722 | 0.106 | 0.025 | 1.24 | 0.998 |
| | KCl 3.5 % | 2.661 | 0.014 | 0.017 | 1.17 | 0.999 |
| | KCl 4 % | 1.852 | 0.016 | 0.008 | 1.37 | 0.999 |

| | | | | | | |
|---|---|---|---|---|---|---|
| NaOL 0.43 M Azorubine 0.18 % UV Irradiation | No KCl | 2.074 | 0.016 | 0.016 | 1.028 | 0.997 |
| | KCl 0.1 % | 13.6 | 0.025 | 0.147 | 1.09 | 0.999 |
| | KCl 0.5 % | 728.3 | 0.002 | 14.01 | 0.873 | 0.999 |
| | KCl 1 % | 736.7 | 0.014 | 3.07 | 1.11 | 0.999 |
| | KCl 2 % | 53.44 | 0.012 | 0.289 | 1.09 | 0.998 |
| | KCl 3 % | 5.205 | 0.016 | 0.019 | 1.34 | 0.999 |
| | KCl 3.5 % | 2.01* | 0.015* | 0.010* | 1.30* | 0.999* |
| | KCl 4 % | 730.1 | 0.009* | 0.015* | 0.96* | 0.999* |

[a] Table Footnote. [b] …

## 2.1 Oscillatory Measurements

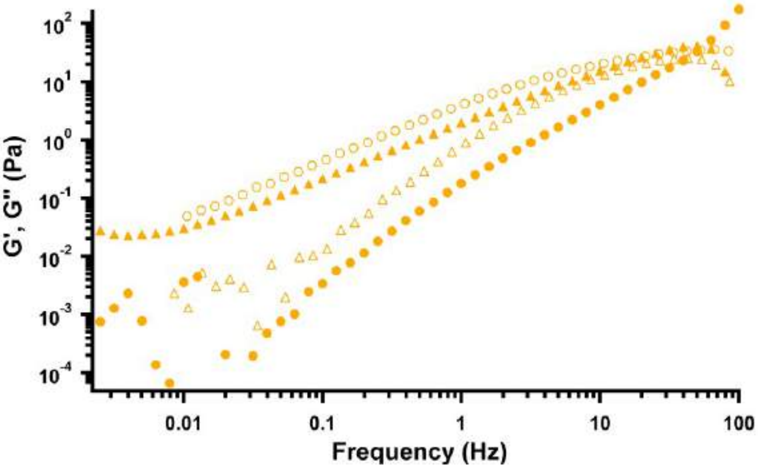

**Figure S3.** Storage (triangles) and loss (circles) moduli before (filled markers) and after (hollow markers) UV irradiation for NaOL 0.43 M mixture in the presence of KCl at 0.1 %.

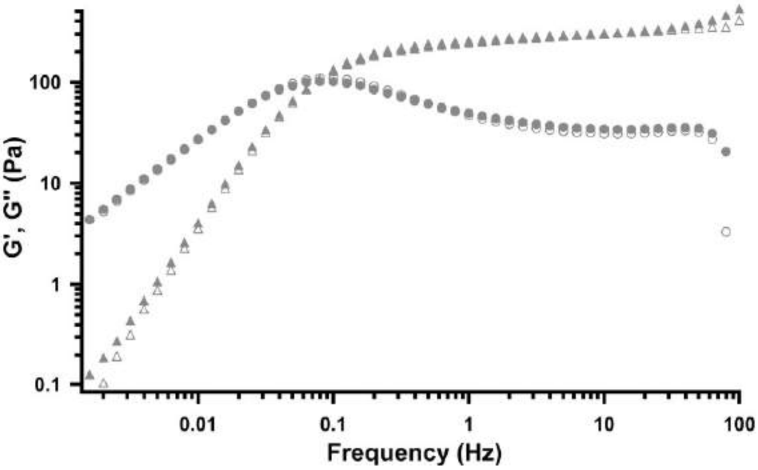

**Figure S4.** Storage (triangles) and loss (circles) moduli before (filled markers) and after (hollow markers) UV irradiation for NaOL 0.43 M mixture in the presence of KCl at 1 %.

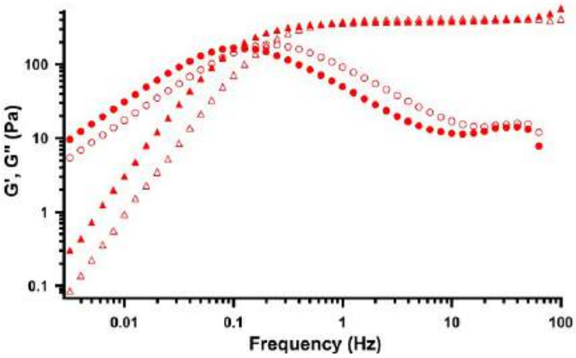

**Figure S5.** Storage (triangles) and loss (circles) moduli before (filled markers) and after (hollow markers) UV irradiation for NaOL 0.43 M mixture in the presence of KCl at 3 %.

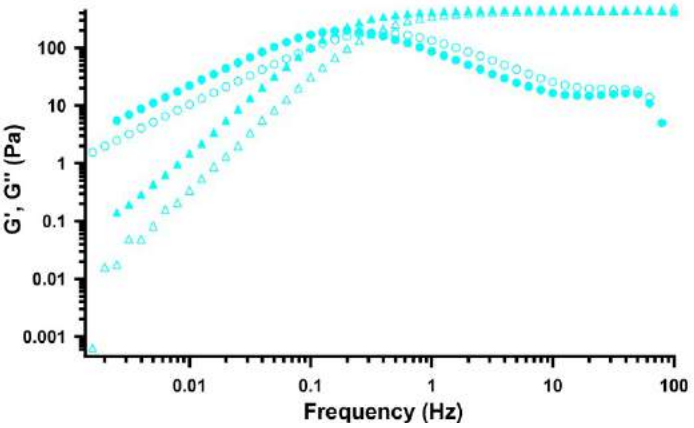

**Figure S6.** Storage (triangles) and loss (circles) moduli before (filled markers) and after (hollow markers) UV irradiation for NaOL 0.43 M mixture in the presence of KCl at 3.5 %.

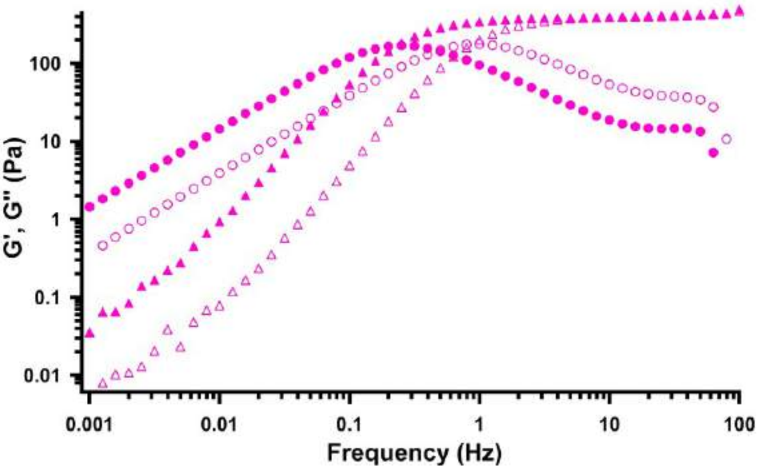

**Figure S7.** Storage (triangles) and loss (circles) moduli before (filled markers) and after (hollow markers) UV irradiation for NaOL 0.43 M mixture in the presence of KCl at 4 %.

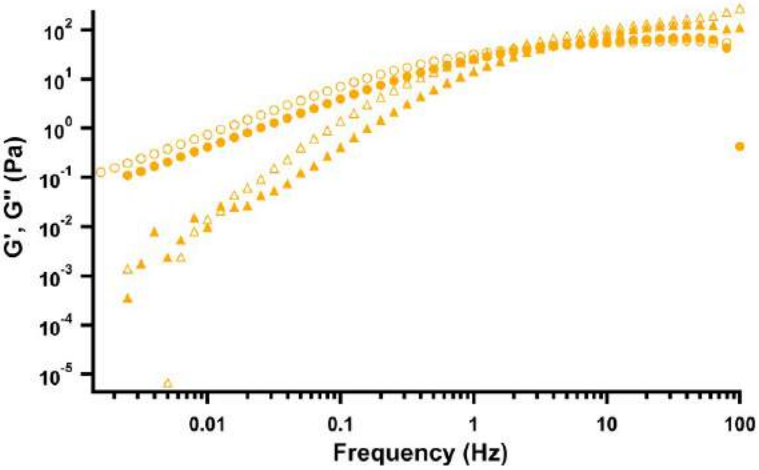

**Figure S8.** Storage (triangles) and loss (circles) moduli before (filled markers) and after (hollow markers) UV irradiation for NaOL 0.43 M + azorubine 0.18 % mixture in the presence of KCl at 0.1 %.

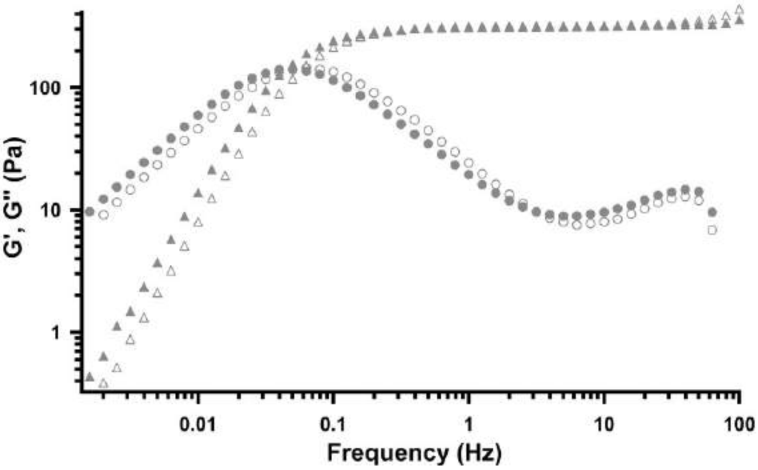

**Figure S9.** Storage (triangles) and loss (circles) moduli before (filled markers) and after (hollow markers) UV irradiation for NaOL 0.43 M + azorubine 0.18 % mixture in the presence of KCl at 1 %.

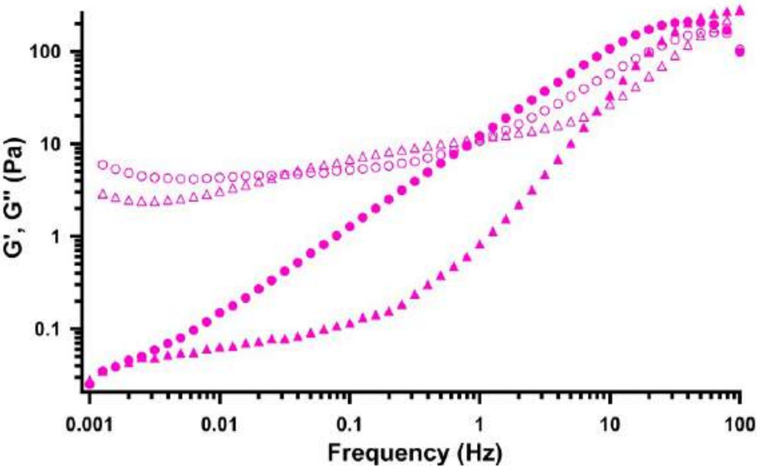

**Figure S10.** Storage (triangles) and loss (circles) moduli before (filled markers) and after (hollow markers) UV irradiation for NaOL 0.43 M + azorubine 0.18% mixture in the presence of KCl at 4 %.

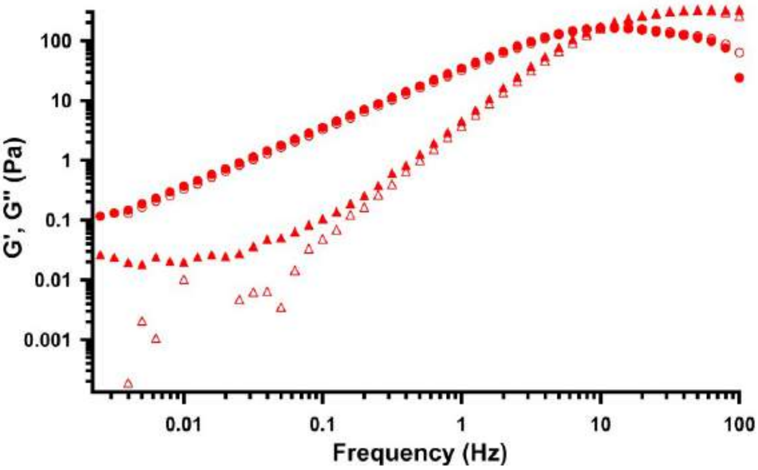

**Figure S11.** Storage (triangles) and loss (circles) moduli before (filled markers) and after (hollow markers) UV irradiation for NaOL 0.43 M + azorubine 0.18 % mixture in the presence of KCl at 3 %.

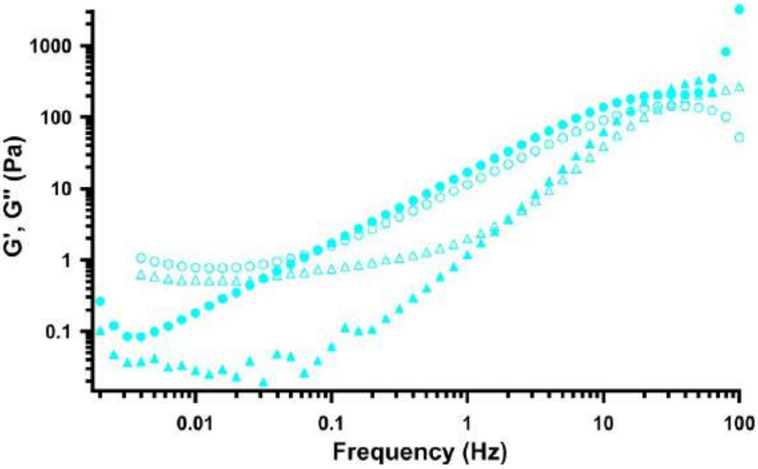

**Figure S12.** Storage (triangles) and loss (circles) moduli before (filled markers) and after (hollow markers) UV irradiation for NaOL 0.43 M + azorubine 0.18 % mixture in the presence of KCl at 3.5 %.

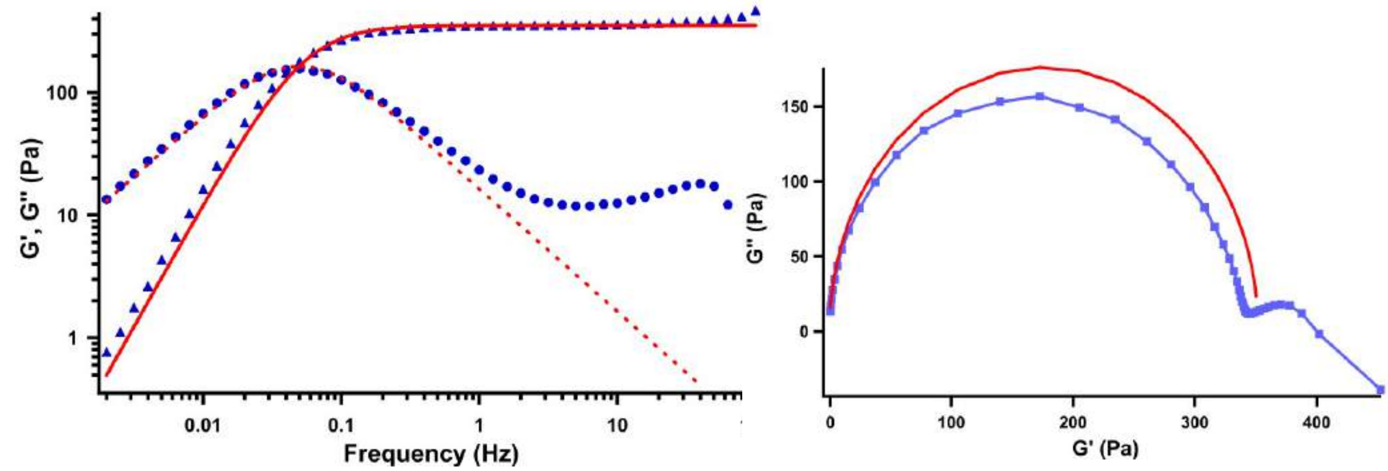

**Figure S13.** On the left, the storage (triangles) and loss (circles) moduli for NaOL 0.43 M in the presence of KCl at 2 % with the respective fitting (red lines) according to the Maxwell model. On the right, the relative Cole-Cole plot.

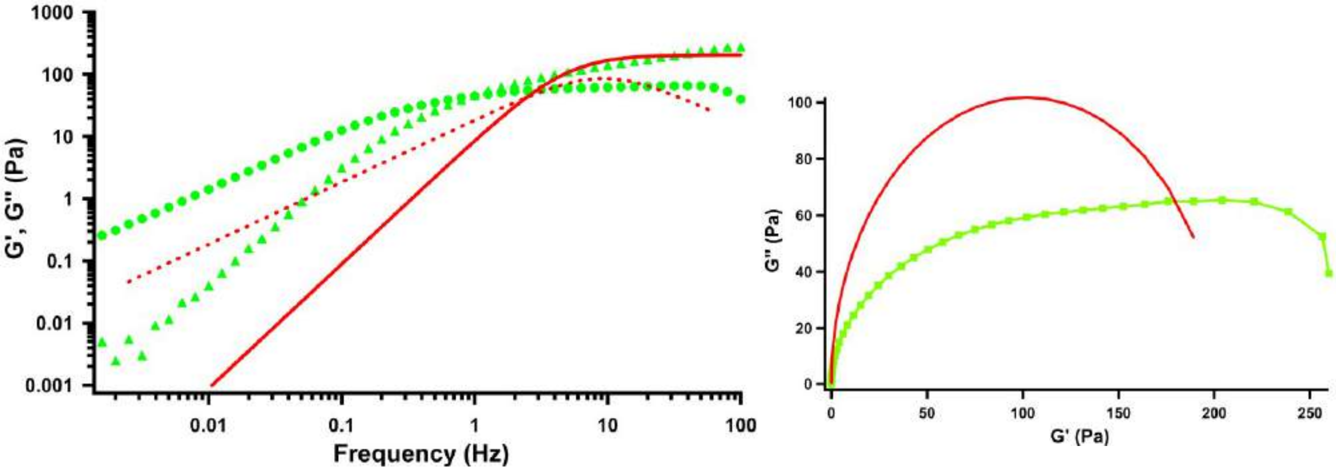

**Figure S14.** On the left, the storage (triangles) and loss (circles) moduli for NaOL 0.43 M in the presence of KCl at 0.5 % with the respective fitting (red lines) according to the Maxwell model. On the right, the relative Cole-Cole plot.

## DSC

**Table S2.** Melting temperature, the relative enthalpy change and amount (%) of free water ($\Delta H_{mf}$, $T_{mf}$ and $W_f$), interfacial water ($\Delta H_{mi}$, $T_{mi}$ and $W_i$) and freezable bound water ($\Delta H_{mb}$, $T_{mb}$ and $W_b$) for all the examined samples, before and after UV irradiation.

| | | $\Delta H_{mf}$ (J/g) | $T_{mf}$ (°C) | $W_f$ (%) | $\Delta H_{mi}$ (J/g) | $T_{mi}$ (°C) | $W_i$ (%) | $\Delta H_{mb}$ (J/g) | $T_{mb}$ (°C) | $W_b$(%) |
|---|---|---|---|---|---|---|---|---|---|---|
| **NaOL 0.43 M** | No KCl | 319.9 | 2.50 | 95.8 | - | - | - | - | - | |
| | KCl 0.1 % | 300.2 | 1.97 | 89.9 | - | - | - | - | - | |
| | KCl 0.5 % | 286.5 | 1.30 | 85.8 | 1.221 | -14.67 | 0.4 | - | - | |
| | KCl 1 % | 232.5 | 1.69 | 70.0 | 8.367 | -12.88 | 2.7 | - | - | |
| | KCl 2 % | 217.7 | 0.39 | 65.2 | 18.22 | -11.58 | 5.8 | - | - | |
| | KCl 3 % | 169.6 | 0.12 | 50.8 | 21.66 | -11.02 | 6.9 | - | - | |
| | KCl 3.5 % | 163.3 | -0.94 | 48.9 | 27.47 | -11.22 | 8.8 | - | - | |
| | KCl 4 % | 152.8 | -1.06 | 45.8 | 25.16 | -11.45 | 8.1 | 3.507 | -22.69 | 1.12 |
| **NaOL 0.43 M UV Irradiation** | No KCl | 314.7 | 1.85 | 94.3 | - | - | - | - | - | |
| | KCl 0.1 % | 305.2 | 1.54 | 91.4 | - | - | - | - | - | |
| | KCl 0.5 % | 288.0 | 1.57 | 86.3 | 2.899 | -15.44 | 0.9 | - | - | |
| | KCl 1 % | 269.4 | 0.14 | 81.0 | 8.0296 | -13.53 | 2.6 | - | - | |
| | KCl 2 % | 231.2 | -0.39 | 69.2 | 18.39 | -12.25 | 5.9 | - | - | |
| | KCl 3 % | 178.2 | -0.72 | 53.4 | 25.52 | -11.54 | 8.2 | - | - | |

| | | | | | | | | | | |
|---|---|---|---|---|---|---|---|---|---|---|
| | KCl 3.5 % | 161.7 | -1.16 | 48.4 | 26.78 | -11.52 | 8.6 | - | - | |
| | KCl 4 % | 153.2 | -1.06 | 45.9 | 19.85 | -12.06 | 6.4 | 2,433 | -23.90 | 0.78 |
| **NaOL<br>0.43 M<br>Azorubine 3.6·10$^{-3}$ M** | No KCl | 312.4 | 2.33 | 93.6 | - | - | - | - | - | - |
| | KCl 0.1 % | 310.1 | 1.54 | 92.9 | - | - | - | - | - | - |
| | KCl 0.5 % | 288.5 | 1.18 | 86.4 | 2.112 | -17.61 | 0,68 | - | - | - |
| | KCl 1 % | 266.4 | 0.46 | 79.8 | 6.545 | -14.54 | 2,10 | - | - | - |
| | KCl 2 % | 209.0 | 1.79 | 62.6 | 11.05 | -12.08 | 3,54 | - | - | - |
| | KCl 3 % | 183.4 | -0.12 | 54.9 | 17.24 | -11.99 | 5,52 | 1.715 | -23.70 | 1,72 |
| | KCl 3.5 % | 163.2 | -0.65 | 48.9 | 19.95 | -11.69 | 6,39 | 0.7329 | -25.81 | 0,73 |
| | KCl 4 % | 167.4 | -1.28 | 50.2 | 23.64 | -12.16 | 7,57 | 3.666 | -24.01 | 3,67 |
| **NaOL<br>0.43 M<br>Azorubine 3.6·10$^{-3}$ M<br>UV Irradiation** | No KCl | 313.6 | 1.52 | 94,0 | - | - | - | - | - | - |
| | KCl 0.1 % | 312.5 | 0.85 | 93,6 | - | - | - | - | - | - |
| | KCl 0.5 % | 306.8 | 0.72 | 91,9 | - | - | - | - | - | - |
| | KCl 1 % | 271.9 | 0.13 | 81,5 | 6.591 | -14.72 | 2,11 | - | - | - |
| | KCl 2 % | 231.3 | -0.45 | 69,3 | 14.92 | -12.75 | 4,78 | - | - | - |
| | KCl 3 % | 186.1 | -0.46 | 55,8 | 15.70 | -12.16 | 5,03 | 1.843 | -23.94 | 0,59 |
| | KCl 3.5 % | 182.7 | -1.18 | 54,7 | 20.47 | -12.40 | 6,56 | 1.396 | -24.42 | 0,45 |
| | KCl 4 % | 153.2 | -1.06 | 45,9 | 19.85 | -12.06 | 6,36 | 2.433 | -23.90 | 0,78 |

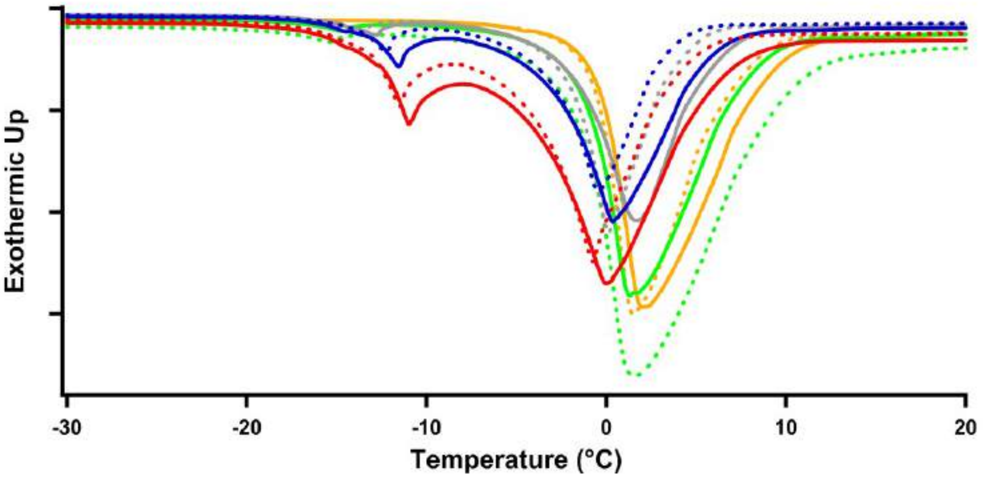

**Figure S15.** DSC thermograms before (solid lines) and after (dashed lines) UV irradiation for NaOL 0.43 M mixture at different concentration of KCl: 0.1 % (orange), 0.5 % (green), 1 % (grey), 2 % (blue) and 3 % (red).

# The effect of temperature and magnetic field on the precipitation of insoluble salts of alkaline earth metals

Martina Raudino[a], Filippo Sarri[a], Duccio Tatini[a], Moira Ambrosi[a],
Giovanni Domenico Aloisi[a], Barry W. Ninham[b], Luigi Dei[a], Pierandrea Lo Nostro[a,c,]*

*a: Department of Chemistry "Ugo Schiff" and CSGI, University of Florence, 50019 Sesto Fiorentino (Firenze), Italy*
*b: Department of Applied Mathematics, Research School of Physical Sciences and Engineering, Australian National University, Canberra ACT 0200, Australia*
*c: Enzo Ferroni Foundation, 50019 Sesto Fiorentino (Firenze), Italy*

---

* Corresponding author. Tel: +39 055 4573010. E-mail address: pierandrea.lonostro@unifi.it (P. Lo Nostro)

## Highlights

- Magnetic field and temperature limit the precipitation of scarcely soluble salts
- The study of the magnetic effect is extended to Sr(II) and Ba(II) carbonates
- The strongest magnetic effect is found for calcium carbonate
- The effect of heavy water on the precipitation of $CaCO_3$ is investigated
- Magnetic field affects the structure of hydration water of ions in solutions

## Abstract

A study of the effects induced by a weak magnetic field of about 0.4 T on the precipitation of insoluble alkali earth salts (mainly carbonates) is reported. Optical microscopy, X-ray diffraction and fluorescence experiments are used. The roles played by temperature and solvent structure are explored via measurements at 25 and 60 °C in $H_2O$ or $D_2O$ solutions. The results suggest that the magnetic field affects the structure of the water molecules in the hydration shell of the ions. The work represents a step forward in our understanding of the curious effects of magnetic fields on salt precipitation. It has application in various areas, from water treatment to shale gas extraction, colloid science, biology and chirality.

## Keywords

carbonate(s); sulfate(s); precipitation; magnetic field effect; temperature effect; chirality

## 1. Introduction

Magnetic water treatment (MWT) is one of the most common methods used for water and wastewater purification (Ambashta and Sillanpää, 2010; Zaidi et al., 2014). It is a physical treatment that avoids the use of expensive and harmful chemicals, such as polyphosphates or corrosive substances. The first examples of commercial devices based on magnetic fields date back to the beginning of the 20th century (Holcomb, 1989). The use of magnetic fields in water treatment remains of great interest, but our understanding of associated phenomena is limited. Different techniques deploying magnetic effects have continued to develop over recent decades. For example, they have been successfully used for separation technologies with membrane distillation (Gryta, 2011). Another is a process called high-gradient magnetic separation (HGMS) that attracts and traps magnetic particles applying a magnetic field across a column of magnetically susceptible plates (Yavuz et al., 2009; Zeng et al., 2017). Other applications are based on the use of magnetic ion exchange resins or magnetic sorbents for the removal of dyes (Hamidzadeh et al., 2015; Wan et al., 2017), heavy metals (Ozay et al., 2009; L. Wang et al., 2018), organic compounds (Bolto et al., 2002), and pollutants (Gutierrez et al., 2017).

At a fundamental level, how magnetic fields affect water and its solutes is still an open question. For example, a magnetic field can modify the coagulation of particles in a suspension of ultrafine polystyrene latexes, $SiO_2$ particles and ions in solution. Changes in both the crystallization rate and the crystal structure of insoluble salts precipitated from water solutions can occur (Higashitani et al., 1993; Oshitani et al., 1999). Relevant effects of external magnetic fields on the formation of complex systems, such as protein crystals, have been reported as well (Okada et al., 2013).

The first application to water treatment was the placement of an external magnet on steel pipelines. This causes a reduction of scale deposition in pipelines (Baker and Judd, 1996; Busch and Busch, 1997). The most common constituents of scales are $CaCO_3$, $CaSO_4 \cdot 2H_2O$ and silica, together with smaller amounts of other sparingly soluble salts, such as strontium and barium carbonates and sulfates, $Ca_3(PO_4)_2$ and ferric and aluminum hydroxides (Kodel et al., 2012). For this reason, most of the relevant literature on the effects of an external magnetic field on the precipitation of salts has focused mainly on $CaCO_3$. It was found that magnetic treatment at ambient temperature and pressure of calcite leads to a significant conversion into aragonite. Calcite is the stable polymorph of calcium carbonate, while aragonite is the predominant form at temperatures higher than 60 °C and at high pressure (Lipus and Dobersek, 2007). Because of the needle-like morphology of aragonite crystals, the magnetic treatment allows the formation of softer and more soluble deposits by comparison with the hard scale formed by the highly adhesive rhombohedral calcite crystals. This result is of great interest since aragonite formation reduces the likelihood of pipelines obstruction (Kozic and Lipus, 2003): consequently, commercial magnetic water treatment devices are widely used.

In this paper, an extensive study is made on the effect of a static magnetic field on calcium carbonate precipitation. The structure and size of $CaCO_3$ crystals precipitated from water solutions is explored in a magnetic field of 0.4 T. In order to deepen the understanding of the mechanism behind the magnetic field effect on the precipitation of scarcely soluble salts, we perform fluorescence, optical microscopy and X-ray diffractometry experiments. To the best of our knowledge, fluorescence experiments have not been used so far to cast light on such phenomena. All measurements are performed at 25 and 60 °C in order to assess the role played by temperature on the process. This was because water is virtually identical in its physical properties with hydrazine and is not hydrogen bonded by 90 °C. So whatever the elusive term “liquid structure” means here it varies over the temperature range 25-60 °C.

The first evidence of temperature as a crucial parameter in salt precipitation was an observation of Claude-Louis Berthollet (1748-1822). A member of Napoleon’s expedition to the Nile, in 1795 he observed that rocks of soda lime (sodium carbonate) precipitate on the banks of the Nile rather than the expected calcium carbonate. The precipitation, from retreating river floods, occurs at high summer temperatures up to 60 °C. Awareness that temperature plays a role in salt precipitation and by extension in chemical reactivity probably marks the beginning of physical chemistry (Ninham, 2017).

In addition to the role of temperature on calcium carbonate precipitation with and without magnetic fields, we investigate the importance of ionic hydration on the phenomenon. It is reported that $D_2O$ displaces water of hydration in Nafion (Bunkin et al., 2018); however, no mention on the salt precipitation in $D_2O$ and in the presence of a magnetic field is made. In the present paper we report on the effect of heavy water on the precipitation of $CaCO_3$ with and without magnetic fields at the two different temperatures.

Finally, the study is also extended to the effect of magnetic fields on the precipitation of Sr(II) and Ba(II) carbonates. In fact, they are also responsible for the formation of scales due to their very low solubility but there are no literature reports regarding the correlation between their precipitation and magnetic fields. Our experiments aim at highlighting the possible differences in the magnetic response between ions with different chemical nature, thus providing more information on the correlation between the magnetic effect and the ionic hydration. In addition, this work can have significant outcomes for the control of naturally occurring radioactive materials (NORM), such as radium salts, from a perspective of using magnetic water treatments as a "green strategy" to reduce the drawback of NORM extraction in applications, for example in shale gas operations (Ebner et al., 1999; Kochen and Navratil, 1997). The last two issues cover a wide range of hot topics in chemical engineering, such as the treatment of industrial waters and/or the confinement of contaminated flowback water.

From a fundamental point of view, the results drawn from this study might be a clue to understand the curious phenomenon of magnetic effects in solution and give rise to fundamental questions related to the sources of chirality (Fujiki, 2014; Ruchon et al., 2004) and the possible implications in biology, for example in the field of protein crystal precipitation (Okada et al., 2013) or DNA assembly (Buchachenko et al., 2013; Lai and Singh, 2004). Apart from fundamental science, we believe that the work could be of interest also from a practical point of view since it has application to a variety of other fields, like water treatment in shale gas extractive process (Khamehchi et al., 2017), and in the design of nanoparticles (Lu et al., 2007).

## 2. Experimental

### *2.1. Samples preparation*

Crystals were precipitated from the corresponding salt solutions by mixing equal volumes (2 mL) of 8 mM $Na_2CO_3$ with 8 mM $CaCl_2$, $BaCl_2$ or $SrCl_2$ either at 25 or 60 °C. The temperature was controlled using a water bath (± 0.1 °C). In the case of calcium sulfate, the crystals were precipitated by mixing 2 mL $Na_2SO_4$ and 0.5 M $CaCl_2$ at 25 °C. The complete list of reactants is reported in the SI file.

### *2.2. Magnetic treatment*

The effect of magnetic field on salt precipitation was investigated by exposing 2 mL of each ion solution to a 0.4 T static magnetic field for 15 minutes at room temperature before the mixing. After the magnetic treatment, the magnetized solutions were removed from the magnet and mixed at 25 and 60 °C. The intensity of the magnetic field (measured with a Hall effect sensor) and the exposure time were chosen on the basis of previous literature data, especially after Higashitani, who showed a magnetic effect on $CaCO_3$ for magnetic field greater than 0.3 T and exposure times longer than 10 minutes (Higashitani et al., 1993).

The terrestrial MF, with an average intensity between 2 and $7 \cdot 10^{-5}$ T, is too weak for practical applications in anti-scaling treatments. Hence, in industrial applications the starting solutions ought to be exposed to a more intense MF before being pumped in the pipelines. However this circumstance does not represent a limit for real applications since previous works already demonstrated a so-called "water memory effect": magnetized water retains its properties from few hours (Holysz et al., 2002) to 60 hours (Barrett and Parsons, 1998) up to 3-4 days (Oshitani et al., 1999).

### 2.3 *Optical microscopy*

A Nikon Eclipse Ti-S Inverted Microscope was used to obtain optical images of crystals precipitating at 25 and 60 °C from either regular or magnetized solutions. All measurements were performed using an objective with a 20X magnification. At least three different regions of each sample were analyzed in order to obtain a statistically meaningful result.

### 2.4 *Fluorescence measurements*

Fluorescence measurements were performed at 25 °C using an LS50B Perkin Elmer spectrofluorimeter equipped with a Haake thermostat. Samples were adjusted into 1 cm optical path length quartz cuvettes. Emission spectra were recorded in the 240−700 nm range using different excitation wavelengths (see Table S1 in the Supplementary Material).

Fluorescence spectra were recorded on crystals in solution after 1 week from the mixing of the starting precursors in order to obtain reproducible signals related to the different species in solution.

### *2.5 X-ray Diffraction (XRD)*

XRD measurements on dry $CaCO_3$ crystals were carried out at room temperature in air by using a Bruker New D8 Da Vinci diffractometer (Cu Kα radiation, 40 kV × 40 mA), equipped with a Bruker LYNXEYE-XE detector, scanning range $2\theta = 20-60°$, 0.03° increments of $2\theta$, and a counting time of 0.3 s/step.

## 3. Results

### *3.1 Effect of temperature*

#### *3.1.1 Optical microscopy*

The comparison between the optical micrographs obtained after 60 minutes from the mixing of the starting solutions at 25 and 60 °C on Ca(II), Sr(II) and Ba(II) carbonates (Figure 1) illustrates the effect of temperature on the precipitation of the insoluble salts.

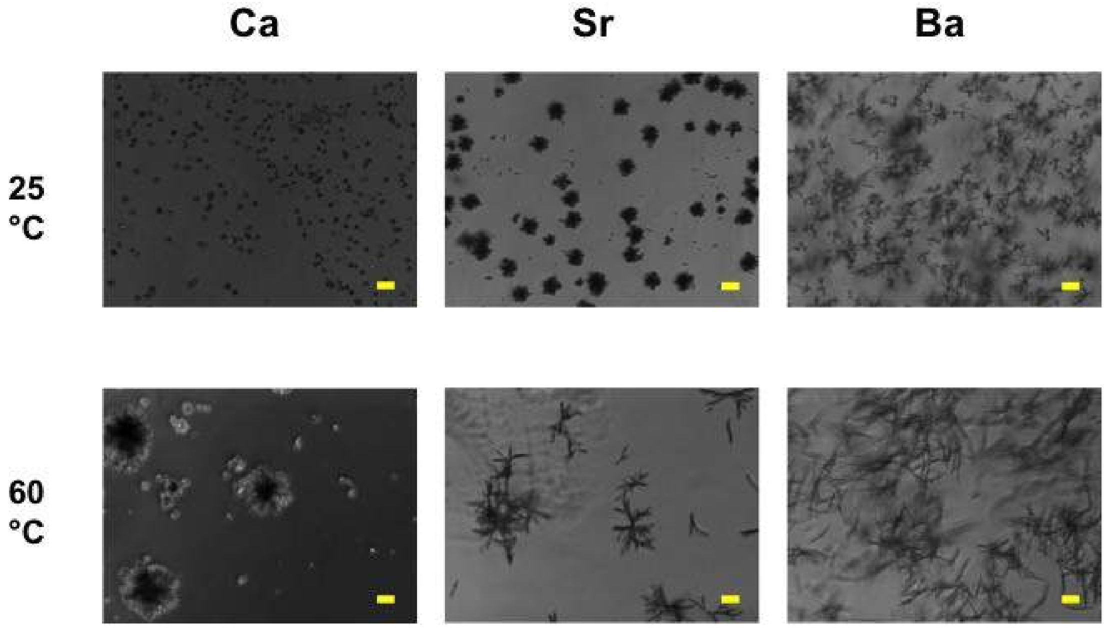

**Figure 1.** Optical micrographs of calcium, strontium and barium carbonates precipitated after 60 minutes from the mixing of non magnetized solutions at 25 and 60 °C. Scale bar: 100 μm.

The optical micrographs recorded at room temperature on calcium carbonate reveal that the predominant polymorphs are calcite (rhombohedral crystals) and vaterite (spherical crystals). This result is in line with previous studies on $CaCO_3$ polymorphs formed from highly super-saturated solutions (Ogino et al., 1987): it was found that vaterite and calcite are formed at low temperature (14−30 °C), while the conversion into aragonite (orthorombic structure, often in form of needle-like crystals) is favoured at higher temperatures (60−80 °C) and becomes the predominant form at about 70 °C (Wray and Daniels, 1957). Accordingly, optical microscopy at 60 °C shows the presence of aragonite together with calcite and hexagonal plate vaterite crystals. This result is of great interest for application purposes since in real operating conditions, for example during shale gas extraction, the temperature reached in the pipelines is well above 100 °C (Ross and Bustin, 2008). Therefore the formation of aragonite is favoured: since aragonite is less densely packed with respect to calcite (see Table S2 in the Supplementary Material), aragonite scales are softer and more soluble with respect to calcite deposits, thus reducing the problem of pipe obstruction. Regarding strontium and barium carbonates, no different allotropic forms exist in the temperature range investigated: in fact, there is reported a γ-β transition of strontium carbonate at 929.13 °C, while γ-β and β-α transitions in $BaCO_3$ occur at 804.37 and 967.94 °C, respectively (Earnest and Miller, 2017). The optical micrographs show that the morphology of crystals remains the same for both samples at 25 and 60 °C: strontianite ($SrCO_3$) crystals possess a dendritic structure, as reported in the literature for the precipitation of $SrCO_3$ in aqueous solutions without additives (Guo et al., 2008), while witherite ($BaCO_3$) precipitates forming floc crystals. Considering the concentrations and pH values of the solutions (8 mM and 8.5-9, respectively), our results for $BaCO_3$ are in line with the detailed study by Chen (Chen et al., 2001) on the dependence of $BaCO_3$ crystal morphology on concentration and pH. There it was demonstrated that floc crystals are formed at high concentration (>> 2 mM) in the pH range between 9.0 and 10.5, while olivary-like and candy-like crystals become the major products in the concentration range 1.0–3.5 mM at $9.0 < pH < 9.5$.

Finally, we observe for all samples that temperature strongly affects crystal dimension causing an increase in their size. This suggests that the alkali earth carbonates are less soluble at temperatures above 25 °C, in agreement with previous studies on the precipitation of carbonate-scaling minerals as a function of T and P (García et al., 2006) and on the mechanism of calcium carbonate formation at different temperatures (Ogino et al., 1987).

### *3.1.2 Fluorescence spectra*

Fluorescence spectra from solid crystals of both calcite and aragonite exhibit different signals in the range 200–700 nm (Gaft et al., 2015). We took advantage of this feature to study the equilibrium calcite $\leftrightarrows$ aragonite as a function of temperature by recording the fluorescence spectra of the two polymorphs in solution (see Figure S1 in the Supplementary Material for the excitation spectra of pure aragonite and calcite in water). The fluorescence spectra of $CaCO_3$ in solution at 25 and 60 °C are shown in Figure 2.

The sample investigated at 25 °C shows strong emission signals centred at about 300 ($\lambda_{exc}$ = 272 nm) and 600 nm ($\lambda_{exc}$ = 238 and 254 nm), while the sample at 60 °C shows a significant broad peak at about 350 nm ($\lambda_{exc}$ = 272 nm) and an emission peak at 555 nm ($\lambda_{exc}$ = 254 nm). Since the signals at 300 and 600 nm are particularly intense only in the sample obtained at 25 °C, we can infer that they are related to calcite, and that this is the most abundant polymorph at such temperature. This finding agrees with the optical images.

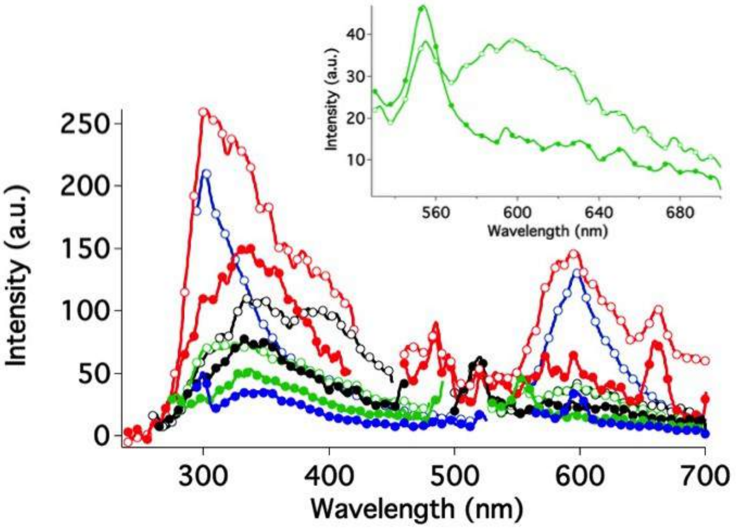

**Figure 2.** Fluorescence excitation spectra of $CaCO_3$ crystals in solution at 25 (empty circles) and 60 °C (filled circles) in the absence of magnetic field. Red: $\lambda_{exc}$ = 220 nm, black: $\lambda_{exc}$ = 238 nm, green: $\lambda_{exc}$ = 254 nm, blue: $\lambda_{exc}$ = 272 nm. Inset: emission spectra in the region 530–700 nm ($\lambda_{exc}$ = 254 nm).

Instead the signals centred at 350 and 555 nm are mainly visible in the sample at 60 °C, so they are probably due to aragonite crystals. This observation, together with a reduction in the intensity of calcite emission bands (300 and 600 nm), indicates a partial conversion of calcite into aragonite at higher temperature, again in agreement with previous works (Lippmann, 1973; Ogino et al., 1987) and with our optical microscopy experiments. It is interesting to note that a small contribution centred at 555 nm is also visible in the emission spectrum of the sample at 25 °C when excited at 254 nm: this evidence prompts us to conclude that, even if calcite is thermodynamically the most stable polymorph at ambient T and P, some aragonite crystals co-exist because aragonite and vaterite phases are kinetically favoured. The same observation was found in the work by Wang (Wang et al., 2013), where XRD experiments carried out on $CaCO_3$ crystals precipitated in bulk solution at 25 °C after 15 h confirmed that calcite is the dominant crystalline phase with an 8 wt % of aragonite.

Another feature derives from the fluorescence spectra: the intensity related to $CaCO_3$ precipitated at 60 °C is about two orders of magnitude lower than that for the sample at 25 °C, in agreement with the presence of fewer particles in solution at high temperature after sedimentation. This is a further confirmation that an increase in temperature promotes the precipitation of $CaCO_3$.

Fluorescence experiments were also performed on Sr(II) and Ba(II) carbonates and shown in Figure 3.

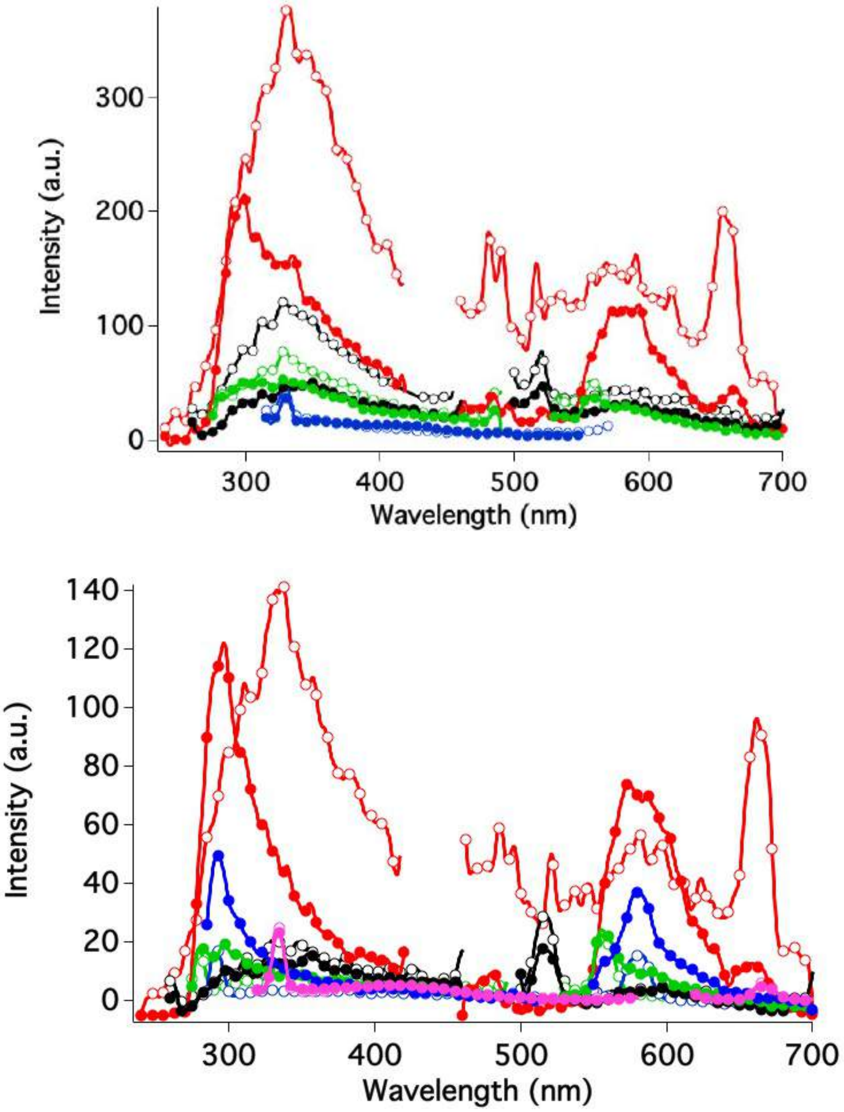

**Figure 3.** Fluorescence excitation spectra of $BaCO_3$ (top) and $SrCO_3$ (bottom) crystals in solution at 25 (empty circles) and 60 °C (filled circles) in the absence of magnetic field. Red: $\lambda_{exc}$ = 220 nm, black: $\lambda_{exc}$ = 238 nm, green: $\lambda_{exc}$ = 255 nm, blue: $\lambda_{exc}$ = 265 nm for $SrCO_3$ and 296 nm for $BaCO_3$, purple: $\lambda_{exc}$ = 300 nm.

The profiles of the emission spectra are the same regardless of the temperature of precipitation for both salts, indicating that there is no significant effect on the polymorph formed after changing the temperature. This is in good agreement with the results of optical microscopy and the previous literature. Regarding the intensity of the spectra, we note in case of barium the same behaviour already observed and discussed for $CaCO_3$, i.e. the temperature-promoted precipitation and the reduction in the fluorescence signal associated to the crystals in solution. Instead the temperature seems to have the opposite effect on Sr(II), where the intensity of the spectra on the precipitated salt at high T is higher than the case of the salt formed at room temperature.

### *3.1.3 X-ray diffractometry*

The temperature-induced formation of aragonite was also confirmed by XRD measurements reported in Figure 4, where the peaks at 26.3, 27.3, 41 and 46° associated with aragonite (Kontoyannis and Vagenas, 2000) appear in the pattern of the sample precipitated at 60 °C.

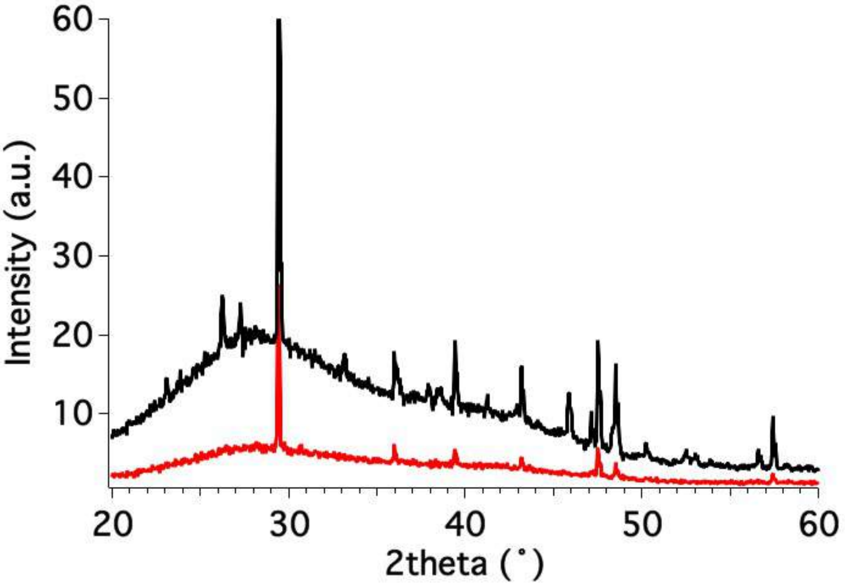

**Figure 4.** XRD patterns of $CaCO_3$ crystals precipitated at 25 (red) and 60 (black) °C. Spectra are offset along the y-axis.

## *3.2 Effect of the magnetic field*

We come now to the remarkable effects of a static magnetic field on the precipitation of these insoluble carbonates. We extend the study to new salts, i.e., Sr(II) and Ba(II) carbonates, and investigated the phenomenon with new techniques, such as fluorescence experiments. Figure 5 shows the optical images obtained at 25 °C on precipitates from solutions exposed to the static magnetic field and compared to those obtained from untreated solutions.

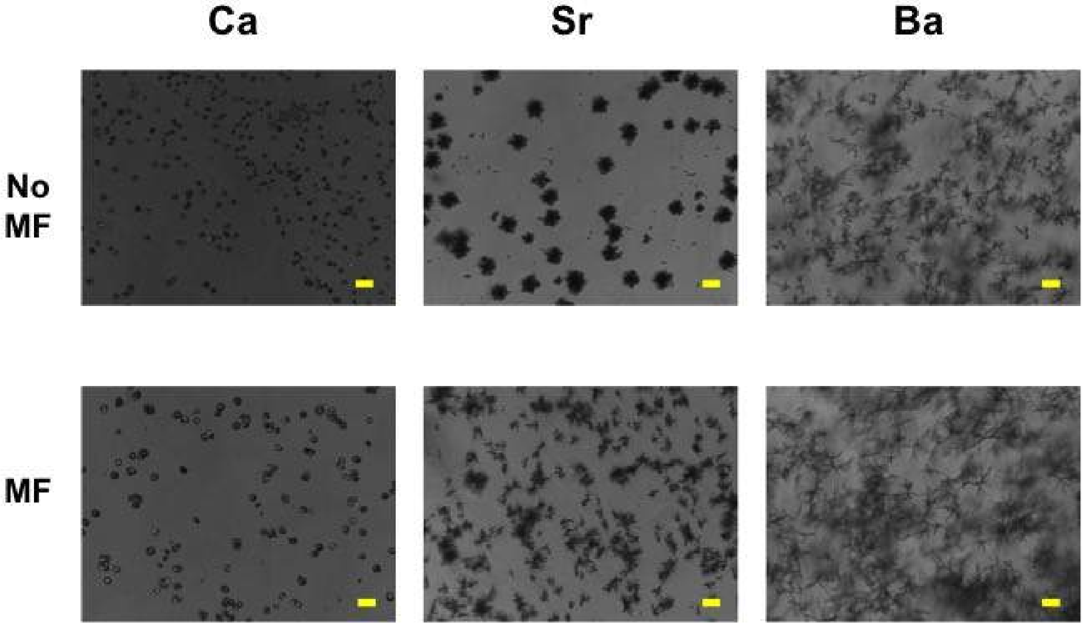

**Figure 5.** Optical micrographs of calcium, strontium and barium carbonates precipitated at 25 °C after 60 minutes from the mixing of non magnetized (top) and magnetized (bottom) solutions. Scale bar: 100 µm.

The effect on $CaCO_3$ and $SrCO_3$ is quite remarkable. In the case of calcium carbonate, according to previous literature results (Higashitani et al., 1993; Tai et al., 2008b), the magnetic exposure of the starting solutions leads to a suppression in the nucleation and an acceleration of the growth that results in the decrease of the number of crystals and an increase of their size. The main advantage of the formation of larger crystals is their smaller surface charge, so they will not adhere together to form a scale in the same way as smaller crystals.

The fluorescence spectra reported in Figure 6 show a strong decrease in the intensity of the magnetized sample in agreement with a lower amount of crystals in solution. Furthermore, the magnetically treated sample shows principally the emission signals of aragonite (defined peak at 555 nm and a visible shoulder at 350 nm) and a small contribution due to calcite (peaks centred at 300 and 600 nm), while the untreated sample reveals a stronger contribution of calcite. This result suggests that a partial transformation of calcite into aragonite occurs at room temperature upon the application of an external magnetic field, as reported in previous works (Chang and Tai, 2010; Kobe et al., 2002).

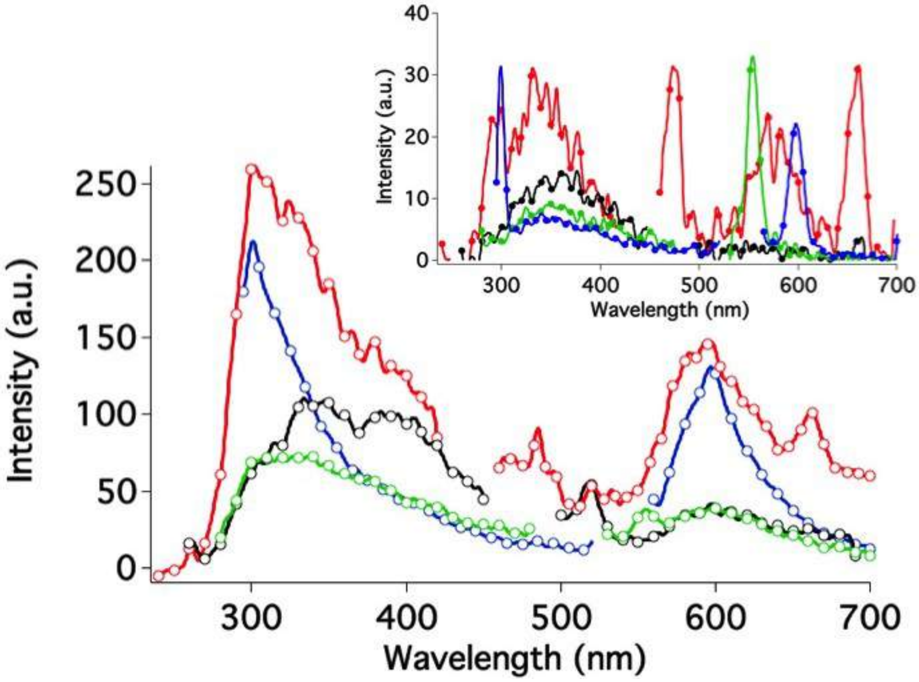

**Figure 6.** Fluorescence excitation spectra of $CaCO_3$ crystals in solution at 25 °C starting from non magnetized (empty circles) and magnetized (inset) solutions. Red: $\lambda_{exc} = 220$ nm, black: $\lambda_{exc} = 238$ nm, green: $\lambda_{exc} = 254$ nm, blue: $\lambda_{exc} = 272$ nm.

On the contrary, the optical images in Figure 5 and the XRD patterns reported in Figure 7 show no aragonite crystals in solution (except for the peaks in the XRD pattern in the region 20°-30°).

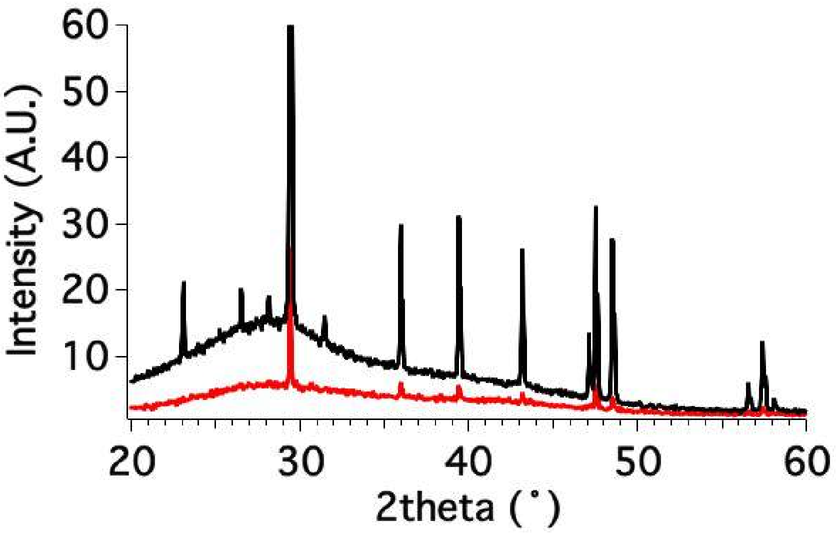

**Figure 7.** XRD patterns of $CaCO_3$ crystals precipitated at 25 °C from non magnetized (red) and magnetized (black) solutions. Spectra are offset along the y-axis.

The discrepancy between the results obtained with the different methods can be explained considering that the sensitivity of the measurements changes depending on the technique, and that the crystals are obtained under different conditions (i.e., concentrations of the starting solutions and equilibration time before the analysis). The dependence of the magnetic effect on several variables, such as supersaturation, pH, ionic strength, intensity of the magnetic field and exposure time is well known and reported in the literature (Chang and Tai, 2010; Tai et al., 2008a).

In the case of Sr(II) and Ba(II) carbonates, there is no effect of the magnetic field on the crystal morphology, as also revealed by the superimposition of fluorescence spectra in Figure 8. However, the suppression of nuclei and the formation of few larger crystals occur for witherite as we previously described for $CaCO_3$. Accordingly, the intensity of the emission spectra is lower in the case of $BaCO_3$ from magnetized solutions. Instead, in the case of strontianite, the exposure to the static MF has the opposite effect, inducing the precipitation of smaller crystals, as can be observed both from optical micrographs and from fluorescence emission spectra.

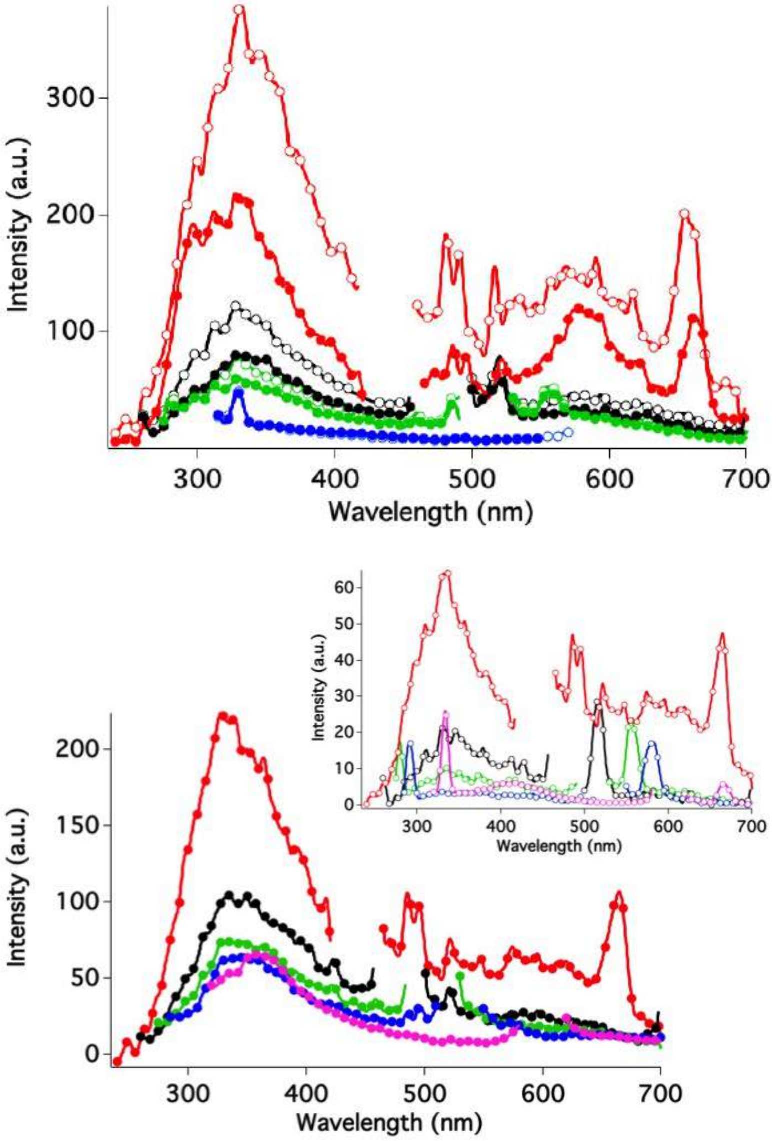

**Figure 8.** Fluorescence excitation spectra of $BaCO_3$ (top) and $SrCO_3$ (bottom) crystals in solution at 25 °C starting from magnetized (filled circles) and non magnetized (empty circles) solutions. Red: $\lambda_{exc} = 220$ nm, black: $\lambda_{exc} = 238$ nm, green: $\lambda_{exc} = 255$ nm, blue: $\lambda_{exc} = 265$ nm for $SrCO_3$ and 296 nm for $BaCO_3$, purple: $\lambda_{exc} = 300$ nm.

External magnetic fields affect also the formation of sulfate scales (Silva et al., 2015), but in this case it was found that there are no significant changes in the crystalline structure of $CaSO_4$ crystals after magnetic treatment of the reactants. We confirm the same result by means of optical micrographs (Figure 9), where the formation of gypsum ($CaSO_4{\cdot}2H_2O$) needle-like crystals is visible in the case of both magnetized and non magnetized solutions at room temperature. Furthermore, it is also reported the opposite effect of MF on the size of sulfate crystals with respect to calcium carbonate: $CaSO_4$ crystals obtained from magnetized solutions are smaller than those precipitated from untreated solutions. Optical micrographs are in agreement with the previous findings and similar results can be obtained also from fluorescence spectra (Figure S2, Supplementary Material), where the higher intensity of the emission signals associated to the magnetized sample is compatible with the presence of a large amount of small crystals in solution compared to the case of the non magnetized sample.

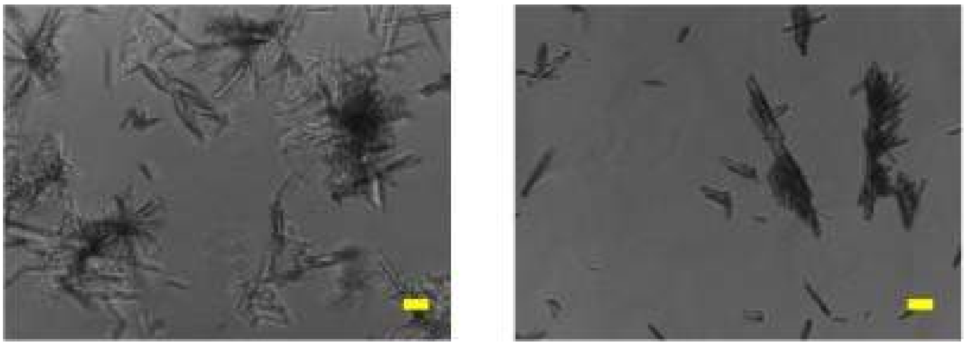

**Figure 9.** Optical micrographs of calcium sulfate precipitated at 25 °C immediately after the mixing of non magnetized (left) and magnetized (right) solutions. Scale bar: 100 μm.

### *3.3 Combined effect of high temperature and magnetic field*

We report here on the combined effect of both temperature and magnetic field. Figure 10 shows the optical micrographs of Ca(II), Sr(II) and Ba(II) carbonates from magnetized solutions at 25 and 60 °C.

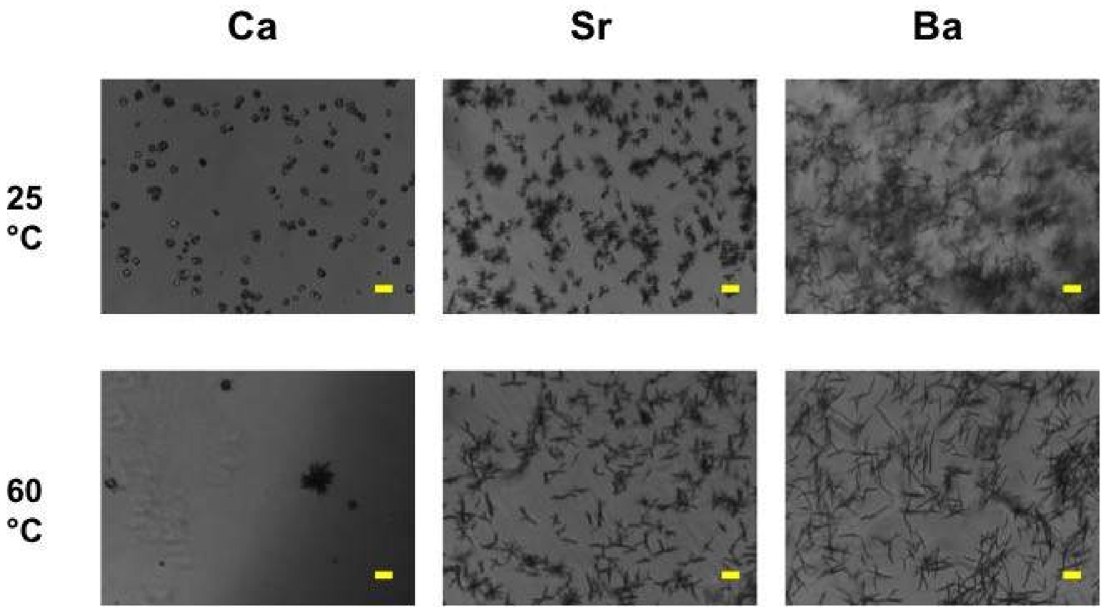

**Figure 10.** Optical micrographs of calcium, strontium and barium carbonates precipitated at 25 (top) and 60 (bottom) °C after 60 minutes from the mixing of magnetized solutions. Scale bar: 100 µm.

In the case of $CaCO_3$, the optical images reveal that the combination of high temperatures and MF leads to: i) a good conversion of calcite into aragonite and ii) a strong suppression of the number of crystals in solution. XRD measurements (Figure 11) show a strong decrease in the signals associated with calcite compared to those obtained after the treatment with the magnetic field at 25 °C where a significant contribution of aragonite peaks appears.

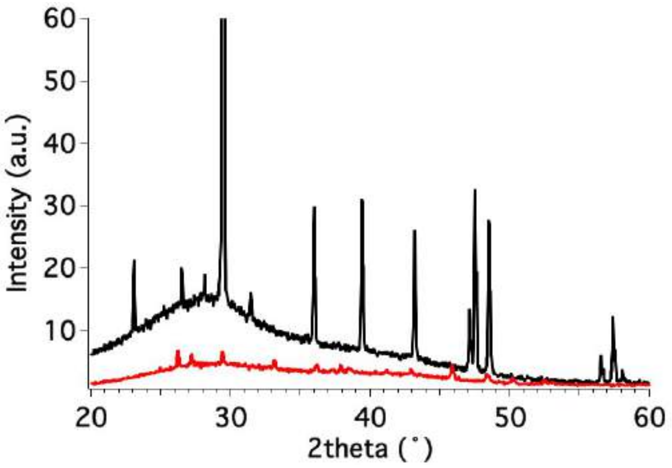

**Figure 11.** XRD patterns of $CaCO_3$ crystals precipitated after the magnetic treatment at 25 (black) and 60 (red) °C. Spectra are offset along the y-axis.

The fluorescence spectra shown in Figure 12 indicate an enhancement in the emission peaks of aragonite when $CaCO_3$ is precipitated at high temperature from magnetized solutions. The sample obtained at 60 °C in the presence of MF produces emission signals roughly twice as intense as those obtained at 25 °C after magnetization of the solutions, indicating the presence of larger amounts of small crystals. The comparison of these results with those obtained from the sample precipitated at 60 °C without any magnetic treatment suggest that the kind of polymorph in solution depends mainly on the temperature. There is an increase in the aragonite content at higher temperatures, while the magnetization prior to mixing the reactants can reduce the amount of precipitate. The preferential growth of aragonite in the presence of the magnetic field and at high temperature was proved in the past by Tai et al. (Tai et al., 2011).

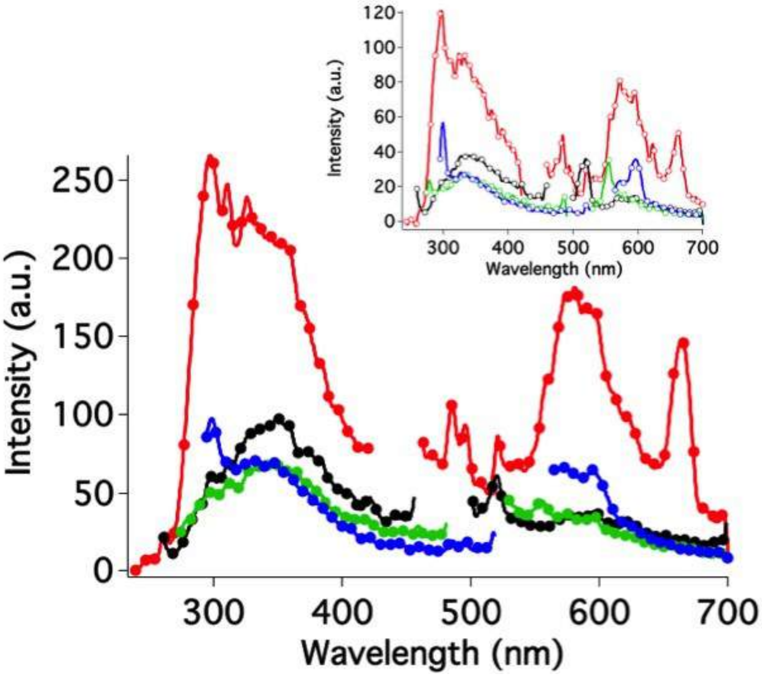

**Figure 12.** Fluorescence excitation spectra of $CaCO_3$ crystals in solution at 25 (inset) and 60 °C (filled circles) in the case of magnetized solutions. Red: $\lambda_{exc}$ = 220 nm, black: $\lambda_{exc}$ = 238 nm, green: $\lambda_{exc}$ = 254 nm, blue: $\lambda_{exc}$ = 272 nm.

Similar results were obtained for witherite and strontianite from optical images. As in the previous cases the crystal morphology remains unchanged, while the formation of fewer larger crystals is favoured. These results are confirmed by the reduction in the intensity of fluorescence spectra (Figure 13) for $SrCO_3$ and $BaCO_3$ when exposed to MF and mixed at high temperature.

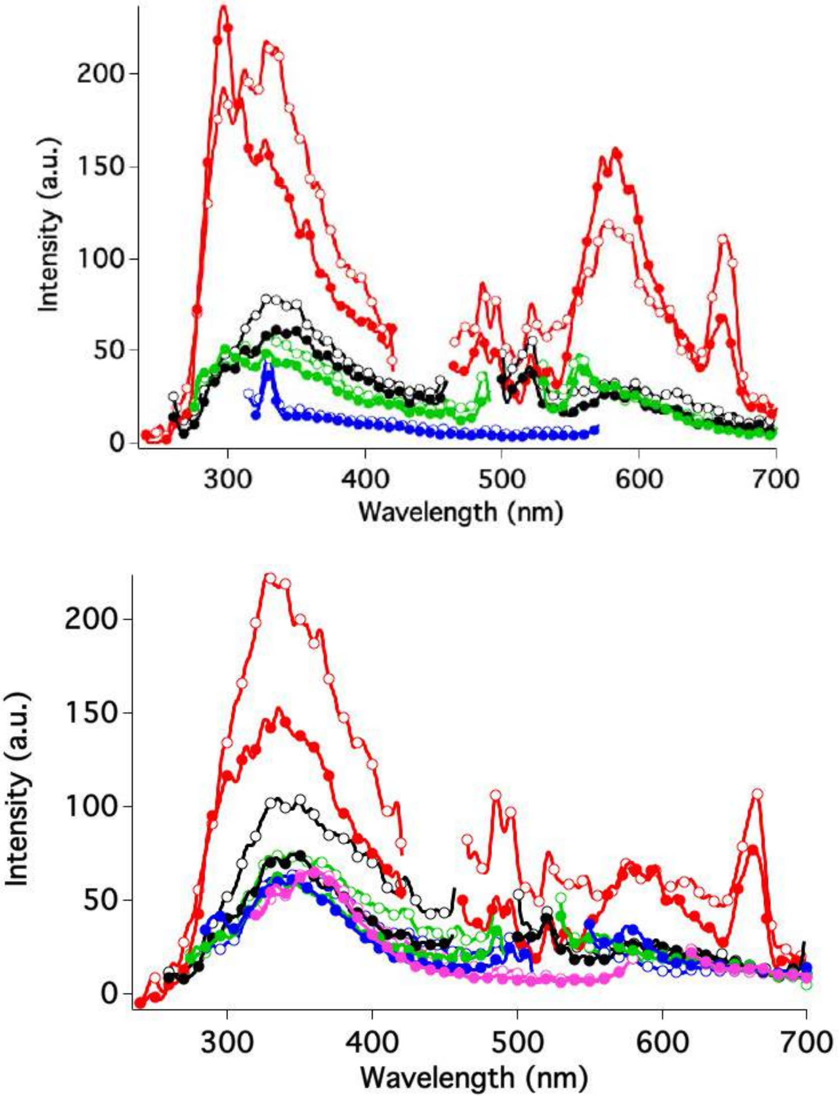

**Figure 13.** Fluorescence excitation spectra of $BaCO_3$ (top) and $SrCO_3$ (bottom) crystals in solution at 25 (empty circles) and 60 °C (filled circles) in the case of magnetized solutions. Red: $\lambda_{exc}$ = 220 nm, black: $\lambda_{exc}$ = 238 nm, green: $\lambda_{exc}$ = 255 nm, blue: $\lambda_{exc}$ = 265 nm for $SrCO_3$ and 296 nm for $BaCO_3$, purple: $\lambda_{exc}$ = 300 nm

In conclusion, the experimental results suggest that the crystal growth is favoured with respect to the nucleation step when high temperature and MF are combined together during the precipitation of the alkaline earth insoluble salts. In addition, the combination of these two parameters affects the allotropic form of $CaCO_3$ crystals, promoting the formation of aragonite. With this in mind, the combined application of high temperature and external magnetic fields can be an easy and feasible way to control scale formation and limit the problem of pipes obstruction.

### 3.4 Effect of deuterium oxide

The same experiments on the precipitation of $CaCO_3$ were performed in $D_2O$ solutions in order to study the behaviour of the system in a different solvent. Figure 14 summarizes the results obtained from optical microscopy and the comparison with those obtained from $H_2O$ solutions.

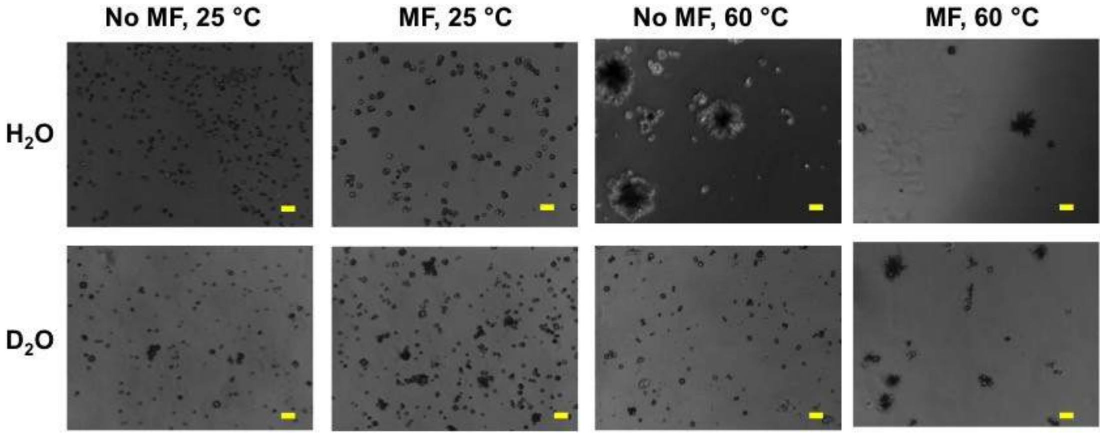

**Figure 14.** Optical micrographs of calcium carbonate in water (top) and deuterium oxide (bottom) precipitated after 60 minutes from the mixing of the starting solutions in the case of magnetically treated or untreated samples and at the two studied temperatures. Scale bar: 100 µm.

The main results are:

1) All $D_2O$ samples show the formation of smaller crystals with respect to $H_2O$ solutions, in line with the higher intensity of the fluorescence spectra due to the presence of larger amounts of smaller crystals in suspension (all fluorescence measurements for the samples in $D_2O$ at different temperatures are reported in Figure S3 in the Supplementary Material).

2) Regarding the polymorphs that precipitate from the solutions, we observed the same behaviour already recorded in the case of water solutions: at room temperature, vaterite and calcite are the predominant polymorphs, while an increase in T favours the formation of needle-like aragonite crystals. However, the conversion of calcite into aragonite seems to be less favoured in $D_2O$.

3) The magnetic field is less effective in the case of $D_2O$ solutions: this is reflected in the formation of a larger amount of crystals with smaller size, as shown by the optical images. This behaviour is detected both at 25 and 60 °C. In particular, at 60 °C, the effect of the magnetic treatment is less marked than that in water even if a synergistic effect between high temperature and MF is still at work with a higher content in aragonite in the sample.

A further evidence of the lower effect of the MF in the case of $D_2O$ solutions comes from the analysis of the XRD spectra reported in Figure 15. These show that the conversion of calcite into aragonite is more evident in the sample exposed to the MF at 60 °C in water with respect to the corresponding item prepared in $D_2O$.

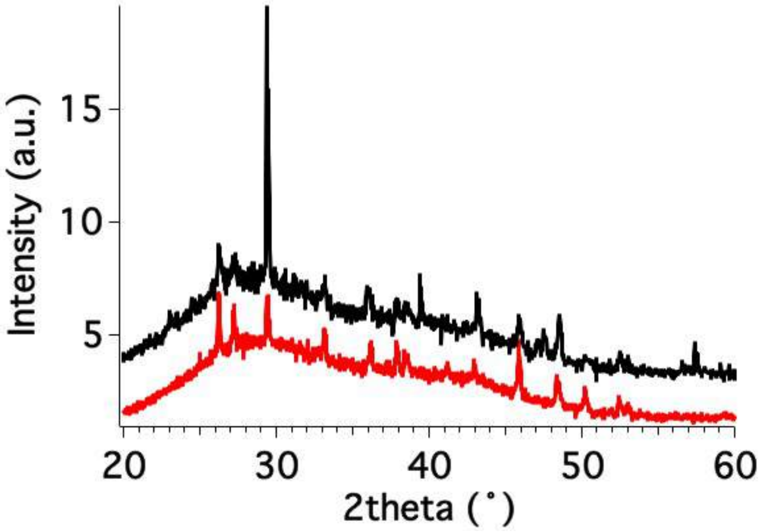

**Figure 15.** XRD patterns of $CaCO_3$ crystals precipitated at 60 °C from $D_2O$ (black) and $H_2O$ (red) solutions of the precursors after the magnetic treatment. Spectra are offset along the y-axis.

The same result is obtained from the fluorescence spectra in water or deuterium oxide reported in Figure 16. The sample precipitated from $D_2O$ shows strong emission signals at 300 ($\lambda_{exc}$ = 272 nm) and 600 nm ($\lambda_{exc}$ = 238 and 254 nm) due to the presence of large amounts of calcite crystals. However, the evidence of the shoulder centred at 555 nm ($\lambda_{exc}$ = 254 nm) indicates the presence of a significant amount of aragonite, according to the optical micrographs. On the other hand, the sample obtained from water solutions mainly exhibits the emission signals of aragonite, especially in the region 500-700 nm, where the peaks centred at 600 nm observed for calcite were not detected.

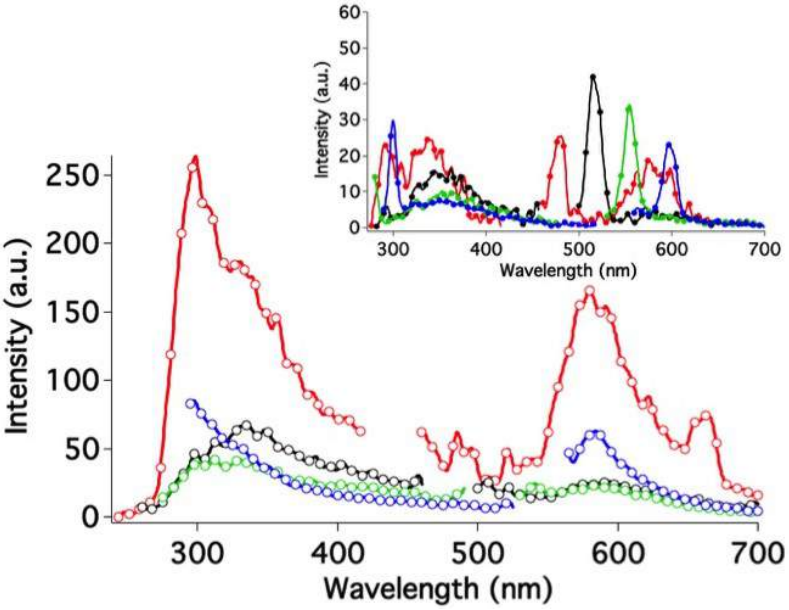

**Figure 16.** Fluorescence excitation spectra of $CaCO_3$ crystals in solution precipitated at 60 °C after the exposure of $H_2O$ (inset) and $D_2O$ (empty circles) solutions to the magnetic field. Red: $\lambda_{exc}$ = 220 nm, black: $\lambda_{exc}$ = 238 nm, green: $\lambda_{exc}$ = 254 nm, blue: $\lambda_{exc}$ = 272 nm.

### 3.5 *Effect of the anion and of the cation*

Previous experiments by Highashitani (Higashitani et al., 1993) and Barrett (Barrett and Parsons, 1998) evidenced that the magnetic field influences the precipitation of $CaCO_3$ by changing the properties of $Na_2CO_3$ solutions and not those of the co-reactant $CaCl_2$. In order to investigate this specific insight, we performed the precipitation of calcium carbonate after the magnetic treatment of only one reactant, i.e. either the anion or the cation solutions. Moreover we studied the effect due to water and $D_2O$. The results are compared to those obtained on crystals precipitated after the magnetic treatment of both the ion precursors. Figure 17 shows the optical images of the samples obtained at 25 °C, while the results at 60 °C are reported in Figure S4, in the Supplementary Material.

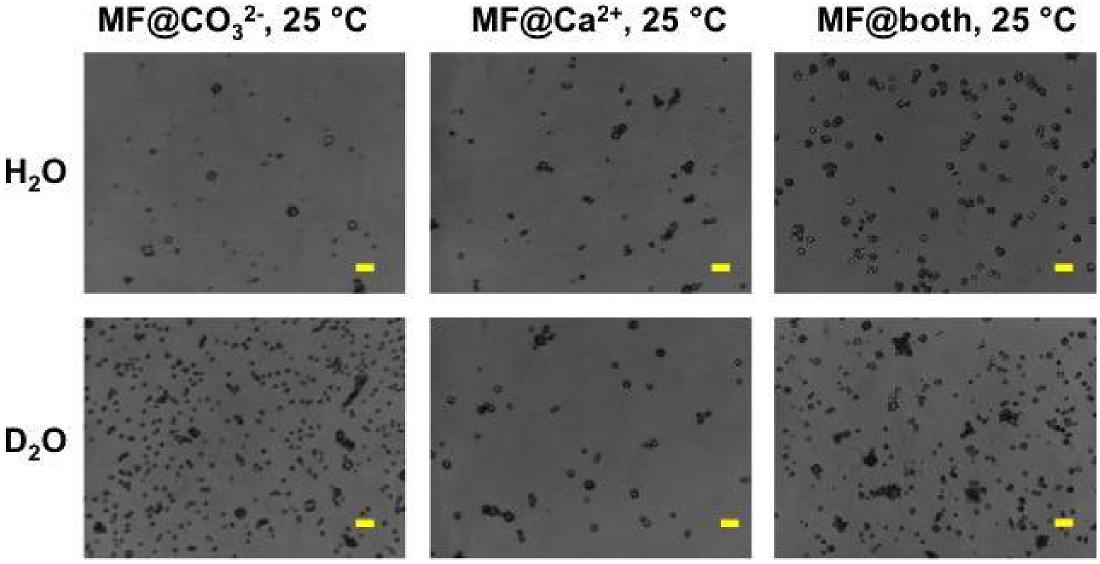

**Figure 17.** Optical micrographs of calcium carbonate precipitated at 25 °C after 60 minutes from the mixing of magnetized $CaCl_2$ with untreated $Na_2CO_3$, magnetized $Na_2CO_3$ with untreated $CaCl_2$, magnetized $CaCl_2$ and $Na_2CO_3$ in water (top) and $D_2O$ (bottom). Scale bar: 100 μm.

In the case of $H_2O$ solutions, a strong suppression of the nucleation and therefore the formation of bigger crystals occur after magnetization of the carbonate solution. This result suggests that MF mainly influences the properties of the anion rather than those of the cation and this concurs with previous observations in the literature. Accordingly, the emission signals at 350 and 555 nm associated with aragonite are slightly more intense in the sample obtained after the magnetization of carbonate solution (see fluorescence spectra reported in Figure 18; the results of fluorescence experiments at 60 °C are reported in Figure S5, in the Supplementary Material).

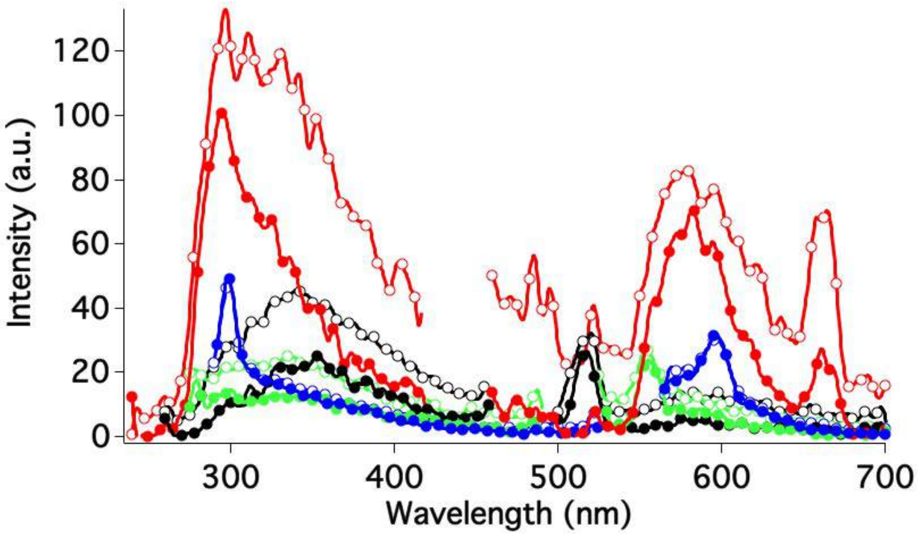

**Figure 18.** Fluorescence excitation spectra of $CaCO_3$ crystals in solution precipitated at 25 °C starting from magnetized $CaCl_2$ (empty circles) or $Na_2CO_3$ (filled circles) solutions mixed with untreated sodium carbonate and calcium chloride, respectively. Red: $\lambda_{exc} = 220$ nm, black: $\lambda_{exc} = 238$ nm, green: $\lambda_{exc} = 254$ nm, blue: $\lambda_{exc} = 272$ nm.

In the case of $D_2O$ solutions, we observed that: i) the magnetic effect is less remarkable than that in water, as already discussed in the previous section; ii) the strongest effect is provided by exposing to the magnetic field the $Ca^{2+}$ solution and not the $CO_3^{2-}$ solution.

## 4. Discussion

Several efforts have been made in the past to discover the mechanisms that determine the "magnetized effect of water", including intra-atomic effects (e.g. changes in the electronic configuration), changes in the ionic hydration of ions, and interfacial effects, like the distortion of the double layer (Ayrapetyan et al., 1994; Kozic and Lipus, 2003). The effect of MF on pure water was recently investigated by evaluating the changes induced by the magnetic field on both microscopic and macroscopic properties of water. The direct observation of changes in infrared, Raman, visible, UV and X-ray spectra of magnetized water with respect to untreated water suggests that an external magnetic field causes displacements and polarization of molecules and atoms, thus changing the dipole moment of water molecules in the transition and vibrational states (Pang and Deng, 2008). In addition, variations of the macroscopic properties of magnetically treated water, such as contact angle (Otsuka and Ozeki, 2006), viscosity (Viswat et al., 1982), boiling point (Y. Wang et al., 2018), evaporation rate (Guo et al., 2012), surface tension (Cai et al., 2009), revealed that magnetic treatments increase the number of hydrogen bonds (HB) between water molecules, thus favouring the formation of larger water clusters and then affecting its macroscopic properties. This peculiar behavior was explained on the basis of the structure of liquid water: since each water molecule has a dipole moment of 1.84 D at room temperature, many linear and closed hydrogen-bonded chains consisting of polarized water molecules exist together with free molecules. When an external magnetic field is applied to the system, the presence of the HB clusters is responsible for a ring proton-current in the closed hydrogen-bond chains that can interact with the MF, thus inducing an ordering effect on the water molecules around the hydrogen-bonded chains (Pang, 2006). Considering that $D_2O$ is more strongly hydrogen bonded (structured) than $H_2O$ (Soper and Benmore, 2008; Swain and Bader, 1960), its more ordered structure has a smaller tendency to be affected by the action of an external magnetic field with respect to water: this is in good agreement with our observations, that reveal a smaller influence of the magnetic field on $D_2O$ solutions both at 25 and 60 °C.

In the presence of ions in solution, AFM measurements evidenced the magnetic thickening of the water adsorbed layer on the particle surface (Higashitani and Oshitani, 1998). This in turn causes an increment in the apparent radius of the hydrated ion, a lower mobility of the ion in solution and thus a reduction in the coagulation rate: this mechanism explains the suppression of the nucleation observed for magnetized solutions.

Previous works also demonstrated that the magnetic response of the solution strictly depends on the structuring effect of the ions on water: it was found that the magnetic effect is stronger on structure-disordering (chaotropic) ions, while no effects are detected in solutions of structure-ordering (kosmotropic) ions (Oshitani et al., 1999). This can be explained considering that kosmotropes strongly interact with water molecules in their hydration shell inducing an ordering of the surrounding water. Hence, water around kosmotropic ions is less sensitive to external forces, such as the presence of a magnetic field. This explanation is in line with our findings that reveal the strongest magnetic effect upon exposure of the anion $CO_3^{2-}$ to the magnetic field: even if both $Ca^{2+}$ and $CO_3^{2-}$ are kosmotropic ions, $Ca^{2+}$ is more ordering than carbonate and less affected by the MF (see Table 1 for the values of the Gibbs free energy of hydration and number of water molecules in the hydration shell of the studied ions (Marcus, 1991)).

**Table 1.** Values of the Gibbs free energy of hydration ($-\Delta G_{hydr}$, in kJ/mol), the radius (r, in nm) and the width ($\Delta r$, in nm) of the hydration shell, and number of water molecules in the hydration shell (n) for the different ions (Marcus, 1991).

| **ion** | **$-\Delta G_{hydr}$** | **r** | **$\Delta r$** | **n** |
|---|---|---|---|---|
| $CO_3^{2-}$ | 1315 | 0.178 | 0.076 | 4.0 |
| $Cl^-$ | 340 | 0.181 | 0.043 | 2.0 |
| $SO_4^{2-}$ | 1080 | 0.230 | 0.043 | 3.1 |
| $Ca^{2+}$ | 1505 | 0.100 | 0.171 | 7.2 |
| $Sr^{2+}$ | 1380 | 0.113 | 0.150 | 6.4 |
| $Ba^{2+}$ | 1250 | 0.136 | 0.118 | 5.3 |

However, this is probably not the sole effect because sulfate and carbonate, which are both kosmotropic ions, behave in opposite ways. Indeed, it is reported in the literature that the strength of the magnetic effect could also depend on the diamagnetic/paramagnetic nature of the ions in solution (Freitas et al., 1999; Madsen, 1995). However, this issue needs to be further considered and more experiments have to be acquired, for example using an alternating magnetic field.

In passing, we note that the trend of the magnetic effect $Ba^{2+}<Sr^{2+}<Ca^{2+}$ follows the “law of matching water affinity” proposed by Collins that relates the feasibility for the formation of ion pairs to the hydration properties of the cation and of the anion (Collins, 2012).

All the results discussed here suggest that one of the factors that has to be taken into account to explain the magnetic effect is the change in the solvent structure induced by the magnetic field, which in turn affects the hydration of the ions and salts precipitation. However, the influence of magnetic field on other parameters, such as the diffusion and the convection of particles in solution recently proposed by Heijna (Heijna et al., 2007), or the effect of solvent chirality on the response to an external magnetic field should be taken into account as well.

## 5. Conclusions

This work presents an extensive study of the effect of a static magnetic field on the precipitation of Ca(II), Sr(II) and Ba(II) insoluble salts. Although the magnetic effect is still not completely understood and the results on this topic are controversial, all the results discussed here lead back to the strong effect of the magnetic field on the solvent structure. Since different ions show a different influence on the structure of the surrounding water molecules, the response to the magnetic treatment changes depending on the magnetically treated ions. The same observation can be inferred from the results obtained in the case of calcium carbonate precipitation from heavy water solutions: since $D_2O$ is more structured than light water, it is less affected by the magnetic field.

The use of new techniques, such as fluorescence, the investigation of parameters such as the chemical nature of the treated ions and the solvent composition provide a new interpretation of the effect of a static magnetic field on the precipitation of poorly soluble salts such as carbonates and sulfates of alkali earth ions. The results are of interest in fundamental science to better explain the mechanism that rules the magnetic effect on water. Further experiments will be carried out in the future by extending the study of the magnetic effect to potassium salts, to the effect of pressure and salt concentration. In conclusion, this work can find potential applications in several fields, such as the magnetic treatment of wastewater or as a green strategy for the reduction of radioactive materials extraction in shale gas/oil basins.

## Acknowledgments

The authors acknowledge the European Union Horizon 2020 research and innovation program "Shale for Environment" (SXT) under grant agreement Nr. 640979.

## Supplementary Material

Supplementary data related to this article: Table S1 and S2, Figures S1-S5.

## References

Ambashta, R.D., Sillanpää, M., 2010. Water purification using magnetic assistance: A review. J. Hazard. Mater. 180, 38–49. https://doi.org/10.1016/j.jhazmat.2010.04.105

Ayrapetyan, S.N., Grigorian, K.V., Avanesian, A.S., Stamboltsian, K.V., 1994. Magnetic fields alter electrical properties of solutions and their physiological effects. Bioelectromagnetics 15, 133–142. https://doi.org/10.1002/bem.2250150205

Baker, J.S., Judd, S.J., 1996. Magnetic amelioration of scale formation. Water Res. 30, 247–260. https://doi.org/10.1016/0043-1354(95)00184-0

Barrett, R.A., Parsons, S.A., 1998. The influence of magnetic fields on calcium carbonate precipitation. Water Res. 32, 609–612. https://doi.org/10.1016/S0043-1354(97)00277-7

Bolto, B., Dixon, D., Eldridge, R., King, S., Linge, K., 2002. Removal of natural organic matter by ion exchange. Water Res. 36, 5057–5065. https://doi.org/10.1016/S0043-1354(02)00231-2

Buchachenko, A.L., Orlov, A.P., Kuznetsov, D.A., Breslavskaya, N.N., 2013. Magnetic isotope and magnetic field effects on the DNA synthesis. Nucleic Acids Res. 41, 8300–8307. https://doi.org/10.1093/nar/gkt537

Bunkin, N.F., Kozlov, V.A., Shkirin, A.V., Ninham, B.W., Balashov, A.A., Gudkov, S.V., 2018. Dynamics of Nafion membrane swelling in $H_2O/D_2O$ mixtures as studied using FTIR technique. J. Chem. Phys. 148, 124901. https://doi.org/10.1063/1.5022264

Busch, K.W., Busch, M.A., 1997. Laborator studies on magnetic water treatment and their relationship to a possible mechanism for scale reduction. Desalination 109, 131–148. https://doi.org/10.1016/S0011-9164(97)00059-3

Cai, R., Yang, H., He, J., Zhu, W., 2009. The effects of magnetic fields on water molecular hydrogen bonds. J. Mol. Struct. 938, 15–19. https://doi.org/10.1016/j.molstruc.2009.08.037

Chang, M.-C., Tai, C.Y., 2010. Effect of the magnetic field on the growth rate of aragonite and the precipitation of CaCO3. Chem. Eng. J. 164, 1–9. https://doi.org/10.1016/j.cej.2010.07.018

Chen, P.-C., Cheng, G.Y., Kou, M.H., Shia, P.Y., Chung, P.O., 2001. Nucleation and morphology of barium carbonate crystals in a semi-batch crystallizer. J. Cryst. Growth 226, 458–472. https://doi.org/10.1016/S0022-0248(01)01408-7

Collins, K.D., 2012. Why continuum electrostatics theories cannot explain biological structure, polyelectrolytes or ionic strength effects in ion–protein interactions. Biophys. Chem. 167, 43–59. https://doi.org/10.1016/j.bpc.2012.04.002

Day, C., 2005. Crushing a Solution of Left-Handed and Right-Handed Crystals Breaks Its Chiral Symmetry. Phys. Today 58, 21–22. https://doi.org/10.1063/1.1955467

Earnest, C.M., Miller, E.T., 2017. An assessment of barium and strontium carbonates as temperature and enthalpy standards. J. Therm. Anal. Calorim. 130, 2277–2282. https://doi.org/10.1007/s10973-017-6539-2

Ebner, A.D., Ritter, J.A., Nuñez, L., 1999. HIGH-GRADIENT MAGNETIC SEPARATION FOR THE TREATMENT OF HIGH-LEVEL RADIOACTIVE WASTES. Sep. Sci. Technol. 34, 1333–1350. https://doi.org/10.1080/01496399908951096

Freitas, A.M.B., Landgraf, F.J.G., Nvltỳ, J., Giulietti, M., 1999. Influence of magnetic field in the kinetics of crystallization of diamagnetic and paramagnetic inorganic salts. Cryst. Res. Technol. J. Exp. Ind. Crystallogr. 34, 1239–1244. https://doi.org/10.1002/(SICI)1521-4079(199912)34:10<1239::AID-CRAT1239>3.0.CO;2-9

Fujiki, M., 2014. Supramolecular Chirality: Solvent Chirality Transfer in Molecular Chemistry and Polymer Chemistry. Symmetry 6, 677–703. https://doi.org/10.3390/sym6030677

Gaft, M., Reisfeld, R., Panczer, G., 2015. Modern luminescence spectroscopy of minerals and materials. Springer.

García, A.V., Thomsen, K., Stenby, E.H., 2006. Prediction of mineral scale formation in geothermal and oilfield operations using the Extended UNIQUAC model. Geothermics 35, 239–284. https://doi.org/10.1016/j.geothermics.2006.03.001

Gryta, M., 2011. The influence of magnetic water treatment on CaCO3 scale formation in membrane distillation process. Sep. Purif. Technol. 80, 293–299. https://doi.org/10.1016/j.seppur.2011.05.008

Guo, G., Yan, G., Wang, L., Huang, J., 2008. Crystallization of strontium carbonate in alcohol or water solution containing mixed nonionic/anionic surfactants. Mater. Lett. 62, 4018–4021. https://doi.org/10.1016/j.matlet.2008.05.052

Guo, Y.-Z., Yin, D.-C., Cao, H.-L., Shi, J.-Y., Zhang, C.-Y., Liu, Y.-M., Huang, H.-H., Liu, Y., Wang, Y., Guo, W.-H., Qian, A.-R., Shang, P., 2012. Evaporation Rate of Water as a Function of a Magnetic Field and Field Gradient. Int. J. Mol. Sci. 13, 16916–16928. https://doi.org/10.3390/ijms131216916

Gutierrez, A.M., Dziubla, T.D., Hilt, J.Z., 2017. Recent advances on iron oxide magnetic nanoparticles as sorbents of organic pollutants in water and wastewater treatment. Rev. Environ. Health 32. https://doi.org/10.1515/reveh-2016-0063

Hamidzadeh, S., Torabbeigi, M., Shahtaheri, S.J., 2015. Removal of crystal violet from water by magnetically modified activated carbon and nanomagnetic iron oxide. J. Environ. Health Sci. Eng. 13. https://doi.org/10.1186/s40201-015-0156-4

Heijna, M.C.R., Poodt, P.W.G., Tsukamoto, K., de Grip, W.J., Christianen, P.C.M., Maan, J.C., Hendrix, J.L.A., van Enckevort, W.J.P., Vlieg, E., 2007. Magnetically controlled gravity for protein crystal growth. Appl. Phys. Lett. 90, 264105. https://doi.org/10.1063/1.2752718

Higashitani, K., Kage, A., Katamura, S., Imai, K., Hatade, S., 1993. Effects of a Magnetic Field on the Formation of CaCO3 Particles. J. Colloid Interface Sci. 156, 90–95. https://doi.org/10.1006/jcis.1993.1085

Higashitani, K., Oshitani, J., 1998. Magnetic Effects on Thickness of Adsorbed Layer in Aqueous Solutions Evaluated Directly by Atomic Force Microscope. J. Colloid Interface Sci. 204, 363–368. https://doi.org/10.1006/jcis.1998.5590

Holcomb, R.R., 1989. Magnetic water treatment device.

Holysz, L., Chibowski, M., Chibowski, E., 2002. Time-dependent changes of zeta potential and other parameters of in situ calcium carbonate due to magnetic field treatment. Colloids Surf. Physicochem. Eng. Asp. 208, 231–240. https://doi.org/10.1016/S0927-7757(02)00149-8

Khamehchi, E., Kaldozakh, H., Arman, S., Alizadeh, A., 2017. An Experimental Investigation of Magnetized Water Effect on Formation Damage. J. Pet. Sci. Technol. 7, 65–76. https://doi.org/10.22078/jpst.2017.2448.1419

Kobe, S., Dražić, G., Cefalas, A.C., Sarantopoulou, E., Stražišar, J., 2002. Nucleation and crystallization of CaCO3 in applied magnetic fields. Cryst. Eng. 5, 243–253. https://doi.org/10.1016/S1463-0184(02)00035-7

Kochen, R.L., Navratil, J.D., 1997. Removal of radioactive materials and heavy metals from water using magnetic resin. US5595666A.

Kodel, K.A., Andrade, P.F., Valença, J.V.B., Souza, D. do N., 2012. Study on the composition of mineral scales in oil wells. J. Pet. Sci. Eng. 81, 1–6. https://doi.org/10.1016/j.petrol.2011.12.007

Kontoyannis, C.G., Vagenas, N.V., 2000. Calcium carbonate phase analysis using XRD and FT-Raman spectroscopy. The Analyst 125, 251–255. https://doi.org/10.1039/a908609i

Kozic, V., Lipus, L.C., 2003. Magnetic Water Treatment for a Less Tenacious Scale. J. Chem. Inf. Comput. Sci. 43, 1815–1819. https://doi.org/10.1021/ci0102719

Lai, H., Singh, N.P., 2004. Magnetic-field-induced DNA strand breaks in brain cells of the rat. Environ. Health Perspect. 112, 687–694.

Lippmann, F., 1973. Sedimentary Carbonate Minerals. Springer Berlin Heidelberg, Berlin, Heidelberg. https://doi.org/10.1007/978-3-642-65474-9

Lipus, L.C., Dobersek, D., 2007. Influence of magnetic field on the aragonite precipitation. Chem. Eng. Sci. 62, 2089–2095. https://doi.org/10.1016/j.ces.2006.12.051

Lu, A.-H., Salabas, E.L., Schüth, F., 2007. Magnetic Nanoparticles: Synthesis, Protection, Functionalization, and Application. Angew. Chem. Int. Ed. 46, 1222–1244. https://doi.org/10.1002/anie.200602866

Madsen, H.E.L., 1995. Influence of magnetic field on the precipitation of some inorganic salts. J. Cryst. Growth 152, 94–100. https://doi.org/10.1016/0022-0248(95)00103-4

Marcus, Y., 1991. Thermodynamics of solvation of ions. Part 5.—Gibbs free energy of hydration at 298.15 K. J Chem Soc Faraday Trans 87, 2995–2999. https://doi.org/10.1039/FT9918702995

Ninham, B.W., 2017. The Biological/Physical Sciences Divide, and the Age of Unreason. Subst. Vol 1 No 1 2017. https://doi.org/10.13128/substantia-6

Ogino, T., Suzuki, T., Sawada, K., 1987. The formation and transformation mechanism of calcium carbonate in water. Geochim. Cosmochim. Acta 51, 2757–2767. https://doi.org/10.1016/0016-7037(87)90155-4

Okada, H., Hirota, N., Matsumoto, S., Wada, H., 2013. A flow simulation study of protein solution under magnetic forces. J. Appl. Phys. 113, 073913. https://doi.org/10.1063/1.4792650

Oshitani, J., Yamada, D., Miyahara, M., Higashitani, K., 1999. Magnetic effect on ion-exchange kinetics. J. Colloid Interface Sci. 210, 1–7. https://doi.org/10.1006/jcis.1998.5952

Otsuka, I., Ozeki, S., 2006. Does Magnetic Treatment of Water Change Its Properties? J. Phys. Chem. B 110, 1509–1512. https://doi.org/10.1021/jp056198x

Ozay, O., Ekici, S., Baran, Y., Aktas, N., Sahiner, N., 2009. Removal of toxic metal ions with magnetic hydrogels. Water Res. 43, 4403–4411. https://doi.org/10.1016/j.watres.2009.06.058

Pang, X.F., 2006. The conductivity properties of protons in ice and mechanism of magnetization of liquid water. Eur. Phys. J. B 49, 5–23. https://doi.org/10.1140/epjb/e2006-00020-6

Pang, X.-F., Deng, B., 2008. The changes of macroscopic features and microscopic structures of water under influence of magnetic field. Phys. B Condens. Matter 403, 3571–3577. https://doi.org/10.1016/j.physb.2008.05.032

Ross, D.J.K., Bustin, R.M., 2008. Characterizing the shale gas resource potential of Devonian–Mississippian strata in the Western Canada sedimentary basin: Application of an integrated formation evaluation. AAPG Bull. 92, 87–125. https://doi.org/10.1306/09040707048

Ruchon, T., Vallet, M., Thépot, J.-Y., Le Floch, A., Boyd, R.W., 2004. Experimental evidence of magnetochiral interaction in Pasteur's tartrates. Comptes Rendus Phys. 5, 273–277. https://doi.org/10.1016/j.crhy.2004.01.023

Silva, I.B., Queiroz Neto, J.C., Petri, D.F.S., 2015. The effect of magnetic field on ion hydration and sulfate scale formation. Colloids Surf. Physicochem. Eng. Asp. 465, 175–183. https://doi.org/10.1016/j.colsurfa.2014.10.054

Soper, A.K., Benmore, C.J., 2008. Quantum Differences between Heavy and Light Water. Phys. Rev. Lett. 101. https://doi.org/10.1103/PhysRevLett.101.065502

Swain, C.G., Bader, R.F., 1960. The nature of the structure difference between light and heavy water and the origin of the solvent isotope effect—I. Tetrahedron 10, 182–199. https://doi.org/10.1016/S0040-4020(01)97806-8

Tai, C.Y., Chang, M.-C., Shieh, R.-J., Chen, T.G., 2008a. Magnetic effects on crystal growth rate of calcite in a constant-composition environment. J. Cryst. Growth 310, 3690–3697. https://doi.org/10.1016/j.jcrysgro.2008.05.024

Tai, C.Y., Chang, M.-C., Yeh, S.-W., 2011. Synergetic effects of temperature and magnetic field on the aragonite and calcite growth. Chem. Eng. Sci. 66, 1246–1253. https://doi.org/10.1016/j.ces.2010.12.036

Tai, C.Y., Wu, C.-K., Chang, M.-C., 2008b. Effects of magnetic field on the crystallization of CaCO3 using permanent magnets. Chem. Eng. Sci. 63, 5606–5612. https://doi.org/10.1016/j.ces.2008.08.004

Viswat, E., Hermans, L.J.F., Beenakker, J.J.M., 1982. Experiments on the influence of magnetic fields on the viscosity of water and a water-NaCl solution. Phys. Fluids 25, 1794–1796. https://doi.org/10.1063/1.863656

Wan, X., Zhan, Y., Long, Z., Zeng, G., He, Y., 2017. Core@double-shell structured magnetic halloysite nanotube nano-hybrid as efficient recyclable adsorbent for methylene blue removal. Chem. Eng. J. 330, 491–504. https://doi.org/10.1016/j.cej.2017.07.178

Wang, H., Alfredsson, V., Tropsch, J., Ettl, R., Nylander, T., 2013. Formation of CaCO $_3$ Deposits on Hard Surfaces—Effect of Bulk Solution Conditions and Surface Properties. ACS Appl. Mater. Interfaces 5, 4035–4045. https://doi.org/10.1021/am401348v

Wang, L., Hu, D., Kong, X., Liu, J., Li, X., Zhou, K., Zhao, H., Zhou, C., 2018. Anionic polypeptide poly(γ-glutamic acid)-functionalized magnetic Fe 3 O 4 -GO-(o-MWCNTs) hybrid nanocomposite for high-efficiency removal of Cd(II), Cu(II) and Ni(II) heavy metal ions. Chem. Eng. J. 346, 38–49. https://doi.org/10.1016/j.cej.2018.03.084

Wang, Y., Wei, H., Li, Z., 2018. Effect of magnetic field on the physical properties of water. Results Phys. 8, 262–267. https://doi.org/10.1016/j.rinp.2017.12.022

Wray, J.L., Daniels, F., 1957. Precipitation of Calcite and Aragonite. J. Am. Chem. Soc. 79, 2031–2034. https://doi.org/10.1021/ja01566a001

Yavuz, C.T., Prakash, A., Mayo, J.T., Colvin, V.L., 2009. Magnetic separations: From steel plants to biotechnology. Chem. Eng. Sci. 64, 2510–2521. https://doi.org/10.1016/j.ces.2008.11.018

Zaidi, N.S., Sohaili, J., Muda, K., Sillanpää, M., 2014. Magnetic Field Application and its Potential in Water and Wastewater Treatment Systems. Sep. Purif. Rev. 43, 206–240. https://doi.org/10.1080/15422119.2013.794148

Zeng, J., Chen, L., Yang, R., Tong, X., Ren, P., Zheng, Y., 2017. Centrifugal high gradient magnetic separation of fine ilmenite. Int. J. Miner. Process. 168, 48–54. https://doi.org/10.1016/j.minpro.2017.09.005

# The effect of temperature and magnetic field on the precipitation of insoluble salts of alkaline earth metals

Martina Raudino[a], Filippo Sarri[a], Duccio Tatini[a], Moira Ambrosi[a], Giovanni Domenico Aloisi[a], Barry W. Ninham[b], Luigi Dei[a], Pierandrea Lo Nostro[a,c,*]

*a: Department of Chemistry "Ugo Schiff" and CSGI, University of Florence, 50019 Sesto Fiorentino (Firenze), Italy*
*b: Department of Applied Mathematics, Research School of Physical Sciences and Engineering, Australian National University, Canberra ACT 0200, Australia*
*c: Enzo Ferroni Foundation, 50019 Sesto Fiorentino (Firenze), Italy*

## Supplementary Material

## Chemicals

All chemicals were used as received without further purification: dehydrated $CaCl_2$ (Fluka, purity 97%), $BaCl_2 \cdot 2H_2O$ (Merck, purity >99%), $SrCl_2 \cdot 6H_2O$ (Riedel de Haën, purity >99%), $Na_2CO_3 \cdot 10H_2O$ (Merck, purity >99%), $Na_2SO_4$ (Merck, purity ≥99%).

Milli-Q water (resistivity > 18 MΩ cm at 25 °C) or deuterium oxide (EurisoTop, purity 99.9%) were used for the preparation of solutions.

## Excitation wavelengths used for fluorescence experiments

**Table S1.** Excitation wavelengths used for fluorescence measurements on all the studied salts.

| Sample | Excitation wavelength (nm) |
|---|---|
| $CaCO_3$ | 220, 238, 254, 272 |
| $BaCO_3$ | 220, 238, 255, 296 |
| $SrCO_3$ | 220, 238, 255, 265, 300 |
| $CaSO_4$ | 220, 238, 290 |

## Crystallographic parameters for calcite and aragonite

**Table S2.** Structural data of calcite and aragonite crystals. a: (Skinner, A.J., LaFemina, J.P., Jansen, H.J.F., 1994. Structure and bonding of calcite: A theoretical study, American Mineralogist. 79, 205–214.); b: (Medeiros, S.K., Albuquerque, E.L., Maia, F.F., Caetano, E.W.S., Freire, V.N., 2006. Structural, electronic, and optical properties of $CaCO_3$ aragonite, Chem. Phys. Lett. 430, 293–296. doi:10.1016/j.cplett.2006.08.133.); c: (DeFoe, O.K., Compton, A.H., 1925. The Density of Rock Salt and Calcite, Phys. Rev. 25, 618–620. doi:10.1103/PhysRev.25.618.).

| | **Calcite** | **Aragonite** |
|---|---|---|
| Volume of unit cell (Å$^3$) | 122.6$^a$ | 227.1$^b$ |
| Density (g/cm$^3$ at 20 °C) | 2.71$^c$ | 2.93$^c$ |

## Fluorescence spectra of pure calcite and aragonite in water

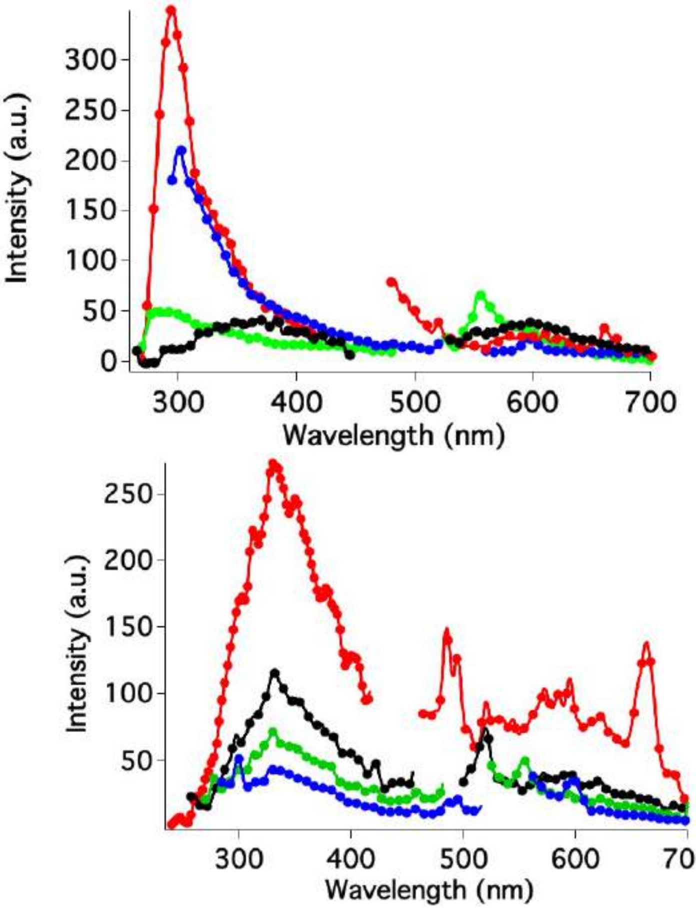

**Figure S1.** Fluorescence excitation spectra of pure calcite (top) and aragonite (bottom) crystals in water at 25 °C.

## Fluorescence spectra of magnetized and non magnetized calcium sulfate

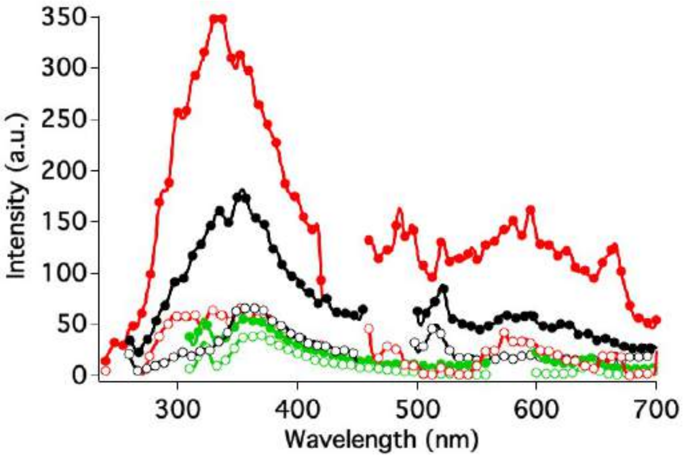

**Figure S2.** Fluorescence excitation spectra of $CaSO_4$ crystals in solution at 25 °C starting from magnetized (filled circles) and non magnetized (empty circles) solutions. Red: $\lambda_{exc} = 220$ nm, black: $\lambda_{exc} = 238$ nm, green: $\lambda_{exc} = 290$ nm.

**Fluorescence measurements on calcium carbonate in $D_2O$ at the two investigated temperatures**

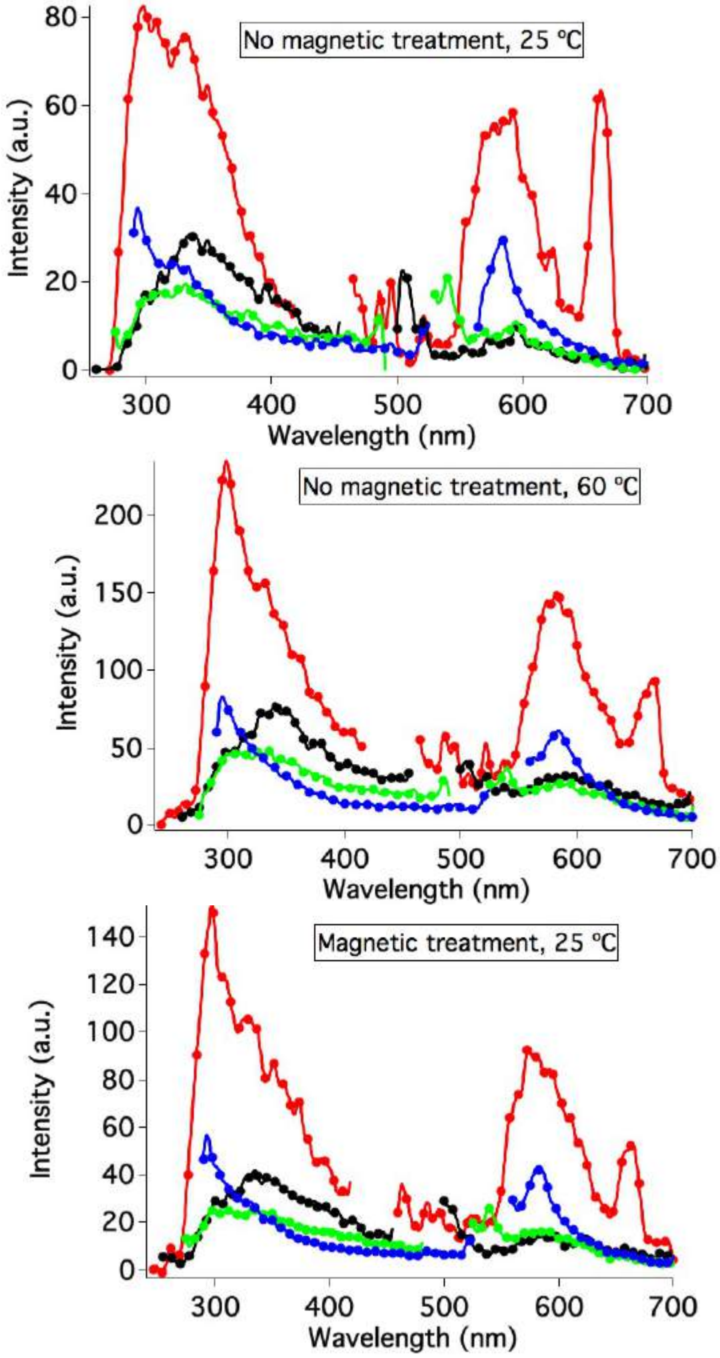

**Figure S3.** Fluorescence excitation spectra of $CaCO_3$ crystals in $D_2O$ solutions with and without the magnetic treatment at the two studied temperatures. Red: $\lambda_{exc}$ = 220 nm, black: $\lambda_{exc}$ = 238 nm, green: $\lambda_{exc}$ = 254 nm, blue: $\lambda_{exc}$ = 272 nm.

## Experiments on the effect of anion/cation magnetization at 60 °C

*Optical microscopy*

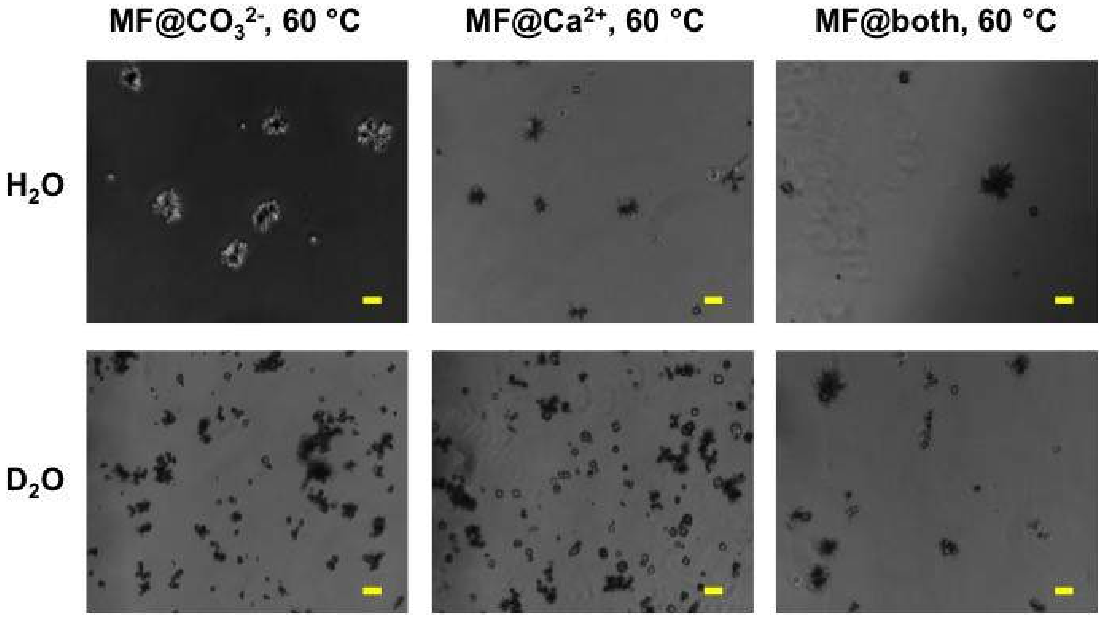

**Figure S4.** Optical micrographs of calcium carbonate precipitated at 60 °C after 60 minutes from the mixing of magnetized $CaCl_2$ with untreated $Na_2CO_3$, magnetized $Na_2CO_3$ with untreated $CaCl_2$, magnetized $CaCl_2$ and $Na_2CO_3$ in water (top) and $D_2O$ (bottom). Scale bar: 100 µm.

*Fluorescence spectra*

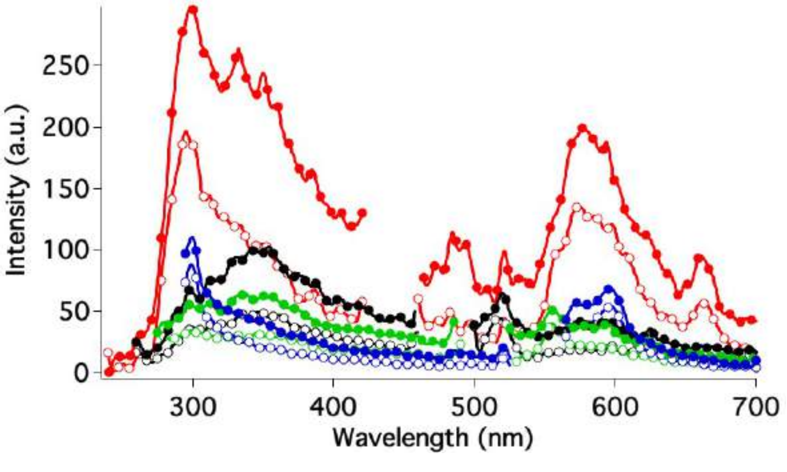

**Figure S5.** Fluorescence excitation spectra of $CaCO_3$ crystals in solution precipitated at 60 °C starting from magnetized $CaCl_2$ (empty circles) or $Na_2CO_3$ (filled circles) solutions mixed with untreated sodium carbonate and calcium chloride, respectively. Red: $\lambda_{exc}$ = 220 nm, black: $\lambda_{exc}$ = 238 nm, green: $\lambda_{exc}$ = 254 nm, blue: $\lambda_{exc}$ = 272 nm.